Design and modeling of a space docking mechanism for cooperative on-orbit servicing

ScuDo
Scuola di Dottorato ~ Doctoral School
WHAT YOU ARE, TAKES YOU FAR

Doctoral Dissertation
Doctoral Program in Mechanical Engineering (29^{th}cycle)

Design and modeling of a space docking mechanism for cooperative on-orbit servicing

By

Tharek Mohtar

******

Supervisor:
Prof. Stefano Pastorelli, Supervisor

Doctoral Examination Committee:
Prof. Riccardo Bevilacqua, Referee, University of Florida
Prof. Ferruccio Resta, Referee, Politecnico di Milano

Politecnico di Torino
2018

Declaration

I hereby declare that, the contents and organization of this dissertation constitute my own original work and does not compromise in any way the rights of third parties, including those relating to the security of personal data.

Tharek Mohtar
2018

* This dissertation is presented in partial fulfillment of the requirements for **Ph.D. degree** in the Graduate School of Politecnico di Torino (ScuDo).

For mom and dad

Abstract

This dissertation addresses the design procedure of a docking mechanism for space applications, in particular, on-orbit servicing of cooperative satellites. The mechanism was conceived to comply with the technical specifications of the STRONG mission. The objective of this mission is to deploy satellite platforms using a space tug with electric propulsion. This mission is part of the SAPERE project, which focuses on space exploration and access to space. A docking mechanism is used for recovering the misalignments left by the guidance, navigation, and control system of the servicer satellite when approaching the customer spacecraft. However, most importantly, the mechanism must safely dissipate the energy associated with the relative velocities between the spacecraft upon contact. Five concepts were considered as possible candidates for the docking mechanism: a system based on the Stewart-Gough platform with a position controller, a Stewart-Gough platform with impedance control, a central passive mechanism (probe-drogue), a central active mechanism, and a mechanism equipped with articulated arms. Several trade-off criteria were defined and applied to the concepts. The result of this trade study was the selection of the central passive mechanism as the most balanced solution. This mechanism is composed of a probe and a conical frustum equipped with a socket to capture the probe. It was further developed and tested using mathematical models of the docking maneuver. The results of the simulations showed that the passiveness of the system prevented the docking maneuver from being fully accomplished. Consequently, a second design iteration was performed. In this new iteration, the degrees of freedom of the mechanism were increased by adding two controlled linear axes in series with the degrees of freedom of the preliminary design. The electromechanical actuators and transmissions of this mechanism were selected following the guidelines of The ECSS standards. Also, in this case, numerical models were used to assess the functioning of the docking system. The results produced by these models demonstrated the suitability of the mechanism for completing the docking operation defined by the

mission's specifications. Furthermore, the results also showed the architecture and functioning of the mechanism to be possibly suitable for other cooperative docking operations between small and mid-sized satellites. In addition, the definition of the mechanical details as well as the control architecture led to the complete design of an engineering prototype for laboratory tests. In this regard, the laboratory tests were defined with the scope of verifying the different operating modes of the docking mechanism. The test rig was designed to be equipped with a serial manipulator connected to the female part of the mechanism through a force and torque module. The objective will be to simulate the relative motion between the docking halves using different techniques to generate the trajectory of the manipulator.

Contents

List of Figures

List of Tables

List of acronyms

APAS Androgynous Peripheral Attachment System

ASTP Apollo-Soyuz Test Project

ATV Automated Transfer Vehicle

CBM Common Berthing Mechanism

CSM Command and Service Module

DARPA Defense Advanced Research Projects Agency

DOF Degree Of Freedom

ECSS European Cooperation for Space Standardization

EMB Electromechanical Brake

ESA European Space Agency

GEO Geostationary Equatorial Orbit

GNC Guidance, Navigation, and Control

GUI Graphical User Interface

IBDM International Berthing and Docking Mechanism

IPC International Patent Classification

ISS International Space Station

LEO Low Earth Orbit

LM Lunar Module

MIUR Italian Ministry of Education, Universities, and Research

NASA National Aeronautics and Space Administration

NDS NASA Docking System

OECS Orbital Express Capture System

OP Operational Phase

SAPERE Space Advance Project for Excellence in Research and Enterprise

SE Support Equipment

STEPS Sistemi e Tecnologie per l'EsPlorazione Spaziale

TAS-I Thales Alenia Space Italty

TRL Technical Readiness Level

Chapter 1

Introduction

On-orbit servicing has proved its importance for space exploration throughout the last decades. The ability to refurbish and repair customer satellites while being in orbit is essential for some missions and may considerably lower the cost for others. These advantages have been demonstrated with several servicing missions to the Hubble Space Telescope that have guaranteed its functioning. Furthermore, the assembly of the ISS was and will continue to be done with in situ constructions.

Besides refurbishment and repairing, transportation is a possible cost effective use of on-orbit servicing. Missions like STRONG aim to deploy payloads and platforms from intermediate orbits to final target orbits such as Geostationary Earth Orbit (GEO). SAPERE-STRONG is a research and development program linked to the theme of space exploration and access to space, aiming to enhance the operation of Italian national space in this area through the construction of an electric propulsion space tug. The program is co-funded by MIUR (Italian Ministry of Education, Universities, and Research) on the "Sviluppo e Potenziamento di Cluster Tecnologici Nazionali" - PON R&C 20072013, and Coordinated by Thales Alenia Space Italy (TAS-I).

A mechanical coupling between the servicer satellite and the customer satellite is necessary for on-orbit servicing missions. This mechanical coupling may be achieved in two different ways: docking or berthing. On the one hand, docking stands for the mechanical coupling of two spacecraft where the GNC system of the chaser controls the relative state of the bodies to be mated. On the other hand, berthing is performed when the GNC delivers the servicer vehicle into a meeting

position to be kept followed by the grappling of one of the satellites by a manipulator, placed on either the chaser or target, that steers them to a common coupling port.

The device presented herein is a central docking mechanism with active degrees of freedom for cooperative on-orbit servicing missions. The scope of the mechanism is to be suitable for the technical specifications of the STRONG mission. The specifications consisted of the inertial properties of the satellites, mass and bulk dimensions of the mechanism, and the relative angular and linear misalignments between the satellites as well as their approaching velocities. This mechanism is the result of a trade study that led to the selection of a passive central mechanism. The passive mechanism evolved into a mechanism with an active control system able to greatly reduce the exchanged forces between the female half of the docking system mounted on the customer satellite and the male half fitted to the servicer. This reduction improves the probability of having a successful docking maneuver as the satellites travel against each other with fewer disturbances. Furthermore, the force reduction improves the attitude and position control of the satellites.

This dissertation contains, besides this introductory part, seven chapters. Firstly, Chapter 2 addresses in detail the definitions of docking and berthing operations. It also describes the evolution in time of the docking mechanisms since the Gemini program and the current patent landscape. In addition, Chapter 2 outlines some testing methodologies and testing facilities for docking systems.

Chapter 3 thoroughly reports the specifications of the STRONG mission. This chapter defines the associated relative misalignments and velocities between the spacecraft. Regarding the spacecraft, they are described in terms of task and inertial properties. Moreover, the chapter outlines the allowed physical characteristics of the docking mechanism.

As stated before, a trade study led to the selection of the architecture of the docking mechanism. Chapter 4 shows the conceptual designs considered for the docking system. Furthermore, the criteria and results of the trade-off are also presented.

Chapter 5 addresses the first design iteration of the mechanism. The results of the trade study pointed toward a solution with a central mechanism passively controlled by a group of elastic devices. This first mechanism was rigorously studied by implementing several numerical models that demonstrated it was not suitable for the docking maneuver.

Chapter 6 describes the second design iteration of the docking mechanism. The initial layout was radically modified. Consequently, the chapter reports the modifications. It also describes the selection of the actuators and transmissions needed based on the ECSS standards, the models used to assess the functioning of the new mechanism, and the control architecture.

Chapter 7 outlines the tests designed to verify the docking mechanism in a laboratory environment. These tests are based on a serial manipulator to simulate the relative movement between the mechanism parts.

Finally, Chapter 8 presents the conclusions of this research project. In addition, it outlines the envisaged future work.

Chapter 2

Preliminary definitions and state of the art

In this chapter, the main concepts concerning mating operations will be introduced. Moreover, several mechanisms will be described so as to create a solid technical reference. This reference will be used throughout this works to outline the similarities and differences between the proposed mechanisms and the implemented and theorized existent solutions. It will also be used to describe the advantages and disadvantages identified. Finally, different test benches used to perform functional verifications of docking mechanisms will be outlined.

2.1 Mating operations

Mating operations between satellites are crucial to human activities in space. These operations allow us to transfer cargo and crew between spacecraft as well as to perform on-orbit servicing missions. In general, the satellites involved in a mating operation are called chaser and target. The chaser assumes an active role while the target maintains its relative kinematic state. In contrast, the terms servicer and customer are used to describe the spacecraft in the case of on-orbit servicing. In this work, both chaser and servicer, and target and customer will be used indistinctly. Regarding on-orbit servicing, NASA [1] has identified several categories that define significant factors in a satellite servicing mission. The categories found are task, execution, rendezvous and capture, location, latency, customer design, and customer

attitude. The *tasks* include on-orbit refueling, the replacement of hardware designed to be replaced, the repair or replacement of hardware not designed to accommodate servicing, the assembly of structures (such as the ISS), and finally the orbit modification using a space tug. This last is precisely the task of the STRONG mission. Regarding the *execution*, the mission may be accomplished by robots, humans, or a combination of both. *Rendezvous and capture* defines a mission based on how the approach and mating are performed. On this regard, the simplest example considers a human crew on board the servicer dealing with a cooperative customer. On the other hand, the most complex example concerns a fully autonomous mating with a space debris, i.e., a non-cooperative customer. This kind of operations is currently being studied to perform active debris removal operations. For instance, ESA [2] is studying a technique called "capture before touching." This technique foresees a clamping mechanism embracing the target before making contact. Furthermore, the use of a robotic manipulator to mate with a non-cooperative satellite is a hot research topic [3]. The *location* categorizes a mission based on the orbit in which it is performed. *Latency* is related to the location as the communication time with Earth depends on the distance. The design of a customer satellite regarding servicing accommodations defines the *customer design*. Finally, *customer attitude* takes into account the cooperativeness of the target. An uncontrolled tumbling customer is the most complex example.

There are two types of mating operations: *docking* and *berthing* [4]. On the one hand, in a docking operation (figure 2.1), the GNC of the chaser satellite controls the relative state with the target so as to ensure suitable contact conditions (relative misalignments, relative velocities, etc). In this case, the capture location coincides with the structural connection.

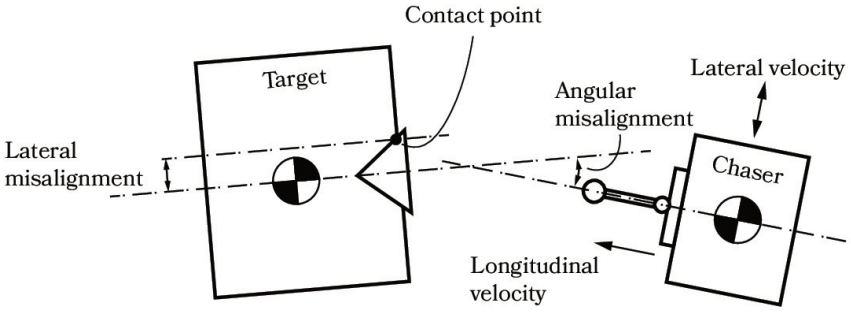

Fig. 2.1 Docking operation

On the other hand, during a berthing operation (figure 2.2), the GNC of the chaser ensures a suitable relative state between the spacecraft. This relative state is characterized by a relative pose and zero nominal relative linear and angular velocities. Subsequently, a manipulator fitted to either the chaser or the target clamps the other vehicle. Finally, the manipulator approaches the matching attachment interfaces mounted on the satellites.

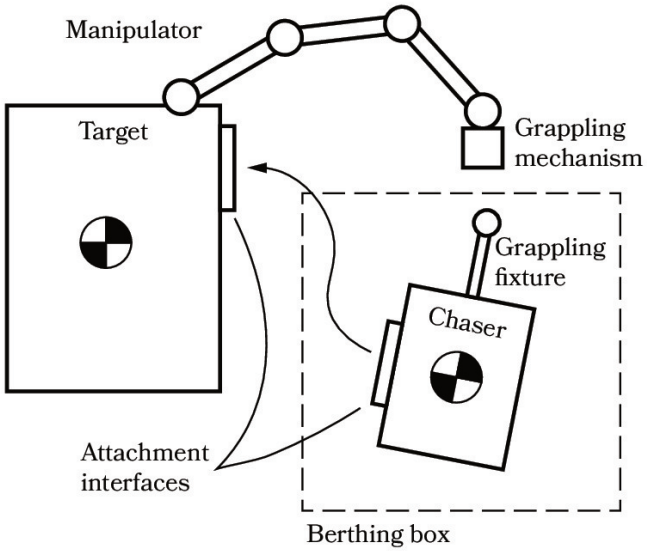

Fig. 2.2 Berthing operation

According to [4], a berthing operation is divided into seven sequential phases. The following description considers a berthing operation between a visiting satellite and the ISS which is equipped with a 7-joint serial manipulator called Canadarm2 (figure 2.3):

1. Acquisition of the berthing box by the chaser: after approaching, the chaser will remain in a station keeping condition within a berthing box. This box is a volume inside the workspace of the robot manipulator.

2. Acquisition of the readiness position by the manipulator: in this phase, the manipulator is positioned at a location where the operation may start. For safety reasons, this is done after the acquisition of the berthing box.

3. Switch-off of chaser thrusters and initiation of capture: the propulsion system of the chaser is inhibited and the grappling tool mounted on the robot will start moving toward the grappling fixture on the chaser.

4. Grappling of the capture interface by the manipulator: once the relative pose between the end-effector and the grappling fixture is reached, the capture takes place.

5. Transfer to the berthing port: the manipulator will steer the chaser to match the attachment interfaces fitted to both the spacecraft.

6. Insertion into the reception interfaces: after the proper relative final pose is reached, the robot will push the attachments one inside the other. However, relative linear and angular misalignments still exist during this phase. For this reason, the attachment interfaces are equipped with coarse and fine alignment guides. In this regard, figure 2.4 shows the active half of the Common Berthing Mechanism (CBM) while figure 2.5 shows its passive half. This system was designed by Boeing for the U.S. pressurized modules.

7. Structural connection: in this phase, structural fastening devices will ensure a stiff connection between the target and the chaser. In this particular case, four capture latches (figure 2.6) on the active side will catch the passive side. Finally, sixteen power bolts will further rigidize the connection.

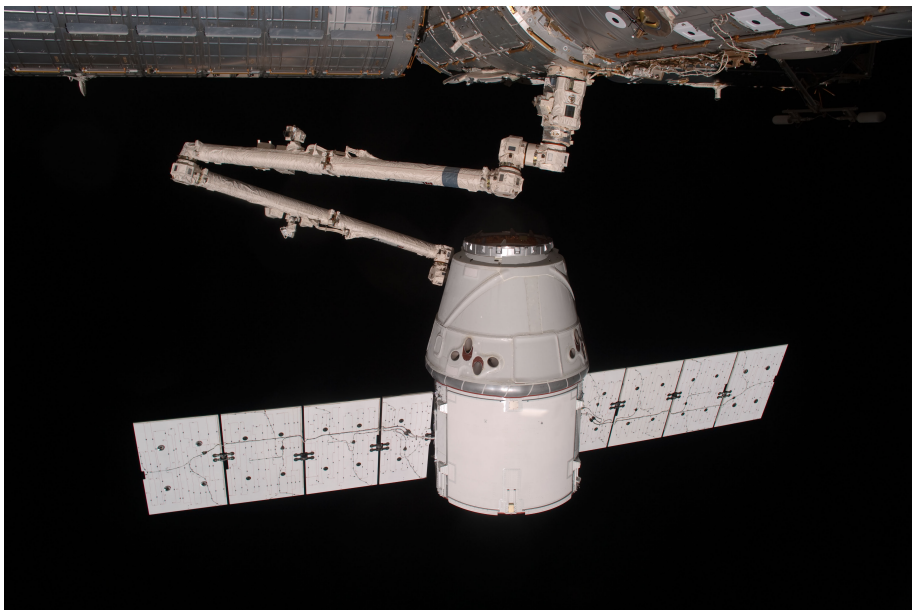

Fig. 2.3 Canadarm2 grappling a Dragon spacecraft (credit: NASA)

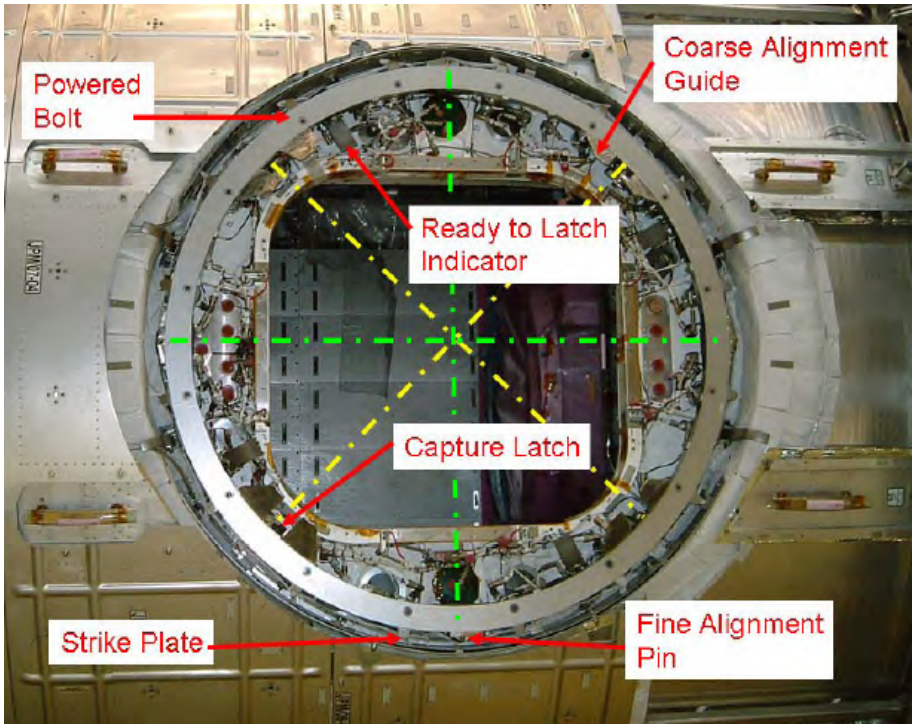

Fig. 2.4 Active half of the CBM (ACBM) [5]

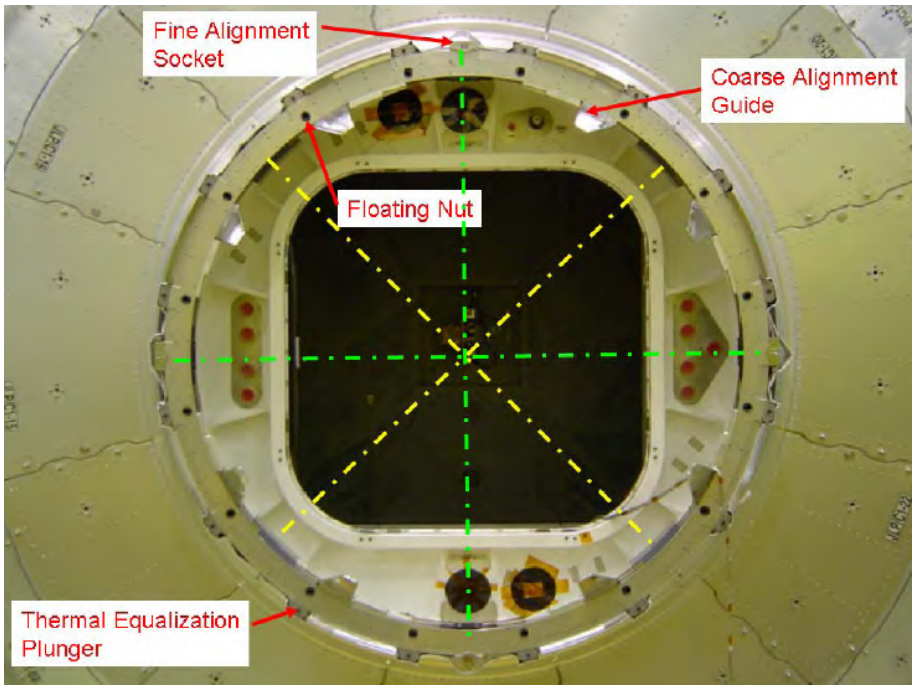

Fig. 2.5 Passive half of the CBM (PCBM) [5]

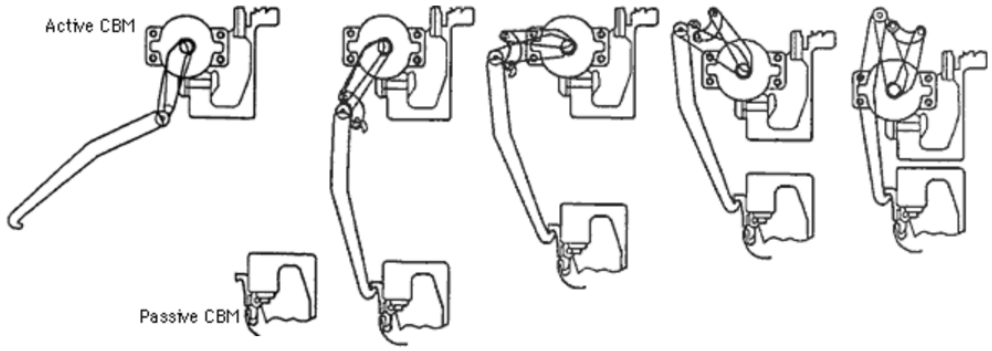

Fig. 2.6 Latching operation performed by the capture latch of the CBM [6]

In this work, four consecutive phases have been defined to describe an unpressurized docking maneuver:

1. Approach and deployment: the chaser spacecraft starts its free drift toward the target. In this phase, the interfaces are deployed and prepared for impact.
2. Alignment: the poses of the docking interfaces are aligned by using geometrical features or by other means (e.g. optical tracking).
3. Soft docking: after alignment, a capture system performs a first connection while the energy associated with the relative velocities of the bodies is safely dissipated. However, after this capture, relative displacements and rotations are still allowed.
4. Hard docking: finally, a secondary fastening device creates a stiff and final connection.

The architecture of a docking system may be either *central* or *peripheral*. All the early Soviet and American space programs used central architectures for their docking mechanisms [4, 5].

A central docking mechanism is composed of a male part mounted on the chaser and a female part fitted to the target. The male part is a probe (also called rod or pin). The female part is a drogue (conical frustum) that guides the probe toward its apex. Once the probe reaches the apex, a first capture device performs soft docking. The retraction of the probe combined with guiding geometries eliminate the relative

motion and align the interfaces. Finally, a set of hooks or bolts, or a combination of both achieves hard docking.

The main advantage of a central architecture is its relative simple design. This simplicity facilitates the analysis and development of this kind of mechanisms. However, this architecture presents a main drawback: after docking the probe and the reception cone obstruct the transfer tunnel needed to exchange crew and cargo. This problem was pointed out during the first meeting between the Americans and the Soviets for the Apollo-Soyuz Test Project (ASTP) in 1970 [7]. In this meeting, the Americans, considering the inconveniences caused by the presence of the Apollo probe assembly after docking, proposed as design criterion the elimination of any docking gear that might have blocked the passageway between the spacecraft. As a result, during this project, the first peripheral docking mechanism was designed and tested in space.

In a peripheral docking system, all the docking gear is accommodated in the periphery of the mechanism. This feature leaves the center of the mechanism free. However, a peripheral docking system is far more complex to design and study than a central mechanism.

The first docking maneuver ever performed took place on March 16, 1966, during the Gemini VIII mission [8]. After this first success, two central mechanisms with more advanced features were tested. On this regard, The Soyuz docking mechanism designed by the Soviets was tested for the first time on October 30, 1967 [9]. This test was the first autonomous unmanned space docking. Moreover, the first mating of the American Apollo docking Mechanism took place on March 7, 1969 [10]. The collaboration between the two superpowers led to the test of the first peripheral docking system; the Apollo-Soyuz docking mechanism, on July 17, 1975 [11]. The former mechanism was further developed becoming the Androgynous Peripheral Attachment System (APAS). It was intended to serve the Buran spacecraft in the late 80s. Subsequently, another update was implemented to the APAS for the Shuttle-Mir missions. The first docking between these spacecraft took place in 1995 [12]. In 2007, the Orbital Express Capture System (OECS) successfully mated the spacecraft Astro and NEXTSat in the DARPAS's Orbital Express Mission [13].

NASA and ESA are developing a new kind of peripheral docking mechanism based on active electric actuators. These systems are respectively the NASA Docking System (NDS) and the International Berthing and Docking Mechanism (IBDM).

Finally, the rapid development of the Chinese activities in space has produced several space systems. One of this is the APAS-2010 which is a new version of the APAS introduced before. Figure 2.7 shows a timeline containing the countries involved in the development of a particular docking mechanism and the year in which each mechanism was tested.

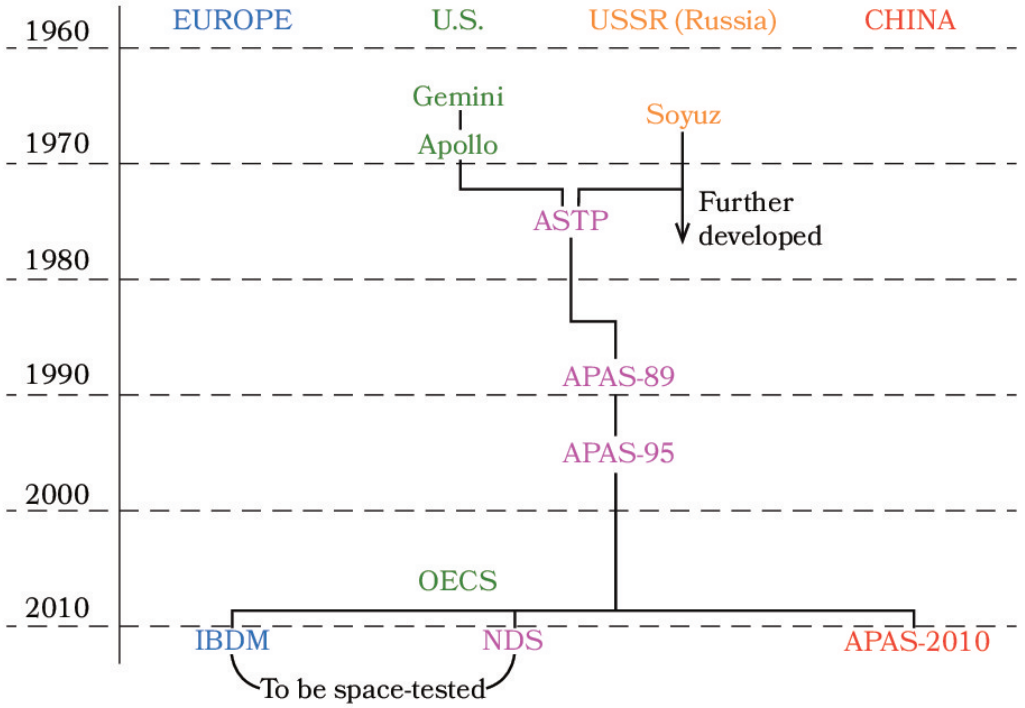

Fig. 2.7 Timeline of the docking systems

2.2 Description of existent docking mechanisms

2.2.1 Gemini docking system

This docking mechanism was a rigid male cone (probe) part of the Gemini spacecraft combined with a cup interface (drogue) fitted to the Agena (figure 2.8) [14]. The drogue was linked to the target spacecraft by seven shock absorbers clustered in three locations (Dampers in figure 2.9) to dampen the relative longitudinal and lateral velocities. The longitudinal shock absorbers were equipped with an orifice damper and a spring in parallel for reusability. Regarding the lateral ones, they were not

equipped with springs. The instroke orifices of the dampers were larger that the outstroke ones to minimize the rebound. The probe was equipped with an alignment feature called the indexing bar. This indexing bar had as its counterpart a v-shaped matching guide in the female cone. For this reason, there was a single possible coupling configuration between the satellites. The capture was accomplished by three latches on the Agena. Finally, the Agena was also equipped with a motorized unit to pull inward the cone latched to the chaser.

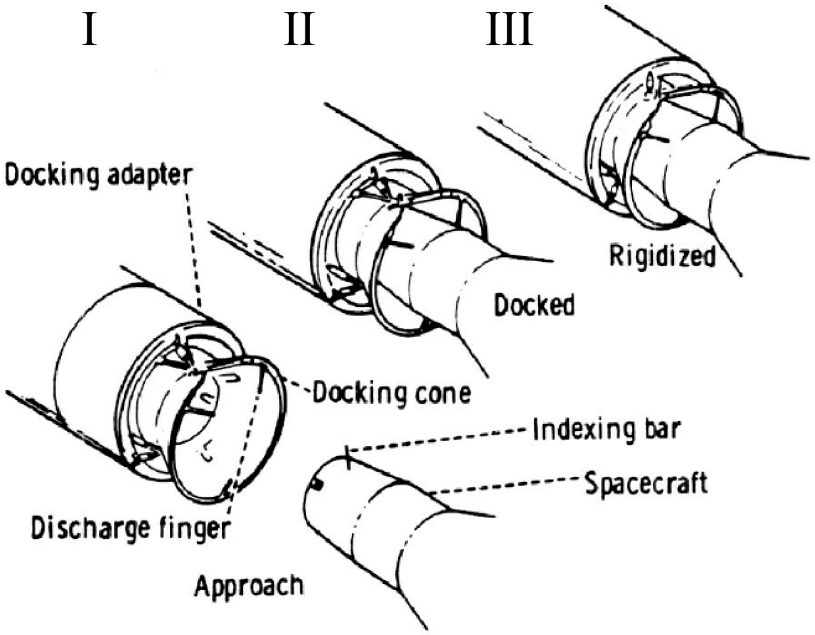

Fig. 2.8 Docking sequence of the Gemini docking mechanism [14]

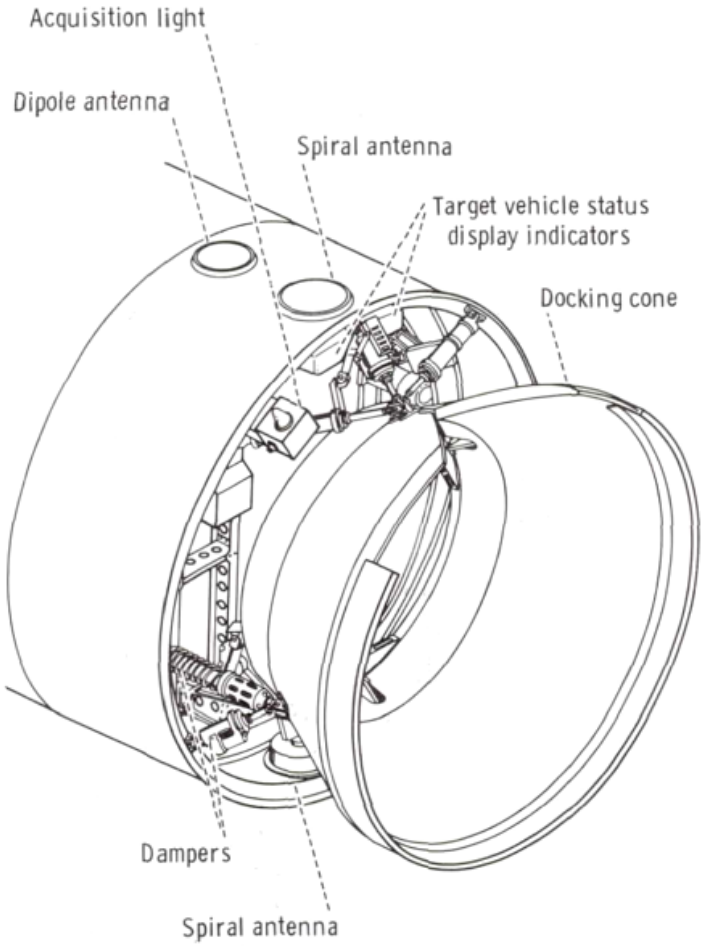

Fig. 2.9 Female cone with shock absorbers [14]

2.2.2 Soyuz docking system

The development of this central mechanism started in the 60s and is still in used today. Also, in this case, the system is based on a probe and a drogue. The original probe of the mechanism may be seen in figure 2.10. The probe was equipped with a small ball screw and a large ball screw [15]. The longitudinal shock attenuation was achieved by using the small screw. The forced retraction of this element caused the compression of a coil and Belleville spring as well as the rotation of an electromechanical brake (EMB). The EMB was composed of a hollow rotor made of aluminum rotating between two magnets [16]. The lateral impact was attenuated by the probe deflection (bending).

In this case, capture was accomplished by combining two latches on the probe head with the female socket. A “catch-up” transducer on the head of the probe verified the operation. The subsequent retraction of the probe was performed by an electric drive acting on the large ball screw. During retraction, the pitch and yaw angular misalignments were eliminated by a linkage assembly. Moreover, the roll misalignment was zeroed by the interaction of narrowing guides in the socket with the latches hinged to the probe head.

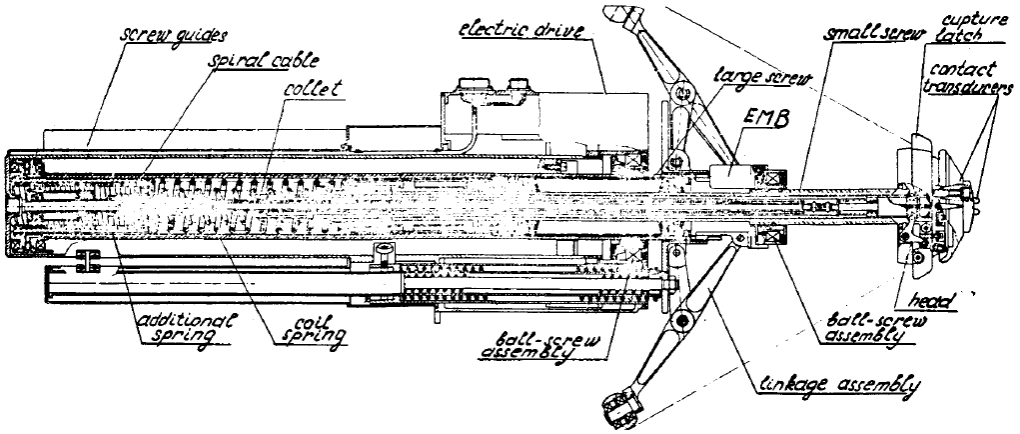

Fig. 2.10 Original probe of the Soyuz docking system retracted [15]

The original mechanism did not allow the crew to transit from one satellite to the other. For this reason, the design of the system was reviewed and updated (figure 2.11). To accommodate the transfer tunnel, both the probe and the drogue became part of the hatches of the spacecraft. This modification led to a more compact docking mechanism. The length of the probe was decreased and therefore its bending was not sufficient to dampen the lateral impact. Thus, it was spherically suspended and connected to one end to two lateral attenuation systems. Another major change was the incorporation of a friction brake to dissipate the longitudinal relative velocity. During the forced retraction of the probe, the rotation of the electromechanical brake dissipates part of the energy up to a certain stroke. After this, when the probe enters the socket, a self-regulating friction brake dissipates a great part of the energy.

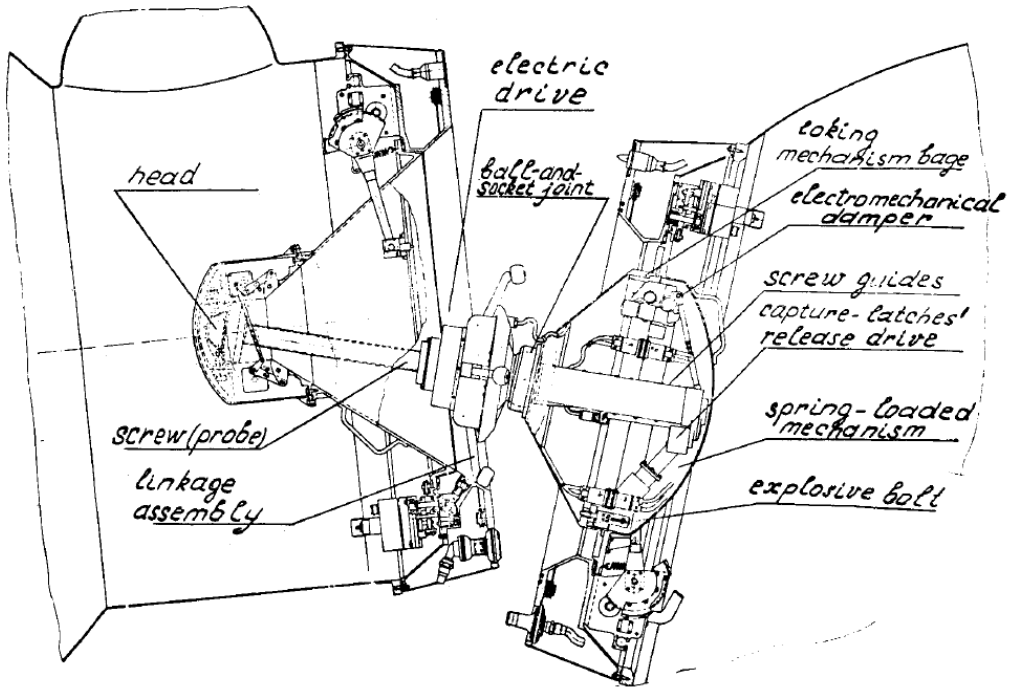

Fig. 2.11 Revised Soyuz docking system [15]

The final structural connection is accomplished by eight latches (hooks) actuated by an eccentric cam (figure 2.12) that provide a rigid connection between the satellites.

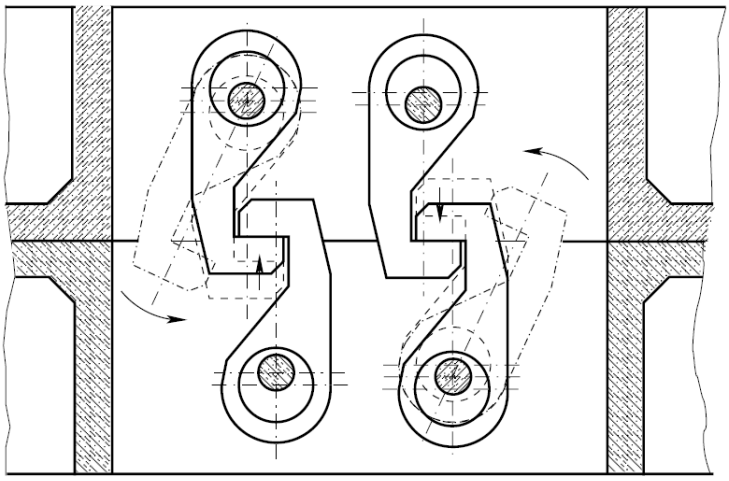

Fig. 2.12 Structural latches (hook type) [4]

Figure 2.13 shows a 3D render of the current version of the Soyuz docking system [17]. This system is currently being used for the docking operations between the ISS and the Soyuz, Progress, and ATV spacecraft.

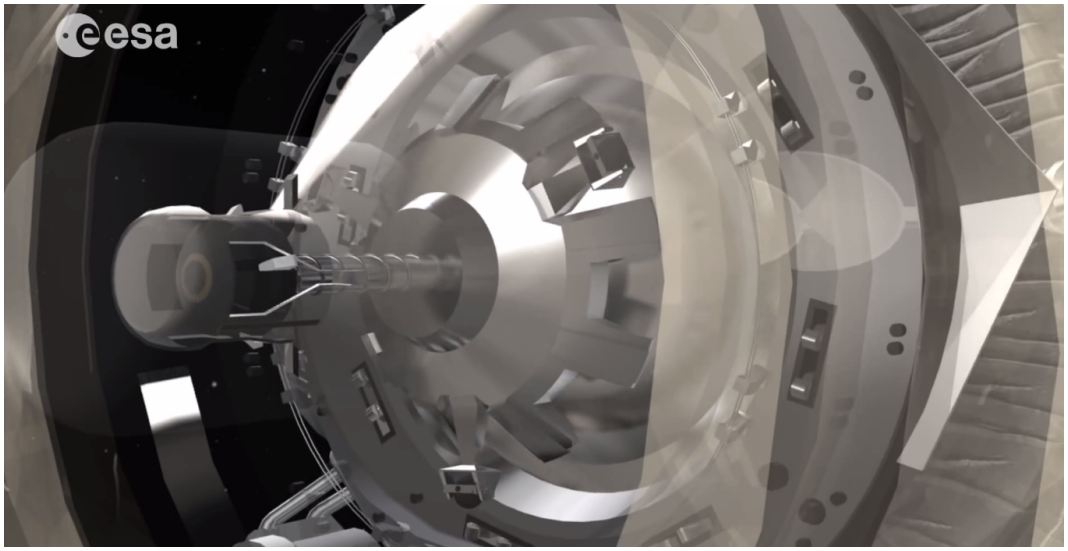

Fig. 2.13 Render of the current Soyuz docking mechanism. The roll alignment is performed by the capture latches and the narrowing v-shaped guides at the vertex of the female cone (credit: ESA)

2.2.3 Apollo docking system

This system was used during the lunar-landing missions to connect and disconnect the Apollo Command and Service Module (CSM) with the Lunar Module (LM) [18]. This system was characterized by a probe and drogue architecture (figure 2.14). The probe was composed of a central piston, three beams for centering, and three piston pitch bungees that served as air/oil shock attenuators.

During the docking maneuver, the initial coupling was accomplished by three spring-loaded latches hinged to the probe head. These latches engage the socket placed on the vertex of the female cone. The release of the latches was performed by dc motors located in the central piston.

The shock attenuation and vehicle centering were accomplished as follows. The centering beam was hinged to both the piston and a link (figure 2.15). In turn, the link was hinged to a collar concentric with the piston. The shock attenuator was hinged to both the beam and the collar. This linkage was duplicated radially around

the probe at three places $120\,deg$ apart. When impact occurred, the compression of the central piston produced a compression in the shock attenuator by the simple lever formed by the beam and the link. With the compression, the linkages expanded providing centering.

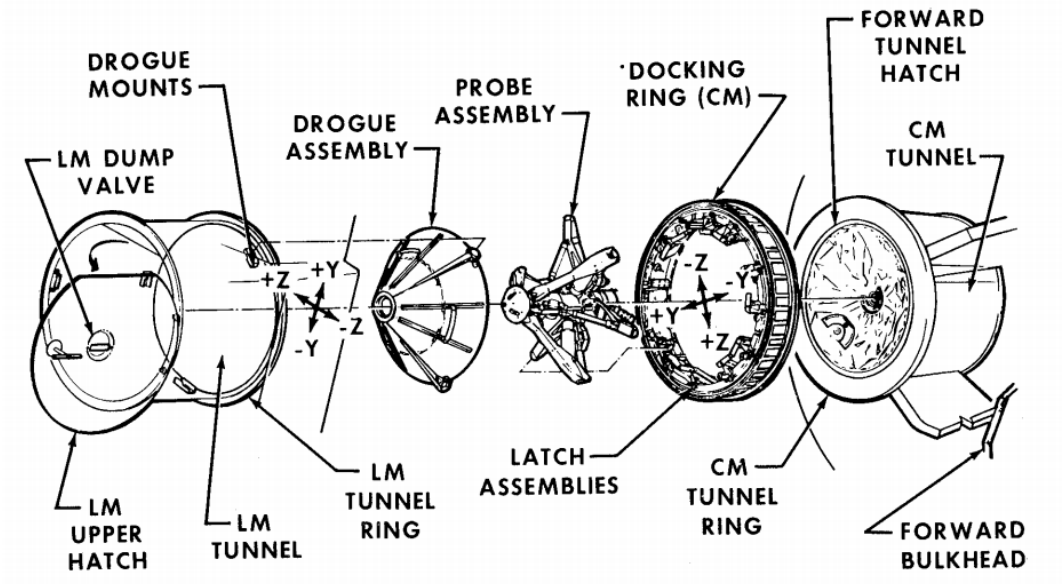

Fig. 2.14 Male and female halves of the Apollo docking system [19]

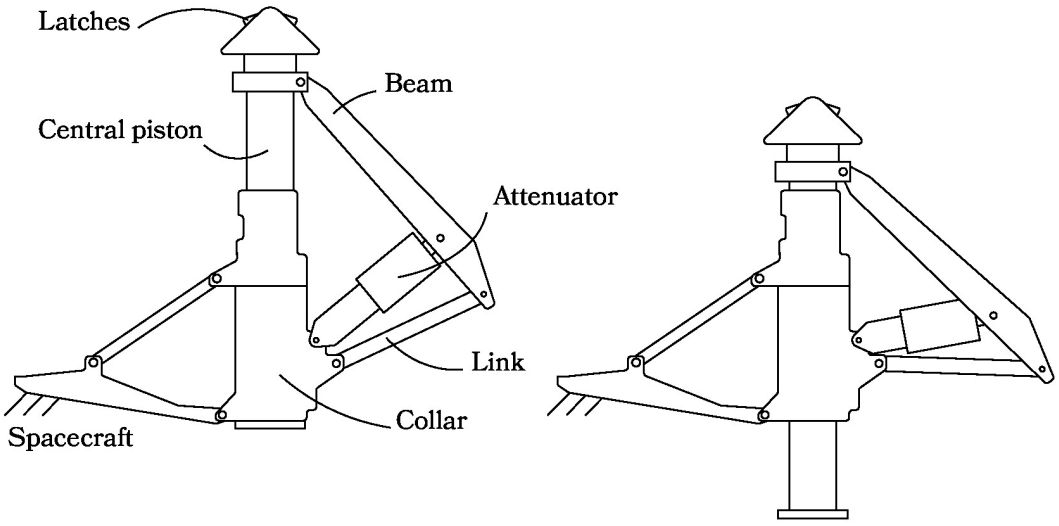

Fig. 2.15 Schematic view of the Apollo docking system in fully deployed (left) and retracted (right) configurations

The shock attenuators were based on air/oil dampers. Inside each damper, the fluid flow through orifices produced the damping effect. The attenuators were sealed by metal bellows. A mixture of argon and helium filled the bellows and the compensator piston cavity to create an air spring.

Dry nitrogen was used during the automatic retraction of the probe. A delta of pressure was generated inside the central piston creating the force needed for the closure. The system was activated by energizing an explosive initiator that pierced a pressure vessel containing the dry nitrogen. The nature of this system allowed for only two prime and two backup retractions.

Finally, twelve individually actuated hooks created the final structural connection between the satellites.

During the Apollo missions, the probe assembly was removed and stored to allow the crew transfer from one vehicle to the other (figure 2.16). Moreover, also the drogue assembly was removed and stored. As stated before, this issue was discussed during the first ASTP meeting in 1970 leading to the design of the first peripheral system.

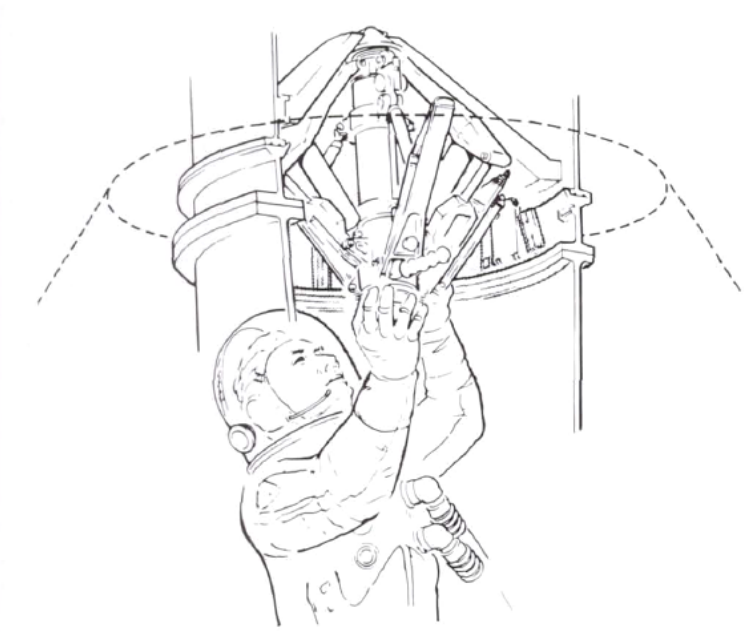

Fig. 2.16 Sketch of an astronaut removing the probe assembly after docking. This image was used during the first meeting of the ASTP by the Americans to state why a central docking mechanism should be avoided [7]

2.2.4 ASTP docking system

This was the first peripheral docking system. Besides being peripheral, it was also androgynous. In an androgynous system, either half of the mechanism may assume an active or passive configuration. This feature increases the safety as if one of the halves fails to deploy the other may be activated.

During the ASTP, several technical meetings were held to define the interfaces of the halves of the mechanism, the attenuation system, the structural connection system, etc. The idea proposed by the Americans in 1970 of creating the peripheral system was well received as in November 1971 they discovered that the Soviet engineer, Vladimir Syromyatnikov, was already working on a solution of this kind. After this November meeting the general layout of the system was defined [7]: "The design concept includes a ring equipped with guides and capture latches that were located on movable rods which serve as attenuators and retracting actuators, and a docking ring on which are located peripheral mating capture latches with a docking seal." Moreover, the partners decided to use the capture spring-loaded latches designed by the Americans and the structural latches used on both the Soyuz and the Salyut. However, each country decided to use their own attenuation technology: the Americans kept the hydraulic damper as in the Apollo lunar missions while the soviets prefer their more sophisticated electromechanical brake.

Figure 2.17 and 2.18 show the concept of the soviet half of the mechanism [20] while figure 2.19 shows a technical drawing of the flight model. In particular, the moving ring of the mechanism was connected to the spacecraft by six ball screws gimbaled to both ends in a 6UPU passive configuration. During impact between the mechanism halves, the forced retraction of each ball screw rotated an EMB. Finally, the synchronized deployment and retraction of the whole ring was accomplished by a single electric motor combined with differential transmissions.

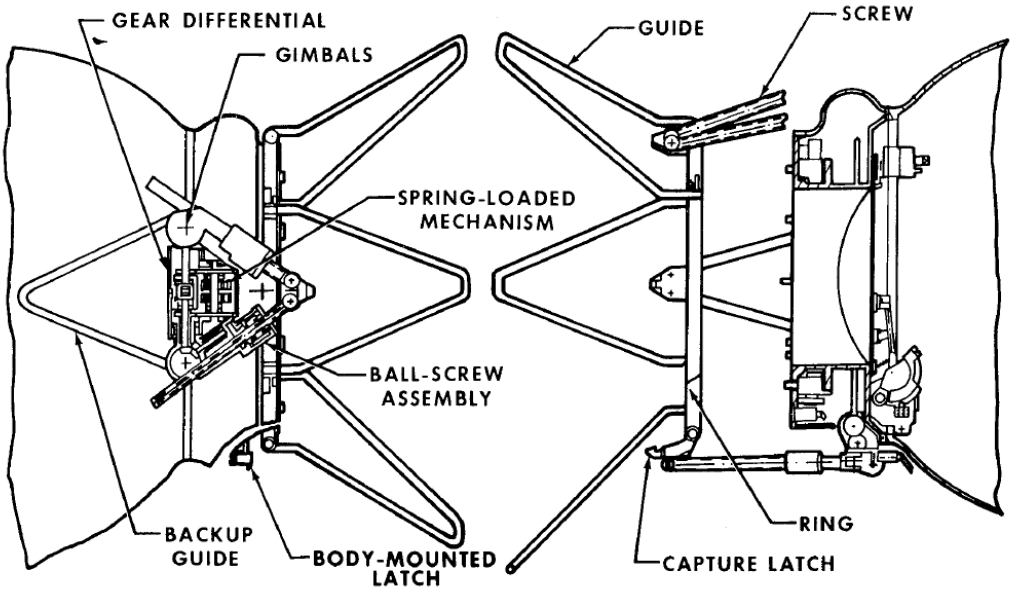

Fig. 2.17 Concept of the androgynous mechanism created by Syromyatnikov [20]

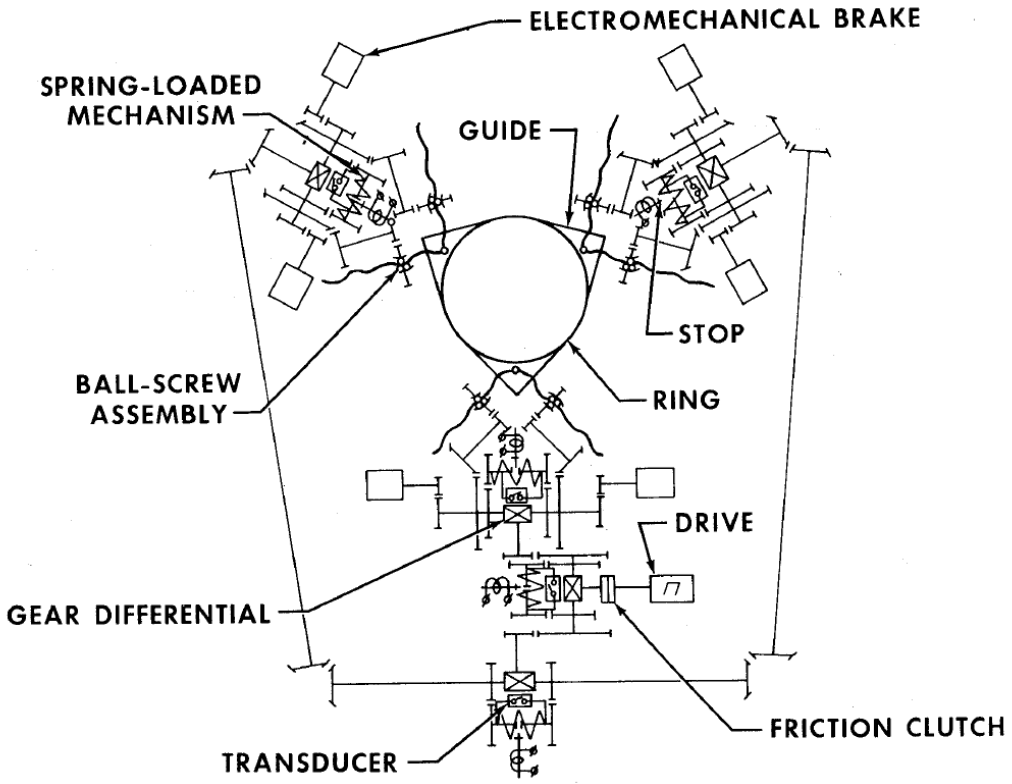

Fig. 2.18 Schematic view of the transmission used to dissipate the energy and to synchronize the assembly [20]

Figure 2.20 shows a technical drawing of the American half. In this figure, the fine alignment features are visible: the alignment socket and pin which had a counterpart on the Soviet half.

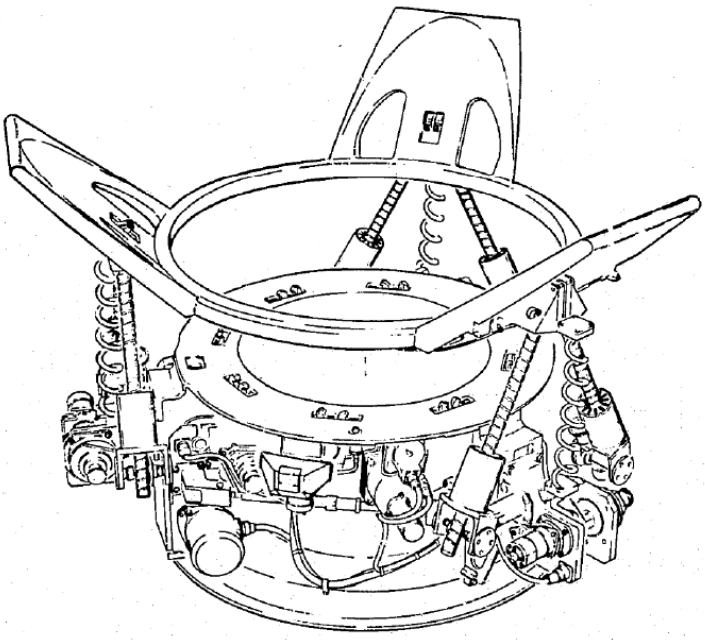

Fig. 2.19 Technical drawing of the flight model of the Soviet half [21]

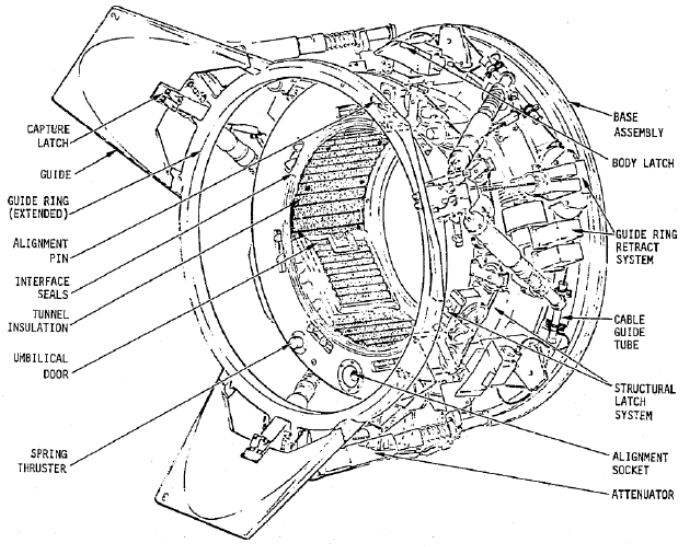

Fig. 2.20 Technical drawing of the flight model of the American half [21]

2.2.5 Androgynous Peripheral Attachment System (APAS)

The ASTP docking system evolved into the APAS-89. It was initially developed for the reusable orbital spacecraft Buran [4, 22]. This system adopted the EMB technology for attenuation and spring-loaded mechanical latches for soft docking. The "petals" used for the coarse guiding were changed from an outwards configuration to an inwards one (figure 2.21). A subsequent version of this mechanism was used during the Shuttle-Mir and Shuttle-ISS missions (APAS-95). The Chinese have developed a variant of this system know as APAS-2010.

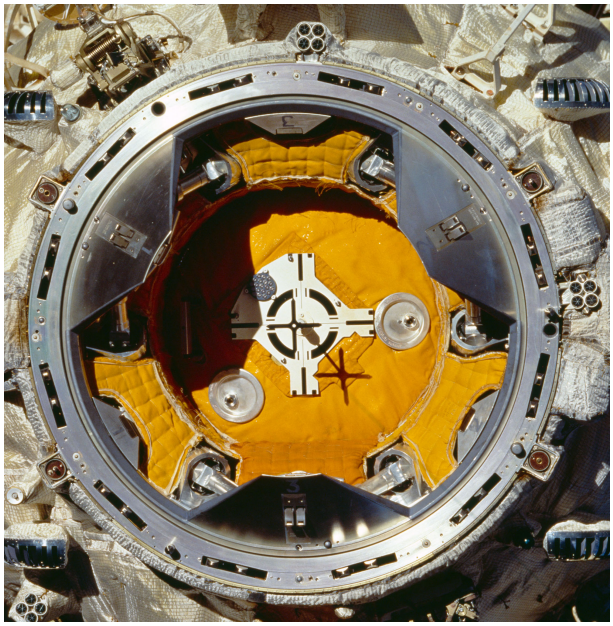

Fig. 2.21 APAS-89 (credit: NASA)

2.2.6 Orbital Express Capture system (OECS)

The OECS was used during the DARPA's Orbital Express mission. During this mission, the satellites Astro and NEXTSat performed several maneuvers showing the feasibility of autonomous mating for on-orbit servicing of unmanned vehicles [13, 23].

The capture system consists of a passive and an active side. The active side is equipped with three grappling fingers with a common actuator. The passive side consists of three wedges between which the fingers may be received. This half of

the mechanism is equipped with laser sensors to verify the presence of the fingers [24]. The docking sequence may be seen in figure 2.22. In the first phase (1), the fingers are deployed while the passive side performs a station keeping maneuver. Subsequently, the motor (figure 2.23) is activated and the fingers are closed toward the target by means of a ball screw. The bodies are aligned by the interaction of the fingers with the passive guides (2). After it (3), the linkage tips bring the bodies together as they engage a shelf feature on the passive side. Push-off rods dampen the impact between the mechanism halves. These rods are equipped with a spring and a Coulomb damper. Finally, the passive side is fully constrained by a set of cavities combined with cones (4). The stiffness of the connection is increased by applying a preload with the motor. Once the desired preload is reached, a brake maintains it.

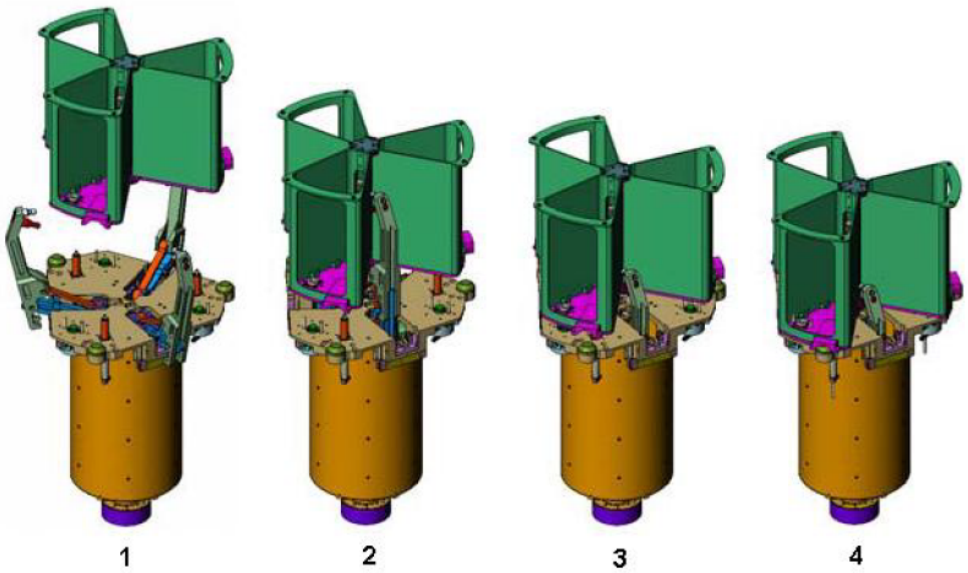

Fig. 2.22 OECS docking sequence [24]

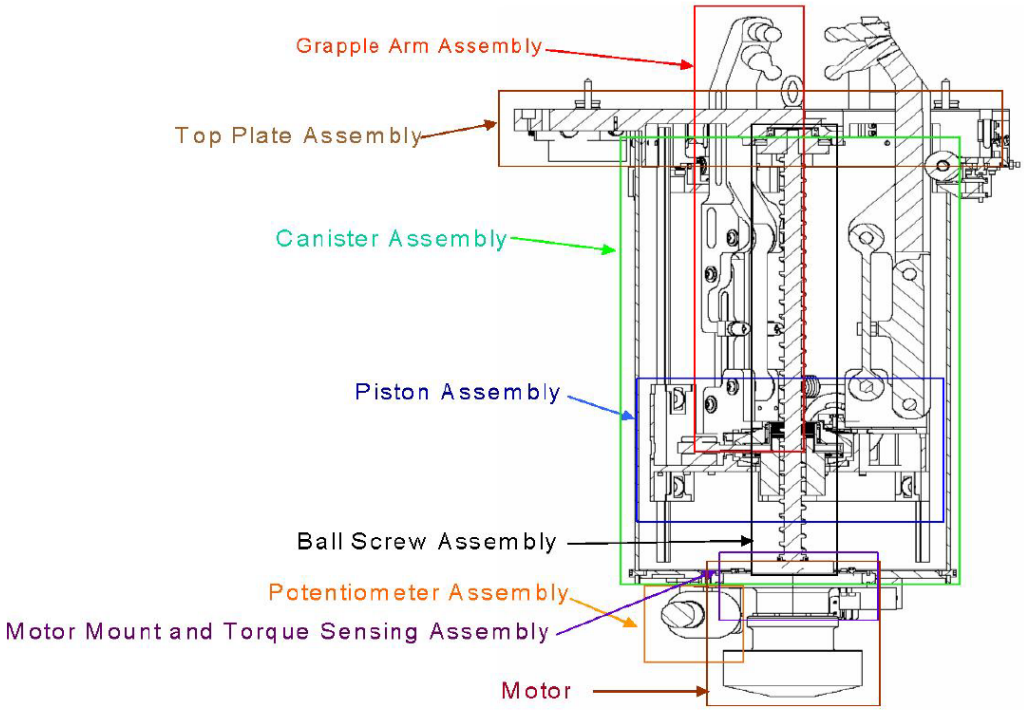

Fig. 2.23 Active part of the OECS [24]

2.2.7 NASA Docking System (NDS)

This system evolved from the also NASA's Low Impact Docking System (LIDS) to be compliant with the International Docking System Standard (IDSS) [25]. The IDSS standardize the physical geometry of mating interfaces so as to enable on-orbit crew rescue operations. It also specifies design parameters that may be used by developers to create independent mechanisms compatible with each other.

The NDS is an androgynous peripheral docking system with two major differences with respect to the APAS systems. Firstly, the spring-loaded latches on the APAS were removed and substituted by a group of electromagnets combined with strikers (contact surfaces) on the other half. Secondly, the active ring is equipped with electromechanical actuators instead of passive dampers forming an active Stewart-Gough platform. A complex control algorithm controls the active platform to dissipate the energy along and about all directions. The control relies on a load sensing device fitted to the ring to create the feedback needed to implement a force control [4, 5]. Finally, to this date, the NDS has yet to be tested in space.

2.2.8 International Berthing and Docking Mechanism (IBDM)

This is the IDSS-compliant solution developed by ESA. According to ESA, this system may be used during docking or berthing operations with the ISS, between two free-flyer vehicles in LEO, or in deep-space missions [26]. Figure 2.24 shows the docking system in its active configuration. The furthermost ring is divided into two rings; the upper and middle rings. Between these, six load cells aligned at 45 deg measure the exchanged wrench [27]. Nor has this mechanism been space-tested.

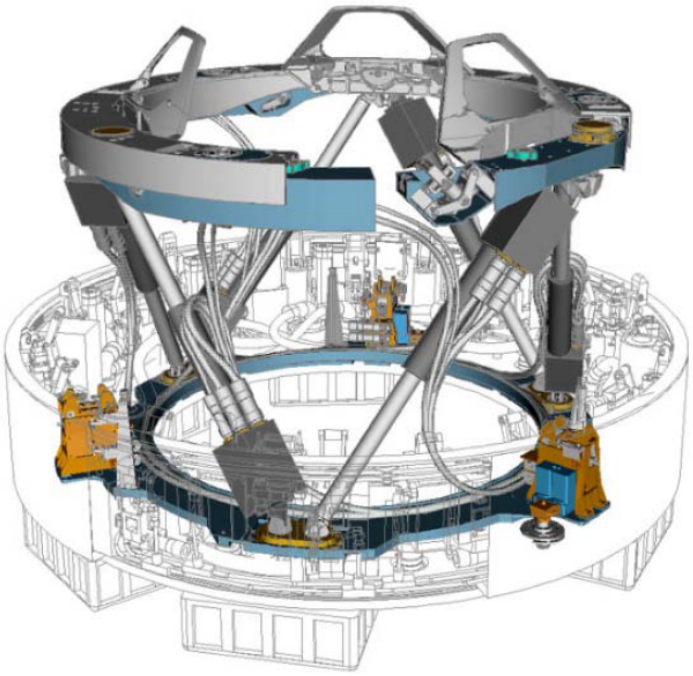

Fig. 2.24 IBDM in its active configuration [27]

2.2.9 Other docking mechanisms

There are some docking mechanisms that, although in an early stage of development, are worth mentioning. An example of said systems is the ARCADE docking mechanism [28]. This mechanism is composed of two mating parts. The first part is a passive spring-damper probe equipped with a soft iron tip. The second part is a conic drogue. The drogue is equipped with an electromagnet to capture the tip of the probe, a miniature linear actuator to approach the interfaces after soft docking, and three locking solenoids for hard docking. Thus, all the active features of the

mechanism are mounted on the female side. Figure 2.25 shows both the female and male parts of the ARCADE docking mechanism.

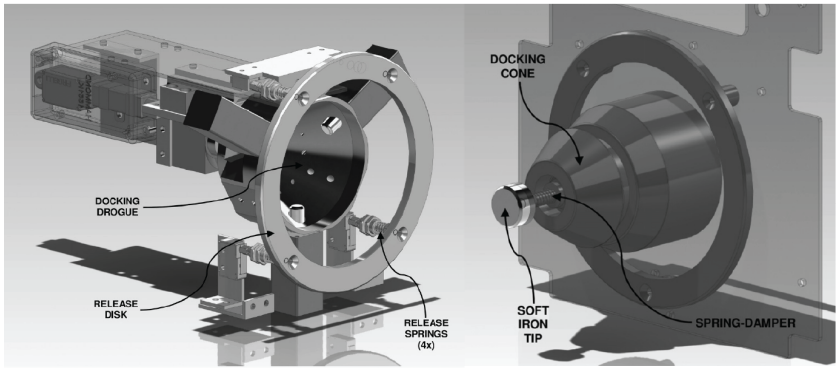

Fig. 2.25 Female part (left) and male part (right) of the ARCADE docking mechanism [28]

Another interesting example is the semi-androgynous mechanism described in [29]. This mechanism was designed for small satellites. It consists of two interfaces equipped with eight petals able to open and close by means of a disk cam mechanism. Before docking, one of the interfaces changes its shape to a drogue configuration while the other deploys the petals. When the passive interface is within the reach of the active one, the petals are closed around the probe securing the mechanical connection between the parts. Figure 2.26 shows a 3D model of this docking system.

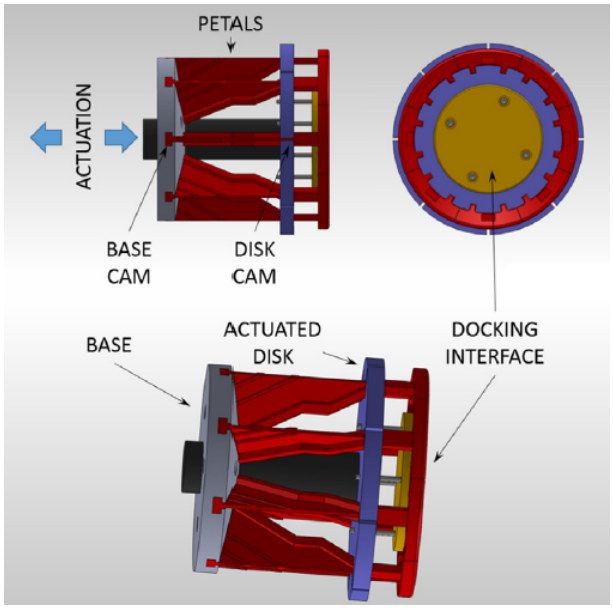

Fig. 2.26 Semi-androgynous docking mechanism for small satellites [29]

2.2.10 Patent landscape

The analysis of the patent landscape regarding the docking mechanisms for space applications showed 156 patent families between 1970 and 2015. This research was performed using the web patent browser Orbit by Questel. The query used contained the key phrase "DOCKING MECHANISM" as well as the International Patent Classification (IPC) code for this kind of technology; B64G 1/64: Systems for coupling or separating cosmonautic vehicles or parts thereof [30].

Figure 2.27 shows the global distribution of patent families by priority country in the period of reference. From the graph, it may be seen that the key nations are China and The U.S. followed by Russia and Japan.

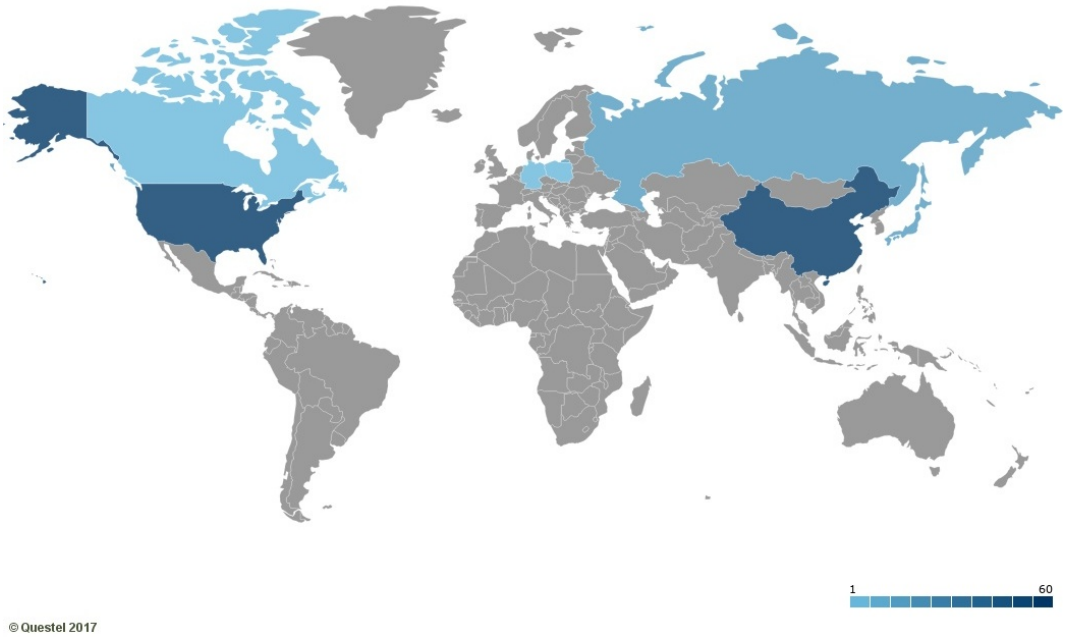

Fig. 2.27 Distribution of patent families by priority country between 1970 and 2015

This patent landscape contains some mechanisms based on technologies to some extent different from the technologies already shown. In this regard, [31] presents a system that exploits a flexible cable to perform the docking operation. On the active side, the system presents a harpoon connected to one of the spacecraft through the aforementioned cable. The harpoon is thrown toward a suitable seat on the target vehicle. When it gets inside, a group of spring-loaded elements acts as a trap preventing the harpoon from escaping. Once these elements link the spacecraft,

the flexible cable is wrapped using a rotary actuator. In [32] a system equipped with parallel bars is disclosed. Two pairs of parallel bars are arranged in such a way as to form an ideally rectangular shape. The ends of each pair of bars are moved using linear actuators, so that the rectangular shape delineated by them may shrink gradually. Regarding the passive part, it is a parallelepiped-shaped element. The entire target is therefore led by the contact between the active part (the group of bars) and passive (the parallelepiped) of the docking system. In [33] a docking system for large structures is presented. This system has a telescopic boom mounted on a spherical joint plus a system to actuate the boom to point it toward a socket mounted on the target. In [34] a docking mechanism for transorbiting and deorbiting missions is presented. The mechanism includes several grasping jaws to grab different extending rings such as the conventional adapters rigs used to couple the satellites to their launchers. The last example may be seen in [35]. This mechanism uses magnetic fields to perform docking. A docking component of the mechanism mounted on one of the vehicles has a magnet that is used to induce a coupled magnetic field with a docking component of the mechanism mounted on the other satellite.

2.3 Testing of docking mechanisms

Testing is a fundamental operation for all space systems. Due to the high complexity, high cost, and to mitigate the risk of human lives, a new mechanism for space applications will be thoroughly tested. On this regard, ESA has defined its own scale for assessing the maturity of new technologies; the Technology Readiness Levels (TRLs) [36]. This scale is divided into nine levels. Besides the TRL 1 and 2, all the levels are characterized by the kind of tests successfully performed. As reported in table 2.1, the environment in which the technology is tested, laboratory, relevant environment (e.g. a thermal vacuum chamber), etc., is the main driver to assign a particular level.

Docking systems such as the Soyuz docking mechanism reached a TRL 9 as it has been used on several space missions. On the other hand, the NDS and the IBDM have a high TRL but they are not space-tested. The objective of the present research is not that ambitious. Instead, the scope is to validate a novel docking mechanism in

Table 2.1 TRLs definitions

Readiness level	Definition
TRL 1	Basic principles observed and reported
TRL 2	Technology concept and/or application formulated
TRL 3	Analytical and experimental critical function and/or characteristic proof-of-concept
TRL 4	Component and/or breadboard validation in laboratory environment
TRL 5	Component and/or breadboard validation in relevant environment
TRL 6	System/subsystem model or prototype demonstration in a relevant environment (ground or space)
TRL 7	System prototype demonstration in a space environment
TRL 8	Actual system completed and "flight qualified" through test and demonstration (ground or space)
TRL 9	Actual system "flight proven" through successful mission operations

a laboratory environment. For this reason, some test benches will be described in the following paragraphs.

Test facilities based on a 6UPU manipulator (Stewart-Gough platform) have been used in the American and Russian space programs, and later by Europe and Japan [4]. A parallel manipulator of this kind provides a six DOFs motion capability at maximum stiffness with a minimum number of actuators and moving parts. Figure 2.28 shows an example of such a facility. The target interface is mounted on the manipulator. The active interface is mounted to a fixed support through a force-torque sensor. Once the interfaces get in contact, the exchanged wrench is measured by the force-torque sensor and, based on the simulated inertial properties of the spacecraft, the equations of motion are solved. The results are combined to estimate the relative movement between the satellites. Finally, this relative configuration is given as the reference to the platform using its inverse kinematics.

ESA's IBDM has been tested using serial manipulators. In figure 2.29, a 6-joint serial manipulator equipped with a force-torque sensor simulates the relative

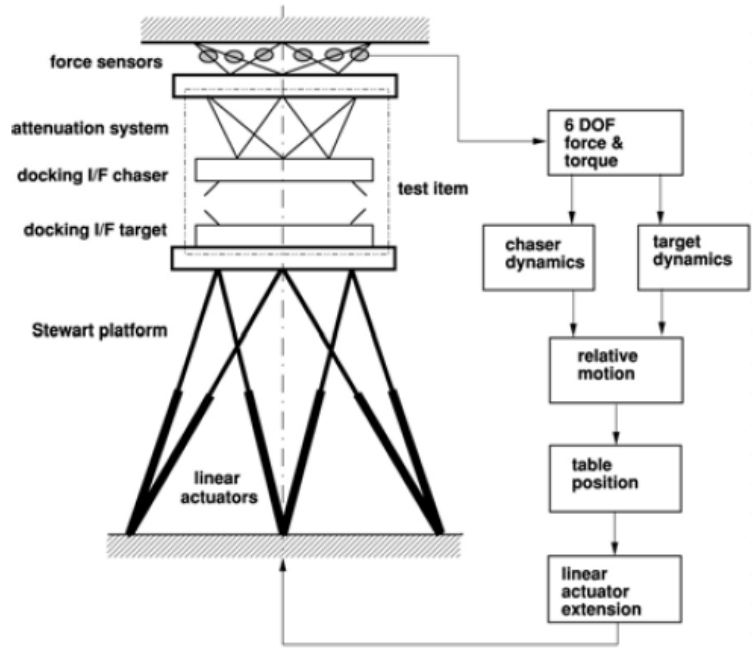

Fig. 2.28 Example of test facility for docking operations [4]

movement between the passive interface carried by it and the active interface. A similar test bench is reported in [27]. The use of a serial manipulator may be advantageous in terms of flexibility on carrying the tests. However, as stated before, a 6UPU manipulator is stiffer and may simulate the relative movement in a more precise way.

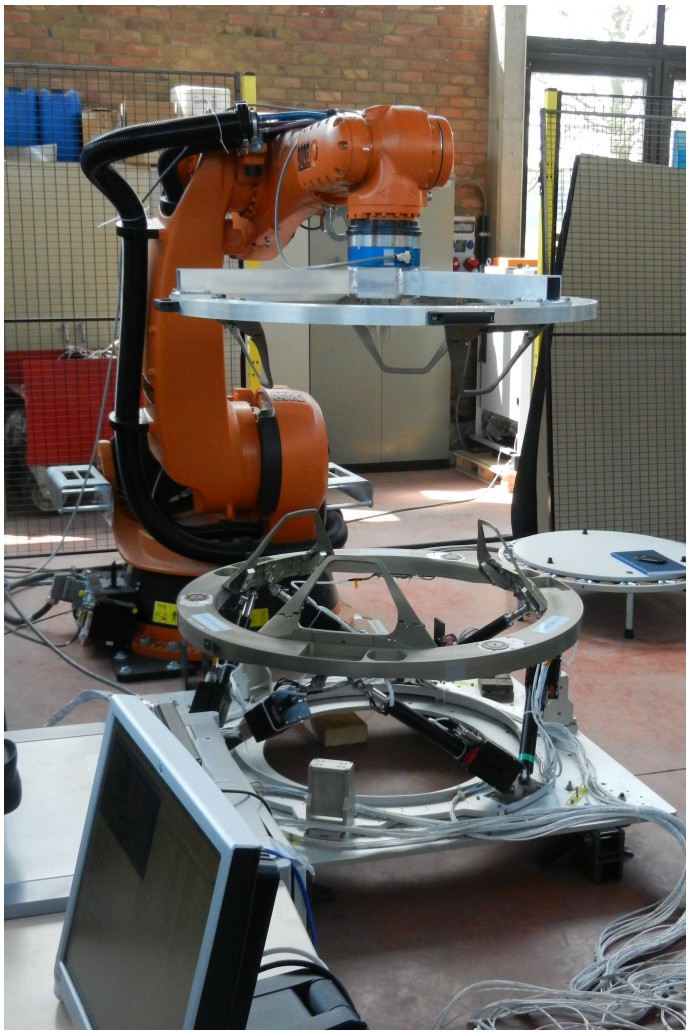

Fig. 2.29 Testing of the IBDM in Leuven, Belgium in 2012 (credit: ESA)

Chapter 3

The STRONG mission

The idea behind this research work is to create a docking mechanism suitable for cooperative on-orbit servicing missions. In this regard, the distinct technical specifications of the STRONG mission were used as driving parameters in the design and verifications phases of the mechanism development.

The aim of the STRONG mission is the development of a reusable space tug with electric propulsion. This tug should be able to deploy satellite platforms from low injection orbits into their final destination orbits with considerable savings in weight and a strong optimization of the payload/platform ratio. The tug has also the objective of allowing the re-entry of vehicles for the retrieval of payload samples. After each orbit raising, the space tug is expected to perform an on-orbit refueling with an orbital tank. Figure 3.1 shows a graphical representation of the mission.

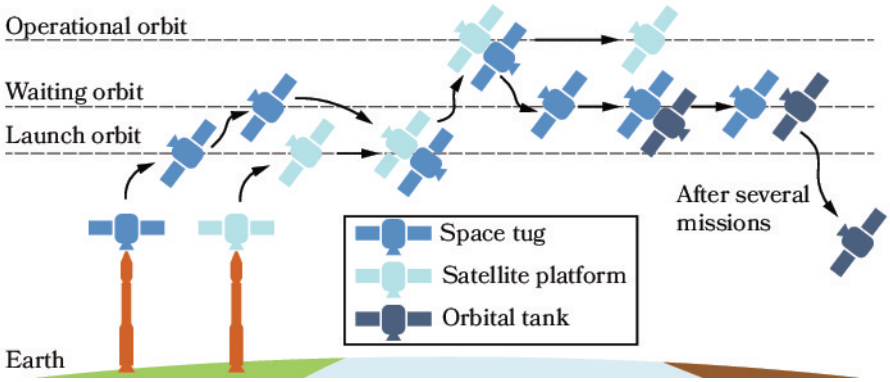

Fig. 3.1 Orbit raising and refueling operations of the STRONG mission

This mission may be defined based on the categories introduced in section 2.1. The tasks of the mission are both on-orbit refueling and orbit modification. Regarding the execution, and the rendezvous and capture, the mission will be accomplished autonomously and the targets will be cooperative. The location of the operations will be in both LEO and GEO. In the latter location, latency should be taken into account as a signal round trip might last a quarter of a second. Moreover, the customers will be equipped with suitable devices to perform the servicing (docking fixtures, valves, etc.). Finally, the customer attitude will be controlled and suitable for docking.

Both the space tug and the satellite platform are being designed to be compatible with the expendable launch system Vega/Vega C (Consolidation). On the other hand, the orbital tank should be launched with the larger Soyuz or Vega E. The orbital tank will carry a large mass of carbon dioxide that will allow the space tug to perform several orbital raisings and re-entries.

Due to the performance of the GNC of the tug, the docking mechanism has to recover some position and angular misalignments as well as to dissipate the energy associated with the relative velocities between the spacecraft. In this regard, figure 3.2 shows two generic spacecraft equipped with a probe and a drogue during the final approach before contact. In particular, TU is the reference frame of the chaser, TA the reference frame of the target, AH is the reference frame of the active half of the mechanism, placed at the furthermost part of the probe, and PH is the reference of the drogue, located at the cone vertex. The linear and angular relative velocities are defined as the relative rates between TA and TU expressed in TA. Moreover, the lateral and angular misalignments are defined as the relative position and orientation between the coordinate systems AH and PH w.r.t. PH when the probe touches the drogue. Concerning the relative orientation, the Euler angles are used with the 123 body-fixed convention.

Table 3.1 shows the technical specifications of the STRONG mission regarding the relative position and angular errors as well as the relative velocities at the beginning of the alignment phase of the docking maneuver. These conditions are valid for both the docking maneuvers considering the tug and the payload, and the tug and the tank. The difference lies in the inertial properties of the bodies.

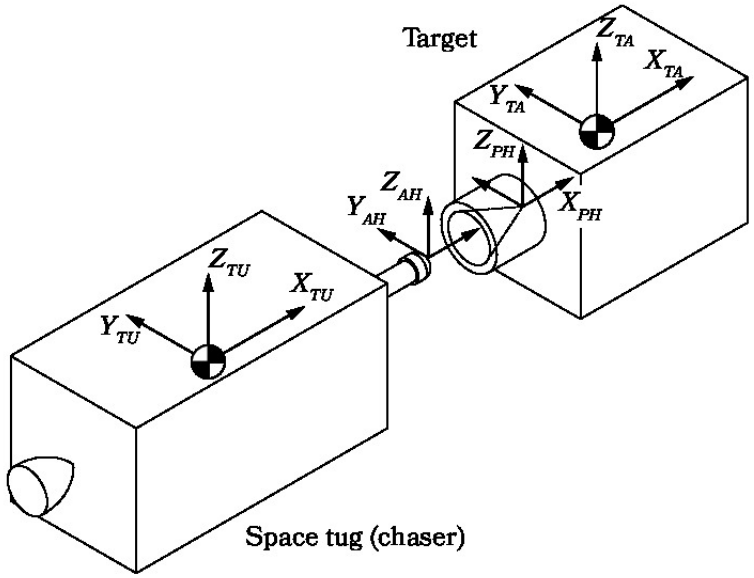

Fig. 3.2 Coordinate systems of generic satellites

Table 3.1 Technical specifications regarding relative misalignments and velocities between the spacecraft

Position misalignment	Lateral Y	$\pm 50\,mm$
	Lateral Z	$\pm 50\,mm$
Relative velocity	Lateral Y	$\pm 10\,mm/s$
	Lateral Z	$\pm 10\,mm/s$
	Longitudinal X	$30 \pm 10\,mm/s$
Angular misalignment	Roll	$\pm 3\,deg$
	Pitch	$\pm 3\,deg$
	Yaw	$\pm 3\,deg$
Relative angular rate	ω_X	$\pm 0.1\,deg/s$
	ω_Y	$\pm 0.1\,deg/s$
	ω_Z	$\pm 0.1\,deg/s$

The values shown in table 3.1 are comparable to the relative misalignments and velocities used to design some of the modern docking mechanisms. As an example, table 3.2 shows the technical specifications of the OECS [24] and the upcoming ESA's IBDM [27]. The similarities between table 3.1 and table 3.2 indicate that a

mechanism designed for the STRONG mission might be used in a wide variety of space mission scenarios.

Table 3.2 Technical specifications regarding relative misalignments and velocities between the spacecraft used to design the OECS and the IBDM

		OECS	IBDM
Position misalignment	Lateral Y	$\pm 50.8\,mm$ $(2\,in)$	$\pm 50\,mm$
	Lateral Z	$\pm 50.8\,mm$ $(2\,in)$	$\pm 50\,mm$
Relative velocity	Lateral Y	–	$\pm 10\,mm/s$
	Lateral Z	–	$\pm 10\,mm/s$
	Longitudinal X	$< 30\,mm/s$	$50 \div 100\,mm/s$
Angular misalignment	Roll	$\pm 5\,deg$	$\pm 5\,deg$
	Pitch	$\pm 5\,deg$	$\pm 5\,deg$
	Yaw	$\pm 5\,deg$	$\pm 5\,deg$
Relative angular rate	ω_X	–	$\pm 0.5\,deg/s$
	ω_Y	–	$\pm 0.15\,deg/s$
	ω_Z	–	$\pm 0.15\,deg/s$

In the STRONG mission, the space tug (figure 3.3) arrives at the waiting orbit, LEO, with a dry mass of $1700\,kg$ (Configuration A). This value is the result of the maximum payload of the Vega launcher. In LEO it refuels with the orbital tank and its mass increases up to $3500\,kg$ (Configuration B). Equations 3.1 and 3.2 show respectively the principal inertia tensors of Configurations A and B calculated in the center of gravity (COG) of the body. The active part of the docking system is mounted on the $+X$ panel of the chaser. The distances from the COG of the spacecraft to this panel are $2061\,m$ in Configuration A and $1942\,m$ in Configuration B.

$$I_{G,TU,A} = \begin{pmatrix} 13803 & 0 & 0 \\ 0 & 17003 & 0 \\ 0 & 0 & 4040 \end{pmatrix} kgm^2 \tag{3.1}$$

$$I_{G,TU,B} = \begin{pmatrix} 13965 & 0 & 0 \\ 0 & 18197 & 0 \\ 0 & 0 & 5235 \end{pmatrix} kgm^2 \tag{3.2}$$

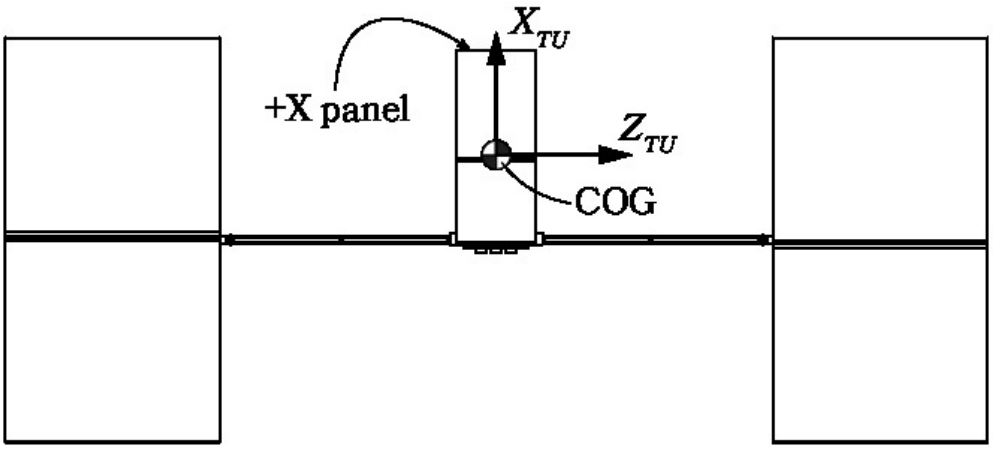

Fig. 3.3 Reference frame of the space tug

The nominal mass of the satellite platform (figure 3.4) is 2000 kg of which 1000 kg is the maximum payload to GEO. The principal inertia tensor about the COG of the satellite is reported in equation 3.3. The passive part of the mechanism is located on the $-X$ panel at 0.65 m from the COG of the satellite.

$$I_{G,TA} = \begin{pmatrix} 3700 & 0 & 0 \\ 0 & 3700 & 0 \\ 0 & 0 & 2000 \end{pmatrix} kgm^2 \tag{3.3}$$

The maximum mass of the orbital tank (figure 3.5) is equal to 6000 kg. The propellant mass is 4000 kg of carbon dioxide. Equation 3.4 reports the principal inertia tensor about the COG of this spacecraft. Also, in this case, the passive half of the docking mechanism is fitted to the $-X$ panel. The distance from the COG to this panel is 1780 m.

$$I_{G,OT} = \begin{pmatrix} 3270 & 0 & 0 \\ 0 & 7926 & 0 \\ 0 & 0 & 7897 \end{pmatrix} kgm^2 \tag{3.4}$$

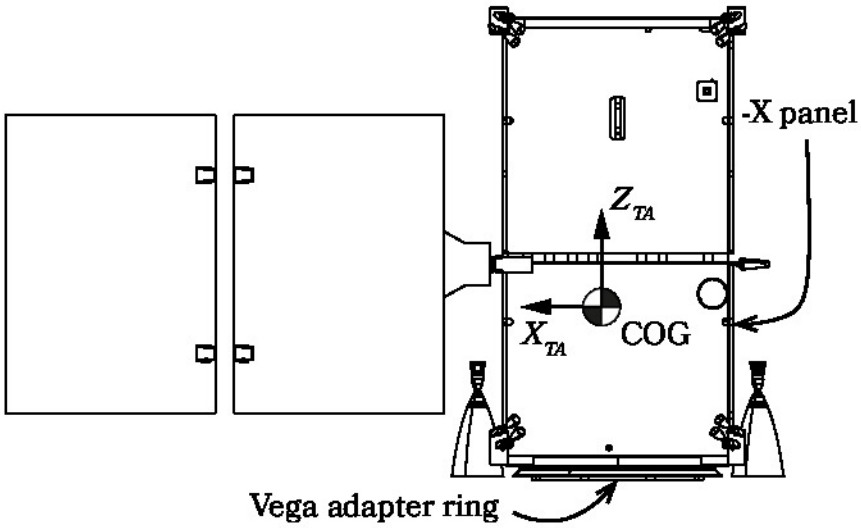

Fig. 3.4 Reference frame of the satellite platform

Furthermore, table 3.3 summarizes the maximum dimensions of the parts of the docking mechanism in launch configuration (stowed). Moreover, the maximum mass of the whole mechanism, passive plus active parts, should be less than $45\,kg$.

Table 3.3 Maximum dimensions of the passive and active halves of the mechanism in launch configuration

Active part	Diameter: $0.5\,m$ Height: $0.45\,m$
Passive part	Diameter: $0.5\,m$ Height: $0.45\,m$

Finally, a non-compulsory specification of the STRONG mission is to exploit the standard adapter ring used to mount a satellite payload to the Vega launcher. This ring might be used as the passive half of the docking mechanism instead of a custom part. By doing so, only the chaser will be equipped with docking equipment leaving all the target capacity available for its mission payload. The Vega expendable system may use two different standard adapters the PLA 937 VG and the PLA 1194 VG [37]. Figure 3.6 shows the section of the PLA 937 VG.

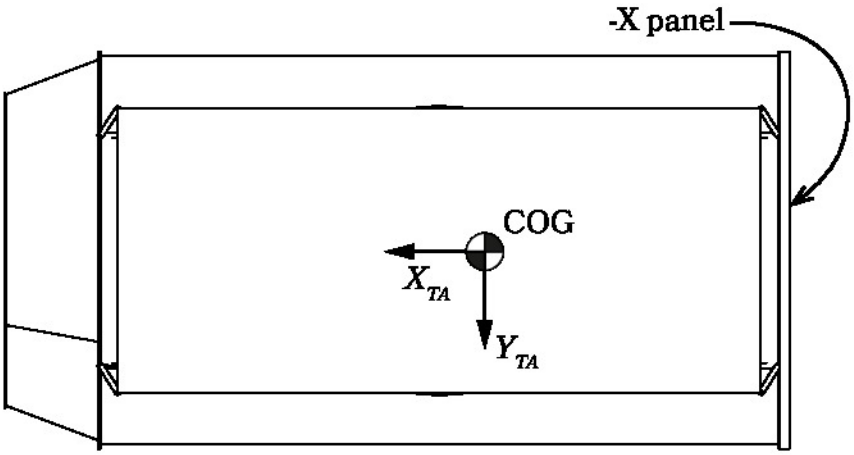

Fig. 3.5 Reference frame of the ortbital tank

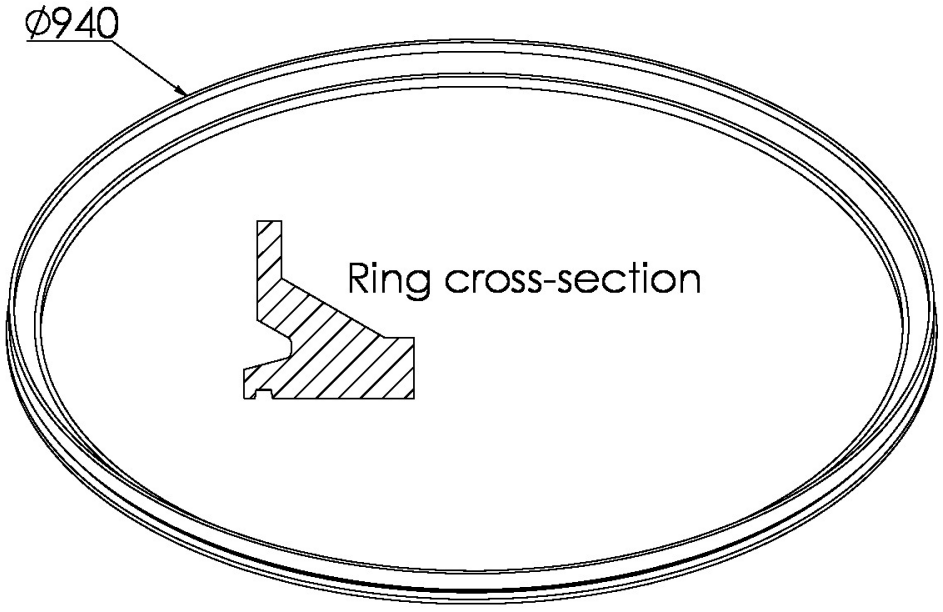

Fig. 3.6 Vega adapter ring PLA 937 VG

Chapter 4

Mechanism concept selection

In this chapter, the mechanism concepts considered as possible candidates for the docking system will be disclosed. These concepts were defined with the scope of suggesting alternative designs amongst which making a motivated choice of the preferred one. The concepts examined were the following: a mechanism based on the Stewart-Gough platform with position control, a Stewart-Gough platform with impedance control, the central passive mechanism developed during the STEPS project [38], a central active mechanism, and a mechanism equipped with articulated arms. Each of these concepts will be described based on the parts it is composed of and the function of those parts during the phases of the docking maneuver: approach and deployment, alignment, soft docking, and hard docking (section 2.1). Finally, the end of this chapter will show the trade study used to evaluate the mechanisms and the final selection.

4.1 6SPS parallel manipulators

Two 6SPS parallel manipulators were investigated as candidates for the docking mechanism. These solutions are composed of an active half based on a Stewart-Gough platform and a drogue as passive half. The first solution relies on a position control algorithm to achieve soft docking. The second concept uses an impedance control logic.

Figure 4.1 shows a graphical summary of the docking maneuver performed with either concept. In the approach and deployment phase, the GNC of the spacecraft

reduces the distance between the satellites. Simultaneously, the platform is positioned in the middle of its workspace. During the alignment phase, the poses of the male and female docking interfaces are matched using only the control system of the docking mechanism. On the one hand, the platform with position control is equipped with an optical system to identify the relative pose between the chaser and the target. Using this information, the position set to the actuators of the platform is generated exploiting the inverse kinematics of the manipulator. On the other hand, the platform with impedance control aligns the interfaces using guiding geometries placed on both sides combined with force sensors. As soon as the contact between the male and female interfaces starts, the force sensors measure the exchanged wrench and the control algorithm works to create suitable force reference values to the actuators of the moving part. These force references are created by means of a stiffness strategy combined with the direct kinematics of the platform. The result is the alignment of the moving part with the female reception cone. For both the position and impedance control architectures, the phase 2 in figure 4.1 shows that the interfaces of the mechanism are aligned regardless the relative pose between the satellites. In the soft docking phase, a capture system guarantees a first mechanical connection. Subsequently, both mechanisms start working with a position control logic so as to approach the spacecraft up to their final pose while limiting the maximum exchanged forces. Finally, hard docking is achieved using fastening devices.

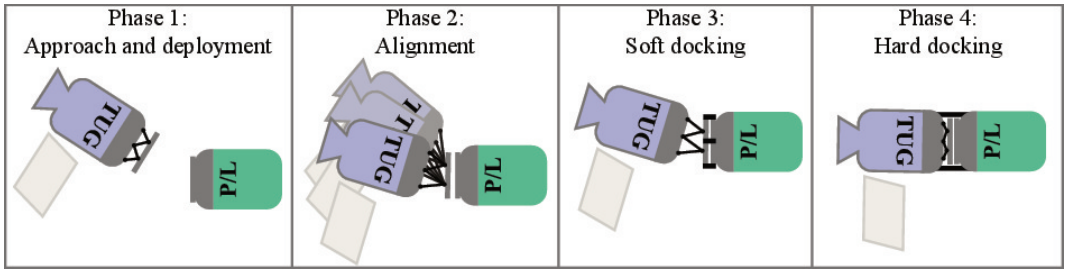

Fig. 4.1 6SPS parallel manipulator docking maneuver

Figures 4.2 and 4.3 show the mechanism concepts. The platforms are composed of six prismatic actuators linked to both a moving ring and a support fixed to the chaser spacecraft. The moving ring is a frustum (1) designed to fit inside the reception cone mounted on the target. Regarding the manipulator with position control (figure 4.2), the dimensions of the female reception cone are very similar to the ones of the moving ring. In this case, the position errors between the parts are eliminated using the optical feedback. In contrast, the unit with impedance control

(figure 4.3) is equipped with a larger reception cone to recover the position errors at the beginning of the maneuver. In the alignment phase, spring-loaded pins (3) guide the male part exploiting conical grooves inside the female part. These conical grooves act as coarse alignment guides to recover rolling angular misalignments about the axes of the cones. The soft docking is completed when the pins enter suitable sockets in the vertex of the conical grooves (not shown). The hard docking is achieved using three actuated hooks (4) combined with suitable seats.

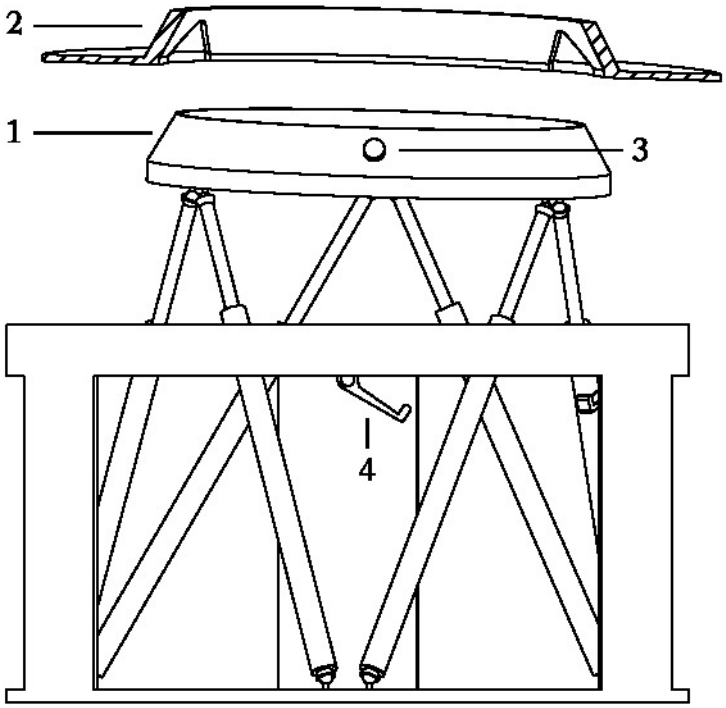

Fig. 4.2 6SPS parallel manipulator with closed loop position control

A geometric model of the platform was created to analyze and select a plausible configuration of the manipulator. This model (figure 4.4) is characterized by the minimum height of the platform h, the diameter of the moving ring d, and the diameter of the support D. The length of the ith leg L_i is calculated based on the relative pose between the moving and fixed rings. For simplicity, the angular distributions of the spherical joints were kept constant: evenly distributed $60\,deg$ apart in the support and $120\,deg$ apart in the moving ring.

A parametric analysis was performed to select the preliminary dimensions of the platform based on its resultant workspace. Two ratios were used for this analysis: D/d and h/d. Given a reference value of the diameter of the moving ring, and values

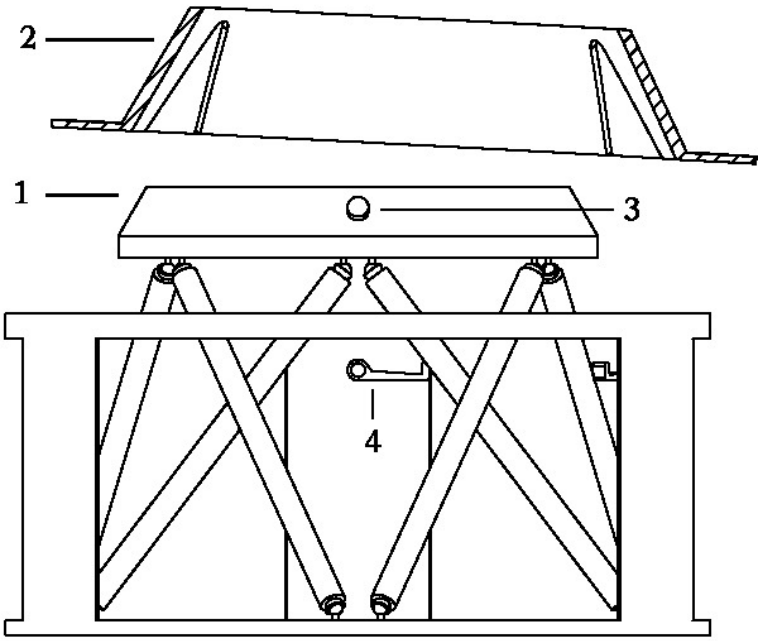

Fig. 4.3 6SPS parallel manipulator with impedance control

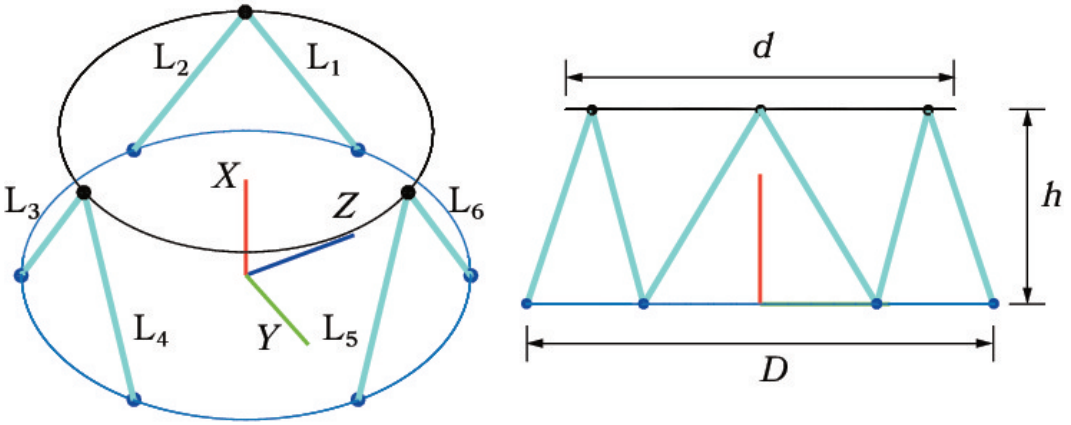

Fig. 4.4 Model of the 6SPS parallel manipulator

of the ratios, the minimum length of the legs may be calculated. On the other hand, the maximum length of the legs was supposed to be 1.8 times the minimum one. It is reasonable to suppose that a prismatic actuator may increase its length by 80% of its retracted configuration. The workspace was studied in the XY plane of the platform. The values of the roll, pitch, and yaw angles of the moving ring were set to zero so as to have a symmetric workspace. The position of the moving ring was swept from the initial height (h) to an upper limit using discrete increments. At each

height, the ring was translated laterally also with discrete increments. At each point, the lengths of the legs were calculated. If the ratios between the current lengths and the minimum ones were both greater than one and less than 1.8 that particular point was stored as part of the workspace.

During the implementation of the parametric analysis, three values of D/d were used: 1.2, 1.5, and 1.7. Regarding h/d, also three values were considered: 0.3, 0.5, and 0.7. Figure 4.5 shows the results of the analysis. The diameter of the moving ring was selected to be 300 mm. The magenta dashed lines in figure 4.5 represent the maximum lateral misalignment between chaser and target as stated in table 3.1. Considering this, the platform with $D/d = 1.5$ and $h/d = 0.7$ was selected as the best solution. It has a suitable workspace and a longitudinal stroke similar to the other platforms. However, the workspace of this platform may be used to dissipate the energy associated with the lateral approaching velocity. Moreover, its mass might be smaller than the configuration with $D/d = 1.7$. The CAD models in figures 4.2 and 4.3 were generated using the selected configuration. This geometric study was useful to further analyze the suitability of the 6SPS concept and to make a rough estimation of the expected masses.

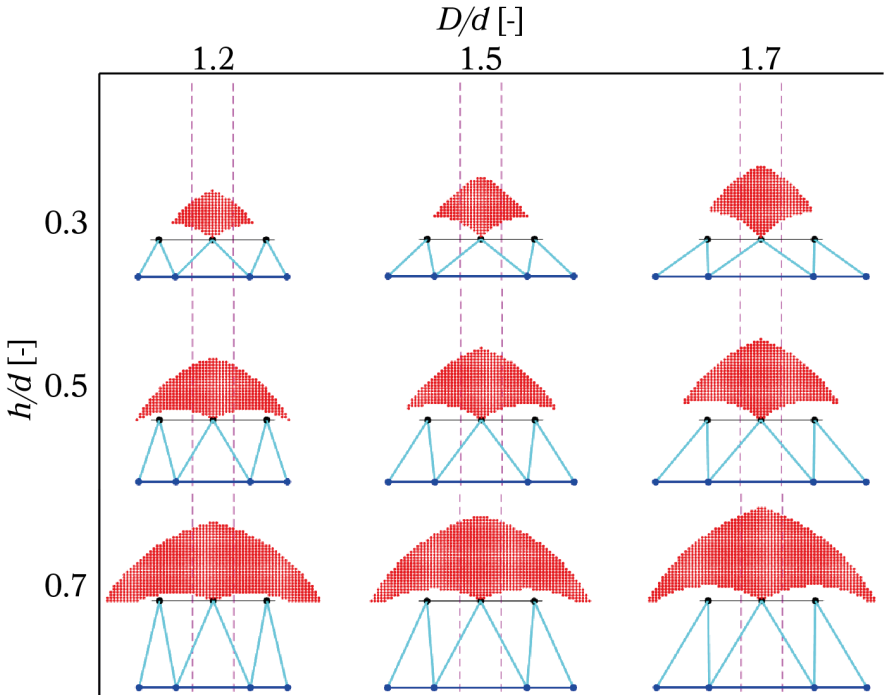

Fig. 4.5 Parametric analysis of the workspace of the manipulator

4.2 STEPS' probe and drogue

TAS-I developed a central docking mechanism during the STEPS project. In this project, the docking mechanism was designed, manufactured, and partially tested. However, in the trade study, only the functional layout of this system will be considered so as to allow a fair comparison between this and the other concepts.

This system (figure 4.6) is equipped with a retractable central probe (1). This part is launched fully retracted and is actuated up to its maximum length in the deployment phase. The probe is mounted on a spherical joint (2) that allow it to rotate about all the axes. These rotations are passively controlled by four preloaded traction springs (3).

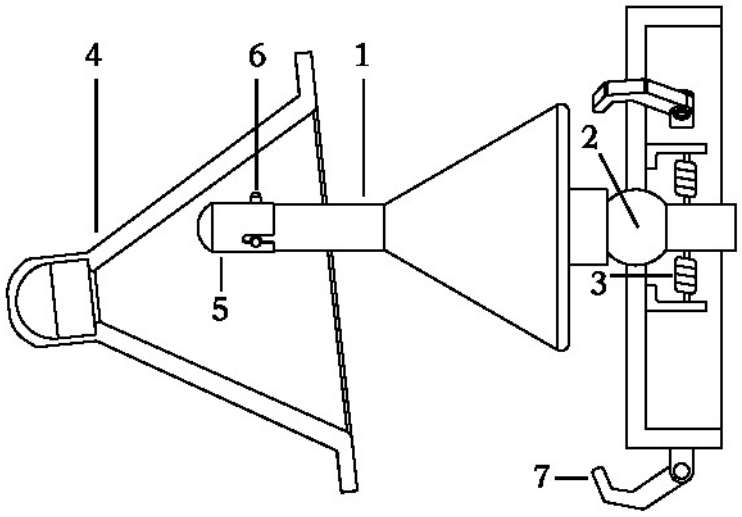

Fig. 4.6 STEPS' probe and drogue docking system

A drogue (4) located on the passive side guides the probe (alignment phase) toward a socket located at its vertex. The probe is equipped with a cap (5) that translates relatively controlled by a preloaded spring. This element is necessary to reduce the contact forces with the drogue upon impact.

Once the tip of the probe reaches the socket, spring-loaded latches (6) perform the first operation of soft docking preventing the bodies from detaching. When soft docking is accomplished, the retraction of the central probe allows the spacecraft reach their final relative pose; the male and female cones guarantee the alignment for

the hard docking. In the hard docking phase, three hooks (7) create a stiff mechanical connection between the satellites.

The four docking phases of the probe and drogue docking concept are depicted in figure 4.7. In particular, during the second phase, post contact thrust of the chaser toward the target may be necessary to guarantee the contact of the probe with the reception cone and the sliding movement toward the soft docking configuration.

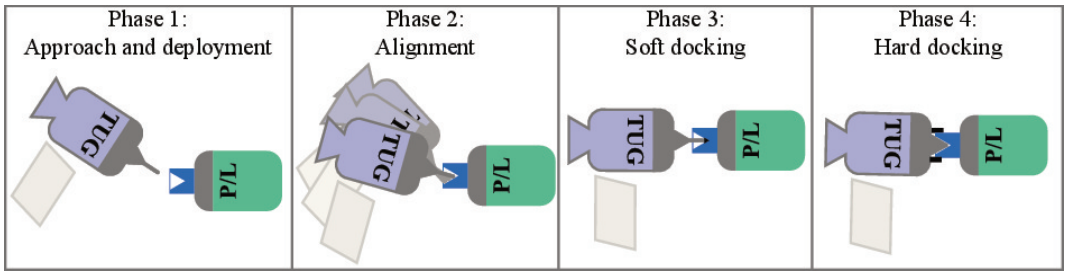

Fig. 4.7 STEPS' mechanism docking maneuver

4.3 Articulated arms with grippers

As stated in chapter 3, a non-compulsory specification of the STRONG mission is to exploit the standard adapter ring used to mount a payload to the Vega launcher as a docking fixture. The main idea behind the articulated arms concept was to be also compliant with this specification. In this case, the active part of the mechanism is composed of three deployable linkages (arms) equipped with clamping devices.

Figures 4.8 and 4.9 show the basic concept of the articulated arms system. In these figures, (1) represents the adapter ring of the Vega rocket that is fixed to the target spacecraft. The adapter is the PLA 937 VG (figure 3.6). The three arms (2) are initially stowed in the chaser (figure 4.8). During the first phase of the docking procedure, the arms are simultaneously and symmetrically deployed using a main central actuator (3). This actuator is connected to each arm through a suitable transmission not depicted in detail in figure 4.9. Each linkage is equipped with a gripper (4) linked to the arm by a spherical joint that allows its rotations in the alignment phase. In this phase, the contact between each gripper and the Vega ring aligns the former as it may rotate about the spherical joint. Once a first gripper comes into contact with the ring, it is closed by an actuator to accomplish a first partial soft docking. Subsequently, due to the motion of the chaser toward the target,

a relative rotation of the two spacecraft takes place about the spherical joint of the clamped gripper. This approaching allows the other grippers to clasp the ring in sequence to conclude the soft docking phase. After it, the main central actuator retracts simultaneously and stows the set of arms into the chaser, bringing the target in the final position relative to the chaser.

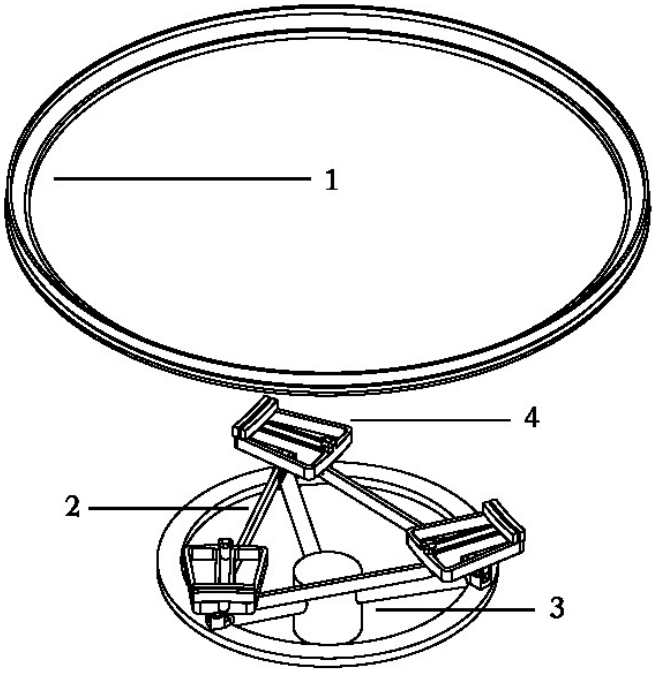

Fig. 4.8 Articulated arms in stowed configuration

Finally, due to the large dimension of the ring, the hard docking is not possible by using hooks, as for the other concepts here presented. It is instead performed by a brake applied to the main actuator. The docking maneuver of this mechanism concept is depicted in figure 4.10.

The cross section of the Vega ring (figure 3.6) was used for the preliminary dimensioning of the linkages and the grippers. This section was translated and rotated following the specifications in table 3.1. Figure 4.11 shows the result of this operation: the limit positions of the ring at the beginning of the approach maneuver. In this figure, the red trace represents the nominal position of the adapter ring. The sections in magenta were translated $-50\,mm$ and rotated by $\pm 3\,deg$ while the green sections were equally rotated and translated $50\,mm$. Finally, the blue traces represent the sections of the adapter after only $\pm 3\,deg$ rotations.

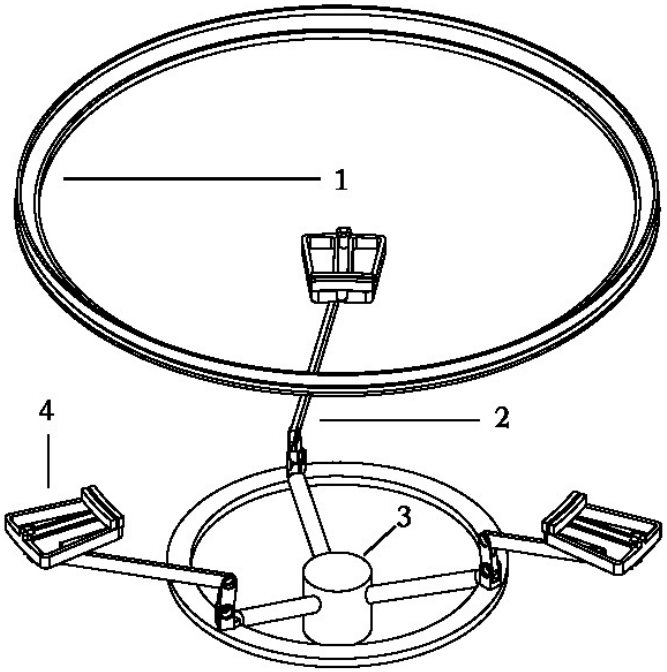

Fig. 4.9 Articulated arms deployed

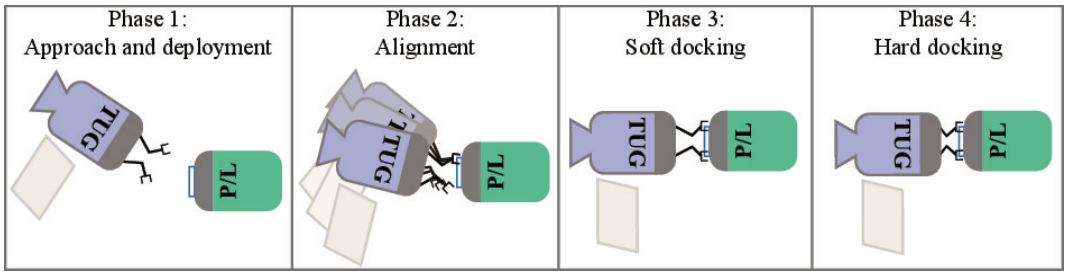

Fig. 4.10 Docking maneuver of the articulated arms with grippers

By using the limit positions of the ring the preliminary dimensions of the gripper were estimated (figure 4.12). This gripper is composed of a sliding finger driven by a non reversible actuator and a fixed finger. Moreover, with both the maximum allowable diameter of the mechanism during launch (table 3.3) and the external diameter of the ring, it was possible to design a suitable deployable linkage for the arms. All the data from this dimensioning was used to create the simplified CAD model of the mechanism depicted in figures 4.8 and 4.9. This model allowed a rough estimation of the mass of the mechanism.

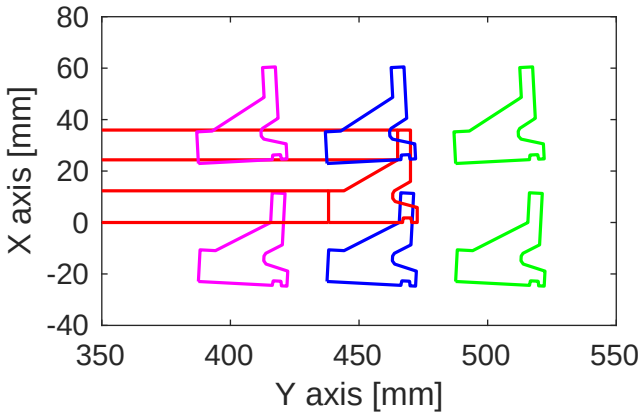

Fig. 4.11 Limit configurations of the Vega adapter ring

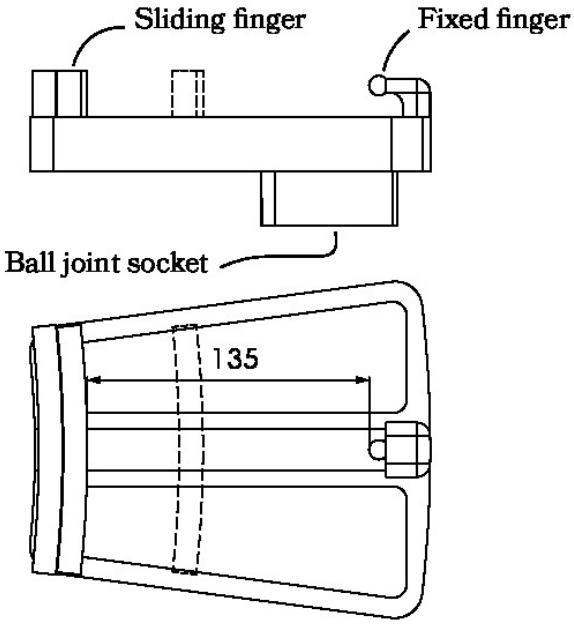

Fig. 4.12 Gripper concept

4.4 Central Active Mechanism (CAS)

The central active system (CAS), shown in figure 4.13, is composed of an active part and a passive one. The active part is equipped with a linear actuator (1) for controlling the longitudinal approaching between the chaser and the target. This actuator is installed on a joint with two rotational degrees of freedom (2), driven

by two actuators (3) useful for eliminating the lateral misalignments between the interfaces. The passive part is a socket with a conical guide built on a spherical joint (4).

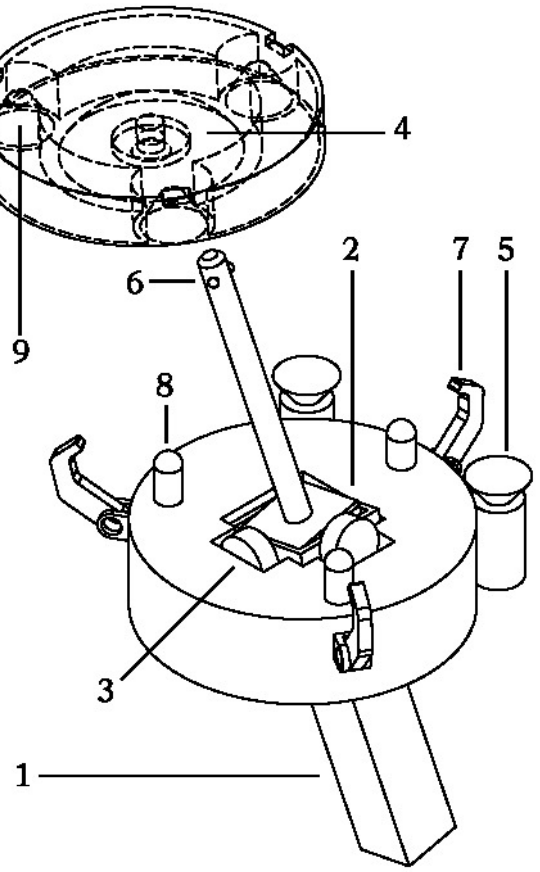

Fig. 4.13 Central active mechanism in deployed configuration

During the alignment phase, the linear actuator is extended nearly to its maximum stroke. Simultaneously, the control system drives the longitudinal actuator to point toward the center of the conical housing using the two lateral actuators. The pointing is achieved exploiting a position feedback system based on optical sensors (5). Subsequently, a further extension of the linear actuator allows its tip to impact the female housing on the passive side. The action of the tip rotates the passive housing aligning the two interfaces. Once the tip is pushed into the housing three spring-loaded elements (6) mechanically connect the two interfaces, achieving soft docking. However, this connection allows relative rotational motion between the spacecraft.

Afterward, the three servoactuators eliminate the relative position errors reducing the distance between the target and the chaser. Before the hard docking is achieved by using a set of hooks (7), dampers (8) combined with conical seats (9) eliminate the residual angular errors between the spacecraft.

Figure 4.14 shows the four phases of the docking procedure performed by the CAS. In particular, it is worth noting that during the alignment phase the probe is pointed toward the passive housing compensating any attitude change of the chaser.

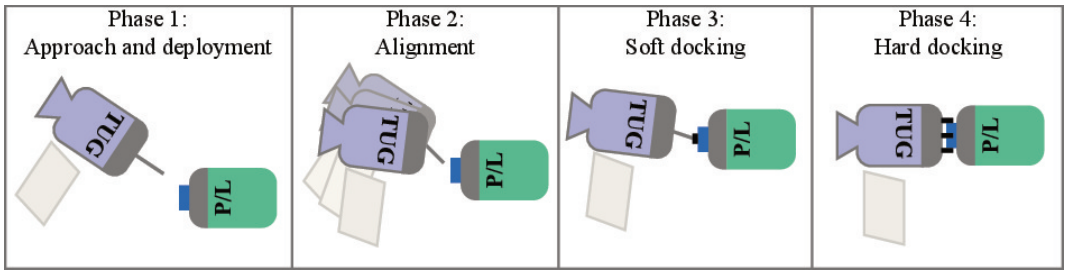

Fig. 4.14 CAS docking maneuver

In this particular case, the CAD model of the active part (figure 4.13) was generated considering the maximum allowable bulk dimensions (table 3.3). The objective was to have the longest non-telescopic actuator possible. A telescopic actuator may reduce the reliability of a system due to its mechanical complexity. The length of the actuator is necessary to increase the distance between the bodies, therefore, making the operation safer. Moreover, the larger the diameter of the active half the wider its workspace. Also, in this case, a rough estimation of the mass of the mechanism was computed using the CAD model combined with suitable materials.

4.5 Trade study

A trade study is a procedure useful to find the most balanced solution amongst a set of possible candidates to solve a certain problem [39]. Trade studies are necessary to avoid committing too early to a design that may not meet all the technical specifications of a project. In this regard, several criteria were defined to evaluate each of the five concepts above described based on a scoring system. Moreover, a weight was introduced to increase the relevance of some parameters. Finally, the total score of each mechanism was computed leading to final concept selection.

4.5.1 Description of the trade-off criteria

Several parameters were considered for choosing the most appropriate mechanism concept for the envisaged mission. Among all the parameters that could have been considered, the main chosen ones were mass, mechatronic complexity, control complexity, the ability to work with targets with different masses, energy consumption, reliability, and functional confidence. The following paragraphs explain the meaning of the parameters above introduced.

The *mass* parameter evaluates the total mass of the mechanism, target plus chaser parts. Considering $3000\,\$/kg$[1] [40], a small mass may moderately reduce the overall cost of the mission.

The *mechatronic complexity* takes into account the intricacy of the mechanism from the hardware point of view. For this purpose three different aspects were evaluated:

- Mechanical complexity: this parameter considers the complexity of the mechanical elements that compose the structure of the mechanism;
- Sensors: this aspect is related to the sensors dedicated to the control and monitoring of the docking mechanism. Both the type and the number of sensors contribute to defining this parameter;
- Actuators: this item assesses the mechanism in terms of actuation. Here again, the evaluation related to this parameter is defined considering the type and number of actuators. A lower number of actuators leads to a better system.

The *control complexity* evaluates a system in terms of the control architecture needed to use it properly during the docking maneuver.

The mission scenario involves interfacing with spacecraft of different masses. During the soft docking, the stiffness and the damping of the mechanism are fundamental parameters that, depending on the masses, affect the relative kinematics between the two bodies. For this reason, the *compatibility with different spacecraft masses* was also taken into account in the trade-off.

[1] As for 2017, the price per kilogram to LEO offered by SpaceX is 2719$. This is an indicative price, as no official price of a launch with the Vega system is publicly available.

Energy consumption takes into account the energy necessary to drive the sensors and actuators dedicated only to the mechanism.

The number of subsystems that combined create the whole docking mechanism is the main parameter used to evaluate the expected *reliability*: a lower number of subsystems leads to a better score. To compute the number of subsystems the actuators, sensors, and transmission chains were considered.

Finally, the *functional confidence* was considered for each technology. This parameter was evaluated taking into account previous space applications of the base technologies as well as the expertise and background of the SAPERE-STRONG project partners.

4.5.2 Trade study results

The following subsections will show in a descriptive fashion the results of the trade-off procedure for each criterion introduced before. At the end of this section, a score between 1 to 5 will be given to the concepts for each criterion and the results will be summarized in a tabular way. Moreover, a description of the weights applied to each score in the trade-off will be presented based on the objectives and critical aspects of the SAPERE-STRONG project.

Mechanism mass

For each mechanism a preliminary mass was estimated considering the sum of the envisaged masses of the structural parts, actuators, transmission chains, mechanism links, etc.. This was accomplished by exploiting the simplified CAD models. Table 4.1 shows the mass values estimated.

Mechatronic complexity

As mentioned before, this criterion is composed by three main aspects: mechanical complexity, sensors, and actuators. The following paragraphs will describe these aspects for each of the mechanism separately.

Table 4.1 Preliminary masses of the docking mechanisms

6SPS with position control	$25\,kg$
6SPS with impedance control	$30\,kg$
Probe and drogue	$15\,kg$
Articulated arms	$20\,kg$
Central active system	$20\,kg$

6SPS parallel manipulator – position control Regarding the mechanical complexity, the male part is composed of a moving platform and a support anchored to the chaser. On the other hand, the female is a solid reception cone. The linear actuators are connected to the moving ring and support by either spherical or universal joints depending on the type of actuator. Besides the sensors to measure the length of the actuators and the applied wrench, the system is also equipped with a stereoscopic optical system to identify the pose of the target.

6SPS parallel manipulator – impedance control This system is equipped with all the elements of the previous concept but the optical system. For this reason, it is simpler than the system with position control from the mechatronic point of view.

STEPS' probe and drogue From the mechanical point of view, this system is composed of a retractable probe equipped with a shock absorber. Furthermore, the probe is mounted on a spherical joint and is connected to four elastic elements. On the female side is located a passive reception cone with a socket at its apex.

There is one servoactuator to retract the probe after soft docking. This system is only equipped with the sensor needed to measure the position of the probe during retraction and deployment, e.g., an incremental encoder.

Articulated arms This system is composed of three 2-bars arms plus three grippers and a transmission system to deploy the arms from their stowed to the deployed configuration. There are three interferometers mounted on the grippers and a torque/-force sensor to control the main actuator. The actuators are the following: the main

central actuator, three non-reversible actuators for the grippers, and a normally closed brake. This brake is necessary to block the system in the hard docking phase.

Central Active Mechanism The male part of this mechanism is composed of a support on which a longitudinal actuator is mounted through a 2 DOFs rotational joint (2-axis gimbal). Additionally, two lateral actuators are needed to eliminate the lateral position errors between the interfaces. There is also a set of shock absorbers mounted on the active part to eliminate the relative angular misalignments and dampen the last part of the approach.

The female part is equipped with a spherical joint that contains the reception socket for the longitudinal actuator. It also has a set of conical seats for receiving the shock absorbers.

Besides the sensors to measure the position of the actuators and the exchanged forces/torques, a stereoscopic vision system is also necessary for guiding the insertion of the end of the longitudinal actuator inside the female half.

Finally, all the concepts but the articulated arms need a couple of systems not yet introduced. A suitable actuation system is mandatory for deactivating the latches used for soft docking once the separation (undocking) takes place. In addition, a system to actuate the hard docking hooks has to be also provided in the design of the mechanisms.

Control complexity

The analysis of the control complexity took into account the four phases of the docking maneuver. In the deployment phase, all the mechanism are controlled in position to place their active interfaces in the desired initial configuration. Both the CAS and the 6SPS parallel manipulator with position control have, for the alignment phase, a position control logic with optical feedback. On the other hand, both the 6SPS with impedance control and the articulated arms system work with impedance control. However, the control of the 6SPS will be much more complex than the one of the articulated arms as it has to be implemented combining six actuators instead of one. In addition, the articulated arms system, using the signal from the interferometers, has to drive the closure of the grippers when the ring is detected.

Regarding the hard docking phase, all the mechanisms work in a similar way. They all are position controlled having as feedback the position of the moving end of the retractable part of the mechanisms. This position feedback is obtained by using the position sensors of the servoactuators. During retraction, the exchanged wrench between the chaser and the target must be maintained below a safety limit.

The undocking phase is very similar to the deployment: the mechanisms are positioned in a desirable and safe position for the separation and all the blocking elements are deactivated. For this phase, spring loaded elements could help to separate the spacecraft.

Compatibility with different spacecraft masses

To ensure the compatibility with different masses the docking mechanism should be able to adapt its overall stiffness and damping to the masses of the spacecraft. The 6SPS systems are fully adaptable along and about six DOFs. The CAS system is adaptable along all the three Cartesian directions. Moreover, the articulated arms mechanism rules its stiffness and damping along the longitudinal direction.

The probe and drogue system works in a passive fashion. For this reason, it has to be designed to work relatively well with all the possible masses of the reference mission. Its advantageous simple design has this issue as one of the main drawbacks.

Energy consumption

The 6SPS mechanism is the most power-hungry concept, especially the position controlled one. Not only six linear actuators have to be driven but also the position and impedance control logic have to be executed on the onboard computers. Something similar happens with the CAS but only three actuators must be driven. The articulated arms are equipped with only one actuator to be controlled. The probe and drogue, due to its passive nature, is expected to have the lowest energy consumption. It has, however, an actuator to retract the rod. All the mechanisms but the articulated arms are equipped with three non-reversible actuated systems to close the hooks. These actuators have to be considered in the power budget of the systems.

Reliability

A measure of the reliability may be given by studying the number of subsystems inside a larger and more complex system. The less reliable concepts from this point of view are the 6SPS parallel manipulators. Both have the larger number of actuators and sensors. The mechanism with position control is less reliable than the one with impedance control due to the stereoscopic optical system. The 6SPS manipulator with position control adds one more subsystem that may increase the failure probability of the whole docking mechanism. Although the CAS is equipped with an optical system, it contains fewer actuators and sensors than the parallel mechanisms. In this regard, the number of actuators and sensors of the articulated arms is smaller than in the case of the CAS. Finally, The most reliable system is the probe and drogue concept. It is equipped with less mechanical and electrical subsystems than the other concepts, therefore, is expected to be more reliable.

Functional confidence

The Soyuz docking system (section 2.2.2) and the androgynous peripheral docking systems (sections 2.2.4 and 2.2.5) have been successfully space-tested throughout several space missions. This gives to the mechanisms based on those technologies, the 6SPS parallel manipulators, and probe and drogue, a high functional confidence. The remaining mechanisms present not yet tested features that reduce the certainty of their proper functional behavior.

4.5.3 Trade-off score synthesis

To summarize all the information above provided table 4.2 shows the scores assigned to all the mechanisms for each criterion. The scores are assigned within the range 1-5; a higher score means a more feasible mechanism concept. The last column in table 4.2 defines the weights associated with each criterion. The total score for each concept is obtained by summing the products between the score for each criterion and its respective weight. The selected weights state that the mechatronic complexity is one of the most important criteria. A higher score implies a simpler design. A simpler design implies a higher confidence related to safety and the schedule risk of the project. Another important criterion is the compatibility with different masses.

The project has as technical specifications different spacecraft masses and the system has to work properly with all of them. Even though mass and energy consumption are important, they were not considered the driving parameters of the design. The remaining parameters were considered equally highly important (weight 4) but less critical than the complexity and compatibility criteria.

Table 4.2 Trade-off results

Trade-off criteria	6SPS position control	6SPS impedance control	CAS	Articulated arms	STEPS	*Weights*
Mass	3	2	4	4	5	2
Mechatronic complexity	3	3	4	2	5	5
Control complexity	2	3	3	4	5	4
Compatibility with different masses	5	4	4	3	1	5
Energy consumption	2	3	3	4	5	2
Reliability	2	3	4	4	5	4
Functional confidence	5	5	4	2	5	4
Total	86	89	98	81	110	

Table 4.2 shows that the mechanism concept with the highest score is the STEPS' probe and drogue system. This system has the highest score for all the criteria but the compatibility with different masses. The CAS is in second place. It has a very balanced set of scores and, in contrast with the probe and drogue, it scores 4 in compatibility. 6SPS with impedance and position control are placed respectively in the 3rd and 4th places. They are more adaptable, have a high functional confidence but were considered less reliable. The last place is occupied by the articulated arms concept. It is the most innovative design which implies a low functional confidence. Moreover, the main central actuator needs to operate the arms simultaneously per-

forming a complex deployment. The former is certainly highly complex from the mechanical point of view.

Conclusively, the STEPS' probe and drogue was further investigated. This mechanism does not exploit the Vega adapter ring. However, using the ring was a desirable feature and not a compulsory specification. This system is advantageous due to its simplicity and proven architecture. Nonetheless, the mechanism lacks in compatibility with different masses due to its passiveness that prohibits the modulation of its stiffness and damping. For this reason, an improvement to this mechanism may come from the second mechanism in terms of trade-off score: the CAS. If needed, the probe and drogue might be bestowed with active degrees of freedom. By doing so, the mechanism may be able to change its dynamic parameters so as to adapt to different initial docking conditions and spacecraft inertial properties. The next chapter will be dedicated to the development of the STEPS' docking mechanism.

Chapter 5

First design iteration: passive central mechanism

The trade study presented in section 4 showed that the most suitable mechanism for the STRONG mission is the central docking system developed by TAS-I during the STEPS project. Back in section 4, this system was described as a concept and only its functional layout was shown (figure 4.6). However, this mechanism was designed, manufactured, and partially tested in a laboratory environment by TAS-I. Nonetheless, the design and test were centered around a planar test bed[1]. This test bed consisted on a servicer spacecraft floating on an air pad over a flat surface. The chaser was programmed to dock with a target bolted to the ground, i.e., fixed. Moreover, neither the inertial properties of the spacecraft nor the relative positions and velocities used during the functional and structural design of this mechanism are consistent with the specifications of the STRONG mission. For these reasons, some modifications were needed to guarantee the functioning in a 3D environment while being compliant with the specifications of the reference mission.

Firstly, this chapter will describe the STEPS' probe and drogue mechanism in more detail. Secondly, it will state the needed changes to the mechanism and their implementations. Thirdly, the models used to select the components that passively control the maneuver will be described. Finally, a group of major modifications to this mechanism will be introduced. These modifications were necessary due to some functional issues that will be illustrated later.

[1] An example of such a facility may be seen in [41].

5.1 Description of the passive docking mechanism

The mechanism studied in this first design iteration is a modified version of the docking mechanism developed by TAS-I during STEPS. The functional layout of the STEPS' mechanism was already introduced in section 4.2. The male part of the mechanism (figure 5.1) consists of a spherically suspended probe controlled by four preloaded springs. This probe is composed of an internal and an external part. On the other hand, the female part (figure 5.2) is a conical frustum that guides the probe toward a socket located at its vertex. Soft docking is achieved by three spring-loaded latches hinged to the probe. Regarding hard docking, it is accomplished by the retraction of the central probe and the closure of three hooks driven by a common actuator.

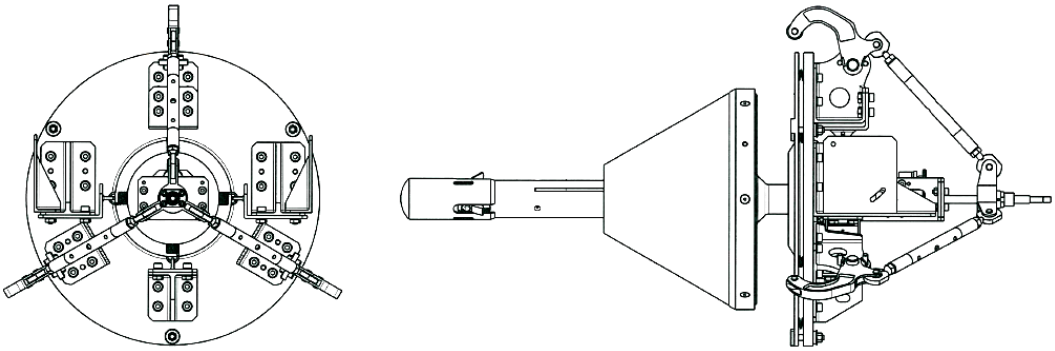

Fig. 5.1 Technical drawing of the male part of the mechanism developed during the STEPS project (credit: TAS-I)

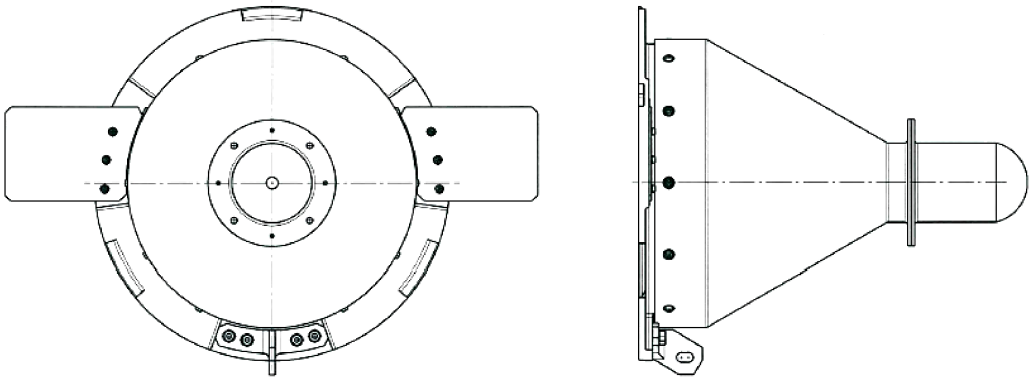

Fig. 5.2 Technical drawing of the female part of the mechanism developed during the STEPS project (credit: TAS-I)

The translational movement of the probe is achieved by using an electric motor and a ball screw (figure 5.3). The torque of the motor rotates the ball screw through a planetary gearhead. The ball nut of the ball screw is rigidly connected to the internal part of the probe. In turn, the rotation of the internal probe is prevented by three dowel pins. These pins are rigidly connected to the internal probe and are constrained to translate longitudinally relative to the external probe by slotted guides machined off the latter. The external probe features three built-in tracks that combined with three low friction Torlon 4301 keys prevent the rotation of both the external and internal parts of the probe. The external probe is also equipped with three ball plungers that keep it in place longitudinally. As a result, the rotation of the motor becomes the forward and backward translation of the internal probe. The backward motion of the internal probe also pushes back the external part through an end stop bolted to it when the force applied to the end stop exceeds the force of the plungers.

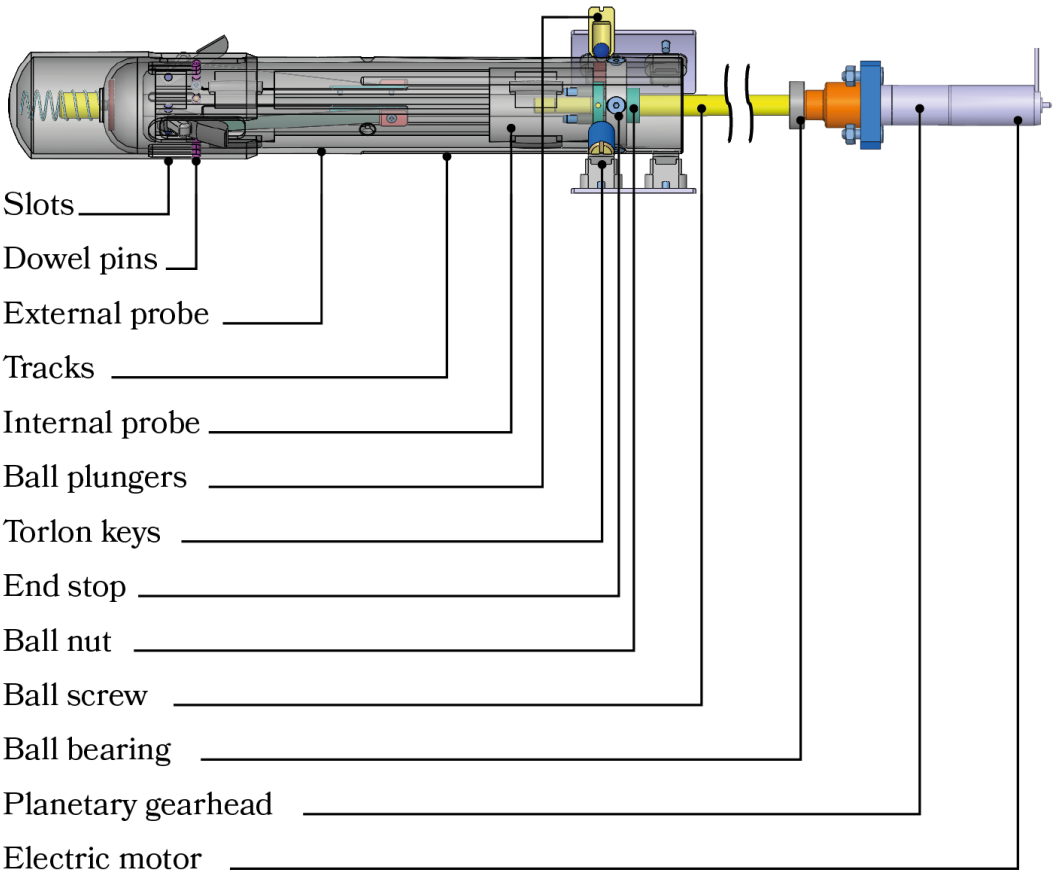

Fig. 5.3 Retraction system of the STEPS' docking mechanism

The probe retraction approaches the female cone up to the male mechanism support plate. Once this position is reached, three hooks driven by a common linear actuator are activated (figure 5.4). The hooks are hinged to the mechanism support, i.e., the interface with the spacecraft structural frame. These hooks are also connected through spherical joints to struts that are in turn spherically connected to a ball nut. This ball nut is translated by a ball screw mounted on the rear end of the probe. The translation closes and opens the hooks so as to create a stiff connection between chaser and target. As a secondary effect, the rotations of the probe force the hooks to rotate as well. This means the probe and the hard docking system are coupled. As a result, the hard docking system increases the stiffness of the docking mechanism during soft docking.

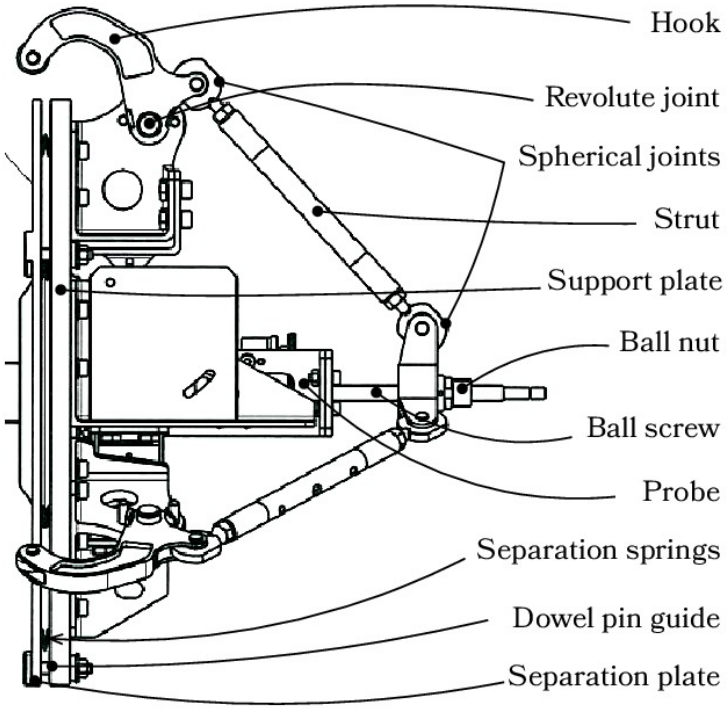

Fig. 5.4 Hard docking system of the STEPS' docking mechanism

The undocking operation starts with the deactivation of the spring-loaded latches. In this case, the internal probe is moved forward. By doing so the latches are folded inward as they make contact with the external part of the probe that is held in place by the ball plungers (figure 5.5).

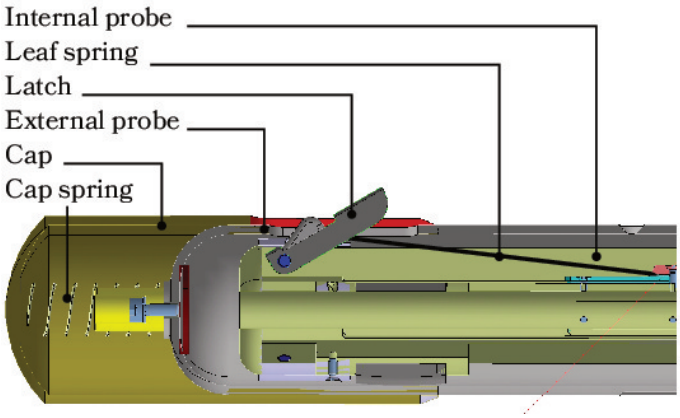

Fig. 5.5 Detail of the tip of the probe

Once the latches are in the closed configuration and the hooks are deactivated, a separation plate pushes the satellites apart (figure 5.4). This plate is connected to a group of compression springs and is guided by dowel pins that allow it to translate only along the longitudinal direction. When the probe is retracted after soft docking, the female cone pushes the separation plate, and with it the separation springs, before making a compact stack with the separation and support plates. The energy stored in the springs is used to separate the spacecraft during undocking. In the laboratory tests, this separation device exhibited mechanical jamming.

The previous paragraphs described the STEPS' mechanism in more detail and introduced some points of improvement: the hard docking and undocking systems. Moreover, since this mechanism was conceived for 2D maneuvers, a system to adjust the relative roll angle between the spacecraft was mandatory. The male and female parts of the first design iteration of the docking mechanism may be seen in figures 5.6 and 5.7. To address the lack of roll adjustment, three v-shaped guides machined out the female part combined with three wedges on the male part act as guiding geometries. Furthermore, the hard docking and undocking subsystems were removed. The new iterations of these subsystems will be introduced and described later.

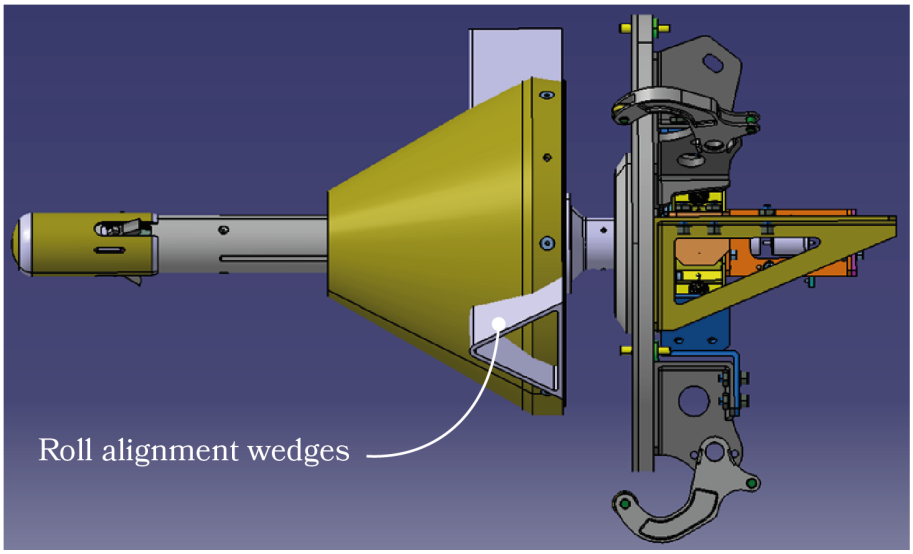

Fig. 5.6 Male half of the first design iteration of the docking mechanism

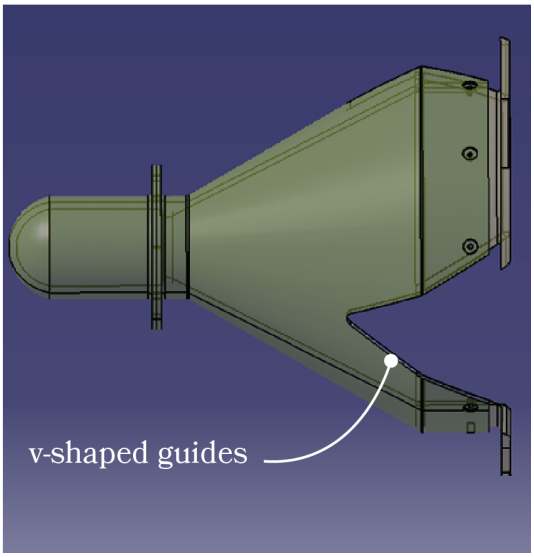

Fig. 5.7 Female half of the first design iteration of the docking mechanism

5.2 Custom 2D mathematical model and implementation

Due to the nature of the docking maneuver, the mathematical modeling of a docking system might result very complex. The geometries of the mechanism parts are fundamental to identify the existence of contact. Moreover, the resultant contact force should be estimated using a suitable model. Additionally, the interaction

between the moving parts (shock attenuators, latches, sockets, etc.) further increases the complexity. For this reason, the industrial approach to tackling the virtual verification of such systems is to implement multibody models using specialized commercial software.

However, several authors have taken analytical approaches and custom numerical implementations instead. For instance, in [42] a mathematical model of the Soyuz docking mechanism is presented. Besides the dynamic equations that describe the motion of the bodies, the model considers the elasticity of the spacecraft. In [43] the theoretical model of a probe and drogue docking mechanism is described. The drogue in this particular docking system is composed of several thin-walled plates making it highly flexible. The non-linear differential equations of Föppl-von Kármán combined with the Hertz contact theory are used to study the impact dynamics. Finally, the model is compared against ANSYS/LS-DYNA simulations, and experimental results. In contrast, in [44] the mathematical model of a docking mechanism with a flexible probe is introduced. In this case, the creation of the model is based on the Lagrange analytical method while the modal equations are derived and compared against numerical methods.

This section describes the custom model used to analyze the evolution in time of the kinematics in 2D of the target and the chaser during the docking maneuver. As stated before, the STEPS' mechanism was designed for different inertial properties and initial conditions than the STRONG mission. In this first iteration of the mechanism, the stiffness of the elastic elements that passively control the maneuver had to be modified in accordance with the new specifications. To do so, the equations of motion of the bodies were written. Subsequently, the model was implemented in Matlab/Simulink^{TM}. The result of this model was a set suitable values for the stiffness of the elastic control elements in a 2D maneuver.

5.2.1 Model description

The target body (figure 5.8) was modeled as a lumped mass: its mass and inertia were concentrated in its center of gravity, G_{TA}. The female cone was rigidly attached to this body at a distance d_{TA}.

There are different coordinate systems associated with the target body. The first one is TA which is positioned at G_{TA}. The second reference system, FC, is

positioned at the base of the docking female cone and is aligned with the cone wall. Finally, FCP is positioned on the contact point between the male probe and the cone. It has the same orientation as FC but may translate relative to it following the contact point. A geometric degree of freedom, l_C, was defined as the distance between the origin of FC and FCP. Finally, the half cone angle of the passive part is θ_{HC}.

The target has three DOFs: $p_{TA,x}$, $p_{TA,y}$, and q_{TA}, respectively, the horizontal and vertical coordinates of G_{TA}, and its angular position. These coordinates are measured with respect to a fixed reference system W.

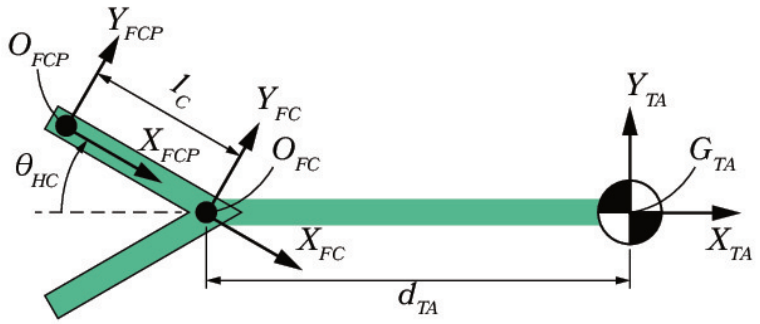

Fig. 5.8 Schematic view of the target and the female cone of the mechanism

The chaser body (figure 5.9) was also modeled as a lumped mass. The spherical joint on which the probe is mounted is equivalent to a revolute joint in the plane XY. This hinge is attached to the spacecraft body at a distance d_{TU}. The hinge acts as a joint between the chaser and the probe allowing the latter to rotate.

The first reference system of the chaser body is TU. It is placed on G_{TU}. The second system R is placed on the hinge and rotates with the probe with its X axis aligned with it. Finally, a third system P is also aligned with the probe but is positioned at its tip. During the contact, the reference systems P (on the probe) and FCP (on the cone) share the same position but differ from each other in orientation.

The chaser has three DOFs: $p_{TU,x}$, $p_{TU,y}$, and q_{TU}. These are respectively the horizontal coordinate and vertical coordinates of G_{TU}, and its angular position. They are measured w.r.t. the fixed reference system W.

In the engineering design of the docking system, four traction springs (figure 4.6) passively control the probe rotation around the spherical joint. These springs are placed in the rear part of the mechanism and have a stiffness equal to k_{rear}. To consider the effect of these springs, an equivalent torsional spring of stiffness k_T was

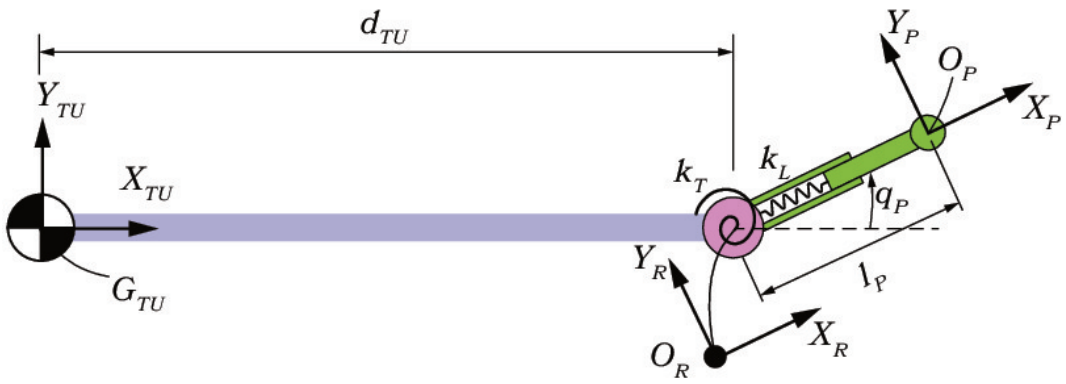

Fig. 5.9 Schematic view of the chaser and male half of the mechanism

attached to the chaser on one side and to the probe on the other. Considering only the two springs in the plane of motion, k_T may be calculated as follows:

$$k_T = 2k_{rear}d_{rear}^2 \tag{5.1}$$

where d_{rear} is the distance between the mounting point of the rear springs on the probe and the spherical joint. Between the probe and the cap, a spring of stiffness k_L is mounted. This spring passively controls the impact between the bodies in the longitudinal direction.

To summarize, the elastic elements introduced before passively control the degrees of freedom of the male half of the mechanism. These geometrical DOFs are the length of the probe, l_P, and the rotation of the probe, q_P.

Several hypotheses were made and are summarized in the following lines. The objects were considered to be free floating; the effect of the orbital motion was not considered. All the docking parts were supposed to have negligible mass. Another hypothesis was the absence of friction between the probe tip and the cone wall.

During the alignment phase, the probe rotates and shrinks relative to the chaser. These compression and rotation generate a force that ends up being the contact force between the mechanism halves, $\underline{F_C}$. Solving the dynamic equations of the bodies considering this force as the external action leads to the integration of the degrees of freedom of the target and chaser. Figure 5.10 shows the free body diagrams of both the target and the chaser in a generic configuration. The above-mentioned force may be seen acting in the contact point between the spacecraft.

This model aims to study the kinematics of the bodies during the alignment phase of the docking. Thus, a constraint was imposed to the contact force. The model works constraining the tip of the probe to slide against the female cone as if a linear guide was present. Since the contact force should only push against the cone surface, the change of direction of the force terminated the simulations. This contact loss means that there is a bouncing which implies a malfunction of the system.

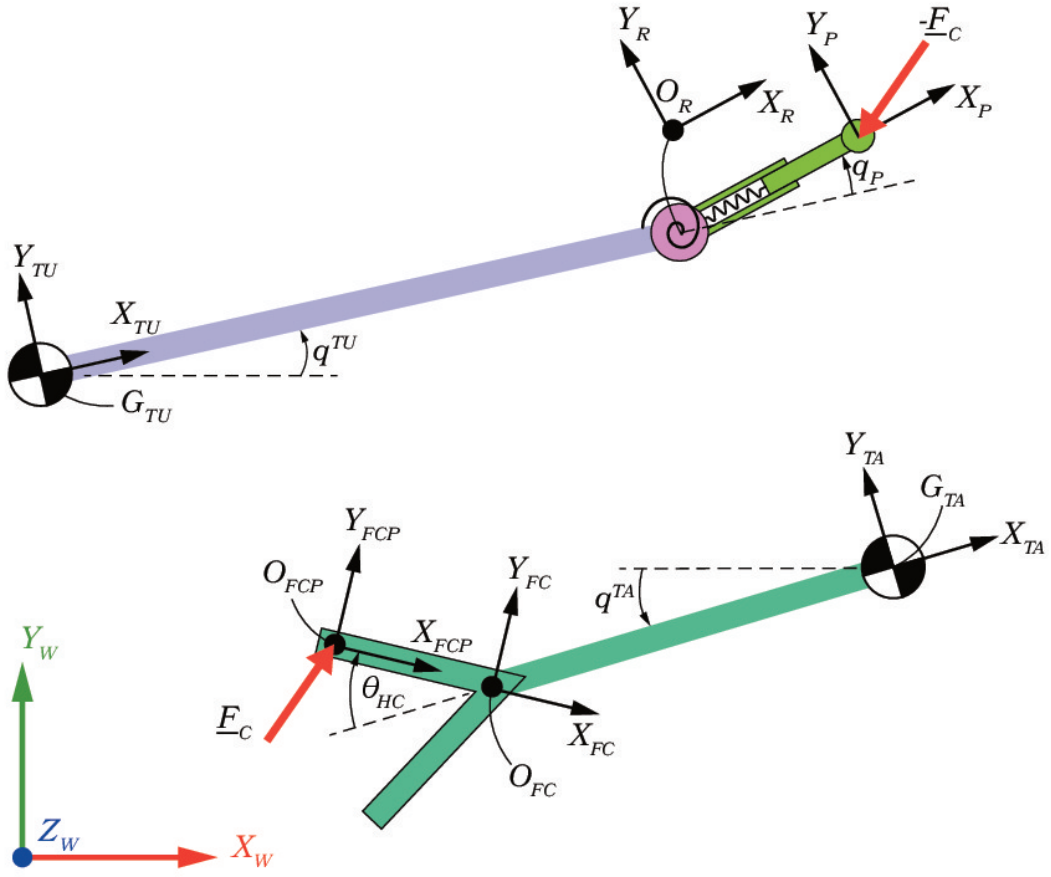

Fig. 5.10 Schematic views of the alignment phase

The equation of motion

$$^{TA}\underline{F}_C = M_{TA}\ ^{TA}\underline{\ddot{p}}_{TA} \tag{5.2}$$

represents the force equilibrium equation of the target. In this equation, M_{TA} is the mass of the target and $\underline{\ddot{p}}_{TA}$ is its acceleration vector. All the quantities in equation 5.2

are expressed w.r.t. TA. The torque equilibrium equation of the target

$$^{TA}(\underline{O}_{FCP} - \underline{G}_{TA}) \times^{TA} \underline{F}_C = I_{G,TA}\ \ddot{q}_{TA} \tag{5.3}$$

is useful to calculate the rotational degree of freedom of this body. In equation 5.3, $I_{G,TA}$ is the moment of inertia of the target about Z_W and $\ddot{\underline{q}}_{TA}$ its angular acceleration.

The same equations may be written for the tug (equations 5.4 and 5.5). In these equations, M_{TU} and $I_{G,TU}$ are respectively the mass and the moment of inertia about Z_W of the chaser, $\ddot{\underline{p}}_{TU}$ is the acceleration vector of the tug, and $\ddot{\underline{q}}_{TU}$ its angular acceleration.

$$^{TU}(-\underline{F}_C) = M_{TU}\ ^{TU}\ddot{\underline{p}}_{TU} \tag{5.4}$$

$$^{TU}(\underline{O}_P - \underline{G}_{TU}) \times^{TU} (-\underline{F}_C) = I_{G,TU}\ \ddot{q}_{TU} \tag{5.5}$$

A geometric closure equation may be written describing the contact point between the bodies starting from the center of mass of the target and doing the same using the one of the chaser:

$$^{W}\hat{\mathbb{A}}_{TA}\ ^{TA}\hat{\mathbb{A}}_{FC}\ ^{FC}\hat{\mathbb{A}}_{FCP} \begin{bmatrix} 0 \\ 0 \\ 1 \end{bmatrix} = {}^{W}\hat{\mathbb{A}}_{TU}\ ^{TU}\hat{\mathbb{A}}_{R}\ ^{R}\hat{\mathbb{A}}_{P} \begin{bmatrix} 0 \\ 0 \\ 1 \end{bmatrix} \tag{5.6}$$

In equation 5.6 ${}^{1}\hat{\mathbb{A}}_{2}$ represents the 3×3 homogeneous matrix that describes the pose of the reference system 2 w.r.t. the reference system 1.

As introduced above the contact force $\underline{F}_C$ is a function of l_P and q_P. This force will be aligned with the unit vector Y_{FCP} ($\hat{Y}_{FCP}$). Expressing this vector w.r.t. P allows writing equation 5.7.

$$\|\underline{F}_C\|\hat{Y}_{FCP} = -\begin{bmatrix} k_L\left(l_P^0 - l_P\right) - \beta_L \dot{l}_P \\ \frac{1}{l_P}\left(k_T q_P + \beta_T \dot{q}_P\right) \end{bmatrix} \tag{5.7}$$

Equation 5.7 shows the relation between k_L, k_T, and $\underline{F}_C$. β_L and β_T are the damping coefficients of the probe and revolute joint. To calculate the values of

these damping coefficients a 3% of modal damping was considered for both the longitudinal and rotational motions.

To calculate β_L, the simplified model in figure 5.11 was considered.

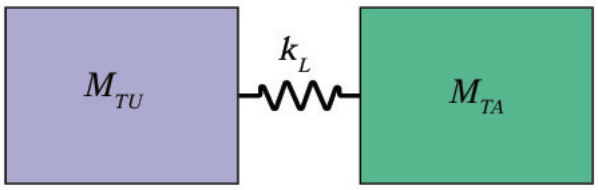

Fig. 5.11 Simplified model considering only the longitudinal translation

The equivalent mass M_{eq} may be defined as

$$M_{eq} = \frac{M_{TA} + M_{TU}}{M_{TA} M_{TU}} \tag{5.8}$$

The natural frequency of this system is $\sqrt{k_L/M_{eq}}$. With this value, it is possible to assign a plausible value to the damping coefficient having a modal damping ζ equal to 0.03

$$\beta_L = 2\zeta\sqrt{k_L M_{eq}} \tag{5.9}$$

Similarly, for the rotational motion, an equivalent inertia may be written as

$$I_{eq} = \frac{I_{G,TA} + I_{G,TU}}{I_{G,TA} I_{G,TU}} \tag{5.10}$$

then, β_T becomes

$$\beta_T = 2\zeta\sqrt{k_T I_{eq}} \tag{5.11}$$

5.2.2 Model Implementation

Equations 5.1 to 5.9 were implemented and solved in Matlab/Simulink™. Figure 5.12 shows the general layout of the model. Four main blocks are present in this graphical language model. Inside the block `TARGET`, the equations of the target

body may be found. The same applies for the block `TUG`. Inside `Calc F`, the versor $\hat{Y}_{FCP}$ is rotated into P and then the magnitude of the contact force is calculated using equation 5.7. Finally, the block `solveGeo` is an embedded Matlab^{TM} function in which equation 5.6 is implemented and solved.

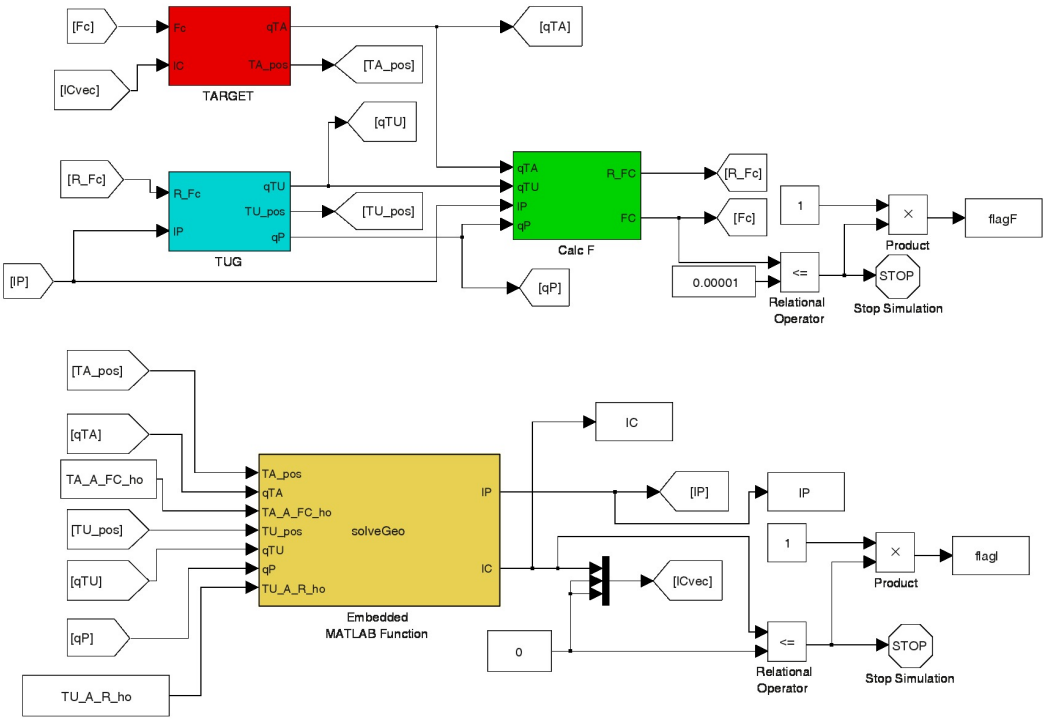

Fig. 5.12 Simulink implementation of the 2D custom model

Figure 5.13 shows the contents of the block `TARGET`. A block called `WRENCH CALCULATION` calculates the wrench applied on the target body. This wrench is the input of the block `3DOFs` that solves the dynamic equations 5.2 and 5.3. Finally, `OUTPUT SELECT` manages the important variables that are used by the other blocks.

Figure 5.14 shows the `CHASER` block. inside the block `WRENCH CALCULATION`, the contact force is translated in the chaser frame as well as the torque produced by it. The wrench is then given to the block `3DOFs`, and equations 5.4 and 5.5 are solved. The block `OUTPUT SELECT` is a service block that selects and operates on the output variable of the subsystem.

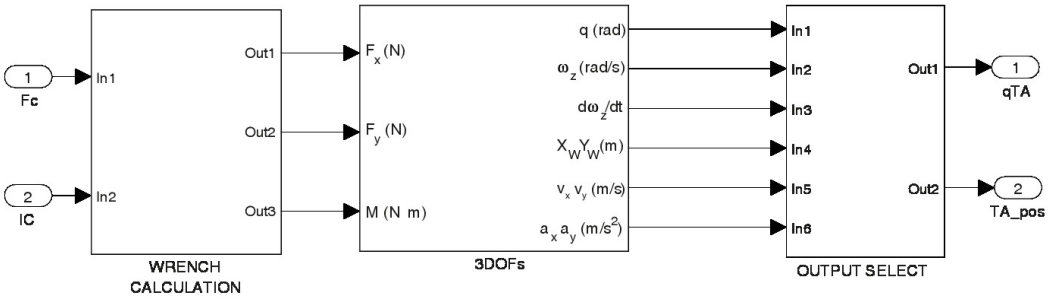

Fig. 5.13 Simulink `TARGET` subsystem

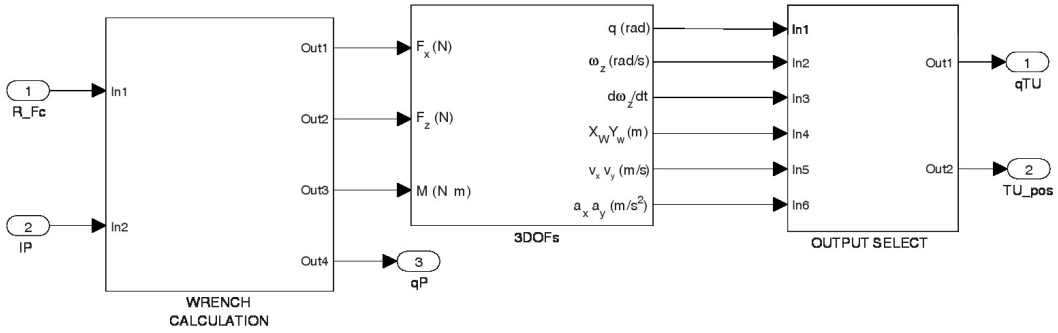

Fig. 5.14 Simulink `TUG` subsystem

5.2.3 Numerical values

The scope of this section is to report the numerical values used during the simulations taking as the reference the specifications of the STRONG mission (chapter 3).

The target used was the satellite platform. This object was selected for having the lowest moment of inertia about Z_W (eq. 3.3). It also has a lower mass than the orbital tank. Lower inertial properties result in higher rates for a given contact force. The properties are the following:

$$M_{TA} = 2000\,kg$$
$$I_{G,TA} = 2000\,kgm^2$$
$$d_{TA} = 0.65\,m$$

A docking maneuver before the orbit raising was considered as the reference case. In this case, the properties of the space tug are consistent with the Configuration B:

$$M_{TU} = 3500\,kg$$
$$I_{G,TU} = 5235\,kgm^2$$
$$d_{TU} = 1.942\,m$$

Regarding the male part of the docking system, the distance d_{rear} in equation 5.1 is equal to $44\,mm$ while the initial length of the probe, l_P^0, is $416\,mm$. On the other hand, the half cone angle of the female part is $30\,deg$.

Finally, only the limits values in table 3.1 were used as initial conditions during the simulations. In particular: the initial relative approaching velocity was set to $30\,mm/s$ throughout all the tests. Regarding the lateral misalignment, it was $50\,mm$, the angular misalignment $3\,deg$, and the initial relative angular rate was $0.1\,deg/s$. Both $10\,mm/s$ and $-10\,mm/s$ were used as initial lateral velocities.

5.2.4 Results

The outputs of the simulation model are the evolution in time of all the degrees of freedom of the chaser and target. The model also generates the geometric degrees of freedom of the docking system and the exchanged contact force. Figure 5.15 shows a graphical output of the model in the initial configuration. By using this figure, the description of the initial conditions becomes easier. Regarding the misalignments, the relative position between the bodies shown in figure 5.15 is the one used for all the tests. The contact point between the tip of the probe and the cone is located at $50\,mm$ along Y_{TA}. Moreover, the chaser spacecraft was rotated by $3\,deg$ w.r.t. the target. The initial velocities of the target were all set to zero. The angular velocity of the chaser used was $0.1\,deg/s$. Finally, the lateral velocity of the chaser was further analyzed so as to individuated the worst case scenario. The tested values were $10\,mm/s$ and $-10\,mm/s$ along Y_{TA}.

Figure 5.16 shows the evolution in time of the components of the velocity of the target and chaser considering an initial lateral velocity equal to $10\,mm/s$. On the other hand, figure 5.17 shows the same velocities considering the initial lateral

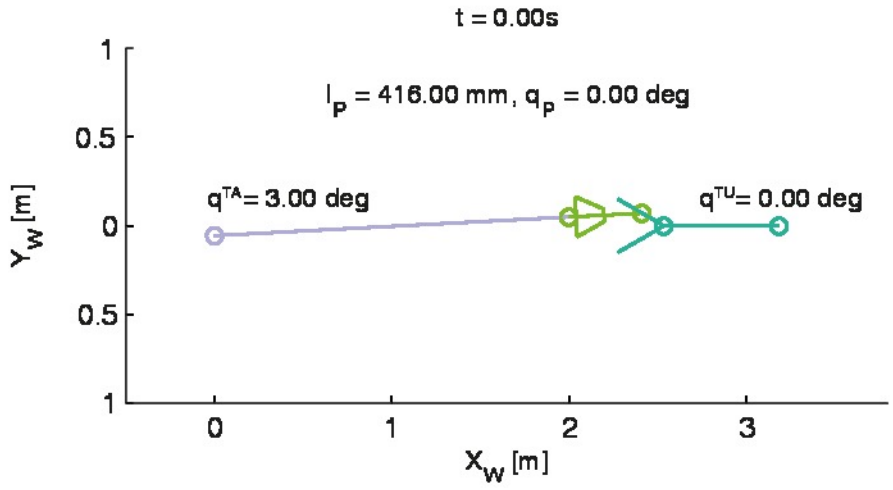

Fig. 5.15 Custom multibody simulation (initial condition)

velocity equal to $-10\,mm/s$. The comparison of figure 5.16 against figure 5.17 shows that the configuration that considers the lateral velocity equal to $10\,mm/s$ produces a higher disturbance on the target.

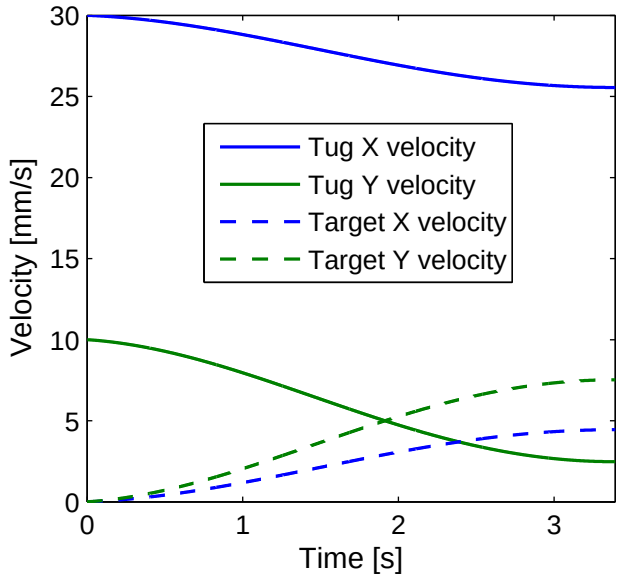

Fig. 5.16 Velocities of target and chaser with an initial chaser lateral velocity equal to $10\,mm/s$. These velocities are expressed in W

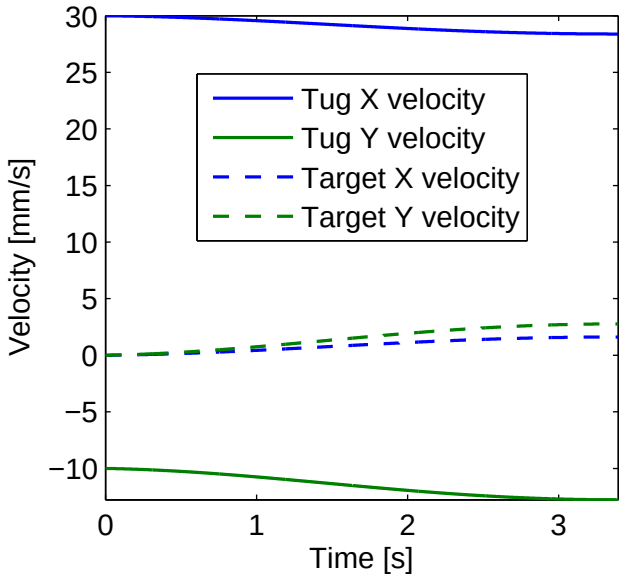

Fig. 5.17 Velocities of target and chaser with an initial chaser lateral velocity equal to $-10\,mm/s$. These velocities are expressed in W

Figure 5.18 supports the aforementioned statement. The maximum value of the exchanged contact force is higher with the initial lateral velocity set to $10\,mm/s$ than the case in which is directed in the opposite direction. For this reason, a maneuver with an initial lateral velocity equal to $10\,mm/s$ was considered as the worst case scenario.

The scope of the female cone is to guide the tip of the probe toward the vertex of the cone for soft capture. Ideally, the tip should arrive at the vertex without bouncing. Bouncing may compromise the docking procedure and has to be avoided. However, if the system loses the contact during the alignment phase it may still be able to dock. Docking is possible if the distance from the vertex upon contact loss is about the diameter of the female socket ($44\,mm$).

Figure 5.19 shows the evolution in time of l_C, i.e., the distance from the probe initial contact point to the cone vertex. Also, in this case, having $10\,mm/s$ as initial lateral velocity worsens the docking maneuver: the distance upon contact loss is higher using this initial condition.

The main objective of this mathematical model is to individuate suitable stiffness values for the elastic elements that passively control the alignment phase of the maneuver. To do so, several simulations were executed considering different

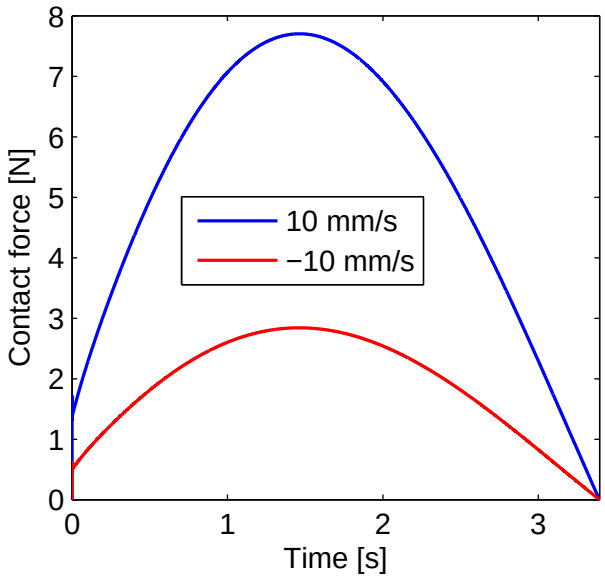

Fig. 5.18 Contact force

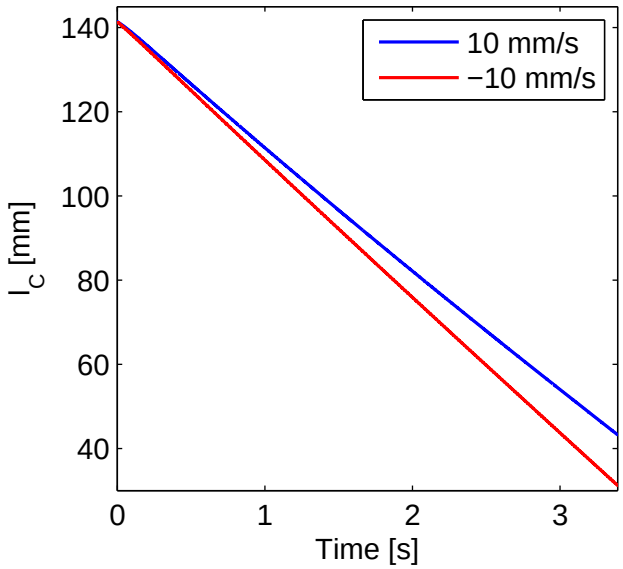

Fig. 5.19 Distance from initial contact point to the cone apex

combinations of stiffness values for both the compression spring connected to cap (k_L) and the traction springs that control the probe rotation (k_{rear}).

Three quantities were investigated: the maximum probe rotation, maximum exchanged force, and l_C upon contact loss. The values found were plotted in contour

plots with 15 isolines using different combinations $[k_L, k_{rear}]$. On the one hand, the minimum value of k_L was $1000\,N/m$. This value was increased up to $50000\,N/m$ taking steps of $2500\,N/m$. On the other hand, the values of k_{rear} ranged from $5000\,N/m$ up to $200000\,N/m$ with steps of $5000\,N/m$.

To find suitable elastic elements, two selection criteria were considered. Firstly, the maximum rotation of the probe considered acceptable was $5\,deg$. The CAD design of the first design iteration (figure 5.6) showed a mechanical interference for higher angles. Secondly, the maximum acceptable displacement of the cap of the probe was $17\,mm$. The stroke of the cap is limited by the interference between the dowel pins and the slotted guides it travels in. During the simulations, if the value of rotation or the value of the displacement exceeded the maximum reference values, the simulation was stopped and the stiffness combination used were discarded.

Figure 5.20 shows the maximum probe rotation. This rotation ranges from about $1\,deg$ to $4.5\,deg$. As expected, for small values of k_{rear}, the resultant probe rotation is higher. On the contrary, high values of k_{rear} imply small angles. It is worth noting that for values of k_{rear} up to $100000\,N/m$ the maximum angle is slightly affected by the value of k_L considering values of k_L greater than $10000\,N/m$. This means that for a large range of combinations $[k_{rear}, k_L]$ the evolution of the alignment phase is only sensitive to the torsional stiffness of the probe.

Figure 5.21 shows that the contact force exchanged becomes larger for high values of both k_L and k_{rear}. These high stiffness values result in a stiffer mechanism and therefore a more rigid, and violent, impact. As noted in figure 5.20, figure 5.21 shows that for a large portion of this map, the value of the force is less sensitive to k_L than it is to k_{rear}. It further proves that the alignment phase is a phenomenon governed by the probe rotation.

The distance between the tip of the probe and the vertex of the cone upon contact loss is a very important indicator of the mechanism functioning. The probe should slide without bouncing during the alignment phase up to soft docking. For this reason, this distance has to be as small as possible when the contact force zeroes. Figure 5.22 shows the contour plot of l_C when F_C zeroes for different combinations $[k_{rear}, k_L]$. Apart from the values of k_L smaller than $15000\,N/m$, this distance is approximately only a function of k_{rear}. It ranges from $30mm$ to almost the distance between O_{FC} and O_{FCP} at the beginning of the simulation.

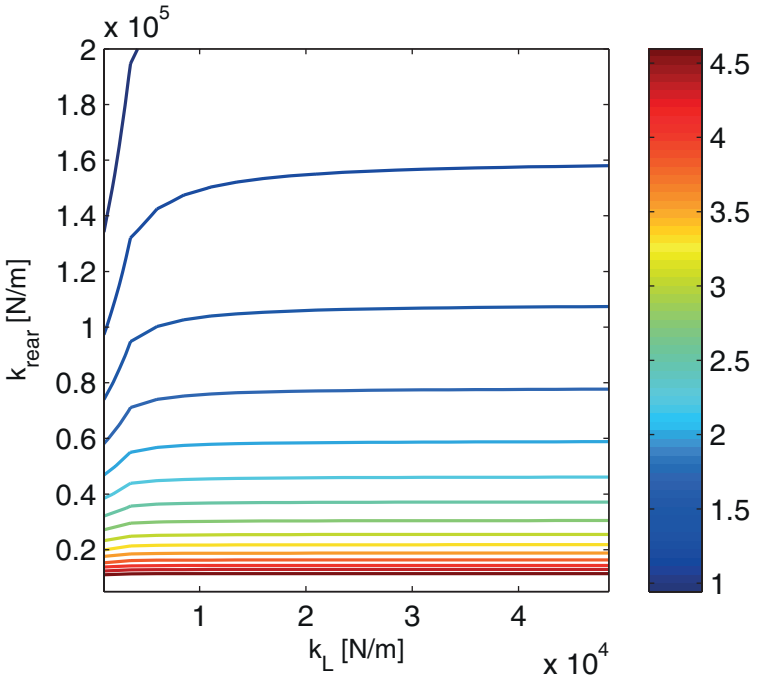

Fig. 5.20 Contour plot of the maximum probe rotation (*deg*)

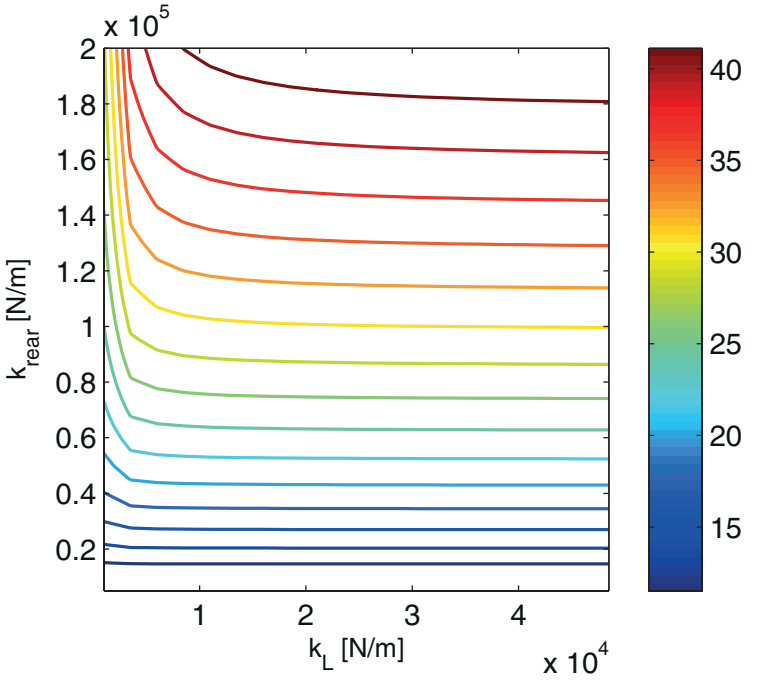

Fig. 5.21 Contour plot of the maximum contact force (*N*)

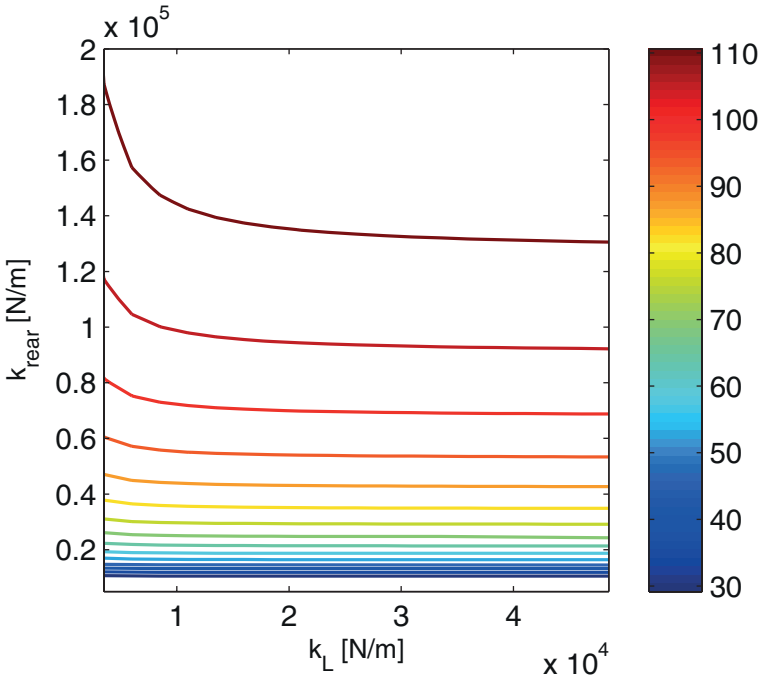

Fig. 5.22 Probe distance from the cone vertex upon contact loss (*mm*)

In figure 5.23 shows a close up of figure 5.22. For values of k_{rear} smaller than $20000\,N/m$, the contour lines are almost horizontal. This reaffirms that the value of k_{rear} dominates the dynamics of the bodies considering the smaller values within the assumed range. These small values may guarantee the absence of bouncing.

At his point, the first conclusion is: low values of k_{rear} allow the docking procedure to be possible regarding bouncing. Moreover, within these low values, only k_{rear} modifies the maximum probe rotation, the maximum exchanged force, and the distance upon contact loss.

There is an import aspect worth mentioning. Having a small value of l_C when the contact loss occurs is not sufficient to state that the docking system functions properly. During soft docking, the complex interactions between the geometries in contact must be studied to properly assess the suitability of the mechanism.

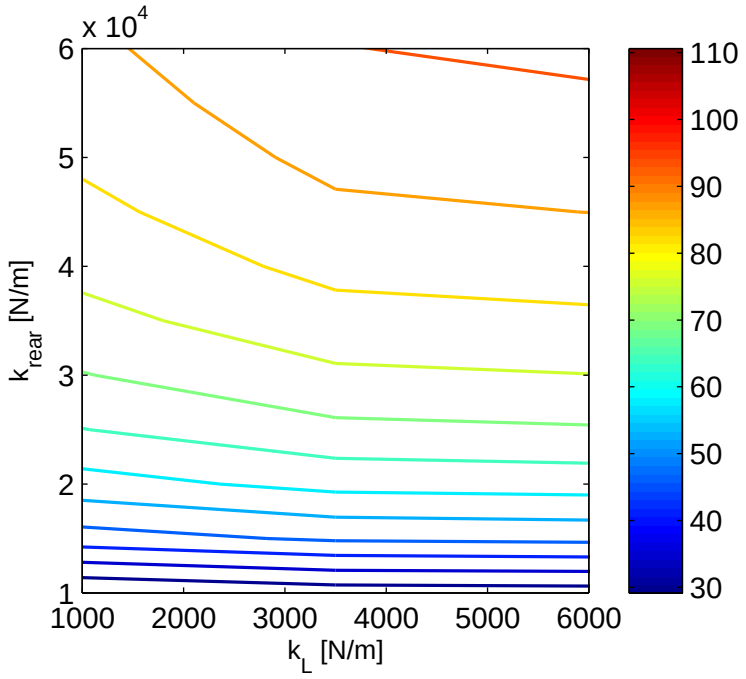

Fig. 5.23 close up of the probe distance from the cone vertex upon contact loss (*mm*)

5.3 MSC Adams multibody model

To study and verify the soft docking phase of the docking maneuver, the geometry of the parts undergoing contact must be taken into account. For this reason, a 2D multibody model was implemented using MSC Adams. In this software, the actual geometries of the bodies may be used during the dynamic simulations. The internal routines of the software verify the existence of contact between the components and calculate the exchanged resultant forces.

5.3.1 Model description

The creation of the model shown in figure 5.24 was accomplished using the Adam's dedicated Graphical User Interface (GUI). The simulation of the chaser spacecraft consisted in implementing a rigid body with the inertial properties shown in section 5.2.3. This body was constrained to move in a plane w.r.t. the ground by using a planar joint. A link element 1942 *mm* long (d_{TU}) was rigidly fitted to the chaser body. At the end of this link, a revolute joint was mounted. This joint connected the chaser link to the probe allowing the bodies to rotate relatively. A torsional

spring-damper, characterized by k_T and β_T, was attached to both the chaser link and the probe. Subsequently, the geometry of the cap was imported from the CAD model. A translational joint was added between the cap and the probe. Finally, a linear spring-damper, characterized by k_L and β_L, was attached to both the probe and the cap to simulate the cap spring.

The target was also created using a rigid body. The inertial properties of this body were consistent with the values reported in section 5.2.3. Also, in this case, a planar joint was added between this body and the ground. The female cone CAD model was imported into the simulation environment and fitted to the target body using a fixed joint. The distance between the target body and the vertex of the female cone was imposed to be $0.65\,m$, i.e., d_{TA}.

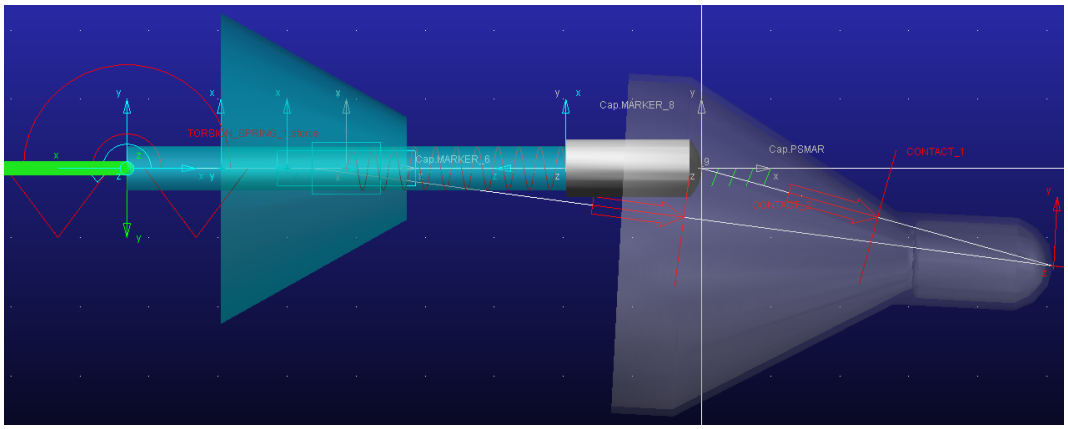

Fig. 5.24 Adams 2D model

The geometries of both the cap and the female reception cone were imported into the software using the Parasolid format (figure 5.25). Moreover, the male alignment cone was created inside Adams View using suitable geometric operations. Two impact constraints were added. The first one between the cap and the female cone, and the second between the female and male cones. These impact constraints were characterized by the values of the stiffness, damping, force exponent, and penetration depth suggested by the software.

The simulations were executed using the maximum misalignments and relative velocities described previously. The 2D custom model showed that low values of k_{rear} allow the probe to slide without bouncing for longer distances. For this reason, $k_T = 39.42\,Nm/rad$ was selected for the Adams simulations. This stiffness is the result of equation 5.1 with k_{rear} equal to $10000\,N/m$. As shown in figures 5.20 and

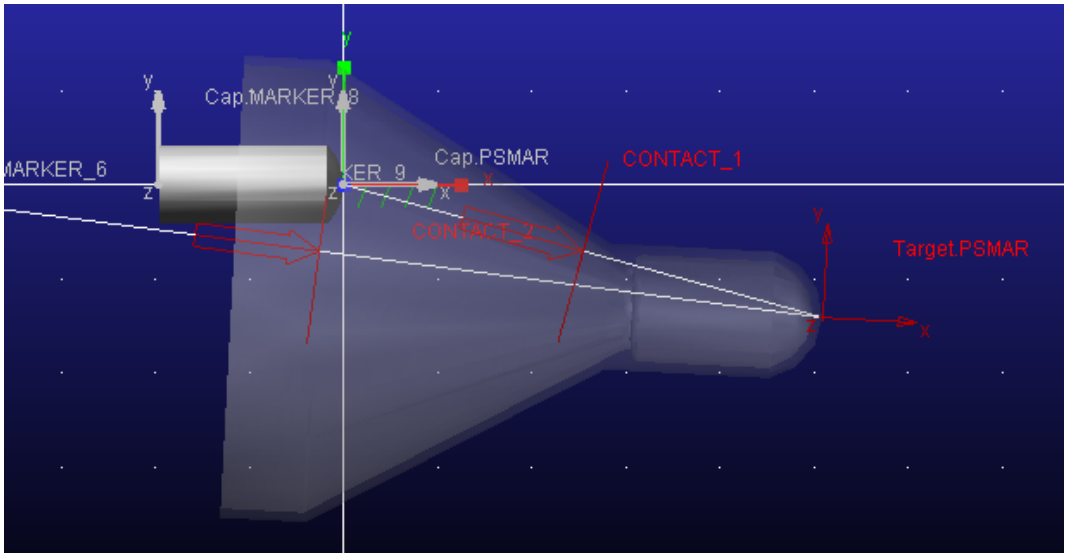

Fig. 5.25 Imported geometries

5.21, the values of the probe rotation and contact force for the selected value of k_{rear} change slightly using different values of k_L. Thus, $k_L = 1000\,N/m$ was selected arbitrarily as a preliminary value.

5.3.2 Results

The main objective of this model was to study the soft docking phase of the docking maneuver. Since the latches of the probe were not included, soft docking was assumed as the whole insertion of the cap inside the cylindrical part of the female reception cone. However, this model was also compared against the 2D custom model during the alignment phase. This comparison was useful to increase the confidence in the results produced by both the models.

Figure 5.26 depicts the contact force during the alignment phase calculated with the 2D custom model and the one with the Adams simulation. The figure shows that the two models predict similar results of the contact force. The values of the peak of force are very similar, around $6.8\,N$, and occur at about $1\,s$ after the first contact. The slight difference may be a result of the geometric simplifications applied in the custom model.

An intermediate configuration during the alignment phase may be seen in figure 5.27. Moreover, figure 5.28 shows a soft docking configuration: the cap is fully

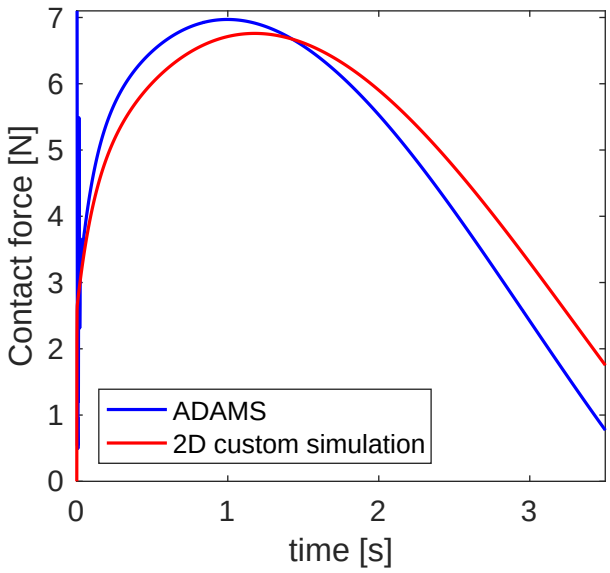

Fig. 5.26 Contact force calculated using 2D custom and the Adams model

inserted in the female socket. This result confirms that the selected stiffness values of the elastic elements are suitable for the alignment phase up to soft docking in a 2D maneuver.

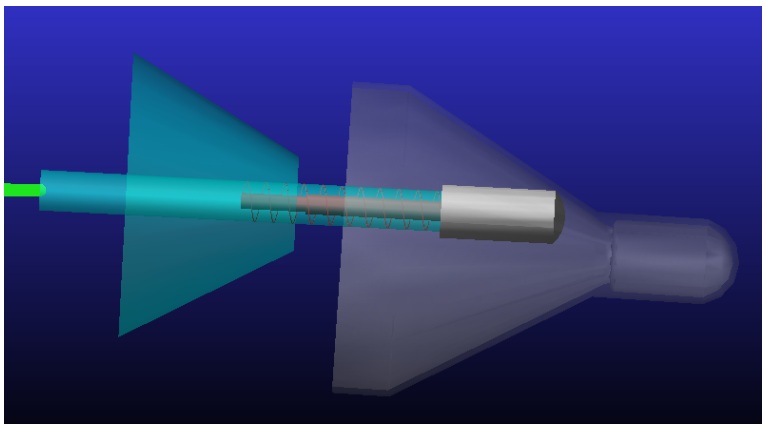

Fig. 5.27 Adams graphical output: intermediate configuration at 3 *s* after the first contact

5.4 3D multibody model

A third and more complex model was created using Altair Hyperworks in a conjoint effort with TAS-I. This model considered a 3D maneuver allowing the bodies to

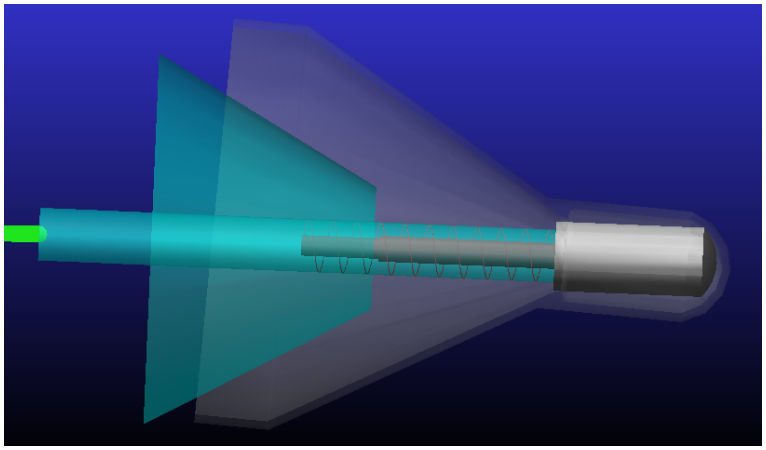

Fig. 5.28 Adams graphical output: soft docking

rotate and translate along and about all the directions. In this case, all the geometries of the mechanism halves were imported from the CAD designs (figure 5.6 and figure 5.7).

Firstly, the bodies in the Hyperworks model were positioned with the misalignments used in the 2D models, i.e., without the off-plane misalignments. Moreover, the same initial velocities were assigned to the bodies (section 5.2.3). In this configuration, a simulation (figure 5.29) was executed mainly to validate the complete Hyperworks model against the 2D custom model. In this regard, figure 5.30 shows the exchanged forces between the target and chaser. It may be seen that both models estimate the contact force with a similar maximum value that is reached at about $1\,s$ after the first impact. Also, in this case, the geometric differences are the reason for the slight discrepancy between the curves.

Figure 5.31 shows the probe rotation generated by both the 2D custom model and the Hyperworks model. The estimated rotations show an almost perfect match up to $1\,s$ when they become slightly different. The custom model reaches a maximum value of $4.4\,deg$ against $4.1\,deg$ estimated with the Hyperworks model. However, this comparison further proves the validity of the models. They were implemented with two different approaches and still estimate similar results.

In contrast with the previous models, the probe in the Hyperworks simulations was equipped with the latches needed to prevent the bodies from escaping. The simulations showed that the latches were able to penetrate the female socket. This

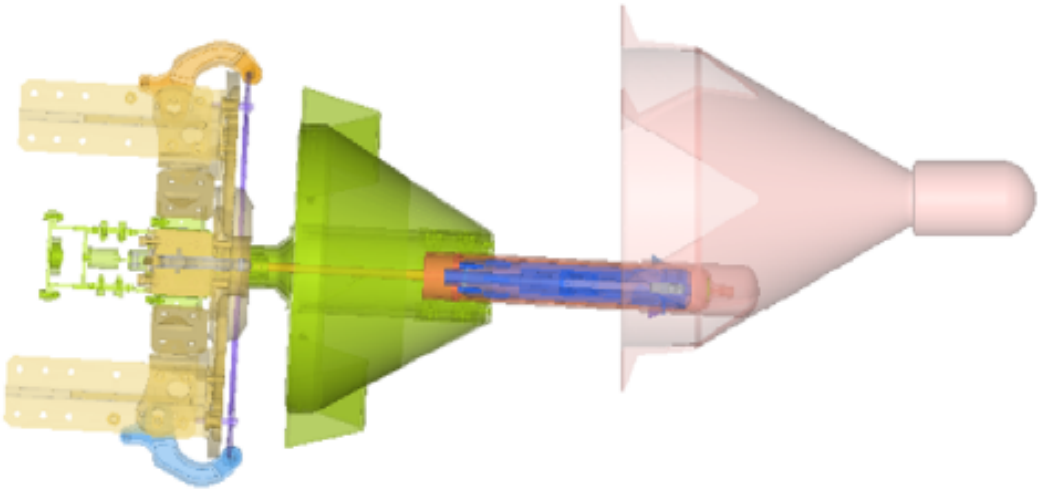

Fig. 5.29 Hyperworks model with initial conditions without off-plane misalignments and velocities

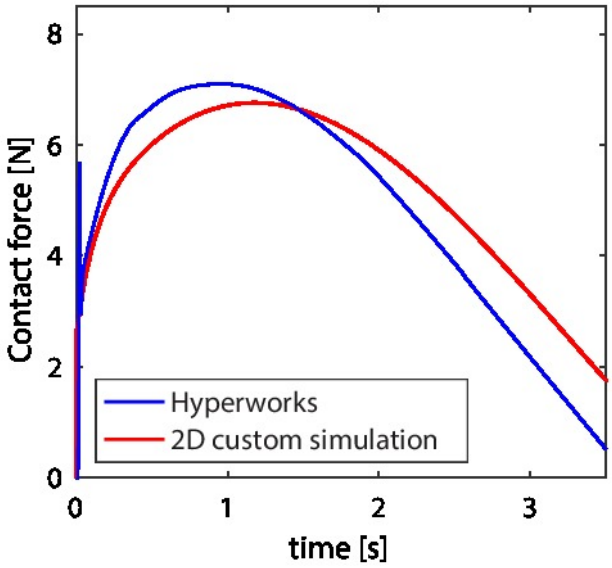

Fig. 5.30 Contact force

proved the suitability of the mechanism in a planar docking maneuver using the selected inertial properties.

The second step was to test the mechanism using all the misalignments (along and about X, Y, and Z) and considering all the relative velocities, both linear and angular. Once the off-plane angles, velocities and position misalignments were imposed, the system was not able to guarantee soft docking between the satellites. In this regard,

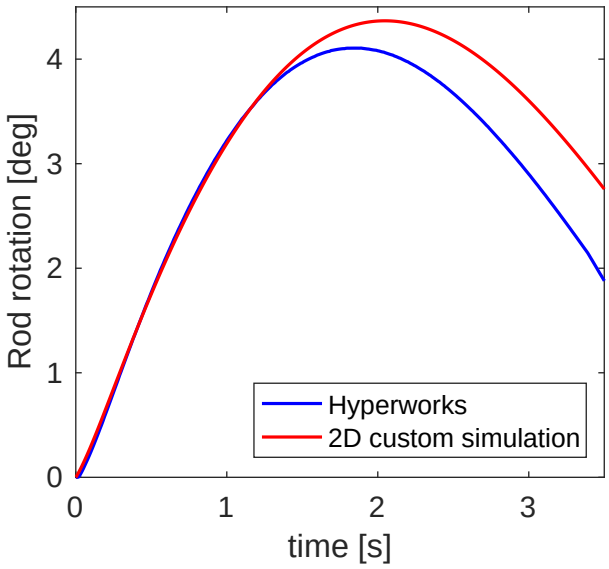

Fig. 5.31 Probe rotation

figure 5.32 shows a sequence of relative positions between the mechanism halves during one of the simulations. Frame I shows the bodies in their initial conditions. In frames II and III, the docking mechanism starts aligning the axis of the probe with the axis of the female cone. By doing so, a large amount of kinetic energy is transferred from the chaser to the target increasing its longitudinal and lateral velocities. In this process, the lateral velocity of the target relative to the chaser creates a geometrical condition in which the probe may not penetrate the socket due to a systematic lateral collision between the halves (frame IV).

Figure 5.33 shows the direction of the force exchanged between the male and female cones when the lateral collision occured. It may be seen that this force has a longitudinal component. This component further increased the longitudinal velocity of the target making it faster than the chaser thus preventing soft docking from occurring.

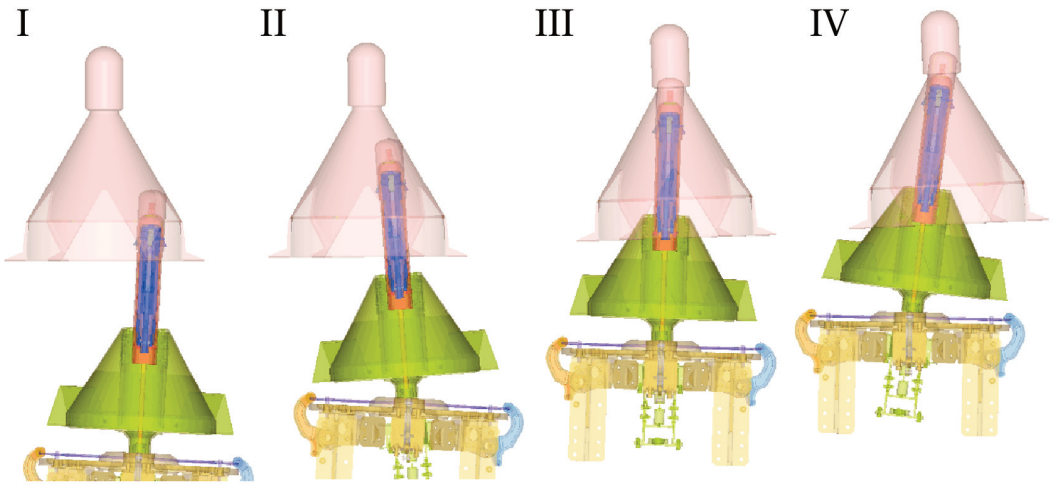

Fig. 5.32 Hyperworks graphical output: failed docking sequence

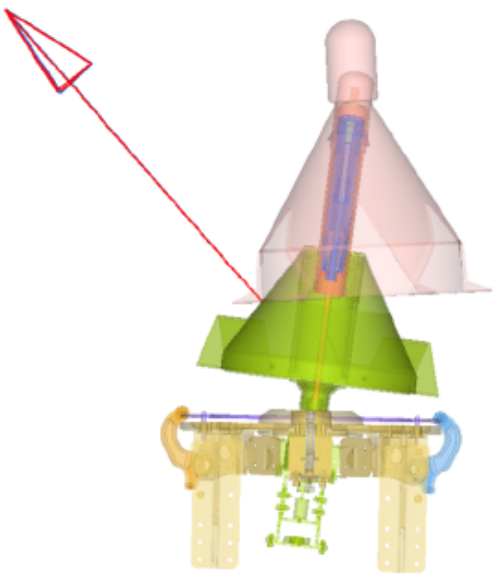

Fig. 5.33 Lateral collision before soft docking. This kind of collision prevented soft docking from occurring

These conditions forced major changes in the design of the mechanism. The objective of these changes was to reduce the exchange of kinetic energy between the bodies with some sort of active subsystem. The next section will describe the solutions proposed and the final decision for the second iteration of the mechanism.

5.5 Necessary modifications

The virtual verification of the first iteration of the docking mechanism showed it is not well suited for the specifications of the STRONG mission. This mechanism is passively controlled by two groups of springs. This passiveness was identified as one of the main problems. Furthermore, the absence of damping devices may be another possible source of the issue.

Regarding the passiveness, the system was tuned for a single combination of inertial properties. It performed as expected only in a 2D maneuver. Considering that the STRONG mission foresees docking operations with different spacecraft, it is conclusive that the mechanism must adapt its characteristics to increase the probability of success. This possibility was already introduced in section 4.5.3.

Concerning damping, it is mandatory in order to safely dissipate the energy associated with the relative motion between the spacecraft. The spring elements are useful to reset the mechanism after each maneuver. However, the energy dissipation associated to the impact between the probe and the cone, and the deformation of the elastic elements of the male part is not sufficient for the STRONG mission specifications.

Different solutions were considered to solve these issues. A first consideration was to exchange the rear springs with a group of electromechanical dampers. The damping coefficient of an electromechanical damper may be changed based on the conditions of the maneuver. A second possible solution considered was the substitution of the rear springs with a group of servoactuators. The servoactuators might change the orientation of the probe based on the exchanged force between the cap and the female cone by using a force sensor. The idea is to maintain the contact force as small as possible during the alignment phase. Then, these actuators would have been used as dampers during the soft docking. A third solution consisted on translating the whole mechanism to accomplish the same force reduction. This solution implied less modification to the existent layout. For this reason, it was further investigated. In this regard, figure 5.34 shows a 2D schematic view of the proposed new solution. The male half of the mechanism translates relative to the chaser during the approaching motion of the chaser toward the target. This translation generates an offset between the longitudinal axes of the probe and the chaser.

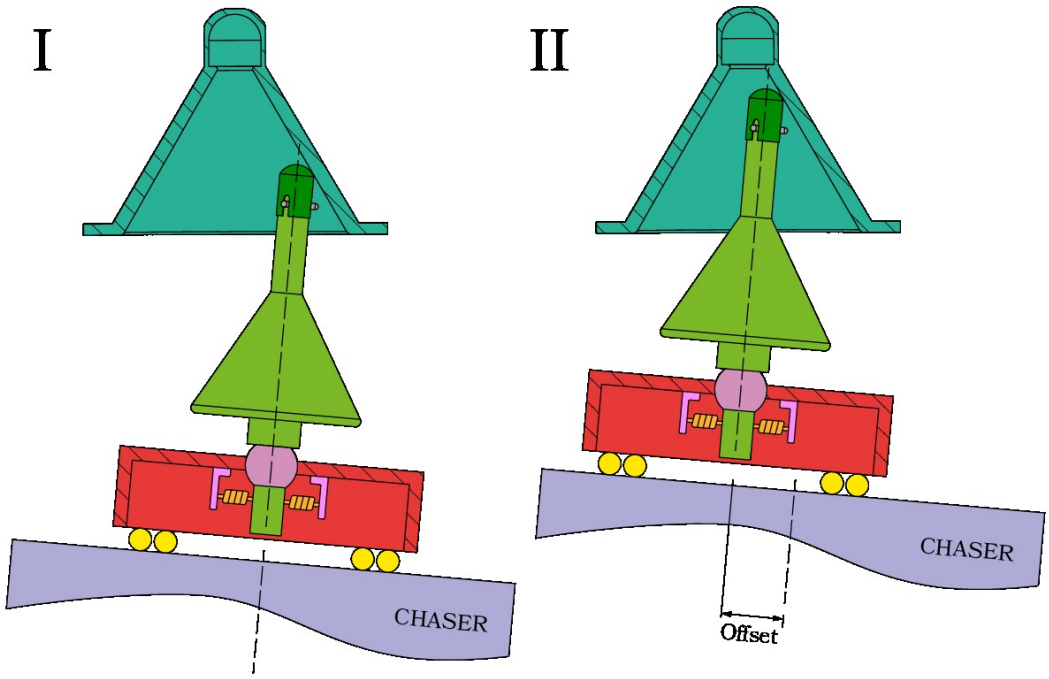

Fig. 5.34 Schematic view of a new mechanism iteration

New simulations were conducted to evaluate this iteration. Inside the 3D Hyperworks model, the male part of the mechanism was modified as follows: a 2 DOFs Cartesian joint was placed between the chaser satellite and the mechanism support plate. The axes of the joint were fully compliant as no friction was added. During the simulations, the contact force applied to the cap of the probe forced the axes of the Cartesian joint to translate w.r.t. the chaser. Since the magnitude of the contact force was almost zero, due to the absence of friction in the Cartesian joint, the chaser was able to maintain its approaching movement toward the target unchanged. The combined effect of the approaching motion of the chaser with the lateral translations of the probe allowed the tip of the probe to penetrate the female socket. This result was verified considering several initial conditions and mass combinations. However, once soft docking was achieved, there was the offset between the probe and its centered deployed position. The centered position is necessary to complete the maneuver with the hard docking. Regardless the hard docking system, the fastening devices must fixed to the structural part of the chaser to increase stiffness and load capacity. For this reason, controlled DOFs of the Cartesian joint were included to create the second design iteration of the docking mechanism. The axes of the Cartesian Joint may be controlled with a force control logic to increase the compliance of

the mechanism during the alignment phase. In addition, the axes may return to their centered positions exploiting a position control algorithm before hard docking phase.

The detailed description and design of the new design iteration will be discussed in the next chapter. The chapter will also show a new set of simulations as well as the selection of the mechanism actuators in accordance with the European standards for space mechanisms.

Chapter 6

Second design iteration: active central mechanism

Chapter 5 showed the proposed docking system needed some major modifications to operate properly. Some preliminary tests demonstrated that a possible suitable new implementation was to increase the degrees of freedom of the mechanism. This was performed by mounting the existent probe on two orthogonal in series prismatic joints. The mechatronic design and testing of the actuators for these prismatic joints will be one of the main topics of this chapter. Moreover, all the remaining subsystems will be described and dimensioned: the undocking system, the actuator for the probe retraction, the longitudinal damping system, the hard docking system, and the control architecture. In this regard, the selected commercial off-the-shelf motors, sensors, and functional elements (e.g. the ball screws) will be outlined.

6.1 Description of the second iteration

In this second iteration, several changes to the layout shown in chapter 5 were implemented. Figures 6.1 and 6.2 show respectively the schematics of the new active part and passive part. Regarding the active part, the architecture of the probe (1) with its retraction system and the system that operates the latches remained unchanged. However, the spherical joint was substituted by a universal joint (2) to constrain the roll rotation of the probe.

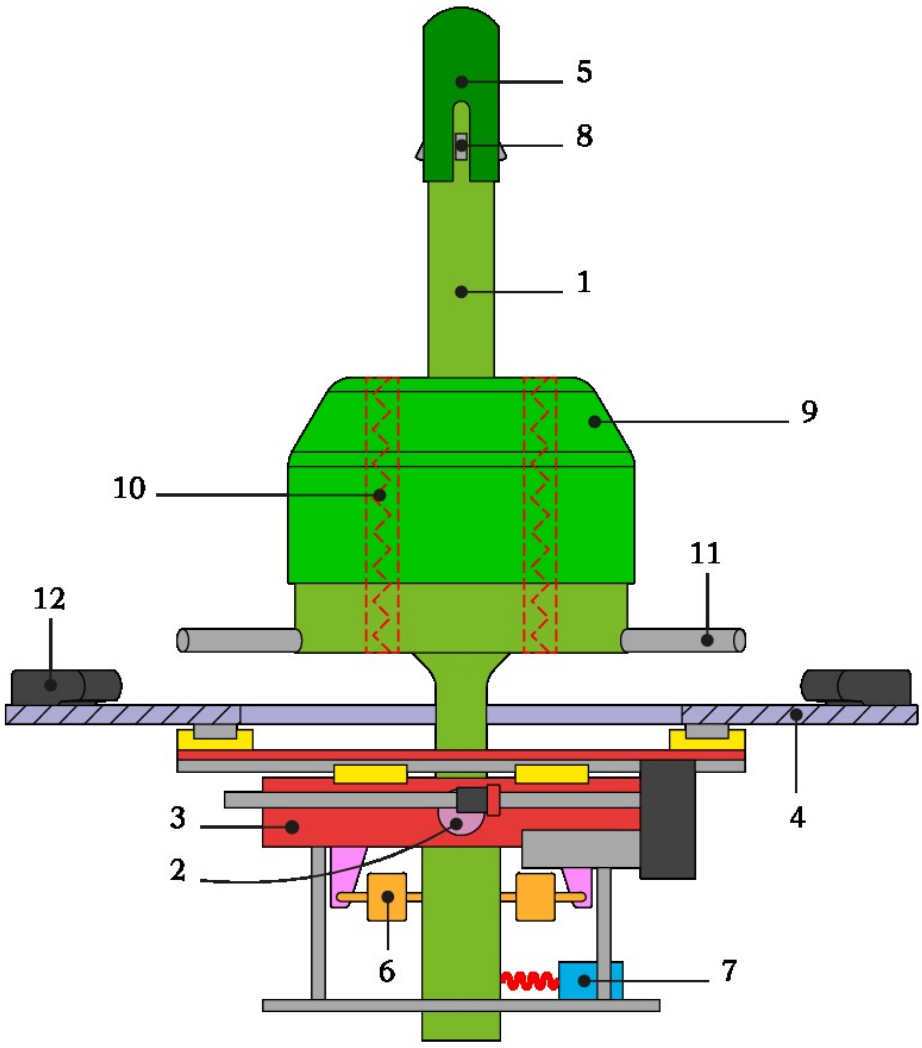

Fig. 6.1 Schematic view of the updated active part

As in the first iteration, in the approach and deployment phase, the probe is deployed up to its maximum length and all the systems needed for docking are prepared for impact. Subsequently, the chaser satellite starts its free drift toward the target.

The base of the universal joint (2) is also a slide (3) and is mounted on recirculating ball profiled linear rails. The slide translates driven by an actuator based on a ball screw. An electric motor equipped with a planetary gearhead rotates the ball screw resulting in a displacement of the ball nut. In turn, the whole slide plus rails may translate orthogonally as these rails are mounted on an analogous slide equipped

with a linear actuator. The rails of this last slide are bolted to the mechanism support plate (4). This plate is the interface between the servicer spacecraft and the active half of the docking mechanism.

With the first contact, the alignment phase begins. During this phase, the conical shape of the passive part (figure 6.2) guides the probe toward its socket. When the contact between the cap of the probe (5) and the female conical wall occurs, the compliance of cap spring avoids large contact forces. As a result, the action of the contact forces rotates the probe around the axes of the universal joint.

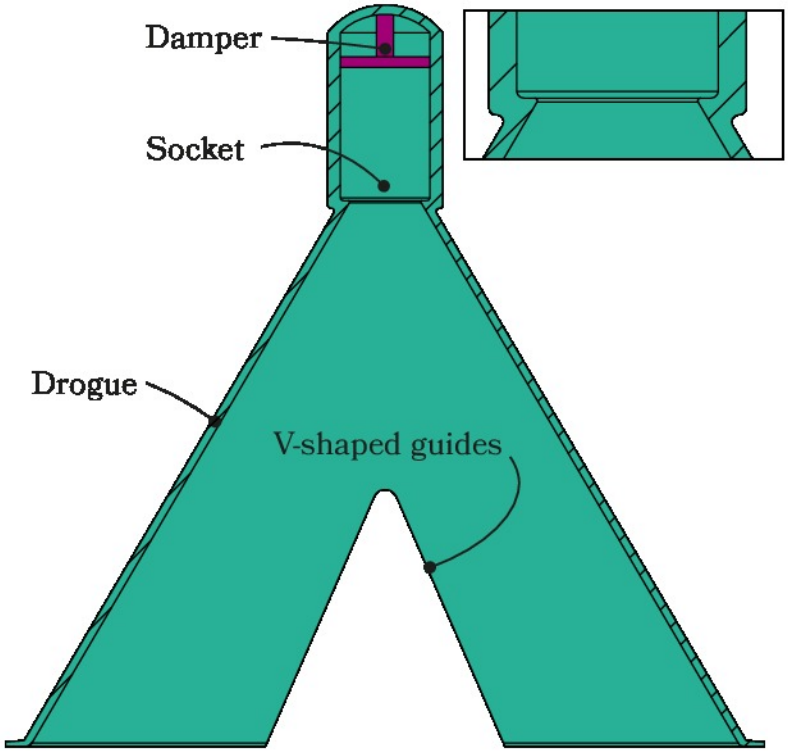

Fig. 6.2 Schematic view of the updated passive part

The traction springs (6) apply elastic forces to the rear end of the probe forcing it to realign with the longitudinal axis of the servicer spacecraft. These elastic forces increase the contact force changing the relative pose between the spacecraft. Mutually orthogonal laser triangulation displacement sensors (7) measure the displacements of the rear end of the probe. These measurements become the reference values to the linear actuators that translate the base of the probe realigning it and therefore reducing the contact force. The approaching motion of the chaser toward the target

combined with the continuous operation of the active actuators approaches the tip of the probe to the socket at the apex of the female cone.

Soft docking takes place when the tip of the probe overpasses the female socket. In this phase, the spring loaded latches (8) prevent the spacecraft from escaping. During soft docking, the energy associated with the relative velocities is dissipated by a damper mounted inside the female socket.

The retraction of the probe approaches the satellites while the contact between the male cone (9) and the female cone eliminates the pitch and yaw misalignments. The male cone may translate along the probe. Both these parts are connected to three compression springs (10) used for the undocking operation. During the retraction, these springs are compressed storing energy.

The roll misalignment is eliminated using three rods (11) fitted to the probe combined with three v-shaped guides built on the female cone. Simultaneously, the linear actuators return to their nominal position allowing the base of the female cone to seat on the support plate. Finally, the conclusive mechanical connection is performed during the hard docking phase. In this phase, three radial hooks (12) lock the position of the female part ending the docking maneuver.

As stated before the undocking system is placed inside the probe. The energy stored in the undocking springs during retraction separates the bodies once the radial hooks are deactivated.

A schematic representation of the docking maneuver up to hard docking is depicted in figure 6.3. This figure highlights several key features of the maneuver. Initially, during Phase 1, the axis of the probe coincides with the longitudinal axis of the chaser spacecraft. In Phase 2, the slides translate the probe creating an offset between the aforementioned axes. This offset approaches the tip of the probe to the female socket. Phase 3 details the latches inside the female socket. After this insertion, the target is prevented from escaping. At this point, the bodies may drift together as represented by the change in orientation between Phase 2 and 3. Finally, Phase 4 depicts the hard docking hooks engaging the target satellite.

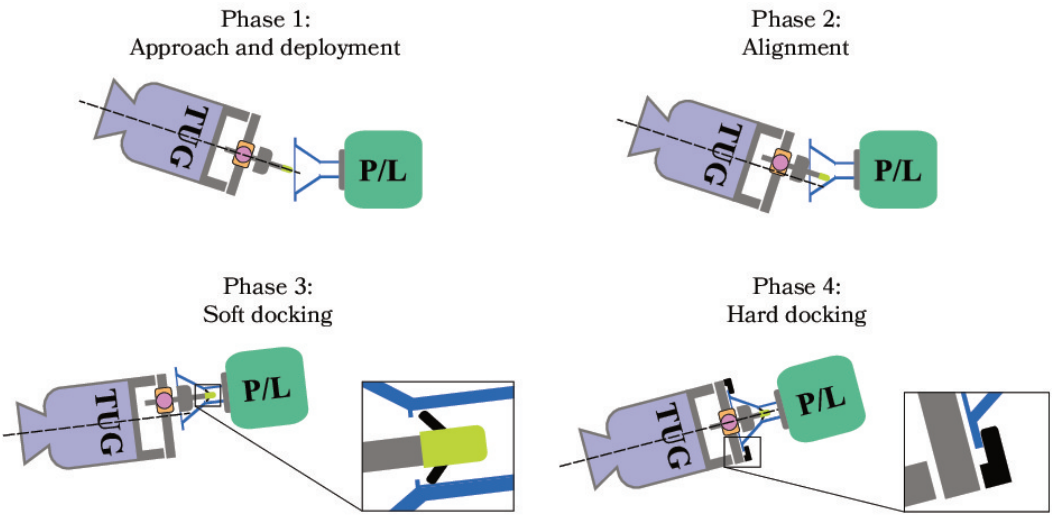

Fig. 6.3 Phases of the docking maneuver

Considering the system layout described above, preliminary engineering models of both the active and passive parts were created (figures 6.4 and 6.5). These CAD models were used as the baseline in the geometric design iterations of the mechanism.

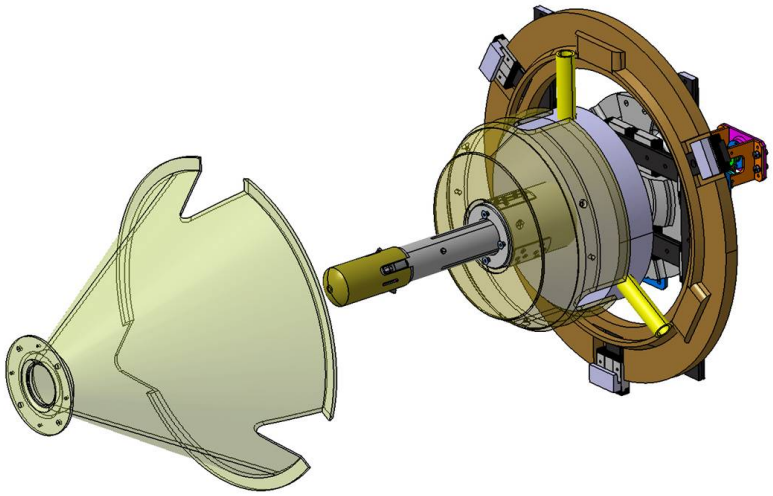

Fig. 6.4 Front view of the preliminary engineering model

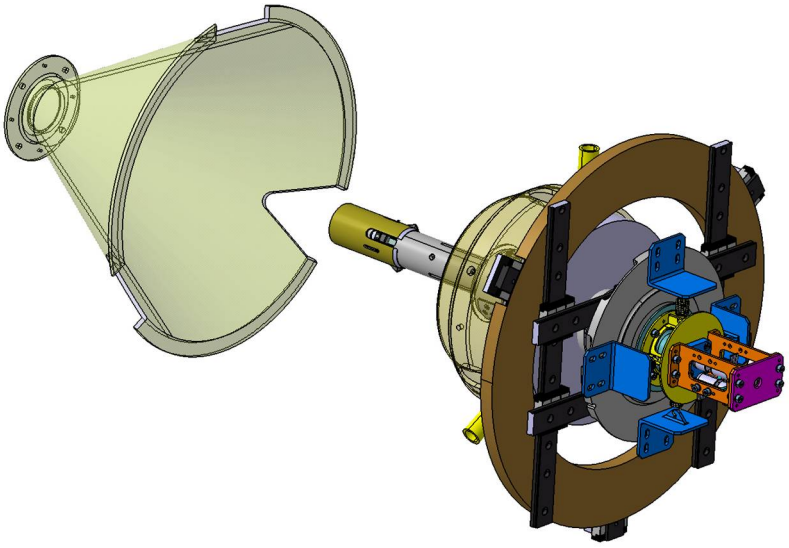

Fig. 6.5 Rear view of the preliminary engineering model

6.2 Undocking system

One of the tasks of the mechanism is to ease the separation between chaser and target, i.e., undocking. This separation is accomplished using the three springs placed inside the male cone (figure 6.6).

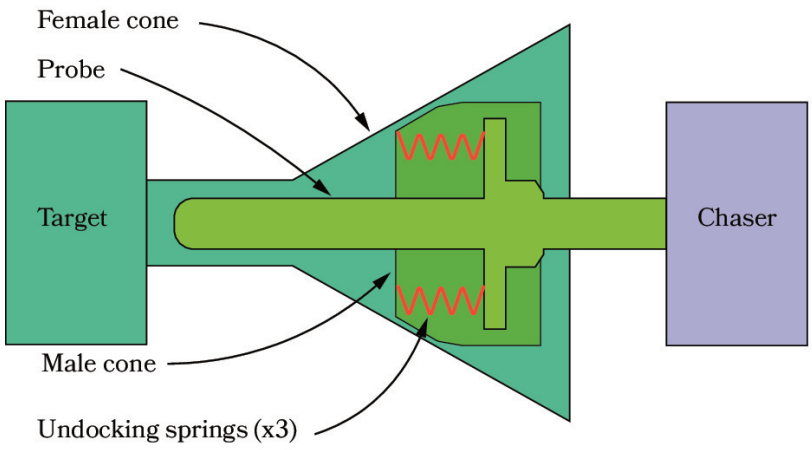

Fig. 6.6 Undocking system

The mission requires a separation velocity v^*_{SEP} at least equal to $30\,mm/s$. Since there are different possible mass combinations, the undocking mechanism will be tuned for the heaviest combinations of satellites. This configuration is characterized by the chaser in Configuration A ($M_{TU} = 1700\,kg$) separating from the orbital tank ($M_{TA} = 6000\,kg$). Given the geometric characteristics of the docking system, the available stroke for the elastic separation device UD_{st} is $33\,mm$. With this data, it is possible to select suitable springs for the undocking based on the needed stiffness. Figure 6.7 depicts a 2 DOFs model of the system in which chaser and target are linked through an elastic element. An equivalent 1 DOF system may be studied using the equivalent mass (figure 6.8). In this equivalent system, the degree of freedom, $p_{rel} = p_{TU} - p_{TA}$, describes the relative movement between chaser and target.

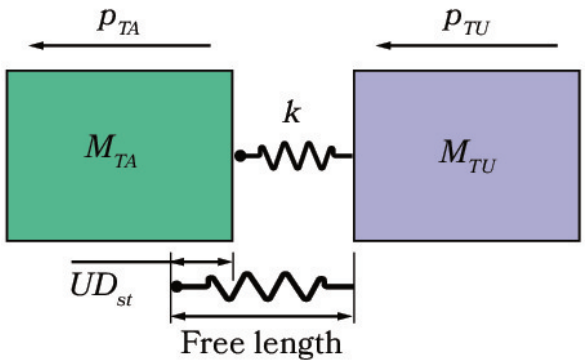

Fig. 6.7 Model with 2 DOFs used for the undocking stiffness selection

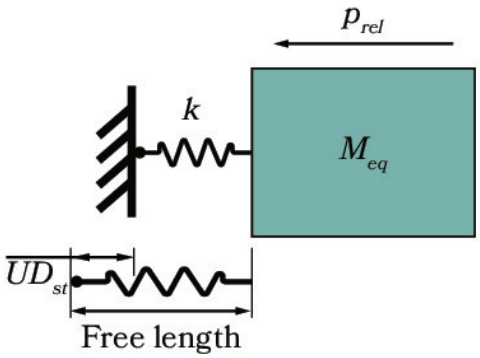

Fig. 6.8 Equivalent 1 DOF model used for the undocking stiffness selection

The equivalent mass is calculated using equation 6.1.

$$M_{eq} = \frac{M_{TU} M_{TA}}{M_{TU} + M_{TA}} = 1324.68\,kg \tag{6.1}$$

By representing the free body diagram of the equivalent mass the associated dynamic equilibrium equation may be written:

$$M_{eq}\ddot{p}_{rel} + k p_{rel} = 0 \tag{6.2}$$

The following equations represent the solution of the ordinary differential equation 6.2 regarding the relative position p_{rel} and velocity $\dot{p}_{rel}$:

$$p_{rel} = -A_0 \cos(\omega_n t + \phi) \tag{6.3}$$

$$\dot{p}_{rel} = \omega_n A_0 \sin(\omega_n t + \phi) \tag{6.4}$$

In equations 6.3 and 6.4, ω_n indicates the natural frequency of the system

$$\omega_n = \sqrt{\frac{k}{M_{eq}}} \tag{6.5}$$

A_0 and ϕ are respectively the amplitude and the phase of the oscillation. Considering that initially the spring is compressed of the quantity UD_{st} and the relative velocity is zero, the values of the constants are the following: $A_0 = UD_{st}$ and $\phi = 0$. When the separation occurs the relative position is zero (spring without deformation), and the relative velocity has to be equal to v^*_{SEP} . In that case, the value of the sine function becomes unitary and the following expression may be written

$$k = 3k^*_{UD} = \left(\frac{v^*_{SEP}}{UD_{st}}\right)^2 M_{eq} = \left(\frac{30\,mm/s}{33\,mm}\right)^2 1324.68\,kg = 1094.77\,\frac{N}{m} \tag{6.6}$$

which implies that each of the undocking springs (k^*_{UD}) should have a stiffness equal to $364.92\,N/m$. A suitable commercial model was found with the specifications shown in table 6.1. With this new stiffness value (k_{UD}) the actual separation velocity v_{SEP} may be calculated by using the energy conservation law:

$$\frac{1}{2}(3k_{UD})UD_{st}^2 = \frac{1}{2}M_{eq}v_{SEP}^2 \tag{6.7}$$

$$v_{SEP} = 31.80mm/s \tag{6.8}$$

Table 6.1 Specifications of the undocking springs

Supplier	D.I.M. Srl
Part number	D12080
Stiffness k_{UD} $[N/mm]$	0.41
Free length $[mm]$	80.5
Maximum compression $[mm]$	53.1

The separation velocity is 6% larger than v_{SEP}^*.

6.3 Dimensioning of the actuator for the probe retraction

The objective of this section is to show the selection process of an actuator suitable for the retraction of the probe. It is important to note that, as a technical requirement, this and all the actuators in the docking system must operate with a nominal voltage equal to $24\,V$.

After soft docking, the approaching of the spacecraft is necessary to perform hard docking. The architecture of the retraction system in this second iteration of the docking mechanism remained unchanged relative to the first design iteration. In this regard, the retraction system was fully described in section 5.1 (figure 5.3).

Due to the geometric characteristics of the system, the total available backward stroke of the probe, RE_{st}, is $63.83\,mm$. The selection presented in this section focuses on the electric motor and its planetary gearhead. A $1mm$ lead ball screw was selected in this iteration. The specifications of this component are shown in table 6.2.

Table 6.2 Specifications of the ball screw

Supplier	Eichenberger Gewinde
Diameter d_{BS}^{RE} $[mm]$	8
Length l_{BS}^{RE} $[mm]$	294
Lead h_{BS}^{RE} $[mm]$	1
Nominal efficiency η_{BS}^{RE} $[\%]$	90

The electric motor has to overcome the inertial forces of the accelerating bodies, the elastic force of the undocking springs, and the force produced by the spring plungers. Regarding the undocking springs, figure 6.9 depicts their position illustrating how these elastic elements load the actuator. Once both the group of latches of the probe and the male cone are in contact with the target, the compression of the three undocking springs progressively loads the motor through the transmission chain previously described.

For the functional dimensioning of an actuator, The European Cooperation for Space Standardization (ECSS), Standard ECSS-E-ST-33-01C clause 4.7.5.3, establishes that some uncertainty factors must be considered when calculating the minimum required actuating torque or force [45]. Some of these uncertainty factors are shown in table 6.3.

Table 6.3 Some ECSS uncertainty factors

Component of resistance	Nomenclature in this document	Theoretical load	Measured load
Inertia	UF_I	1.1	1.1
Spring	UF_S	1.2	1.2
Friction	UF_F	1.5	3

The ECSS standard also establishes that the minimum force, or torque, needed for an operation should be doubled for safety reasons. Moreover, all the components of resistance must be considered in the in-orbit worst-case condition:

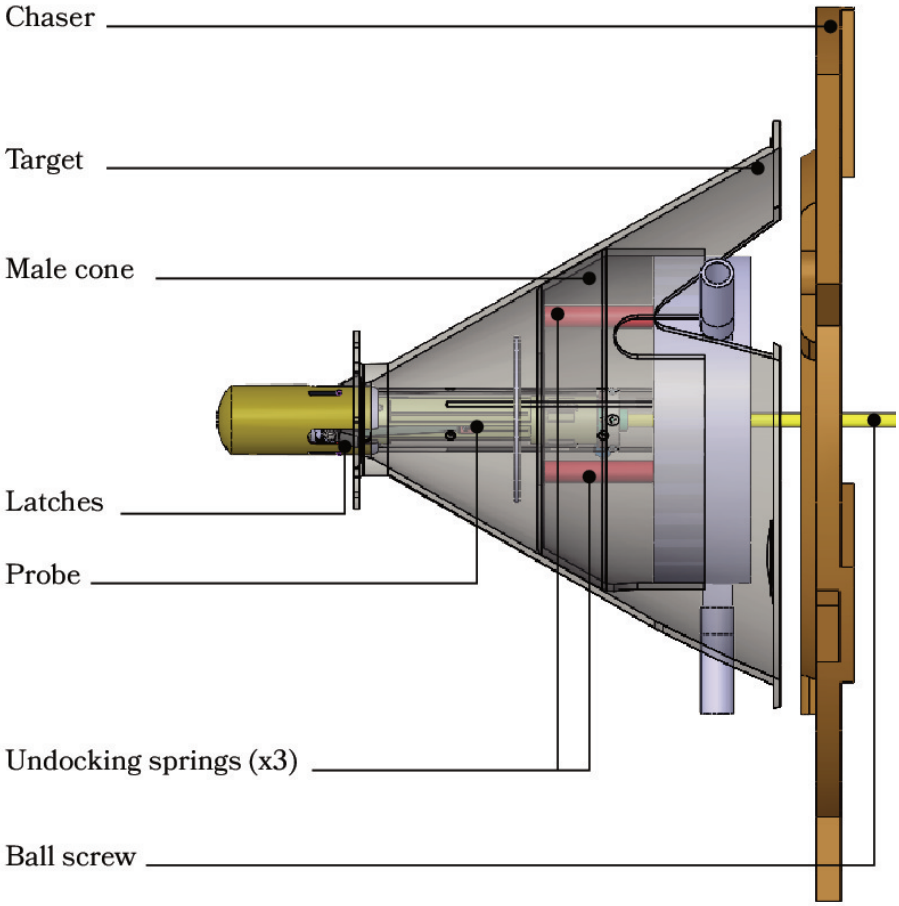

Fig. 6.9 Effect of the undocking system on the probe actuator

$$F_{min}^{ECSS} = 2 \cdot (\Sigma\,(\text{Uncertainty factor} \times \text{Resistance load})) \tag{6.9}$$

Regarding the docking springs, the worst-case scenario corresponds to the final stage of the retraction in which the compression of the springs is equal to UD_{st}. Equation 6.10 describes the load produced by the three undocking springs.

$$\begin{aligned} F_{UD} &= 2 \cdot (3 \cdot (UF_S \cdot k_{UD} \cdot UD_{st})) \\ &= 2 \cdot (3 \cdot (1.2 \cdot 410\,N/m \cdot 33\,mm)) \\ &= 97.42\,N \end{aligned} \tag{6.10}$$

The external probe is equipped with three conical seats with 45 *deg* half cone angles. These seats combined with the three spring plungers lock the position of the external probe during soft docking. The spring plungers create elastic forces plus friction on the surface of the external probe holding it in position. The characteristics of these spring plungers may be seen in table 6.4.

Table 6.4 Characteristics of the spring plungers

Supplier	Romeo Cobalchini
Threading	M10X1.5
Length $[mm]$	19
Stroke $[mm]$	2
Ball diameter $[mm]$	6
Initial load $[N]$	24
Maximum load $[N]$	45
Ball material	AISI 304

Figure 6.10 depicts one of the above-mentioned conical seats as well as the ball plunger. It shows that the distance between the enclosure of the ball plunger and the surface of the probe is equal to $0.3\,mm$. Considering that the maximum ball displacement is $2\,mm$, the maximum compression of the ball plunger, Δ_{BP}, will be $1.7\,mm$. The elastic force of the spring plunger is a function of the ball displacement c. This force was calculated using the maximum load, initial load, and the stroke of the ball (table 6.4) as follows:

$$F_{BP}(c) = \frac{45\,N - 24\,N}{2mm}c + 24\,N \tag{6.11}$$

Using equation 6.11, the maximum elastic force applied by the plunger F_{BP}^{max} corresponds to F_{BP} (Δ_{BP}) which is equal to $41.85\,N$.

To calculate the load on the motor applied by the single spring plunger, F_{SP}^{*}, the free body diagram of the ball was represented (figure 6.11). Using this diagram the following equations were found:

$$\frac{\sqrt{2}}{2}N = F_{BP} + \mu\frac{\sqrt{2}}{2}N \tag{6.12}$$

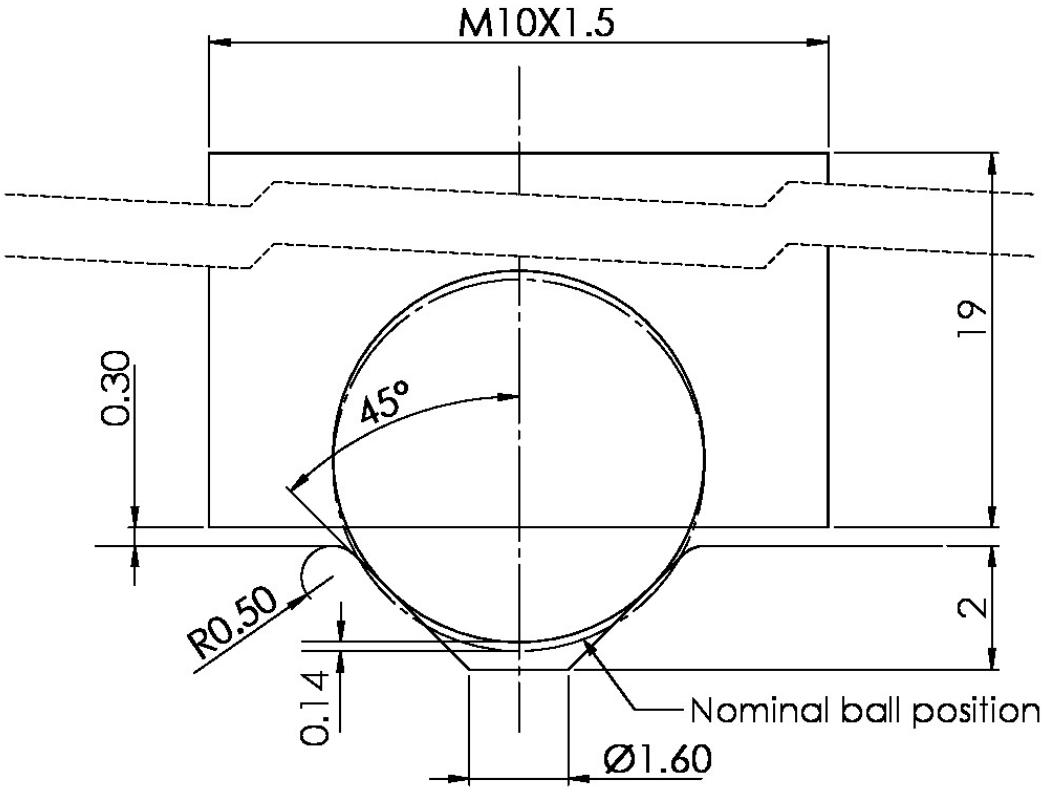

Fig. 6.10 Ball plunger and conical seat

$$F_{SP}^{*} = \frac{\sqrt{2}}{2}N + \mu\frac{\sqrt{2}}{2}N = \frac{\sqrt{2}}{2}(1+\mu) \tag{6.13}$$

In equation 6.12 and 6.13, N and μ are respectively the force normal to the conical seat and the friction coefficient. Combining these equations, the force of the single spring plunger becomes:

$$F_{SP}^{*} = \left(\frac{1}{1+\mu}F_{BP}\right) + \left(\frac{\mu}{1-\mu}F_{BP}\right) \tag{6.14}$$

The first term of equation 6.14 will be considered the elastic force term while the second the friction contribution. This distinction was made to make possible a non-redundant application of the ECSS uncertainty factors.

The worst-case scenario is characterized by the maximum load of the ball plungers. Since the material of the ball is stainless steel, and the material of the external probe is aluminum, the static friction factor μ is approximately equal to

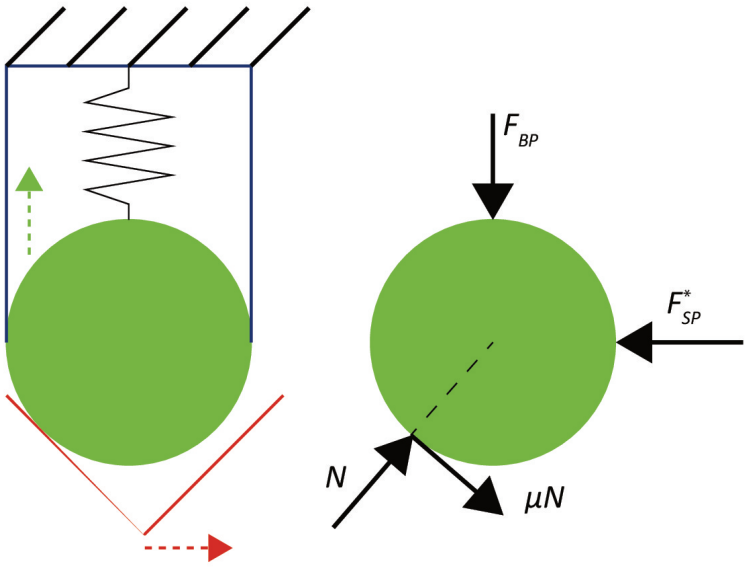

Fig. 6.11 Diagram used to calculate the spring plunger forces

0.61 [46]. With this data, and considering the uncertainty factors, the resistive load created by the three ball plungers F_{SP} becomes:

$$\begin{aligned} F_{SP} &= 2\left(3\left(UF_S\frac{F_{BP}^{max}}{1-\mu}+UF_F\frac{\mu F_{BP}^{max}}{1-\mu}\right)\right) \\ &= 2\left(3\left(1.2\frac{41.85\,N}{1-0.6}+3\frac{0.6\cdot 41.85\,N}{1-0.6}\right)\right) \\ &= 1950.85\,N \end{aligned} \tag{6.15}$$

Regarding the inertial forces, two minutes for completing the probe retraction, and a trapezoidal velocity profile were considered to calculate the acceleration of the moving parts. A short accelerating time was selected consisting on a $0.5\,s$ velocity ramp (t_{ramp}). With this value and the total time, $t_{tot} = 120\,s$, the maximum velocity and acceleration were calculated. Figure 6.12 shows the acceleration, velocity profile and position of the probe.

$$V_{max} = \frac{RE_{st}}{t_{tot} - t_{ramp}} = 0.53\,mm/s \tag{6.16}$$

$$A_{max} = \frac{V_{max}}{0.5s} = 1.07\,mm/s^2 \tag{6.17}$$

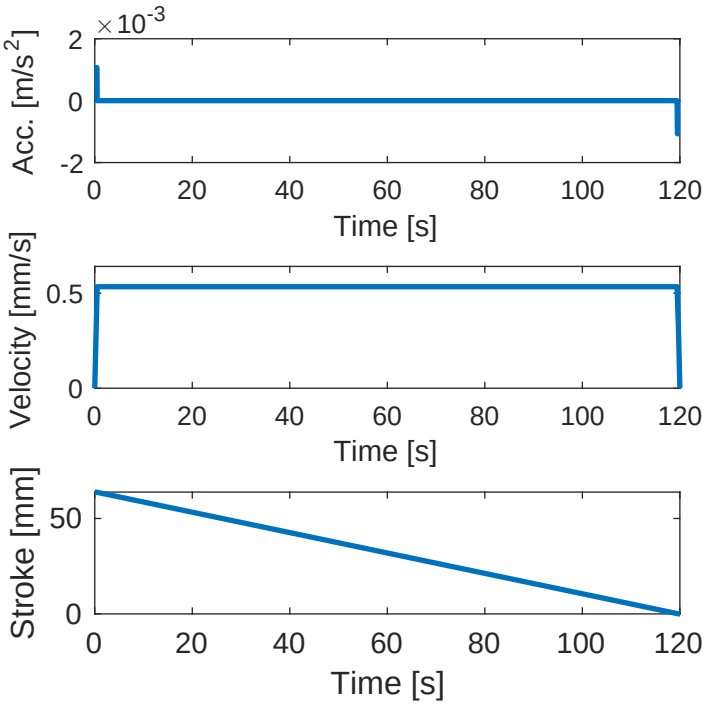

Fig. 6.12 Non smoothed velocity profile, acceleration, and position

The accelerating elements considered are the spacecraft masses (an equivalent translating mass), the inertia of the motor, and the inertia of the ball screw. Since the motor has yet to be selected, its inertial contribution will be added during the final verification. Regarding the ball screw, using the data in table 6.2, and assuming a steel density, ρ_{steel}, equal to $7800\,kg/m^3$, its inertia J_{BS}^{RE} was calculated using the following formula:

$$J_{BS}^{RE} = \frac{1}{2}\left(\rho_{steel}\frac{1}{4}\pi {d_{BS}^{RE}}^2 L_{BS}^{RE}\right)\left(\frac{d_{BS}^{RE}}{2}\right)^2 = 9.22\times10^{-7}\,kgm^2 \tag{6.18}$$

The inertia of the ball screw may be transformed into an equivalent mass if multiplied by the transmission ratio:

$$M_{BS}^{RE} = J_{BS}^{RE}\left(\frac{2\pi}{h_{BS}^{RE}}\right)^2 = 36.41\,kg \tag{6.19}$$

Considering the same worst-case scenario as in section 6.2 in which the mass of the chaser is $1700\,kg$ and the one of the target $6000\,kg$, the inertial resistance is given by equation 6.20.

$$F_I = 2 \cdot \left(UF_I \cdot \left(M_{eq} + M_{BS}^{RE}\right)\right) = 3.20\,N \tag{6.20}$$

Now it is possible to estimate the needed power P considering an overall efficiency equal to 50%:

$$P = \frac{1}{0.5}\left(F_{UD} + F_{SP} + F_I\right) = 2.17\,W \tag{6.21}$$

Given this power, an $8\,W$ EC motor was selected from the Maxon Motor catalog. This $8\,W$ motor was the model with the smallest rated power higher that P with a nominal voltage equal to $24\,V$. This motor is a $16\,mm$ bore actuator with a maximum continuous torque equal to $8.19\,mNm$. The main characteristics of the motor are shown in table 6.5.

Table 6.5 Specifications of the EC-max 16

Supplier	Maxon Motor
Nominal voltage V_0 $[V]$	24
Maximum continuous torque $[mNm]$	8.19
Maximum continuous current i_{max} $[A]$	0.461
Terminal resistance R $[\Omega]$	20.5
Terminal inductance L $[mH]$	0.566
Torque constant k_t $[mNm/A]$	18.7
Speed constant k_ω $[rpm/V]$	510
Rotor inertia $J_M^{RE}[gcm^2]$	0.85

A compatible 157:1 planetary gearhead was also selected. Its specifications are shown in table 6.6.

Table 6.6 GP 22 HP planetary gearhead specifications

Supplier	Maxon Motor
Transmission rate τ_{PGH}^{RE} $[-]$	157:1
Maximum continuous torque $[Nm]$	0.4
Maximum input speed $[rpm]$	12000
Mass inertia J_{PGH}^{RE} $[gcm^2]$	0.04
Nominal efficiency η_{PGH}^{RE} $[\%]$	73

6.3.1 Motor verification

By using all the gathered data, it is possible to perform the final verification of the motor. The total transmission ratio i^{RE} between the motor and the translating load is

$$i^{RE} = \frac{h_{BS}^{RE}}{2\pi}\frac{1}{\tau_{PGH}^{RE}} = 1.01 \times 10^{-6}\, m \tag{6.22}$$

Inertial effects

The acceleration of the spacecraft produces a torque acting on the motor calculated by the following formula

$$\frac{i^{RE}}{\eta_{BS}^{RE}\eta_{PGH}^{RE}} M_{eq} A_{max} = 2.18 \times 10^{-3}\, mNm \tag{6.23}$$

The inertial load produced by the accelerating ball screw is

$$\frac{1}{\tau_{PGH}^{RE}}\frac{1}{\eta_{PGH}^{RE}} J_{BS}^{RE}\left(A_{max}\frac{2\pi}{h_{BS}^{RE}}\right) = 5.40 \times 10^{-5}\, mNm \tag{6.24}$$

The planetary gearhead and motor inertia contributions are the followings:

$$J_{PGH}^{RE}\left(A_{max}\frac{1}{i^{RE}}\right) = 4.21 \times 10^{-3}\, mNm \tag{6.25}$$

$$J_M^{RE}\left(A_{max}\frac{1}{i^{RE}}\right) = 8.96\times10^{-2}\,mNm \tag{6.26}$$

Springs

There are two elastics elements: the spring plungers and the undocking springs. The loads created by those elements are calculated using the following formulas:

$$\frac{i^{RE}}{\eta_{BS}^{RE}\eta_{PGH}^{RE}}3\frac{F_{BP}^{max}}{1-\mu} = 4.97\times10^{-1}\,mNm \tag{6.27}$$

$$\frac{i^{RE}}{\eta_{BS}^{RE}\eta_{PGH}^{RE}}3F_{UD} = 6.26\times10^{-2}\,mNm \tag{6.28}$$

Friction

During the rod retraction, the spring plungers create a friction load that may be estimated using the formula:

$$\frac{i^{RE}}{\eta_{BS}^{RE}\eta_{PGH}^{RE}}3\frac{\mu F_{BP}^{max}}{1-\mu} = 3.03\times10^{-1}\,mNm \tag{6.29}$$

Conclusively, table 6.7 summarizes the verification process.

Considering the maximum value of the torque (2xSum) combined with the maximum motor speed

$$\omega_{max} = V_{max}\frac{1}{i^{RE}} = 5031.62\,rpm \tag{6.30}$$

a conservative worst-case operating point was individuated. Figure 6.13 shows that this worst-case point is inside the continuous operating area of the selected motor.

6.3.2 Driver and encoder

The Maxon Motor catalog suggests three possible encoders with three different CPT that may be combined with the selected motor: 128, 256 or 512 CPT. All the

Table 6.7 Motor verification in accordance with the ECSS standards

Type of resistance	Component of resistance	Value at origin	Value at motor shaft $[mNm]$	ECSS uncertainty factor	Final resistance $[mNm]$
Inertia	Spacecraft masses	$1.42N$	0.00	1.1	0.00
	Ball screw	$0.00mNm$	0.00	1.1	0.00
	Gearhead	$0.00mNm$	0.00	1.1	0.00
	Motor	$0.09mNm$	0.09	1.1	0.10
Springs	Spring plungers	$321.92N$	0.50	1.2	0.60
	Undocking Springs	$40.59N$	0.06	1.2	0.08
Friction	Spring plungers	$196.37N$	0.30	3	0.91
Sum					1.69
2xSum					3.37

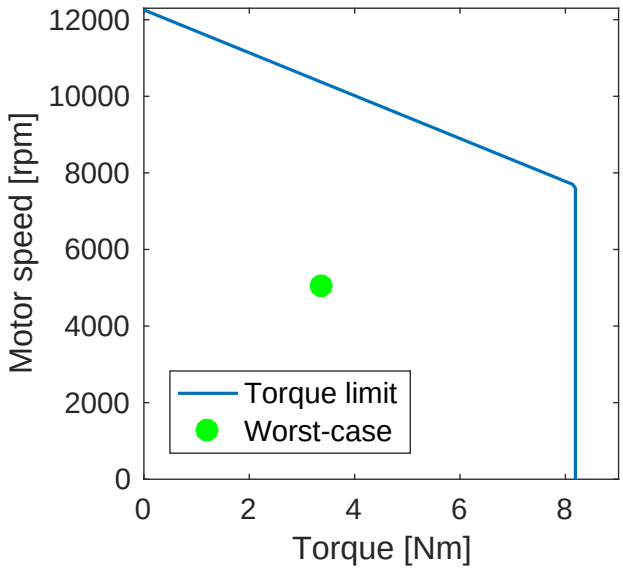

Fig. 6.13 Motor continuous operating area and worst-case operating point

encoders are available in two versions: 2 or 3 channels. Table 6.8 shows the final resolution regarding the probe position for each of the encoders.

Table 6.8 Position resolution

Counts per turn	Final resolution $[\mu m]$
128	0.05
256	0.02
512	0.01

From table 6.8 it becomes clear that the resolution associated with the 128 CTP encoder is more than enough for this application. Regarding the controller, the EPOS2 24/2 was selected. Table 6.9 shows the technical specifications of this component.

Table 6.9 EPOS2 24/2 specifications

Supplier	Maxon Motor
Motor	EC up to 48 W
Sensors	Digital Hall sensor, digital incremental encoder (2-channel, differential), and digital incremental encoder (3-channel, differential)
Operating modes	Current controller, Speed controller, Position controller
Interfaces	RS232, USB 2.0, CAN
Dimensions $[mm]$	$55 \times 40 \times 19.6$
Mounting	Flange for M2.5 screws

6.4 Dimensioning of the actuators for the Cartesian stage

The scope of this section is to show the selection process of the actuators that make the alignment between the docking interfaces possible. The alignment of the docking interfaces guarantees the functioning of the mating system. The tip of the probe has to enter the female socket regardless the initial impact point and relative velocities. To do so, the male part of the mechanism is mounted on an XY stage. This stage adds up to the male part two additional controlled degrees of freedom. The position set to the X and Y axes of the stage is created using two laser sensors. These sensors measure the displacements of the rear part of the probe which is then used to calculate the needed displacements of the slides with the scope of eliminating the probe rotations.

Every axis of the stage works as follows: once the position set of the axis is computed, an electric motor generates an actuating torque. This torque rotates a ball screw through a planetary gearhead and a couple of gears with a 1:1 transmission ratio. This last element was inserted so as to position the axes of the motor and the ball screw side to side reducing the overall length. The rotational movement of the screw becomes a translation of the ball nut. The ball nut is rigidly connected to the slide which is forced to translate along a couple of linear guides with recirculating ball bearings. Both the axes of the stage are equipped with the elements above. On the one hand, the guides of the Y Slide (figure 6.14) are bolted to the spacecraft. On the other hand, the guides of the X Slide are bolted to the Y Slide. Finally, the whole probe assembly is mounted to the X slide through a universal joint.

In the following paragraphs, the selection process of a suitable motor model for both the slides, as well as a planetary gearhead, and a ball screw for all the operational modes of the XY stage will be shown.

The actuators of the Cartesian stage have two operational modes. On the one hand, the actuators should travel at high speed to keep the axis of the probe aligned with the axis of the chaser, reducing the exchanged contact force between the docking interfaces. On the other hand, once the soft docking is accomplished they should reposition the target plus chaser system so as to make the hard docking possible.

1-Planetary gearhead
2-Electric motor
3-Ball screw
4-Ball nut
5-Y Slide
6-X Slide
7-Linear guides
8- Laser sensors

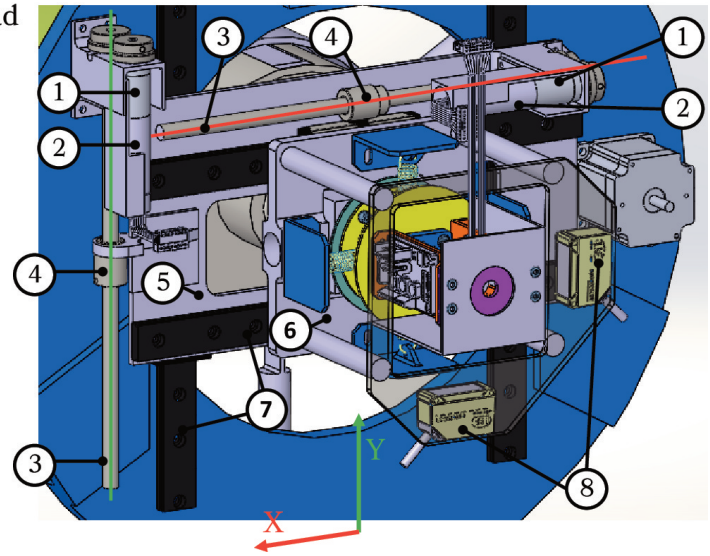

Fig. 6.14 XY stage

6.4.1 Alignment phase

As introduced above the actuators have to move the stage to avoid exchanging forces between the tip of the probe and the female cone. To do so, the velocity of the tip should be directed along the wall of the female cone. In figure 6.15 the desired velocity, v_D, is depicted. A 2D configuration without angular misalignment was selected to simplify the estimation of this velocity. In this regard, the relative axial velocity between chaser and target, $v_{rel,x}$, in the worst-case scenario is equal to $40\,mm/s$ (table 3.1). Concerning the lateral one, $v_{rel,y}$ is equal to $10\,mm/s$. The relative angular velocity of the chaser $\omega_{rel,z}$ times the distance from the chaser COG to the tip of the probe, $d_{TU}+l_P^0$, may further increase the total lateral relative velocity. Considering the Configuration A of the chaser, the distance $d_{TU}+l_P^0$ is equal to $2477\,mm$.

To reach the desired velocity, the tip of the probe have to match a desired lateral velocity v_{DL} estimated using the axial relative velocity and the half cone angle of the female cone:

$$v_{DL} = v_{rel,x}\tan(\theta_{HC}) = 40\,mm/s\,\tan(30\,deg) = 23.09\,mm/s \tag{6.31}$$

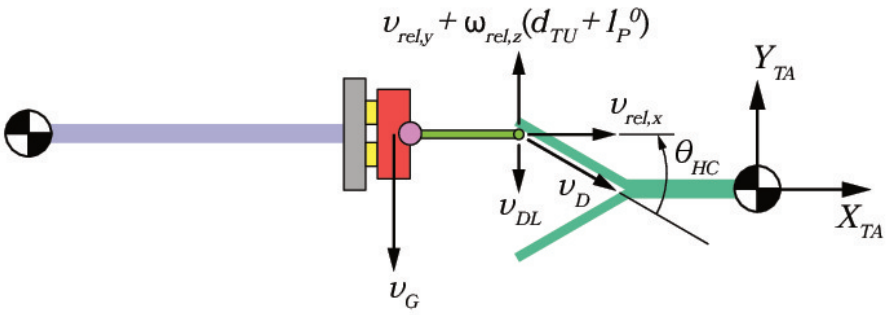

Fig. 6.15 Velocity diagram used to estimate the velocity of the slides

With this velocity, it is possible to calculate the needed velocity of the linear slide relative to the chaser:

$$\begin{aligned} v_G &= v_{DL} + v_{rel,y} + \omega_{rel,z}\left(d_{TU} + l_P^0\right) \\ &= 23.09\,mm/s + 10\,mm/s + 0.0017\,rad/s \cdot 2.48\,m = 37.30\,mm/s \end{aligned} \tag{6.32}$$

The axis of the XY stage must be able to travel at a velocity at least equal to v_G.

The selection process starts with the inertial loads. The mass to be translated by the most loaded guide was assumed to be $20\,kg$ based on a preliminary CAD model. Moreover, an acceleration equal to $0.5\,m/s^2$ was considered as the maximum reference value to calculate the inertial loads. Table 6.10 summarizes the requirements of the controlled guides discussed so far.

Table 6.10 Requirements of the controlled slides

Preliminary mass of the active part of the mechanism M_{ADM} $[kg]$	20
Theoretical maximum velocity v_G $[mm/s]$	37.30
Maximum acceleration A_G $\left[m/s^2\right]$	0.5

Besides the slide mass, the inertia of the ball screw must be considered. Two possible preloaded ball screw options were investigated:

- **Option 1** with a $2\,mm$ lead;

- **Option 2** with $4\,mm$.

These ball screws are manufactured by SKF and their characteristics are shown in table 6.11.

Table 6.11 Specifications of the ball screw options

	Option 1	Option 2
Diameter d_{BS}^{XY} $[mm]$	10	10
Estimated length l_{BS}^{XY} $[mm]$	300	300
Lead h_{BS}^{XY} $[mm]$	2	4
Preload torque T_{BS}^{PRE} $[Nm]$	0.01	0.02

Since both ball screws share the same diameter and length, their moments of inertia are approximately the same, and they may be calculated with the following formula:

$$J_{BS}^{XY} = \frac{1}{2}\left(\rho_{steel}\frac{1}{4}\pi {d_{BS}^{XY}}^2 L_{BS}^{XY}\right)\left(\frac{d_{BS}^{XY}}{2}\right)^2 = 2.30\times10^{-6}\,kgm^2 \tag{6.33}$$

This inertia may be translated into equivalent masses as follows:

$$M_{BS} = J_{BS}^{XY}\left(\frac{2\pi}{h_{BS}^{XY}}\right)^2 \tag{6.34}$$

A first estimation of the needed power was done considering the inertial loads plus the preload torques of the screws combined with the maximum velocity acting simultaneously. To calculate the actuator force, the ECSS standard for mechanisms assigns to an inertial resistance an uncertainty factor equal to 1.1 while 1.5 for a tested friction force (or torque):

$$F_{BS1}^{MAX} = 2\cdot\left(UF_F T_{BS1}^{PRE}\frac{2\pi}{h_{BS1}^{XY}} + UF_I\,(M_{ADM}+M_{BS1})A_G\right) = 141.19\,N \tag{6.35}$$

$$F_{BS2}^{MAX} = 2 \cdot \left(UF_F T_{BS2}^{PRE} \frac{2\pi}{h_{BS2}^{XY}} + UF_I \left(M_{ADM} + M_{BS2} \right) A_G \right) = 122.48\,N \tag{6.36}$$

An overall 50% efficiency η was assumed to calculate the actuator power for each ball screw option:

$$P_{BS1} = \frac{F_{BS1}^{MAX} v_G}{\eta} = 10.53\,W \tag{6.37}$$

$$P_{BS2} = \frac{F_{BS2}^{MAX} v_G}{\eta} = 9.14\,W \tag{6.38}$$

A suitable $25\,W$ motor was selected from the Maxon Motor catalog. It is a $22\,mm$ bore, $24\,V$ EC motor. Table 6.12 shows some of its characteristics.

Table 6.12 Specifications of the EC-max 22, brushless, $25W$, with Hall sensors

Supplier	Maxon Motor
Nominal voltage V_0 $[V]$	24
Maximum continuous torque $[mNm]$	22.7
Maximum continuous current i_{max} $[A]$	1.4
Terminal resistance R $[\Omega]$	3.44
Terminal inductance L $[mH]$	0.182
Torque constant k_t $[mNm/A]$	17.4
Speed constant k_ω $[rpm/V]$	549
Rotor inertia J_M^{XY} $[gcm^2]$	4.45
Mass $[g]$	110

Regarding the planetary gearhead, several transmission ratios were considered: 16:1, 19:1 and 24:1. From the Maxon catalog, all the Planetary gearheads with these ratios and an outer diameter compatible with the selected motor ($22\,mm$) have a maximum input speed of $12000\,rpm$. Considering v_G, the leads of the screws and the transmission ratios, the input velocity of the reducer may be calculated. Table 6.13

shows the speeds of the motor for both the ball screw options and all the transmission ratios.

Table 6.13 Maximum input speeds

	16:1	19:1	24:1
Option 1	17904 rpm	21261 rpm	26856 rpm
Option 2	8952 rpm	10631 rpm	13428 rpm

For all the considered ratios, the Option 1 generates speeds higher than the gearhead maximum limit. For this reason and the higher needed power, this screw was discarded. Moreover, the Option 2 combined with the 20:1 gearhead also exceeds the speed limit. Finally, the 19:1 option was selected for producing the smallest motor torque within the planetary gearhead speed limits. Table 6.14 shows the characteristics of this planetary gearhead.

Table 6.14 GP 22 HP planetary gearhead specifications

Supplier	Maxon Motor
Transmission rate τ_{PGH}^{XY} $[-]$	19:1
Maximum continuous torque $[Nm]$	2
Maximum input speed $[rpm]$	12000
Mass inertia J_{PGH}^{XY} $[gcm^2]$	0.4
Nominal efficiency η_{PGH}^{XY} $[\%]$	70

Motor verification

With all the gathered data it is possible to perform the final verification of the motor. The total transmission ratio i^{XY} from the motor to the translating load is

$$i^{XY} = \frac{h_{BS2}^{XY}}{2\pi}\frac{1}{\tau_{PGH}^{XY}} = \frac{4mm}{2\pi}\frac{1}{19} = 3.35 \times 10^{-5}\, m \tag{6.39}$$

Inertial effects The acceleration of the translating parts of the mechanism produces a torque acting on the motor that may be estimated by the following formula:

$$\frac{i^{XY}}{\eta_{PGH}^{XY}} M_{ADM} A_G = 4.79 \times 10^{-1}\, mNm \tag{6.40}$$

The inertial load created by the accelerating ball screw is

$$\frac{1}{\tau_{PGH}^{XY}} \frac{1}{\eta_{PGH}^{XY}} J_{PGH}^{XY} \left(A_G \frac{2\pi}{h_{BS2}^{XY}} \right) = 1.36 \times 10^{-1}\, mNm \tag{6.41}$$

while the inertial loads of the planetary gearhead and motor are

$$J_{PGH}^{XY} \left(A_G \frac{1}{i^{XY}} \right) = 5.97 \times 10^{-1}\, mNm \tag{6.42}$$

$$J_{M}^{XY} \left(A_G \frac{1}{i^{XY}} \right) = 6.64\, mNm \tag{6.43}$$

Friction The preload on the ball screw creates a resistive torque estimated as follows:

$$\frac{1}{\tau_{PGH}^{XY}} \frac{1}{\eta_{PGH}^{XY}} T_{BS2}^{PRE} = 1.50\, mNm \tag{6.44}$$

Conclusively, table 6.15 summarizes the verification process.

Figure 6.16 shows that the worst-case operating point of the motor is located inside its continuous operating range. The former means that the motor might be suitable for the space mission.

However, a second possible candidate was investigated. It is a $100\,W$ motor with the characteristics shown in table 6.16. By comparing table 6.16 against table 6.12 it may be seen that the $100\,W$ motor is only $10\,g$ heavier than the $25\,W$ motor. Moreover, the nominal torque of the $100\,W$ motor is 2.2 times the torque of the $25\,W$ version. This means that selecting the $100\,W$ results in a large torque margin with very small quantity of added weight. For this reason, the verification process was repeated with this motor. In this case, without knowing a priori the characteristics of the test bench, the weight of the translating mass of the mechanism was considered as if one of

Table 6.15 Motor verification in accordance with the ECSS standards

Type of resistance	Component of resistance	Value at origin	Value at motor shaft $[mNm]$	ECSS uncertainty factor	Final resistance $[mNm]$
Inertia	Translating parts	$10N$	0.48	1.1	0.53
	Ball screw	$1.80mNm$	0.14	1.1	0.15
	Gearhead	$0.60mNm$	0.60	1.1	0.66
	Motor	$6.64mNm$	6.64	1.1	7.31
Friction	Ball screw	$20mNm$	1.50	1.5	2.26
Sum					10.89
2xSum					21.79

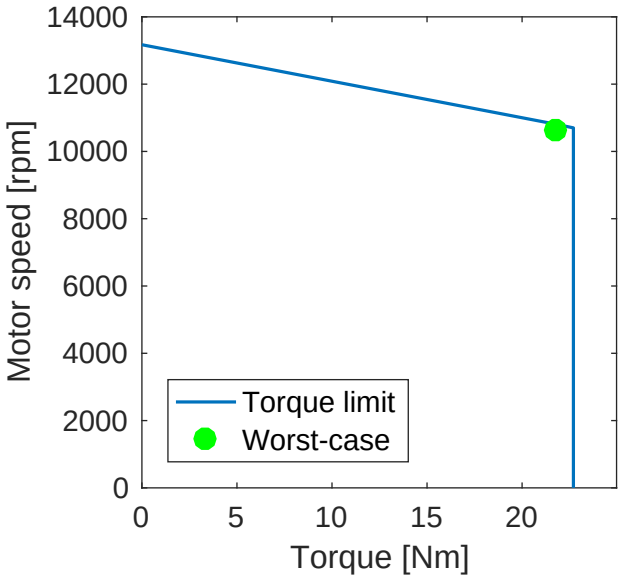

Fig. 6.16 Motor continuous operating area and worst-case operating point

the axes of the XY stage was aligned with the gravity vector. The results of the verification process may be seen in table 6.17.

Figure 6.17 shows the worst operating point of the tested motor. It may be seen that this operating point is inside the continuous operating area of the motor.

Table 6.16 Specifications of the EC 22, brushless, 100 W, with Hall sensors

Supplier	Maxon Motor
Nominal voltage V_0 $[V]$	24
Maximum continuous torque $[mNm]$	50.5
Maximum continuous current i_{max} $[A]$	6.59
Terminal resistance R $[\Omega]$	0.269
Terminal inductance L $[mH]$	0.035
Torque constant k_t $[mNm/A]$	7.75
Speed constant k_ω $[rpm/V]$	1230
Rotor inertia J_M^{XY} $[gcm^2]$	4.09
Mass $[g]$	120

Table 6.17 Second motor verification in accordance with the ECSS standards

Type of resistance	Component of resistance	Value at origin	Value at motor shaft $[mNm]$	ECSS uncertainty factor	Final resistance $[mNm]$
Inertia	Translating parts	$10N$	0.48	1.1	0.53
	Ball screw	$1.80mNm$	0.14	1.1	0.15
	Gearhead	$0.60mNm$	0.60	1.1	0.66
	Motor	$6.10mNm$	6.64	1.1	6.71
Weight		$196.20N$	9.39	1.1	10.33
Friction	Ball screw	$20mNm$	1.50	1.5	2.26
Sum					20.02
2xSum					40.04

6.4.2 Pre-hard docking repositioning

After soft docking, the slides of the XY stage have to reposition the probe. This operation is necessary to align the longitudinal axes of the spacecraft so as to make the hard docking operation possible. The maximum stroke that the slides should travel in this phase was estimated to be $100mm$. A $30\,s$ time interval to complete the

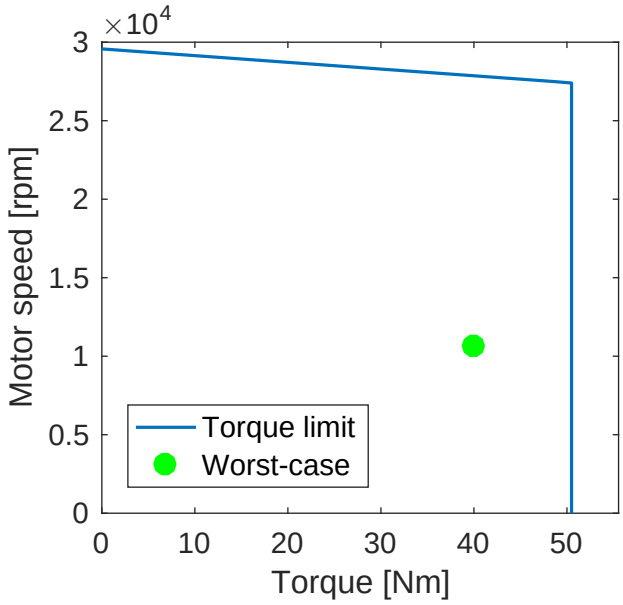

Fig. 6.17 Motor continuous operating area and worst-case operating point

stroke was considered combined with a 0.5 s velocity ramp. Figure 6.18 shows the velocity profile, acceleration, and slide position.

$$V_{max} = \frac{100\,mm}{30\,s - 0.5\,s} = 3.39\,mm/s \tag{6.45}$$

$$A_{max} = \frac{V_{max}}{0.5\,s} = 6.78\,mm/s^2 \tag{6.46}$$

Table 6.18 shows the motor verification during this phase. It is important to note that, in this case, the mass of translating parts is equal to the equivalent mass of the spacecraft (1324.68 kg).

Both worst-case scenario operating points are shown in figure 6.19.

6.4.3 Driver and encoder

The Maxon Motor catalog suggests three possible encoders that may be combined with the selected motor: 128, 256 or 512 CPT. All the encoders are available in two versions: 2 or 3 channels. Table 6.19 shows the final resolution regarding the slide position for each of the encoders mentioned.

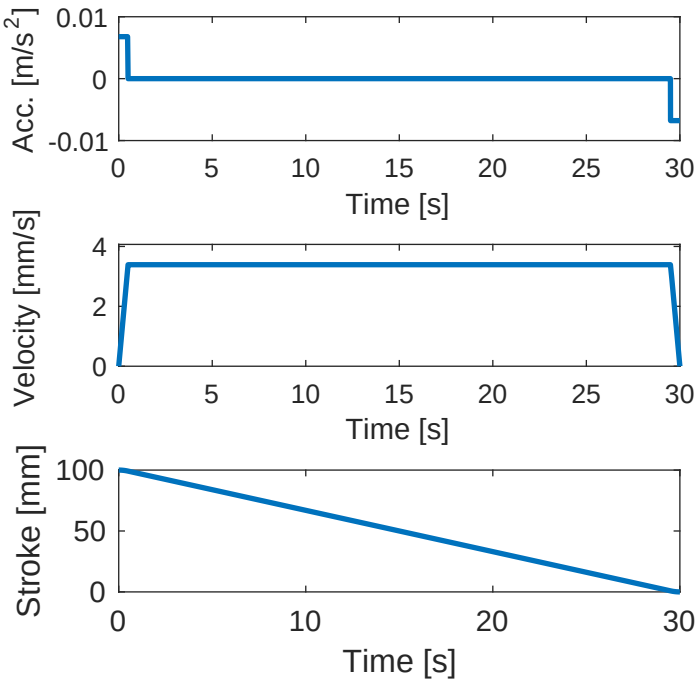

Fig. 6.18 Non smoothed velocity profile, acceleration, and position during repositioning

Table 6.18 Motor verification for the repositioning phase

Type of resistance	Component of resistance	Value at origin	Value at motor shaft $[mNm]$	ECSS uncertainty factor	Final resistance $[mNm]$
Inertia	Translating parts	$8.98N$	0.43	1.1	0.47
	Ball screw	$0.00mNm$	0.00	1.1	0.00
	Gearhead	$0.00mNm$	0.00	1.1	0.00
	Motor	$0.08mNm$	0.08	1.1	0.09
Friction	Ball screw	$20mNm$	1.50	1.5	2.26
Sum					2.83
2xSum					5.66

By analyzing table 6.19, it is clear that a 128 CTP encoder is enough for this application. The three channel version was selected.

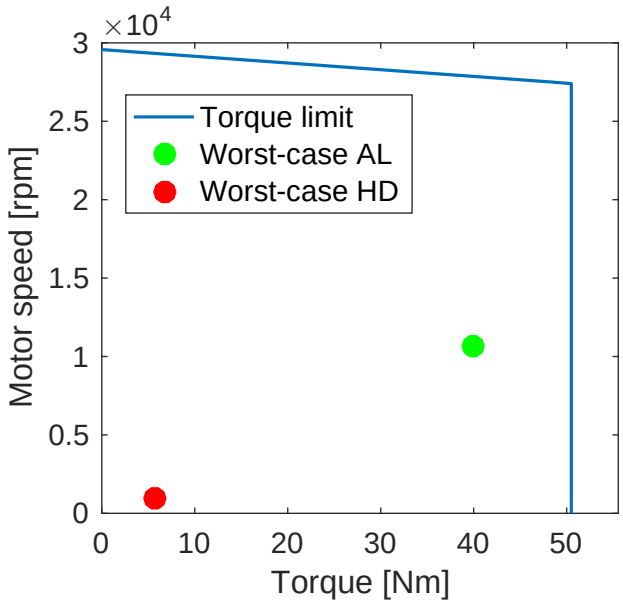

Fig. 6.19 Motor continuous operating range and worst-case operating points for the alignment (AL) and hard docking (HD) phases

Table 6.19 Position resolution

Counts per turn	Final resolution $[\mu m]$
128	1.65
256	0.82
512	0.41

There are several compatible controllers suggested by the Maxon Motor catalog: EPOS2 24/5, 50/5, 70/10 as well as EPOS2 P 24/5 and MAXPOS 50/5. EPOS2 P 24/5 and MAXPOS 50/5 are highly programmable but are more expensive. EPOS2 24/5 was selected due to the nominal voltage of the motor ($24V$); EPOS2 50/5, and 70/10 are best suited for higher tensions and powers.

Table 6.20 EPOS2 24/5 specifications

Supplier	Maxon Motor
Motor	DC and EC from 5 up to 120 W
Sensors	Digital Hall sensor, digital incremental encoder (2-channel, differential), and digital incremental encoder (3-channel, differential)
Operating modes	Current controller, Speed controller, Position controller
Interfaces	RS232, USB 2.0, CAN
Dimensions [mm]	$105 \times 83 \times 24$
Mounting	Flange for M3 screws

6.5 2D numerical model

The ECCS Standard for mechanisms [45], clause 4.8.2.13, establishes that a mathematical model describing the dynamic behavior of a mechanism, and its associated control system, shall be implemented to analyze stability, bandwidth, dynamic and static accuracy, etc. In this regard, the main objective of this section is to perform a preliminary functional analysis of the docking mechanism during the alignment phase via a numerical model. In the alignment phase, the docking mechanism must drive the tip of the probe to the female socket exchanging a small contact force in the process. Besides the functional verification, the suitability of the actuators designed in section 6.4 had to be assessed.

6.5.1 Model of the functional layout

This section deals with the mathematical model used to study the proposed mechanism. In this regard, Figure 6.20 shows a schematic view of the mechanism halves mounted on their respective spacecraft.

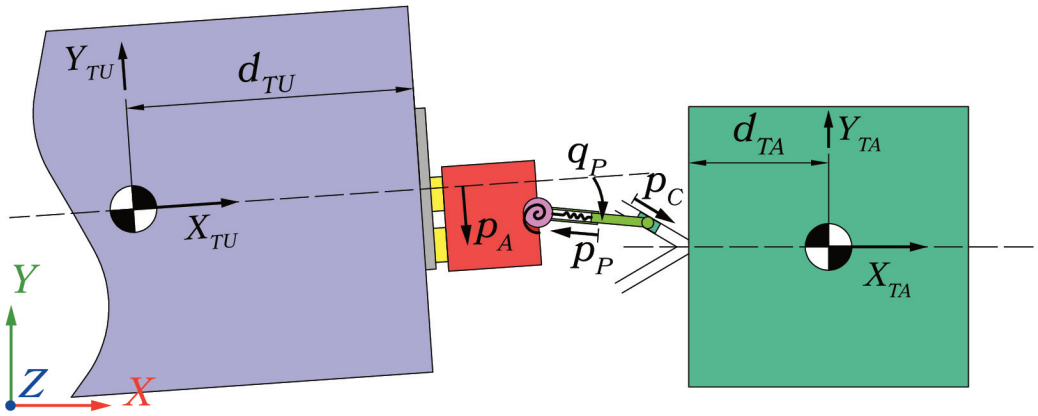

Fig. 6.20 Model of the mechanism with active slides

As a 2D model, it only considers a planar motion of the bodies. The male part of the docking mechanism is mounted on the chaser spacecraft at the distance d_{TU} from its COG. The lateral translation of the male half p_A is accomplished by an actuated prismatic joint that links the chaser body to the slide. Regarding the probe, it is connected to the slide through a revolute joint. The probe rotation q_P is then passively controlled by an equivalent torsional spring. The deformation of the spring of stiffness k_T generates a torque

$$T_S = k_T q_P + \beta_T \dot{q}_P \tag{6.47}$$

on the probe equivalent to the torque applied by the traction springs on the universal joint (figure 6.1). In equation 6.47, β_T indicates the damping constant associated with the spring (damping ratio equal to 3%). A prismatic joint links the probe to the cap while a linear spring with stiffness k_L and damping constant β_L controls their relative displacement p_P by creating an elastic force

$$F_S = k_L p_P + \beta_L \dot{p}_P \tag{6.48}$$

On the other hand, the female cone was modeled using an inclined wall mounted at the distance d_{TA} from the COG of the target. This wall is inclined w.r.t. the axis of symmetry of the target by $\theta_{HC} = 30\,deg$.

The physical interaction between the parts of the mechanism is accomplished by using a prismatic joint in series with a revolute joint. The base of the prismatic joint

is mounted on the female inclined wall. On the other hand, the base of the revolute joint is fitted to the cap tip. During the alignment phase of the maneuver, the position p_C of the moving part of the prismatic joint is measured from the initial contact point. By using this joints, the relative rotation between the spacecraft is allowed while the mechanism parts slip against each other. However, this kind of model prohibits the bodies from separating. For this reason, the direction of the force perpendicular to the prismatic joint, F_C, was monitored. This force may only push against the female cone wall.

The friction force, F_F, associated with the contact between the probe and the equivalent female cone was estimated by multiplying the normal force F_C by the friction coefficient between the materials of the cone and the probe μ:

$$F_F = \mu F_C \tag{6.49}$$

6.5.2 Model of the linear actuator and control

As stated in section 6.4, the linear actuator consists of an electric motor connected to a ball screw through a planetary gearhead. The rotation of the motor generates a linear displacement of a ball nut constrained by the linear guides of the slide. This subsection deals with the model of the electric motor. The selected motor was an EC manufactured by Maxon Motor. An equivalent DC model (figure 6.21) was formulated considering the motor specifications: nominal voltage V_0, maximum current i_{max}, terminal resistance R, terminal inductance L, torque constant k_t, and speed constant k_ω.

The differential equation associated with the circuit shown in figure 6.21 is the following:

$$V_a = Ri_a + L\frac{di_a}{dt} + k_\omega \omega_M \tag{6.50}$$

In equation 6.50, V_a is the armature voltage and ω_M is the motor angular velocity. The solution of this equation leads to the estimation of the torque-generating current i_a. The torque of the motor T_M is then calculated by multiplying the current time the torque constant:

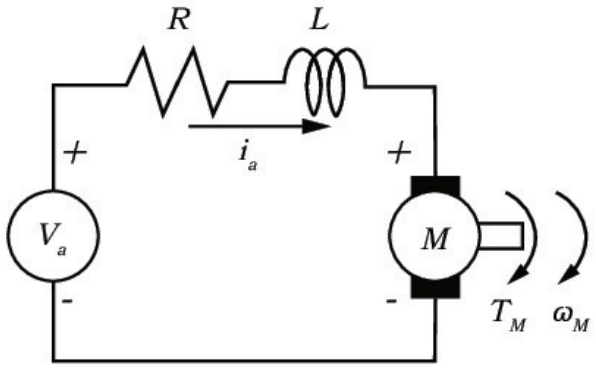

Fig. 6.21 DC motor model

$$T_M = k_t i_a \tag{6.51}$$

The motor torque overcomes the inertial torques of the accelerating bodies as well as the preload torque of the screw, T^{PRE}. Thus, the dynamic equilibrium equation of the motor rotor is the following:

$$T_M - \frac{1}{\tau_{PGH}^{XY}} T^{PRE} - T_L = \left(J_M^{XY} + J_{PGH}^{XY} + \frac{1}{{\tau_{PGH}^{XY}}^2} J_{BS}^{XY} \right) \dot{\omega}_M \tag{6.52}$$

where J_M^{XY}, J_{PGH}^{XY}, and J_{BS}^{XY} are respectively the polar inertia of the motor rotor, the planetary gearhead, and the ball screw. Moreover, τ_{PGH}^{XY} is the transmission ratio of the gearhead and T_L is the torque of the load. The resultant force applied by the actuator on the slide, F_L, is then calculated using the total transmission ratio i^{XY}:

$$F_L = \frac{1}{i^{XY}} T_L \tag{6.53}$$

In this model, the control of the system relies on the measurement of the probe rotation q_p. This rotation is the result of the contact force between the spacecraft. Therefore, keeping the value of this rotation small translates into fewer disturbance actions applied on the satellites. However, a deadband is applied to the angle measurement to avoid issues related to mounting errors. The needed displacement Δp_A to maintain q_P within the design limits is considered to be the following:

$$\Delta p_A = l_P^0 \sin(q_P) \tag{6.54}$$

As shown in figure 6.22, the linear actuator has to translate the body of the male part of this quantity starting from its current position to eliminate the rotation.

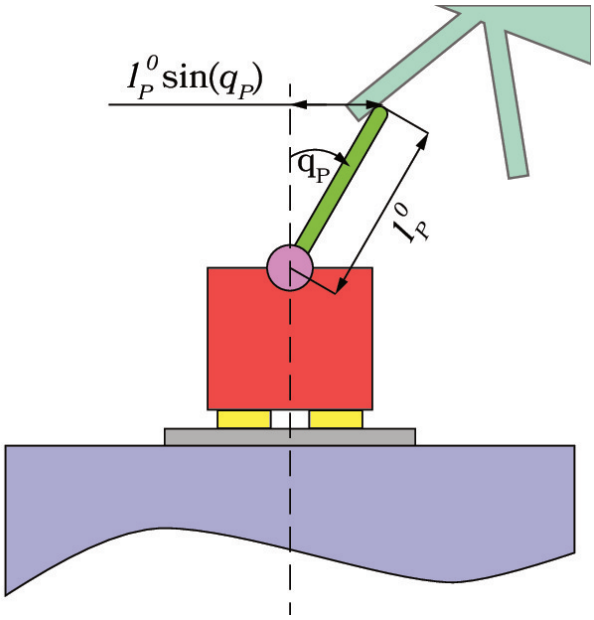

Fig. 6.22 Slide displacement calculation

A suitable velocity gain K_v transforms the needed differential translation into a velocity set:

$$v_{set} = K_v \Delta p_A \tag{6.55}$$

This set is compared against the actual axis velocity $\dot{p}_A$ to generate the velocity error. After this phase, two PI controllers are used to obtain the desired velocity and current of the electric motor (figure 6.23). The result, after suitable saturations, becomes the armature voltage of the electric motor.

6.5.3 Numerical implementation

The model of the system was implemented in Simscape Multibody^{TM}. This software exploits a graphical programming language to create complex mechanical

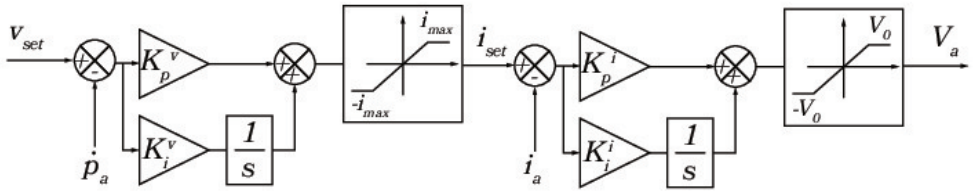

Fig. 6.23 Model of the controller

systems combining blocks representing bodies, joints, constraints, force elements, and sensors. At the highest level, the model contains four subsystems: a group of blocks that defines the simulation environment configuration, the tug subsystem, target subsystem, and a subsystem that simulates the contact constrain between the satellites (figure 6.24).

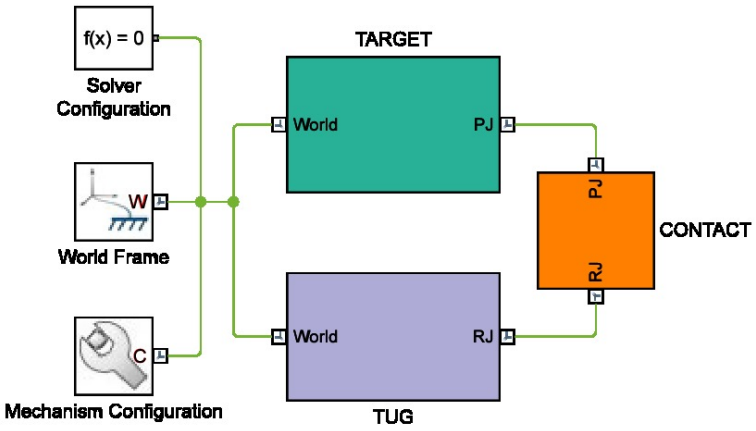

Fig. 6.24 Layout of the numerical model

Regarding the subsystem of the tug (figure 6.25), it consists of the body of the servicer mounted on a planar joint. Subsequently, the slide of the Cartesian stage is mounted on the servicer through a prismatic joint. This joint simulates the active axis of the mechanism. In this regard, the subsystem `SERVO` contains the model of the DC motor as well as the speed and current controllers. The slide transports the revolute joint on which the rod is fitted. A sensor measures the revolute joint angular position and velocity. In addition, the block `TORQUE CALC` estimates the resulting torque on the revolute joint as stated in equation 6.47. Inside this block the angle deadband is also applied. The resulting angular position is the input of the block `SET CREATION`. This block computes the value of Δp_A. Finally, the block `FORCE CALC` generates the resultant force applied on the probe (equation 6.48).

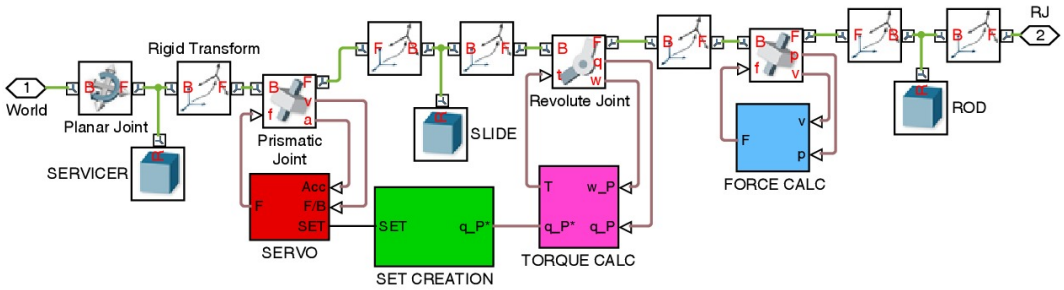

Fig. 6.25 Model of the space tug

Figure 6.26 shows the model of the target satellite. As for the tug, the body of the target is mounted on a planar joint. The inclined cone wall of the mechanism is positioned on the customer using a rigid transform block.

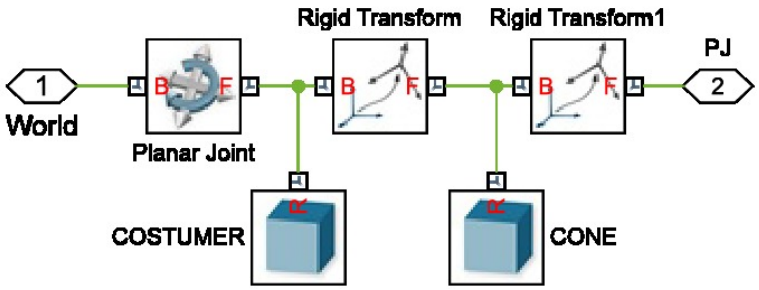

Fig. 6.26 Model of the target

As introduced before, the system that simulates the contact between the mechanism halves is based on a prismatic joint in series with a revolute joint (figure 6.27). On the one hand, the prismatic joint is mounted on the cone bode with is axis aligned with the cone wall. On the other hand, the revolute joint is linked to the tip of the rod. In this `CONTACT` subsystem, a group of sensors measures the position of the prismatic joint, its velocity, and the forces exchange between its parts. The block `FRICTION CALC` implements equation 6.49. Finally, the block `BOOL` monitors the contact force to establish whether the simulation has to stop. It also monitors the positions of the prismatic joint. Once the vertex of the cone is reached, the alignment phase ends.

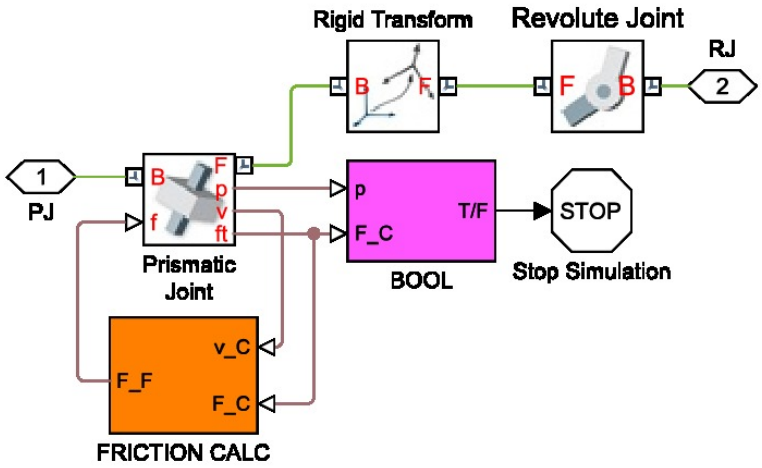

Fig. 6.27 Model of the contact

6.5.4 Results

This section shows the numerical values used during the simulations, the test performed, and discuss the results obtained.

Numerical values

This section summarizes the numerical values used during the simulations. Regarding the spacecraft inertial properties, the target used was the satellite platform. Thus, the properties are the following (chapter 3):

$$M_{TA} = 2000\,kg$$
$$I_{G,TA} = 2000\,kgm^2$$
$$d_{TA} = 0.65\,m$$

A docking operation just before the orbit raising was considered as the reference scenario. In this case, the chaser is in Configuration B:

$$M_{TU} = 3500\,kg$$
$$I_{G,TU} = 5235\,kgm^2$$
$$d_{TU} = 1.942\,m$$

The mass of the mechanism assigned to the slide was $20\,kg$. Moreover, the nominal length of the probe, l_P^0, was $440\,mm$. Regarding the elastic elements, the stiffness of the cap spring, k_L, is equal to $37.17\,N/mm$ while the equivalent torsional stiffness, k_T, is $22.97\,Nm/rad$.

The properties of the electric motor are the following (table 6.16):

$$V_0 = 24\,V$$
$$i_{max} = 6.59\,A$$
$$R = 0.269\,\Omega$$
$$L = 0.035\,mH$$
$$k_t = 7.75 \times 10^{-3}\,Nm/A$$
$$k_\omega = 7.76\,Vs/rad$$
$$J_M^{XY} = 4.45\,gcm^2$$

Regarding the planetary gearhead and the ball screw, the properties are (table 6.11 and 6.14, and equation 6.33):

$$\tau_{PGH}^{XY} = 19$$
$$J_{PGH}^{XY} = 0.40\,gcm^2$$
$$J_{BS}^{XY} = 2.30 \times 10^{-6}\,kgm^2$$
$$T^{PRE} = 0.02\,Nm$$

Furthermore, the total transmission rate, i^{XY}, is equal to $3.35 \times 10^{-5}\,m$ (equation 6.39).

Finally, table 6.21 shows the specific initial conditions used throughout all the tests.

Table 6.21 Considered initial conditions

Y_{TA} misalignment $[mm]$	50
Yaw misalignment $[deg]$	3
Y_{TA} relative linear velocity $v_{rel,y}$ $[mm/s]$	10
X_{TA} relative linear velocity $v_{rel,x}$ $[mm/s]$	40
Yaw relative angular velocity $[deg/s]$	0.1

Tests and numerical results

Two testing conditions were studied to assess the suitability of the mechanism for the docking maneuver. The first one considered the active linear axis switched off and blocked. This case served as a reference. It is equivalent to the first design iteration in which there were no active features. Instead, during the second test, the linear axis was active. The relative velocities between the satellites were observed as indicators of the disturbance applied to the customer by the servicer. On this regard, the contact force was also monitored.

Concerning the first test, figure 6.28 shows the relative velocity between the spacecraft expressed in the reference frame TA of the target. The longitudinal relative velocity $v_{rel,x}$ drops about 65%. This velocity is fundamental to penetrate the cone socket so as to accomplish soft docking. Moreover, the lateral velocity changes sign and increases. This condition reduces the chances of reaching the soft capture.

The analysis of the contact force supports the former considerations. During the simulation, the contact force zeroed before reaching the vertex of the cone. Moreover, the values of this force F_C and the resultant friction force F_F (figure 6.29) increase after the first contact. These forces alter the kinematic state of the bodies resulting in the effects seen in figure 6.28.

In contrast, figures 6.30 and 6.31 show the relative velocity and exchanged force during the second test. Firstly, the longitudinal relative velocity (figure 6.30) only decreases of about 9.58% while the lateral velocity drops 56.99%. The reduction of

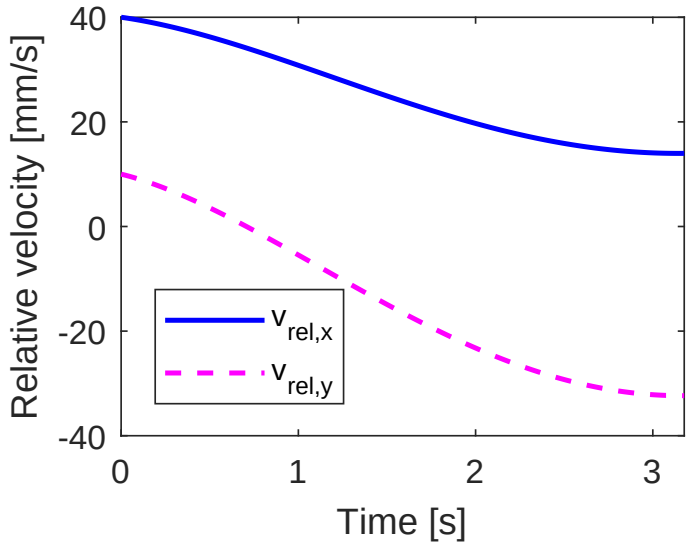

Fig. 6.28 Relative velocity of the servicer w.r.t. *TA* during the first test

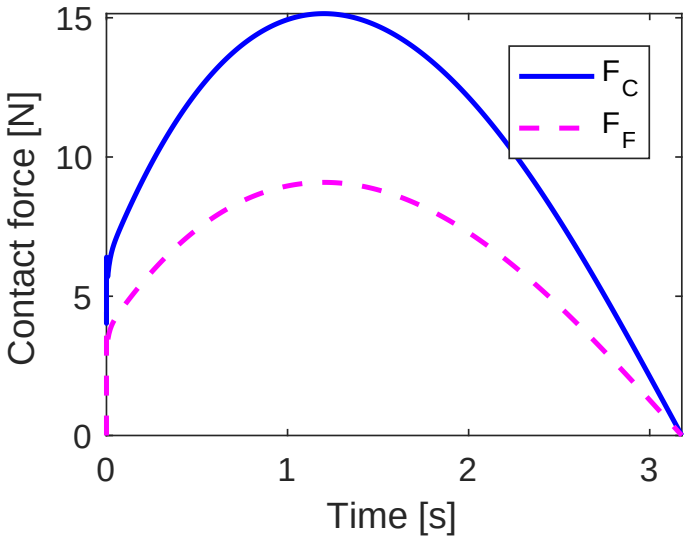

Fig. 6.29 Contact force and resulting friction force during the first test

the lateral velocity is a positive effect as this velocity worsens the conditions of the maneuver.

Regarding the contact force (figure 6.31), after the first contact, it plunges reaching a value of about 1.5 N. This force diminution and its dynamic effect indicate that the linear controlled axis fulfills its purpose.

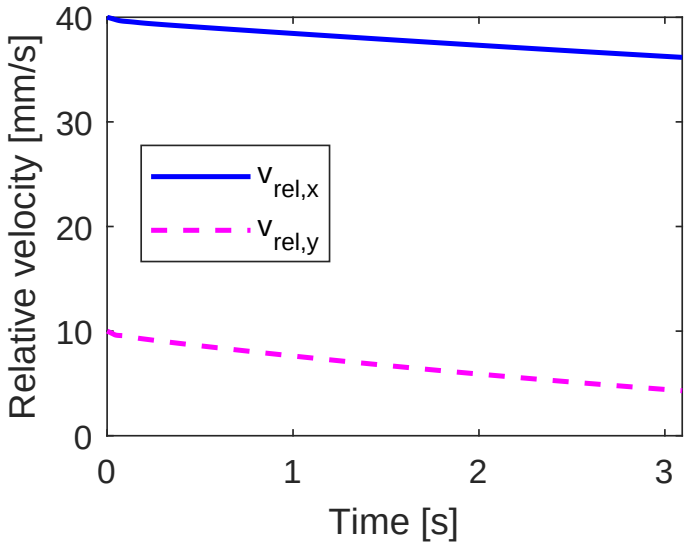

Fig. 6.30 Relative velocity of the servicer w.r.t. *TA* during the second test

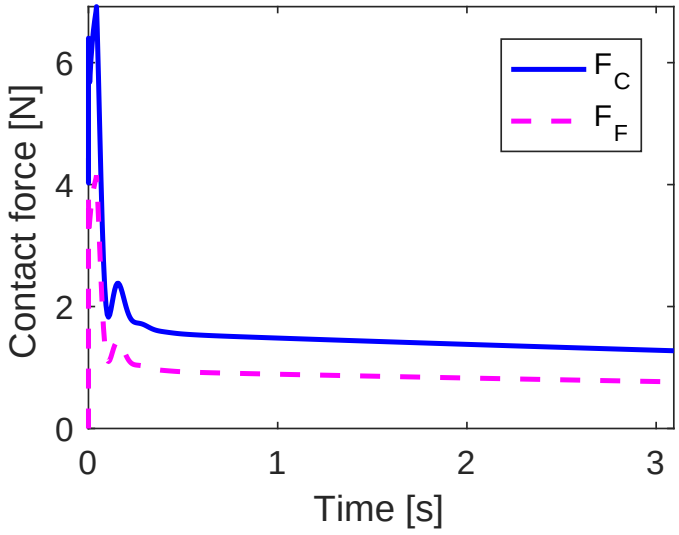

Fig. 6.31 Contact force and resulting friction force during the second test

Figure 6.32 helps to assess the suitability of the selected motor. It shows the limit of the continuous operating range of the motor. All the operating points of the motor during the active maneuver are well inside this range.

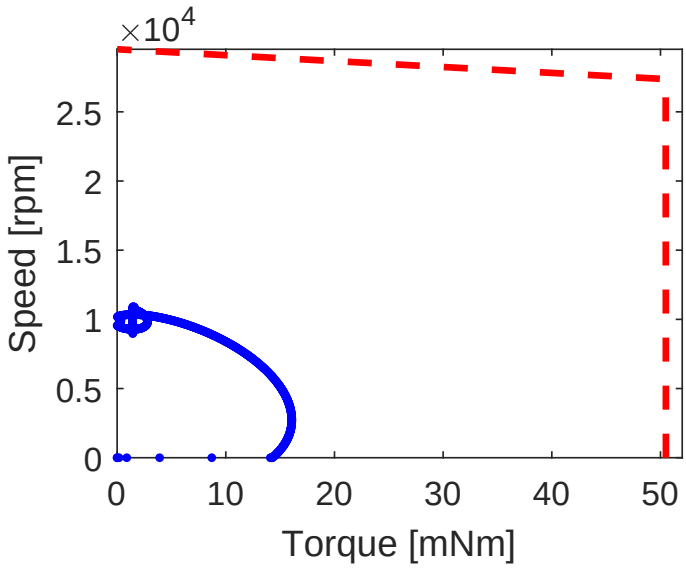

Fig. 6.32 Operating points of the electric motor (solid line) inside its continuous operation range (dashed line)

6.6 Damping system

The docking mechanism has two main objectives: to recover the misalignments between chaser and target left by the GNC errors, and most importantly to dissipate or accumulate in a safe way the energy associated with the relative velocities between the bodies. The damping system that dissipates the kinetic energy associated with the relative longitudinal velocity between the spacecraft is located at the apex of the female cone as shown in figure 6.2. Once the tip of the probe surpasses the female socket, it pushes the damping system dissipating the energy in a controlled fashion. The objective of this chapter is to describe the design of this damping system.

6.6.1 Considered solutions

Several technologies were evaluated: hydraulic dissipation, Coulomb damping, eddy current braking, and electromechanical damping.

Hydraulic shock absorber

A hydraulic shock absorber dissipates energy using viscous friction. This kind of system was used in the dampers of the Gemini docking system cone [14] and in the Apollo probe [18]. It was also used in the American half of the ASTP docking system [21].

Hydraulic shock absorbers are relatively simple but present several issues that led to the rejection of this type of technology. The first issue is related to the sealing problems in a ultra-high vacuum environment. Secondly, heaters may be necessary to avoid large changes in the fluid viscosity. An increase in viscosity may create large impact forces.

Coulomb damper

The Coulomb brake relies on Coulomb friction to dissipate energy. In this case, the friction force is proportional to a force applied perpendicularly to a sliding surface. In figure 6.33, the sliding surface is represented by a rod and the force is applied using a spring loaded element.

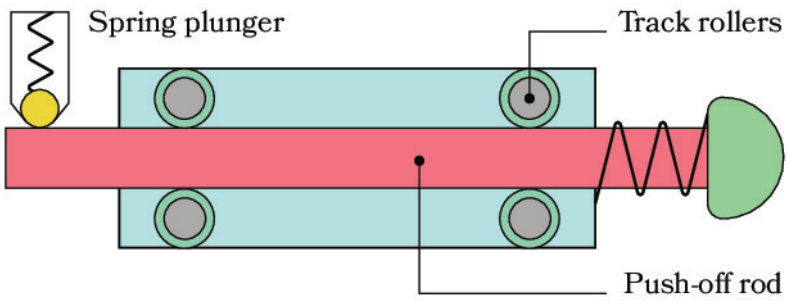

Fig. 6.33 Example of Coulomb damper

An example of a Coulomb friction damper may be found in the OECS [24]. In this case, the final phase of the docking maneuver is governed by a group of push-off struts equipped with compression springs and adjustable Coulomb dampers.

Although this solution has been space-tested, concerns regarding the use of Coulomb dampers in a space environment with high-temperature variations led to the rejection of this kind of system. These temperature variations translate into material dilatation and contraction that change the designed friction force.

Electromechanical damper

Electromechanical damping is another form of "dry" damping. In this kind of damping system, an electric generator is used for dissipating energy. In this case, the damping force is proportional to the velocity. This kind of damping has been proposed as shock absorber for landing gears of planetary exploration probes and rovers [47].

Figure 6.34 shows a possible implementation of this system based on a ball screw. The ball screw is translated by an impact force. This translation is converted into rotation by a ball nut. Subsequently, the ball nut is connected to an electric DC motor through a couple of spur gears. The mechanical energy is converted into electric energy and then is dissipated as heat.

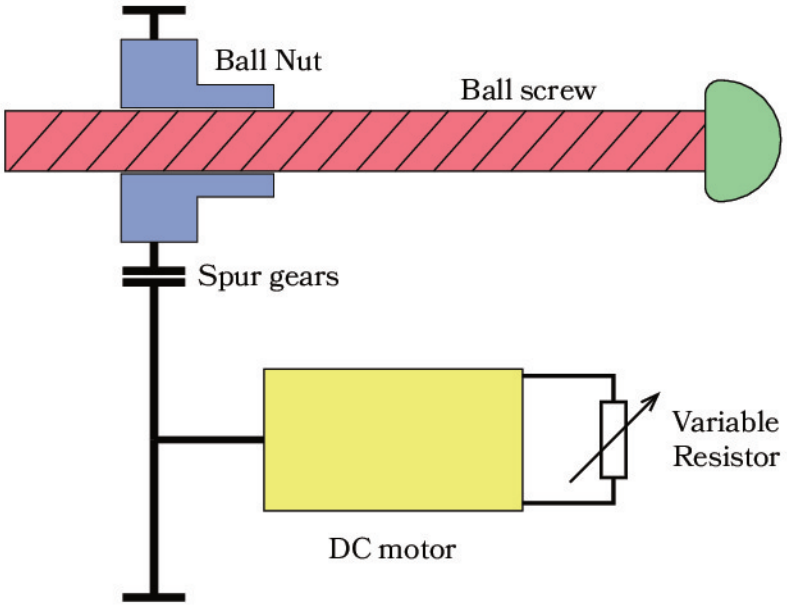

Fig. 6.34 Schematic view of an electromechanical damper

As stated before, the damping effect is proportional to the translating velocity of the ball screw v_{screw}^{DS}. The angular velocity of the nut is defined by the following formula:

$$\omega_{nut}^{DS} = \frac{2\pi}{h_{bs}^{DS}} v_{screw}^{DS} \tag{6.56}$$

In equation 6.56, h_{bs}^{DS} is the lead of the screw. The angular velocity of the DC motor may be calculated as follows:

$$\omega_{DC}^{DS} = \tau \omega_{nut}^{DS} = \tau^{DS} \frac{2\pi}{h_{bs}^{DS}} v_{screw}^{DS} \tag{6.57}$$

where τ^{DS} is the transmission ratio of the spur gears. The electric equation of the motor, that in this case acts as a generator, is the following:

$$k_\omega \omega_{DC}^{DS} = R i_a + L \frac{di_a}{dt} \tag{6.58}$$

where k_ω, R, L, and i_a are respectively the electric constant, the armature resistance, the inductance, and the armature current of the motor. Moreover, the motor torque T_{DC}^{DS} is proportional to the current:

$$T_{DC}^{DS} = k_t i_a \tag{6.59}$$

In DC motors, the torque constant k_t is equal to the electric constant. In stationary conditions the motor torque becomes

$$T_{DC}^{DS} = \frac{k_t^2}{R} \omega_{DC}^{DS} = \frac{k_t^2}{R} \tau^{DS} \frac{2\pi}{h_{bs}^{DS}} v_{screw}^{DS} \tag{6.60}$$

The motor torque is then transformed into a damping force, F_D, through the transmission chain

$$F_D = \tau^{DS} \frac{2\pi}{h_{bs}^{DS}} T_{DC}^{DS} = \frac{k_t^2}{R} \left(\tau^{DS} \frac{2\pi}{h_{bs}^{DS}} \right)^2 v_{screw}^{DS} \tag{6.61}$$

From equation 6.61 the damping constant β_D may be individuated

$$\beta_D = \frac{k_t^2}{R} \left(\tau^{DS} \frac{2\pi}{h_{bs}^{DS}} \right)^2 \tag{6.62}$$

This solution was considered as one of the main candidates for the damping system.

Eddy current brake

This kind of system is used in the Soyuz docking system [16]. In this system, eddy currents are induced in a piece of metal when the piece is moved in a magnetic field (figure 6.35). Thus, the kinetic energy is dissipated as heat. Also, in this case, the damping effect is proportional to the angular velocity of the disc [48].

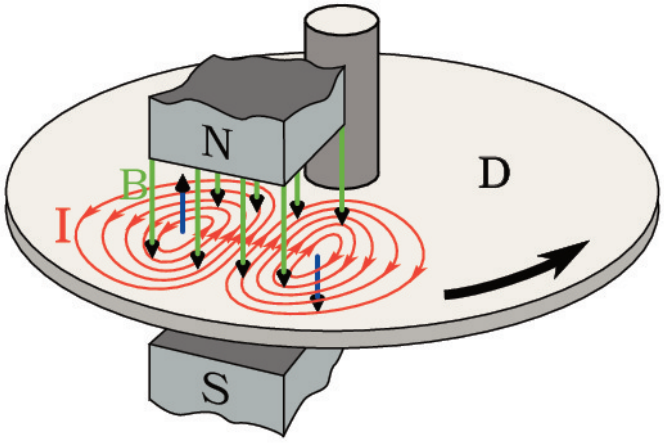

Fig. 6.35 Schematic view of an eddy current brake

The damping constant is a function of the geometry of the magnet and the geometry of the disc. It also depends on the intensity of the magnetic field, and the properties of the disc material. The design of an Eddy current brake was regarded as complex since many custom components are needed to achieve the desired damping constant. For this reason, the electric damper solution was chosen as the preferred one.

6.6.2 System layout and design

The damping system has to dissipate the kinetic energy associated with the maximum relative approaching velocity, $v_{rel,x}$, which is equal to $40\,mm/s$. This has to be accomplished considering the worst-case configuration regarding the masses of the spacecraft. This configuration is characterized by a $1700\,kg$ (M_{TU}) chaser docking with the orbital tank ($M_{TA} = 6000\,kg$). Moreover, the damping system has to be mounted on the female part, thus it has to be passive. To achieve a fully passive system, an elastic element has to be connected in parallel to the damper. This element is useful to reset the damping system after each docking maneuver.

A 2 DOFs model was created to study the damping system. Figure 6.36 shows the model of the chaser and the target equipped with the damper.

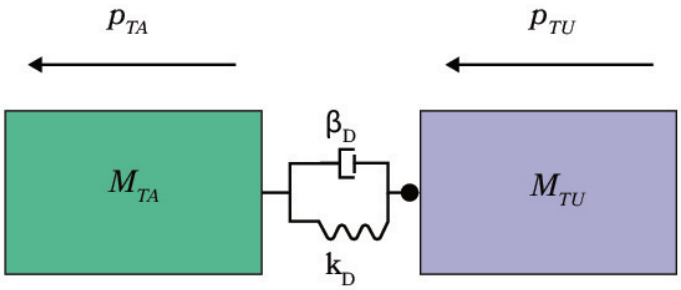

Fig. 6.36 2 DOFs model of the system during attenuation

The damping constant and stiffness of the system may be estimated assuming critical damping (critical ration $\zeta = 1$). However, this condition is not sufficient to determine the needed characteristics of the system. The maximum allowable force upon contact with the damping system may be used to calculate the needed damping constant β_D. This maximum force is equal to the damping constant times the contact velocity. It must be less than the maximum resultant axial force applied by the three spring plungers on the probe (F_{SP} in section 6.3)

$$\beta_D \cdot vrel, x < F_{SP} \tag{6.63}$$

As seen in section 6.3, friction "helps" the ball plungers to keep the external part of the probe in place. For this reason, to be compliant with the ECSS, the friction factor associated with the ball-conical seat contact ($\mu = 0.6$) was divided by 3. Moreover, the resultant force was halved. With this data, the inequality 6.63 leads to the estimation of β_D:

$$\begin{aligned} \beta_D &= \frac{1}{2}\frac{1}{v_{rel,x}}\left(3\left(\frac{F_{BP}^{max}}{1-\mu}+\frac{\mu F_{BP}^{max}}{1-\mu}\right)\right) \\ &= \frac{1}{2}\frac{1}{40\,mm/s}\left(3\left(\frac{41.85\,N}{1-0.2}+\frac{0.2\cdot 41.85\,N}{1-0.2}\right)\right) \\ &= 2354.06\,Ns/m \end{aligned} \tag{6.64}$$

If an equivalent 1 DOF model of the system presented in figure 6.36 is used considering the equivalent mass and using as degree of freedom the relative position

p_{rel} between the bodies

$$\ddot{p}_{rel} + \frac{\beta}{M_{eq}}\dot{p}_{rel} + \frac{k_D}{M_{eq}}p_{rel} = \ddot{p}_{rel} + 2\zeta\omega_n\dot{p}_{rel} + \omega_n^2 p_{rel} = 0 \tag{6.65}$$

it is possible to estimate the stiffness of the spring needed to achieve critical damping:

$$k_D = \left(\frac{1}{2}\frac{\beta_D}{\sqrt{M_{eq}}}\right)^2 = 1045.84\,N/m \tag{6.66}$$

Having estimated the stiffness and damping, it is possible to solve equation 6.65 to study the system performance. Firstly, the force exchanged through the damper was analyzed. Figure 6.37 shows the force produced by the damping system (spring plus damper) zeroes at 2.25 s after impact. When this occurs, the spacecraft continue traveling at a separation velocity equal to 5.41 mm/s (figure 6.38). This separation stops when the probe latches meet the bulkhead of the female cone resulting in a collision. Although this collision occurs, it theoretically happens at a relative velocity significantly smaller than the approaching one (14% of the initial $v_{rel,x}$).

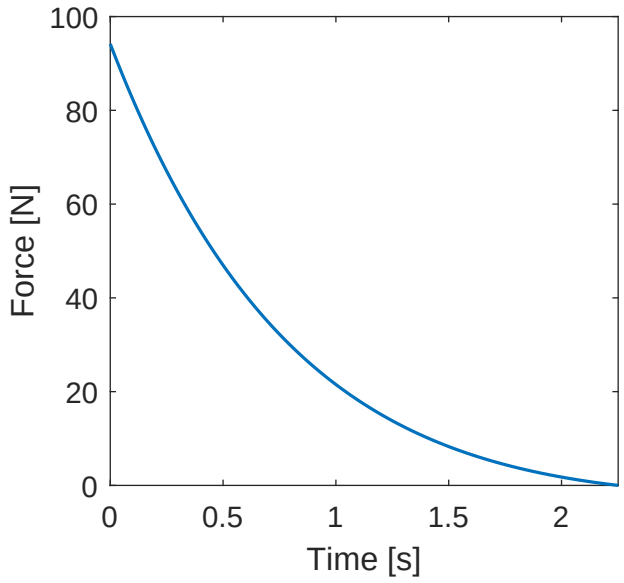

Fig. 6.37 Force produced by the damping system

To achieve the desired damping constant, a suitable ball screw, spur gears, and electric motor were selected. The designed configuration (figure 6.39) is slightly

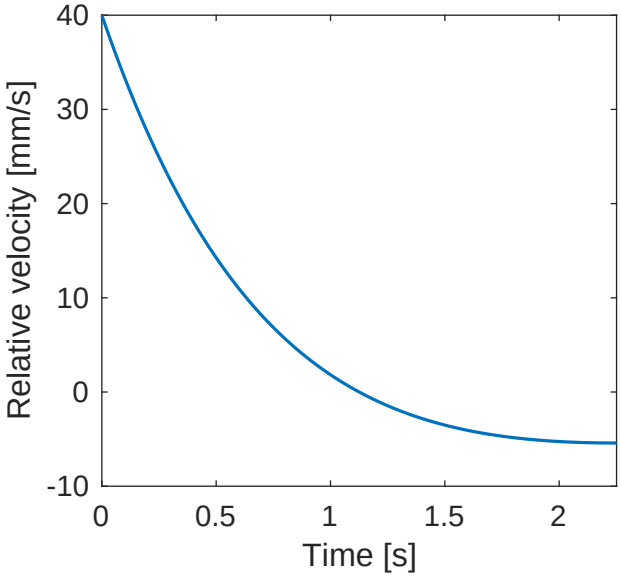

Fig. 6.38 Relative velocity between spacecraft

different from the one shown in figure 6.34. In this case the ball nut is the translating part. However, the previous equations hold.

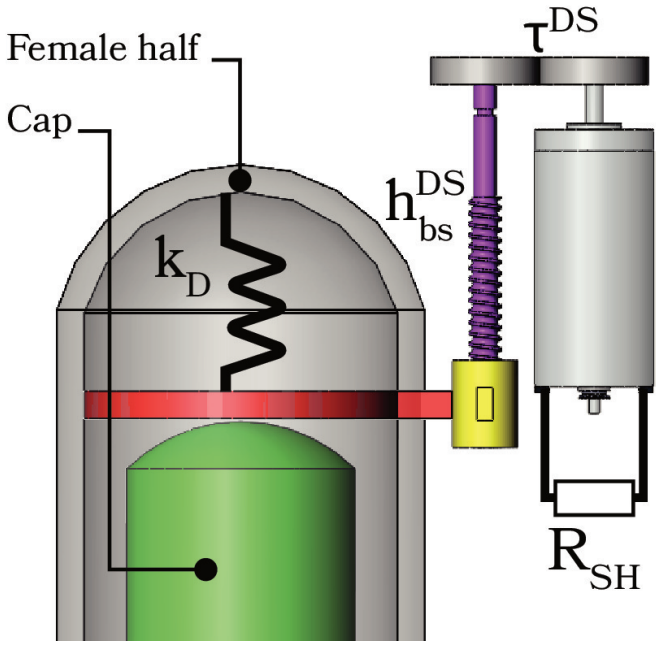

Fig. 6.39 Concept of the damping system

The Maxon DCX 22 L $\phi 22$ brushed motor, was individuated as a suitable generator. This motor has the characteristics shown in table 6.22.

Table 6.22 Specifications of the DCX 22 L $\phi 22$ with graphite brushes

Supplier	Maxon Motor
Terminal resistance R_{GEN} $[\Omega]$	7.39
Torque constant $k_{t,GEN}$ $[mNm/A]$	45.2
Speed constant $k_{\omega,GEN}$ $[rpm/V]$	211

If a ball screw with a lead equal to $4\,mm$ is selected, together with a 1:2 transmission ratio τ^{DS}, it is possible to estimate the shunt resistance R_{SH} needed to achieve the estimated damping β_D by using equation 6.62.

$$R_{SH} = \frac{k_{t,GEN}^2}{\beta_D}\left(\tau^{DS}\frac{2\pi}{h_{bs}^{DS}}\right)^2 - R_{GEN} = 1.17\Omega \tag{6.67}$$

6.7 Hard docking system

The hard docking system is a critical mechanism that creates a stiff mechanical connection between chaser and target. Without this system, the orbit raising is not possible. This section will show the different mechanisms considered, the design of the transmission from the actuator to the fastening devices, and the selection of the actuators based on the system requirements regarding velocity and torque.

6.7.1 Considered solutions

A couple of solutions were considered for the hard docking system. Both solutions were based the three radial hooks mounted on the periphery of the chaser interface plate. These hooks translate along the radial direction to meet a set of strikers on the target cone (see figure 6.40). The first solution was based on one actuator for each hook for a total of three actuators. The second solution considered only one actuator to actuate all the hooks simultaneously.

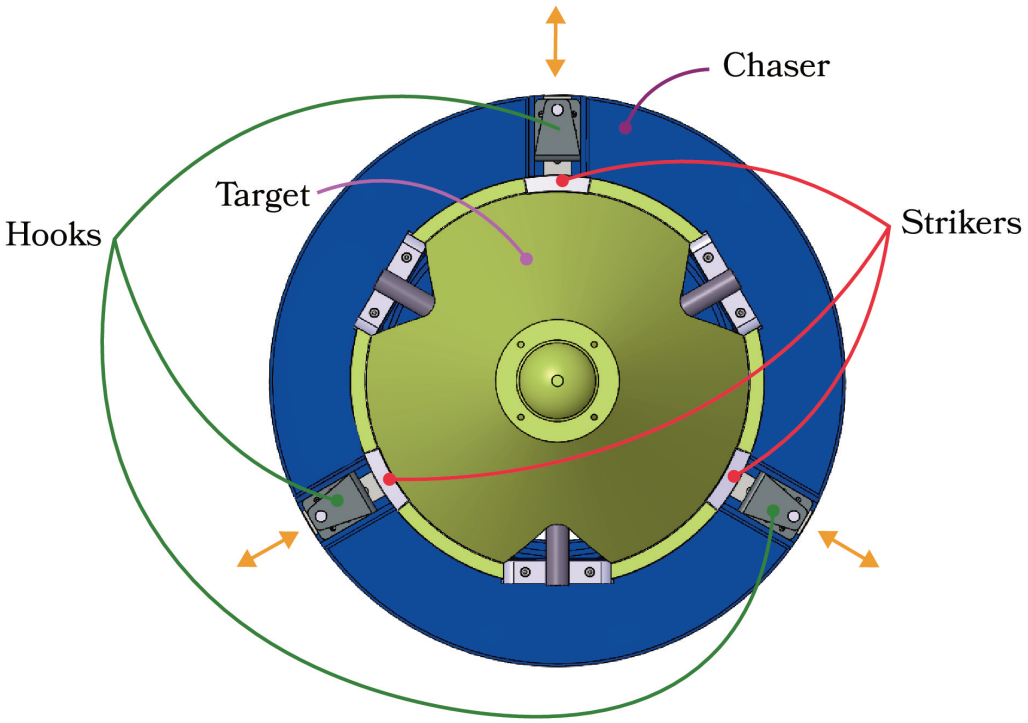

Fig. 6.40 Layout of the hard docking hooks

The second solution was selected for being more reliable than the first one. Having single-actuated hooks implies that the failure of only one actuator makes the undocking impossible. For each actuator, a backup system is needed. This may be accomplished by either redundant motor windings or by duplicating each actuator. If duplication is chosen, the first solution will lead to six motors (instead of two). More mechanical systems lead to a less reliable mechanism. Although the second solution will present several challenges, like the transmission chain, it was selected as the preferred solution.

6.7.2 Design of the hooks and the strikers

As stated before there are three hooks and three strikers used as blocking devices. The contact zones between these elements were selected to be inclined walls. The objective of this section is to select a suitable angle of the incline as well as a suitable preload. Figure 6.41 shows a schematic view of one of the hooks and one of the strikers. A force F_{SEP} tries to separate the target cone from the chaser. This force is a combination of external forces and the elastic force created by the undocking springs.

The normal and friction forces between hooks and strikers stop the separation. In order to do so, each hook is preloaded by the common actuation system. The needed preload F_{PRE} is calculated based on the angle of the incline θ and the applied separation force.

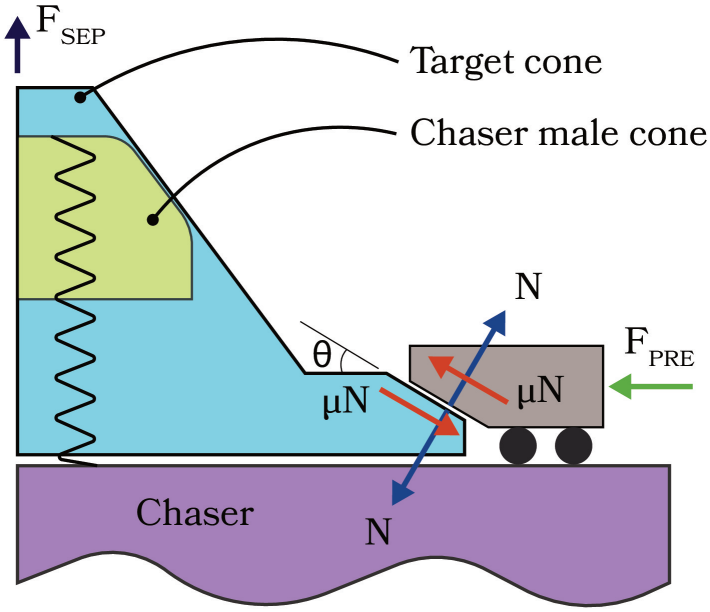

Fig. 6.41 Blocking system and forces applied

The normal force applied to the target cone, N, may be calculated using its free body diagram. Taking figure 6.41 as a reference, the vertical equilibrium equation of the target cone is the following:

$$N = \frac{F_{SEP}}{3} \frac{1}{\cos\theta + \mu \sin\theta} \tag{6.68}$$

In equation 6.68, the $1/3$ factor was included to consider the presence of the three couples hook/striker. Moreover, μ indicates the friction coefficient between the two aluminum pieces. This is theoretically equal to 0.6. Also, in this case, considering that the friction "helps" the system to maintain the closure, it has to be divided by three following the ECSS indications. In conclusion, $\mu = 0.2$ was used during the preload calculations.

Once the normal force is known, it is possible to calculate the preload writing the horizontal equilibrium equation of the hook:

$$F_{PRE} = N(\sin\theta - \mu\cos\theta) = \frac{F_{SEP}}{3}\frac{\sin\theta - \mu\cos\theta}{\cos\theta + \mu\sin\theta} \tag{6.69}$$

To select the angle of the incline, the ratio F_{PRE}/F_{SEP} was calculated for different values of the angle ranging from 0 to 25 deg (figure 6.42).

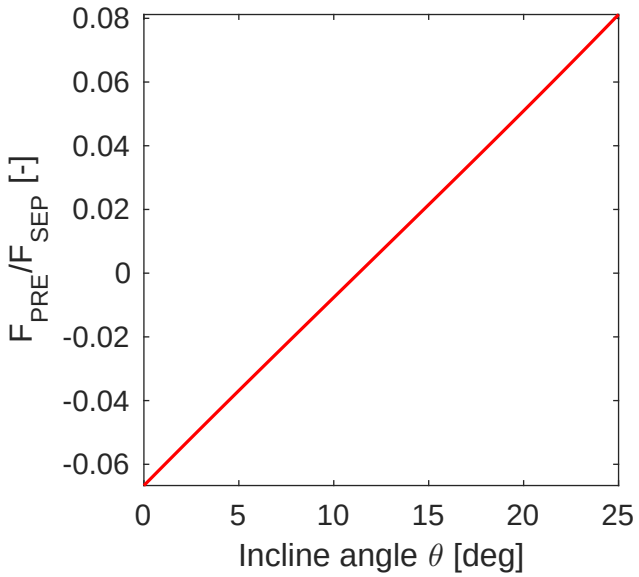

Fig. 6.42 Ratio between the preload force of one hook and the separation force as a function of the angle of the striker

Figure 6.42 shows that from 0 to 11.31 deg the ratio is negative. This means that for those angles there is a condition of mechanical jamming. In this condition, no preload is needed to guarantee the closure regardless the separation force. For this reason, 5 deg was selected as the angle of the incline θ^*.

Since the selected angle creates a mechanical jamming condition, an opening force F_{OPEN} must be applied to the hooks to deactivate the hard docking system at the beginning of the undocking phase. During this phase, the separation force will be the one of the three undocking springs (equation 6.10)[1]:

[1] In equation 6.10 the force was doubled following the indication of the standard. However, in this case, the factor of 2 will be applied during the final verification of the actuator.

$$\begin{aligned} F_{SEP} &= 3\,(UF_S \cdot k_{UD} \cdot US_{st}) \\ &= 3\,(1.2 \cdot 410\,N/m \cdot 0.033\,mm) \\ &= 48.71\,N \end{aligned} \tag{6.70}$$

While opening, friction becomes a resistance force. For this reason, the equation for calculating the opening force takes into account a friction coefficient three times greater than the nominal 0.6 value, i.e., 1.8.

$$F_{OPEN} = -\frac{F_{SEP}}{3}\frac{\sin\theta^* - \mu\cos\theta^*}{\cos\theta^* + \mu\sin\theta^*} = 24.02\,N \tag{6.71}$$

Conclusively, $24.02\,N$ is the force needed to open each hook.

6.7.3 Cam synthesis

Three cams machined on a common ring were selected as the transmission for the actuation of the hooks. This cam synthesis describes the design process of the three identical cams placed at $120\,deg$ to each other. These cams have to be desmodromic. The former means they must be able to actuate the hooks in both the closing and opening phases. An external and internal cam profile must be designed for this purpose. The easiest solutions for this type of cam consists in a groove machined out of the ring with a milling cutter of the same diameter of the roller follower. However, to allow the roller to rotate without sliding this solution must be avoided. Instead, an alternative solution with two rollers was adopted (see figure 6.43). In this solution, one of the rollers is in contact with the external profile of the cam while the other with the internal profile. With this configuration, both rollers roll without sliding.

From the available geometry and space, the followers of the cams, which in this case are the hooks of the blocking device, should travel a distance equal to $25\,mm$. The prime circle was selected to have a radius r_p equal to $212\,mm$. The major circle is therefore $237\,mm$. $15\,deg$ were selected to complete the travel.

The $25\,mm$ travel $S(\alpha)$, a function of the cam angle of rotation α, was divided into two phases. In the first one, the follower travels $20\,mm$. In the second one, the travel is equal to $5\,mm$. Each phase is accomplished in $7.5\,deg$. Starting from the major circle, the hooks will get close to the strikers on the female cone and, in the

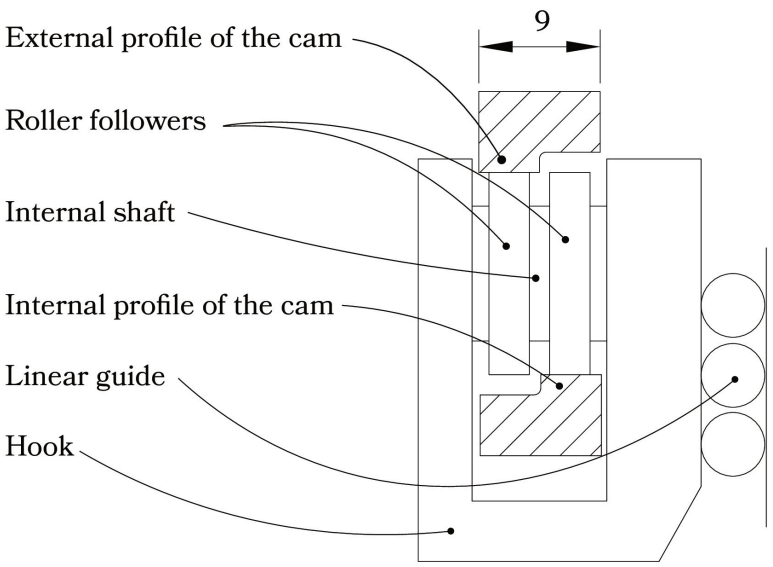

Fig. 6.43 Cam cross-section. The selected width of the cam is shown in the drawing

very last part of the travel, their contact will load the structures. For this reason, the velocity on that last part should be small, as well as the pressure angle.

During the first travel, the hook is practically unloaded; there is no contact force, the inertial forces are negligible, and the friction is very small due to the linear guides with recirculating ball bearings the hooks are mounted on. The velocity profile was selected to be triangular in this first phase.

During the second travel, the velocity profile was also selected triangular. The objective was to have a low velocity during the last part of the travel. As seen in figure 6.44, the triangular profile gives the lowest geometric velocity during the last degree of the cam rotation compared to the other trapezoidal velocity profiles. This may be seen at the base of the triangular profile. Considering the angular velocity of the cam constant as well as the resistance loads, the motor torque needed to actuate the cam will decrease with the reduction of the geometric velocity. For this reason, the triangular profile was chosen.

The whole geometric velocity profile $S'(\alpha)$, resulting from combining the first and second travels, may be seen in figure 6.45. Figure 6.46 shows the travel $S(\alpha)$ of the follower (hook).

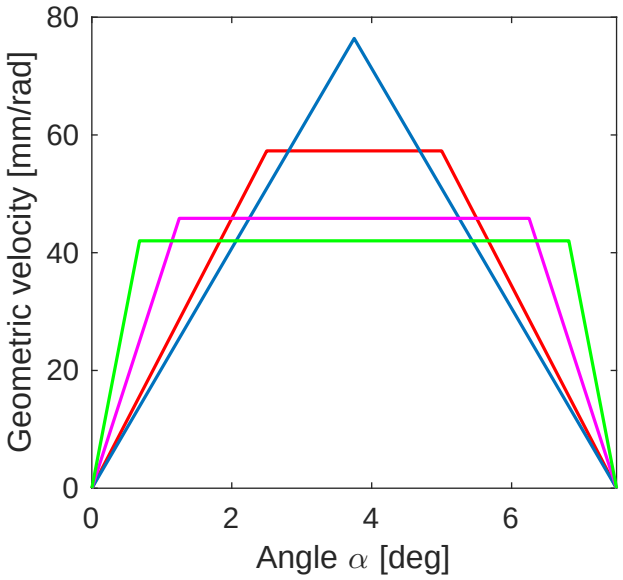

Fig. 6.44 Comparison between different trapezoidal velocity profiles

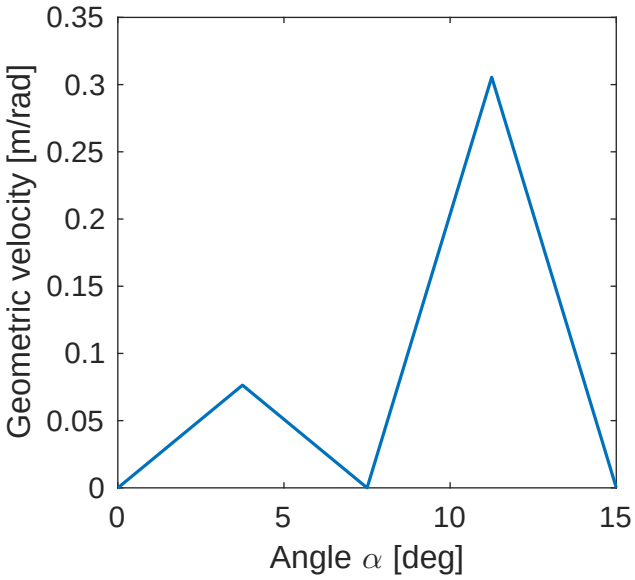

Fig. 6.45 Complete geometric velocity

In order to choose this profile some verifications must be performed. Several authors, such as [49], suggest that the pressure angle Φ should be less than $30\,deg$. Moreover, undercutting must be avoided. The pressure angle may be calculated using the following formula:

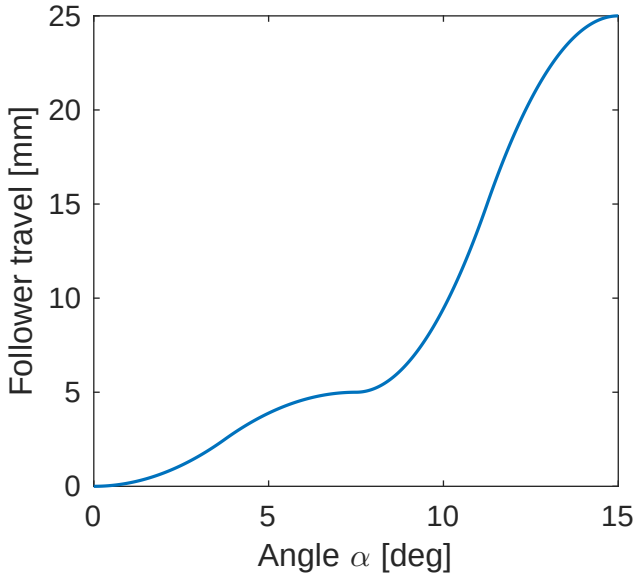

Fig. 6.46 Follower travel

$$\Phi = \arctan\left(\frac{S'(\alpha)}{r_p + S(\alpha)}\right) \tag{6.72}$$

Figure 6.47 shows that the pressure angle in the first travel surpasses $30\,deg$ but this happens during the unloaded part of the travel. Regarding the second phase, the maximum pressure angle is $19.59\,deg$.

Concerning undercutting, it is avoided when the minimum radius of curvature ρ_{min} is larger than the radius of the roller follower r_f:

$$|\rho_{min}| > r_f \tag{6.73}$$

The selection of the roller was conducted using the following specifications:

- For structural reasons the shaft where the rollers are mounted was selected to have a $10mm$ diameter. This implies that the roller bore diameter should be equal to $10mm$;
- The height of the cam was selected to be $9mm$ considering the available space. This means that the combined width of the two rollers should be less than

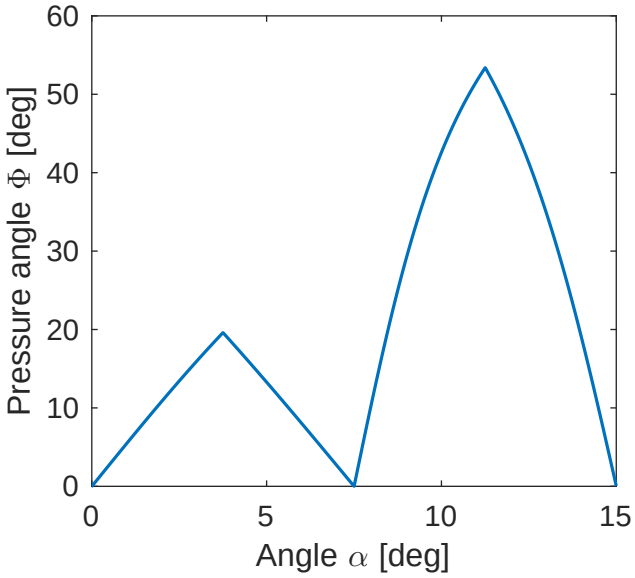

Fig. 6.47 Pressure angle

9*mm*. This is necessary because some spacers are needed between the roller followers;

- The roller external radius, r_f, should be as small as possible so as to avoid undercutting (see equation 6.73).

A suitable roller bearing was found with the characteristics shown in table 6.23.

Table 6.23 Characteristics of the roller follower

Supplier	AST
Bore diameter $[mm]$	10
Outer radius r_f $[mm]$	7.5
width $[mm]$	3
Material	52100 Chrome steel

Moreover, the formula of the radius of curvature of the pitch curve is the following:

$$\rho_{pitch} = \frac{\left[(r_p + S(\alpha))^2 + S'(\alpha)^2\right]^{\frac{3}{2}}}{(r_p + S(\alpha))^2 + 2S'(\alpha)^2 - S''(\alpha)(r_p + S'(\alpha))} \tag{6.74}$$

In equation 6.74, the term $S''(\alpha)$ indicates the geometric acceleration of the follower. ρ_{pitch} was computed and the result may be seen in figure 6.48. No undercutting was found: the modulus of the radius of curvature is always larger that the radius of the roller follower.

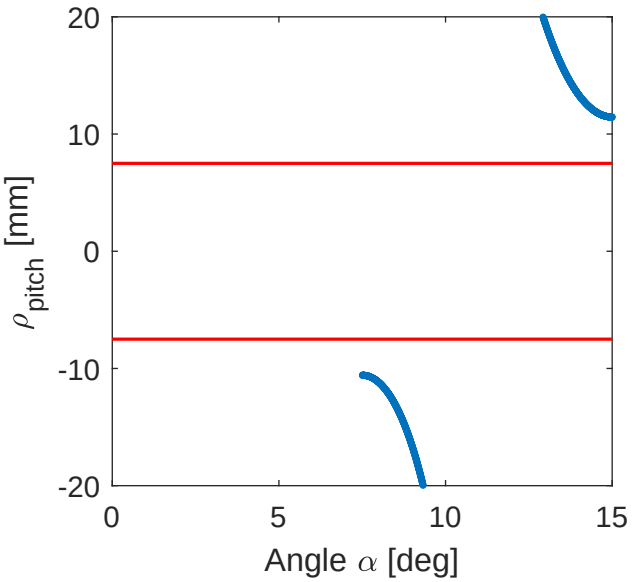

Fig. 6.48 Radius of curvature of the pitch curve. The solid red lines represent the radius of the roller follower

After the above-described verifications, the cam profile was traced in an XY plane. To do so, the travel was transformed from polar coordinates into Cartesian ones:

$$X_{coor} = S(\alpha)\cos\alpha \tag{6.75}$$

$$Y_{coor} = S(\alpha)\sin\alpha \tag{6.76}$$

In figure 6.49 the magenta line represents the pitch curve of the cam. The blue circles represent several positions of the roller followers, while the internal and external profiles of the cam may be seen in black.

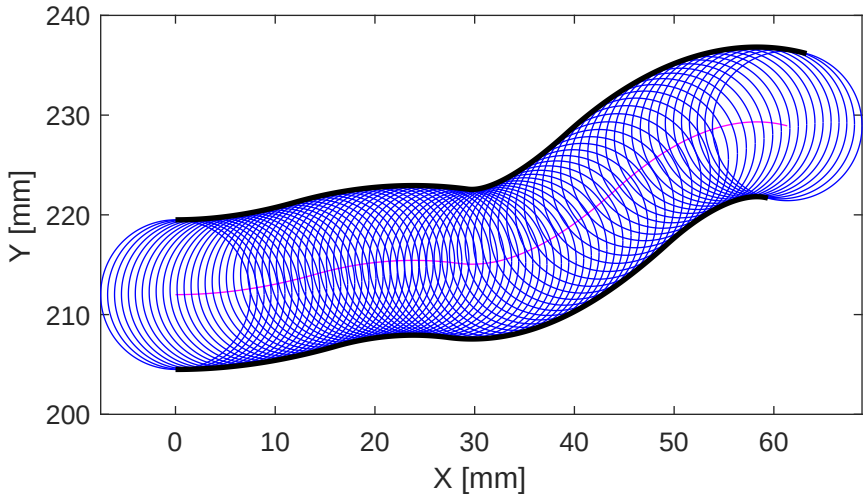

Fig. 6.49 Cam profile

The cam design was translated into a 3D model (figure 6.50). It may me be seen that a couple of $1.5\,deg$ constant radius parts were added to the profile for a total angular travel, α_{tot}, equal to $18\,deg$. These parts were added to allow the motor to accelerate and decelerate outside the travel of the hook.

6.7.4 Spur gear transmission

In order to rotate the ring with the cams, a spur gear transmission was selected. Given the available space, and the dimension of the ring (the prime radius of the cams is $212\,mm$) a small pinion combined with an internal spur gear were selected (figure 6.51). The internal gear is bolted to ring with the cams forming a rigid body.

Regarding the pinion, considering a 20-degree pressure angle α_p and a null profile shifting x_s, the minimum number of teeth z_{min} is given by the following formula:

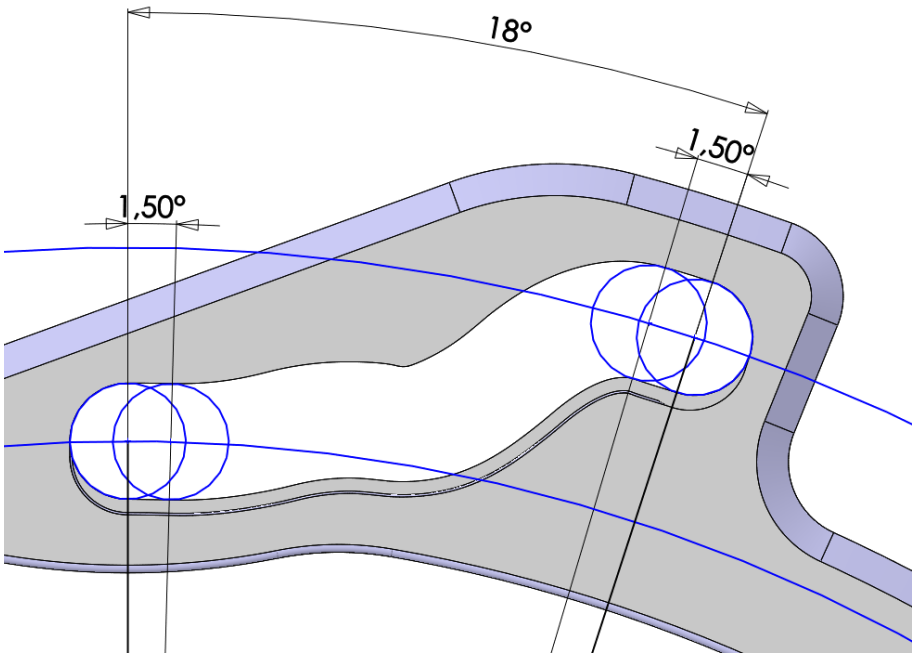

Fig. 6.50 3D model of one of the cams

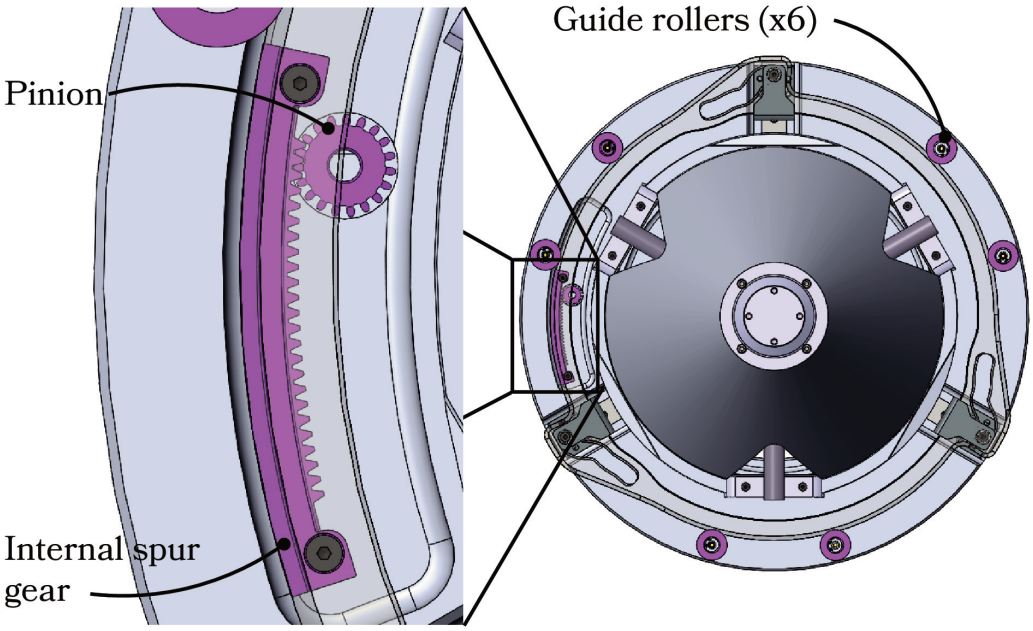

Fig. 6.51 Transmission system for the actuation of the cams

$$z_{min} = \text{ceil}\left(\frac{2\,(1-x_s)}{\sin^2\alpha_p}\right) = 18 \tag{6.77}$$

A unitary gear module m was selected. For simplicity, a suitable commercial pinion was individuated. Table 6.24 shows the characteristics of the pinion.

Table 6.24 Specifications of the pinion

Module m $[mm]$	1
Number of teeth z_1 $[-]$	19
Pitch diameter d_1 $[mm]$	19
Major diameter d_{a1} $[mm]$	21
Face width b $[mm]$	8

If a stepper motor is selected, it is possible to actuate the ring in an open loop fashion counting the steps of the motor, N_{STEP}. Normally, if no microstepping is considered, the minimum angular rotation rot_{STEP} of a stepper motor is $1.8\,deg$. The number of steps needed to complete the cam total angular rotation α_{tot} will depend on the pitch diameter d_2 of the internal spur gear as follows:

$$N_{STEP} = \frac{\alpha_{tot}}{rot_{step}} \frac{d_1}{d_2} = 10 \frac{d_2}{19\,mm} = 10 \frac{z_2}{19} \tag{6.78}$$

To select d_2 it is possible to start from the cam prime diameter $424\,mm$ and find a smaller integer diameter that generates an integer number of steps. With 418 teeth the transmission ratio τ^{SPUR} becomes 22 and the number of steps 220. The characteristics of the internal gear are shown in table 6.25.

Table 6.25 Specifications of the the internal spur gear

Module m $[mm]$	1
Number of teeth z_2 $[-]$	418
Pitch diameter d_2 $[mm]$	418
Major diameter d_{a1} $[mm]$	416
Root diameter d_{t1} $[mm]$	420.5
Face width b $[mm]$	8

6.7.5 Step motor sizing

As stated before, a stepper motor was selected as the type of actuator for the hard docking system. This motor has to overcome the inertial forces during acceleration as well as the force needed to open the hooks. If a redundant system is considered, the motor also has to overcome the detent torque of the redundant actuator as well as its rotational inertia.

The ring with the cams has to rotate $18\,deg$ (α_{tot}). Since the cams have a couple of resting sections of $1.5\,deg$ (α_{res}), the system may be accelerated and decelerated exploiting those sections. Moreover, to complete the travel, $60\,s$, t_{tot}, were considered. With this data, a trapezoidal velocity profile may be generated. First of all, the angular quantities have to be rewritten in the motor shaft. The total motor rotation is

$$\alpha_{tot}^{stp} = \tau^{SPUR}\alpha_{tot} = 22 \cdot 18\,deg = 396\,deg \tag{6.79}$$

and the resting angle of the cam becomes

$$\alpha_{res}^{stp} = \tau^{SPUR}\alpha_{res} = 22 \cdot 1.5\,deg = 33\,deg \tag{6.80}$$

The maximum angular velocity of the stepper motor ω_{max}^{stp} is then calculated using the following formula:

$$\omega_{max}^{stp} = \frac{1}{t_{tot}}\left(\alpha_{tot}^{stp} + 2\alpha_{res}^{stp}\right) = 7.70\,deg/s \tag{6.81}$$

and the maximum motor acceleration as follows:

$$\dot{\omega}_{max}^{stp} = \frac{\left(\omega_{max}^{stp}\right)^2}{2\alpha_{res}^{stp}} \tag{6.82}$$

Figure 6.52 shows the angular position, velocity and acceleration profiles of the stepper motor.

To calculate the inertial torque, the inertia of the ring plus the internal spur gear J^{ring} was estimated assigning the selected materials to the 3D models and using the internal routines of the CAD software. The inertia found was $3.56 \times 10^{-2}\,kgm^2$.

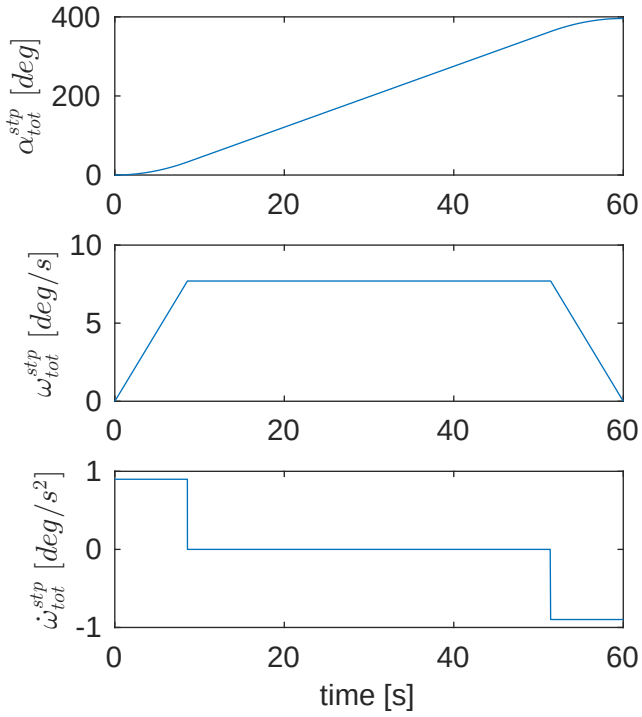

Fig. 6.52 Angular position, velocity, and acceleration profiles of the stepper motor

With this data and the maximum acceleration, part of the inertial torque applied on the stepper motor may be estimated as follows:

$$T_I = \frac{1}{\tau^{SPUR^2}} U F_I J^{ring} \dot{\omega}_{max}^{stp} = 1.27 \times 10^{-6} Nm \tag{6.83}$$

Regarding the force to open hooks F_{OPEN}, it has to be translated into motor torque as well. The torque needed to overcome the force applied by the three followers of the cams may be calculated using the following formula

$$T_{OPEN} = \frac{1}{\tau^{SPUR}} \frac{3}{\eta_{cam}} \frac{F_{OPEN} V^{FOLL}}{\omega^{ring}} \tag{6.84}$$

where η_{cam} is the efficiency of the cam, V^{FOLL} is the linear velocity of the follower of the cam, and ω^{ring} is the angular velocity of the ring during the travel of the followers. Since the velocity of the follower is equal to the angular velocity of the ring times the geometric velocity of the follower, equation 6.84 may be rewritten as follows:

$$T_{OPEN} = \frac{1}{\tau^{SPUR}} \frac{3}{\eta_{cam}} F_{OPEN} S'(\alpha) \tag{6.85}$$

It is clear that to calculate the maximum opening torque it is necessary to find the maximum geometric velocity during the loaded phase of the follower opening. Using the CAD model of the system as a reference (figure 6.53), it may be seen that the total travel under the load of the incline is $7.09\,mm$.

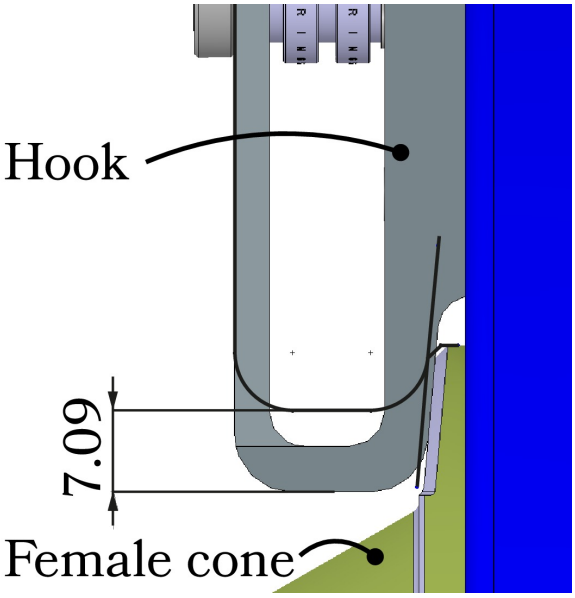

Fig. 6.53 Travel of the follower (hook) under the incline load

Figure 6.54 shows that the geometric velocity when the follower has been opened $7.09\,mm$ is equal to $0.1398\,m/rad$.

Using the estimated maximum geometric velocity, and assuming a cam efficiency equal to 80%, the maximum opening torque may be calculated recalling equation 6.85:

$$T_{OPEN} = \frac{1}{22} \frac{3}{0.8} 24.02N \cdot 0.1398m/rad = 0.57\,Nm \tag{6.86}$$

With the values of T_I and T_{OPEN} a first estimation of the torque needed T^{stp} may be performed:

$$T^{stp} = 2\,(T_I + T_{OPEN}) = 1.14\,Nm \tag{6.87}$$

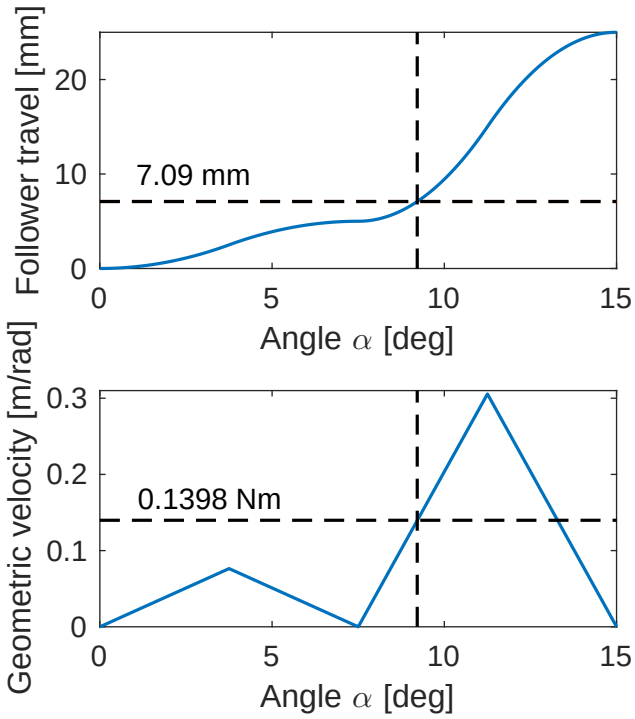

Fig. 6.54 Maximum geometric velocity during the loaded phase of the hooks aperture

The Kollmorgen stepper motor CTM21NLF25FAA00 was considered as a suitable actuator. The characteristics of the actuator are shown in table 6.26. Moreover, figure 6.55 shows the torque curve of the motor.

Table 6.26 Characteristics of the CTM21NLF25FAA00 stepper motor

Supplier	Kollmorgen
Holding torque $[Nm]$	1.84
Detent torque T_{det}^{stp} $[Nm]$	0.092
Rotor inertia J^{stp} $[kgm^2]$	2.5×10^{-5}
Driver supply $[V]$	24

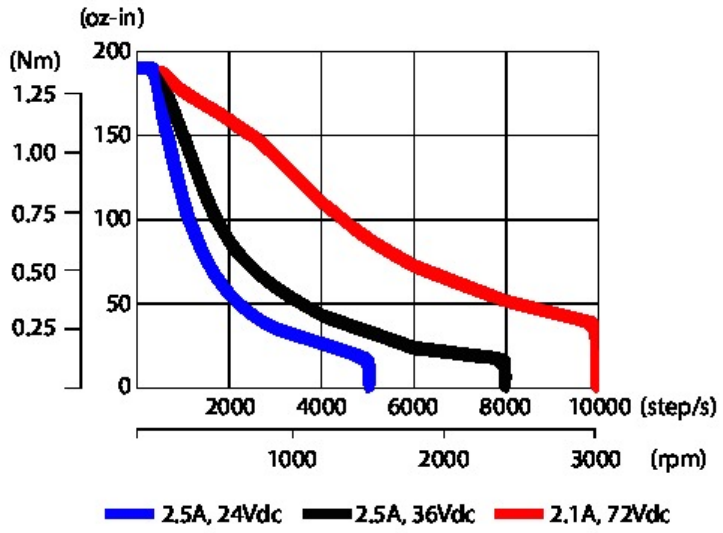

Fig. 6.55 Torque vs. speed curve of the stepper motor ($24\,V$)

Step motor verification

This subsection will describe the final verification of the stepper motor in accordance with the ECSS standards.

Inertial effects The acceleration of the motor and the ring produces an inertial torque. Since a redundant system with two motors was selected, the inertia of the motor was doubled

$$2J^{stp}\dot{\omega}^{stp}_{max} = 7.84 \times 10^{-7}\,Nm \tag{6.88}$$

Furthermore, the acceleration of the ring generates the following torque:

$$\frac{J^{ring}}{\tau^{SPUR^2}}\dot{\omega}^{stp}_{max} = 1.15 \times 10^{-6}\,Nm \tag{6.89}$$

External force As shown in equation 6.86, the torque to open the hooks, T_{OPEN} is equal to $0.57\,Nm$.

Detent torque of the redundant motor The detent torque of a stepper motor is the torque required to rotate the output shaft of the motor with no current applied to the windings. The detent torque of the redundant motor has to be overcome by the active one.

Finally, table 6.27 summarizes the verification process.

Table 6.27 Stepper motor verification

Type of resistance	Component of resistance	Value at origin	Value at motor shaft $[Nm]$	ECSS uncertainty factor	Final resistance $[Nm]$
Inertia	Motor	$0.00mNm$	0.00	1.1	0.00
	Ring	$0.00mNm$	0.00	1.1	0.00
External Force		$72.06N$	0.57	1	0.57
Detent torque		$0.09Nm$	0.09	1	0.09
Sum					0.66
2xSum					1.33

Figure 6.56 shows that the needed torque, $1.33\,Nm$, is smaller than the stepper motor torque at the required speed, $1.38\,Nm$. The former means that the stepper motor is able to rotate without losing steps.

6.8 Final functional verification

The results of section 6.5 assessed in a preliminary fashion the functioning of the mechanism together with the active control system. They also showed the suitability of the actuators of the stage during the alignment phase of the maneuver. However, those results were obtained using a model that considered a planar changing of the poses of the spacecraft. For this reason, a complete 3D model was developed in close collaboration with TAS-I. This model differs from the previous one in several aspects besides the 3D environment. Firstly, there are several contact constraints between the components of the male and female halves. Secondly, both the in-series controlled

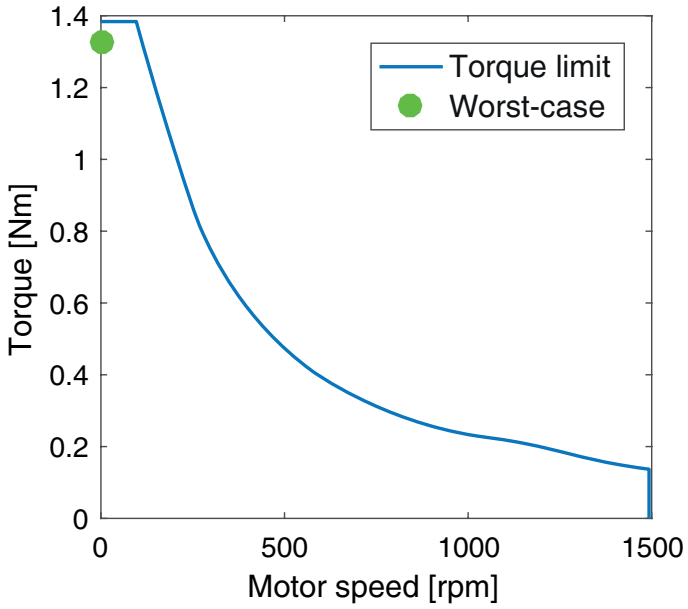

Fig. 6.56 Stepper motor torque using the stepper controller P70530 at 24V

axes of the Cartesian stage were included. Thirdly, the latching system of the probe as well as its interaction with the female socket were implemented to confirm soft docking. Finally, the addition of the damping system inside the female cone allowed verifying the suitability of the docking mechanism to safely dissipate the residual kinetic energy. This section will describe the 3D model, its implementation, and will present the results of the simulations.

6.8.1 Multibody Model and implementation

The 3D multibody model of the docking maneuver was implemented in a co-simulation between Altair Hyperworks and solidThinking Activate. On the one hand, Hyperworks simulated the interaction between the mechanical parts. On the other hand, the control system and the electrical response of the motors were implemented in Activate.

Model of the mechanical parts

As stated before, the interactions between the mechanical parts were implemented in Hyperworks. The spacecraft were modeled as lumped masses (figure 6.57). The

space tug was attached to the interface plate of the male half. On the other hand, the female cone was rigidly connected to each of the targets. The inertial properties of the spacecraft are outlined in chapter 3.

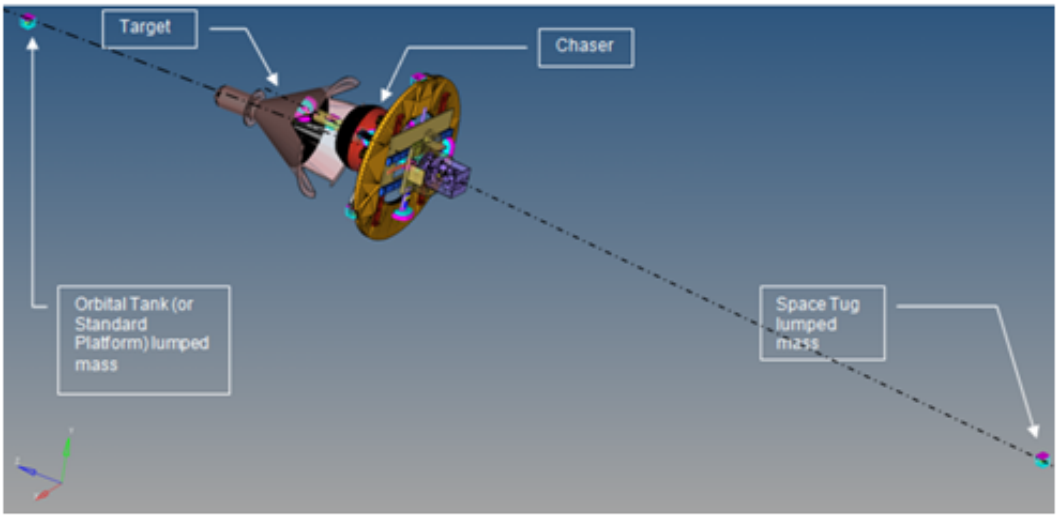

Fig. 6.57 Model of the mechanism halves attached to the spacecraft

The different analyses shown in this chapter led to the improvement of the preliminary models shown in figures 6.4 and 6.5. The improvement regarded the detailed geometric definition of the interfaces and the addition of all the missing mechanical subsystems. In this regard, figures 6.58 and 6.59 depict the 3D models of the updated halves of the mechanism used during these multibody simulations.

Once the CAD model of the male half was loaded into the multibody software, the joints between its components were added as well as the spring-damper elements. Firstly, a prismatic joint was used to link the cap and the probe. Between these components, the cap spring was included (figure 6.60). Moreover, the latches were hinged to the probe. In this case, equivalent torsional springs were connected between each latch and the probe to simulate the preloaded leaf springs that arm the capture system (figure 6.60).

Secondly, another prismatic joint allows the relative translation between the base of the probe and the male cone. A single equivalent undocking spring was connected to both the bodies (figure 6.61). The stiffness of this spring is equal to three times the stiffness of one undocking spring (table 6.1).

Finally, the probe was mounted on the furthermost slide of the XY stage by using a universal joint. Each of the traction springs is connected to both the probe and a

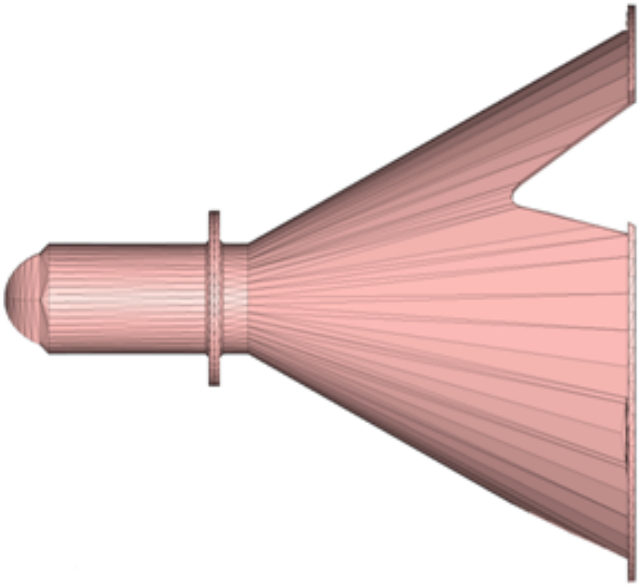

Fig. 6.58 CAD model of the female half used during the simulations

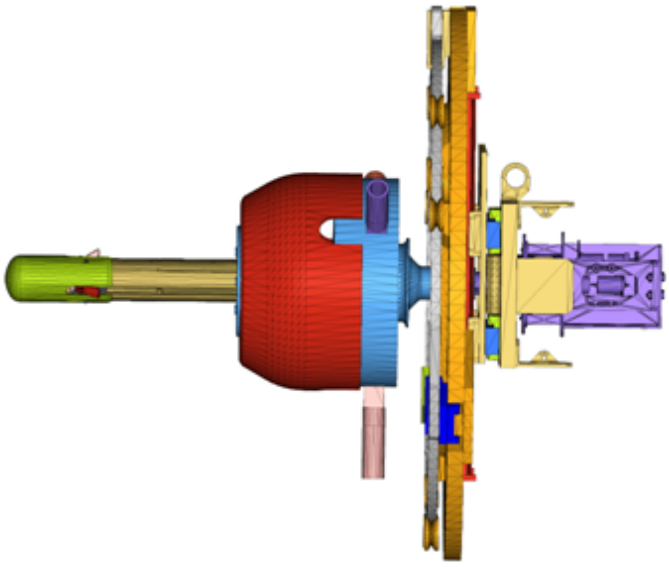

Fig. 6.59 CAD model of the male half used during the simulations

support bolted to the slide (figure 6.62). Table 6.28 shows the values of the stiffness values of the elastic elements discussed so far. Damping elements were added in parallel to the springs to consider the losses of these mechanical elements.

Regarding the XY stage, figure 6.63 shows its implementation inside the simulation environment. The Y slide is mounted on the interface plate by using a prismatic

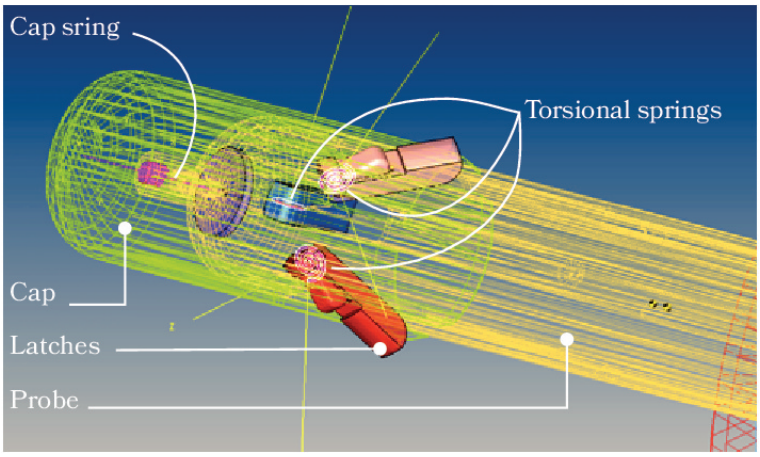

Fig. 6.60 Cap and latches springs

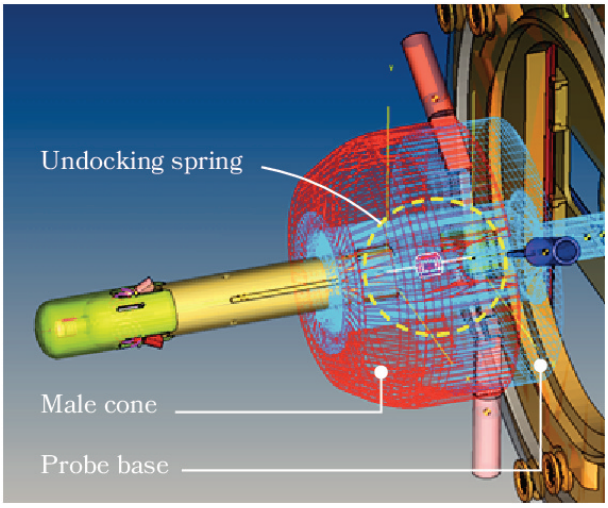

Fig. 6.61 Undocking spring

Table 6.28 Spring-dampers of the male half

Conponent	Q.ty	Stiffness	Damping
Cap spring	1	$37.15\,N/mm$	$0.05\,Ns/mm$
Latch torsional spring	3	$48.03\,Nmm/deg$	$10\,Nmms/deg$
Undocking spring	1	$1.23\,N/mm$	$0.08\,Ns/mm$
Traction spring	4	$11.23\,N/mm$	$5.43\,Ns/mm$

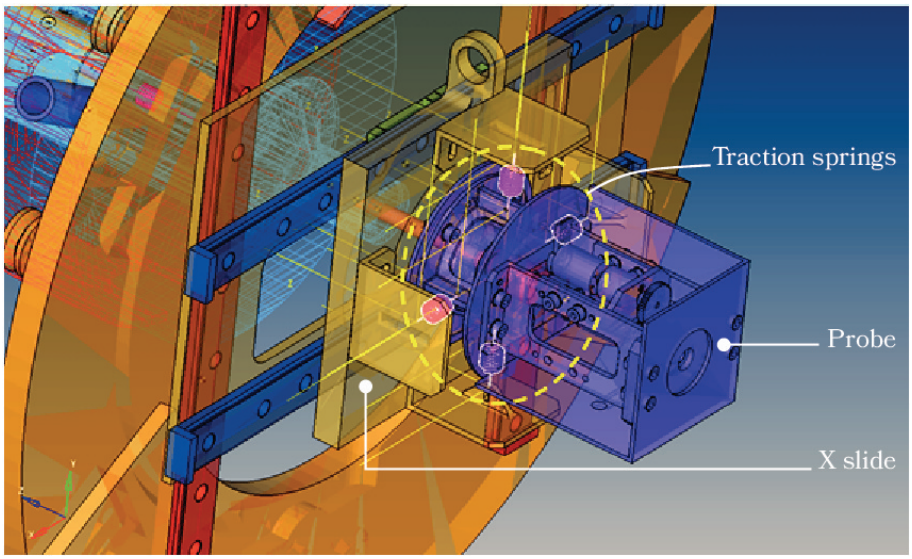

Fig. 6.62 Rear traction springs of the probe

joint that represents the linear guides. On the other hand, the actuator of the Y slide was modeled by using two parallel cylinders linked to each other by a coupler joint. They were also linked to the support plate by revolute joints. The value of the transmission ratio of the coupler joint was equal to 19 : 1. The polar inertias of the cylinders are equal to the inertia of the ball screw and the inertia of the servomotor (motor plus gearhead). A screw joint with a lead equal to 4 *mm* was introduced between the ball screw cylinder and the Y slide. Similarly, the X slide was mounted orthogonally to the Y slide by a prismatic joint. The mechanical components of the X actuator were modeled analogously to the Y actuator. However, in this case, the cylinders were mounted on the Y slide and the ball screw was connected to the X slide.

The torques generated by the windings of the motors and estimated using solidThinking Activate were directly applied to the cylinders that represent the motor rotors.

The complete female cone was imported into the simulation software as a single rigid body. Subsequently, a disk that represents the interface of the damping system was linked to the female socket through a prismatic joint (figure 6.64). A spring damper was attached to both the disk and the female cone with the characteristic shown in equations 6.64 and 6.66.

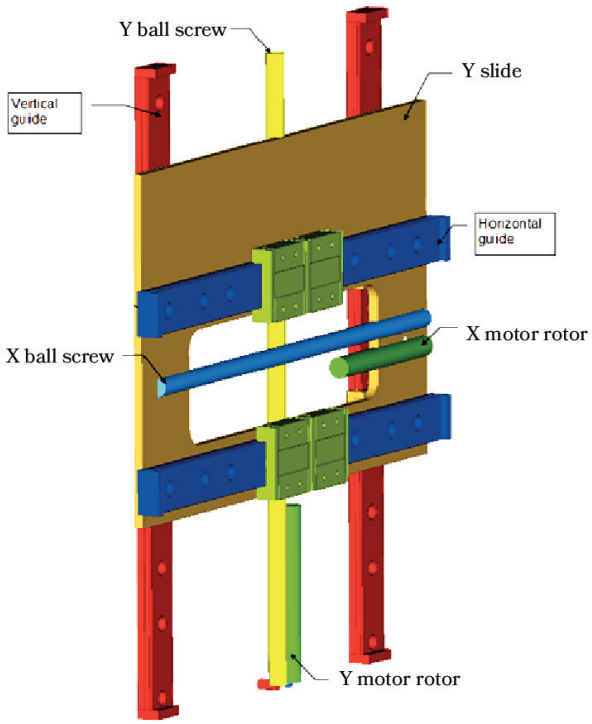

Fig. 6.63 Model of the Cartesian stage

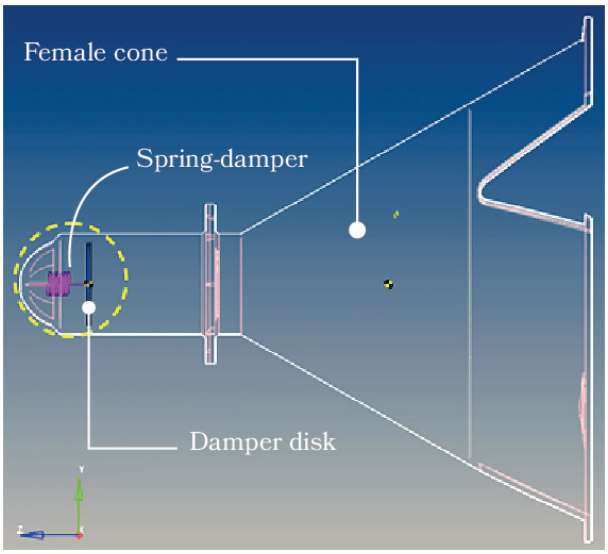

Fig. 6.64 Damper in the female cone

The last aspect of the multibody model is the contact constraints between the components of the mechanism. The constraints included the following pairs of components:

1. Male cone and female cone;
2. The roll alignment bars and the v-shaped guides of the female cone;
3. the cap and the female cone;
4. the cap and the damping system interface disk;
5. the probe latches and the female cone.

For instance, figure 6.65 shows the mesh used to identify the contact between the female and male cones.

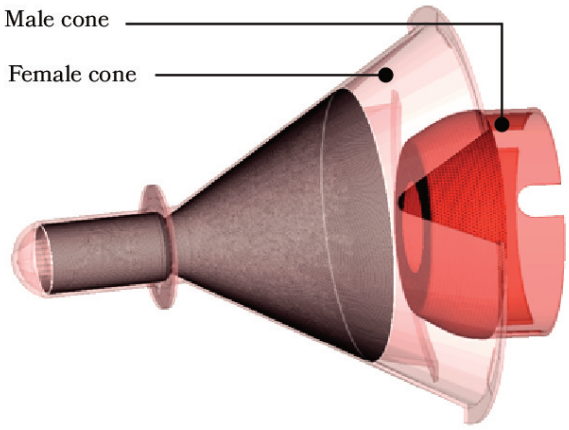

Fig. 6.65 Contact between the male and female cones

6.8.2 Model of the control system and the electric motors of the XY stage

The models of the control system and the electric motors were implemented in solidThinking Activate. Inside this simulation environment, block diagrams are built using a visual programming language.

The multibody (MB) simulation was introduced in Activate as a single block `MB PLANT` (figure 6.66). This plant generates as output three groups of results: `XParam`, `YParam`, and `latch_rot`. `XParm` contains the angular position and velocity of the motor rotor of the X actuator, `APOS_X`, and `OMEGA_X`. It also contains the rotation of the probe about the axis perpendicular to the X actuator, `AY` (figure 6.67). `YParam`

contains the angular position and velocity of the motor rotor of the Y actuator, `APOS_Y` and `OMEGA_Y`, and the probe rotation about the X axis of the stage, `AX`. Finally, `latch_rot` contains the rotation in degrees of each of the probe latches.

The inputs of the `MB PLANT` are the torques applied to the motor rotors necessary to maintain the probe axis aligned with the spacecraft longitudinal axis, `TorqueX`, and `TorqueY`. The following paragraphs will explain how these torques are created.

The velocity reference values of the motors are created inside the `SET GENERATION` blocks. These blocks have as inputs the slide position and probe rotation. As an example, figure 6.68 shows the contents of the `X SET GENERATION` block. Initially, the needed slide displacement is calculated as in equation 6.54. However, a deadband is applied to the probe rotation within the interval $(-0.2\,deg, 0.2\,deg)$. This deadband is necessary to avoid unwanted displacements produced by mounting errors or mechanical vibrations. Subsequently, the current slide position is added and saturated based on the slide maximum stroke. The current position is then subtracted to calculate only the relative displacement. The velocity set is generated by multiplying by the velocity gain (equation 6.55) and saturating using the planetary gearhead velocity limit (table 6.14).

The velocity sets feed the `CONTROLLER` blocks. Inside these blocks, the model shown in figure 6.23 is implemented. The output of these blocks are the armature tensions of the motors. As stated in section 6.5.2, the EC motors were modeled using an equivalent model of a DC motor. To these tensions, the back-EMF are subtracted. The result is fed to the transfer function of the electric circuit of the motor (equation 6.50). The motor torque is then produced multiplying the torque-generating current by the torque constant (equation 6.51). Finally, the friction torques are subtracted to generate `TorqueX` and `TorqueY`. The friction torque is equal to the torque produced by the preload of the ball screw divided by the transmission ratio of the planetary gearhead.

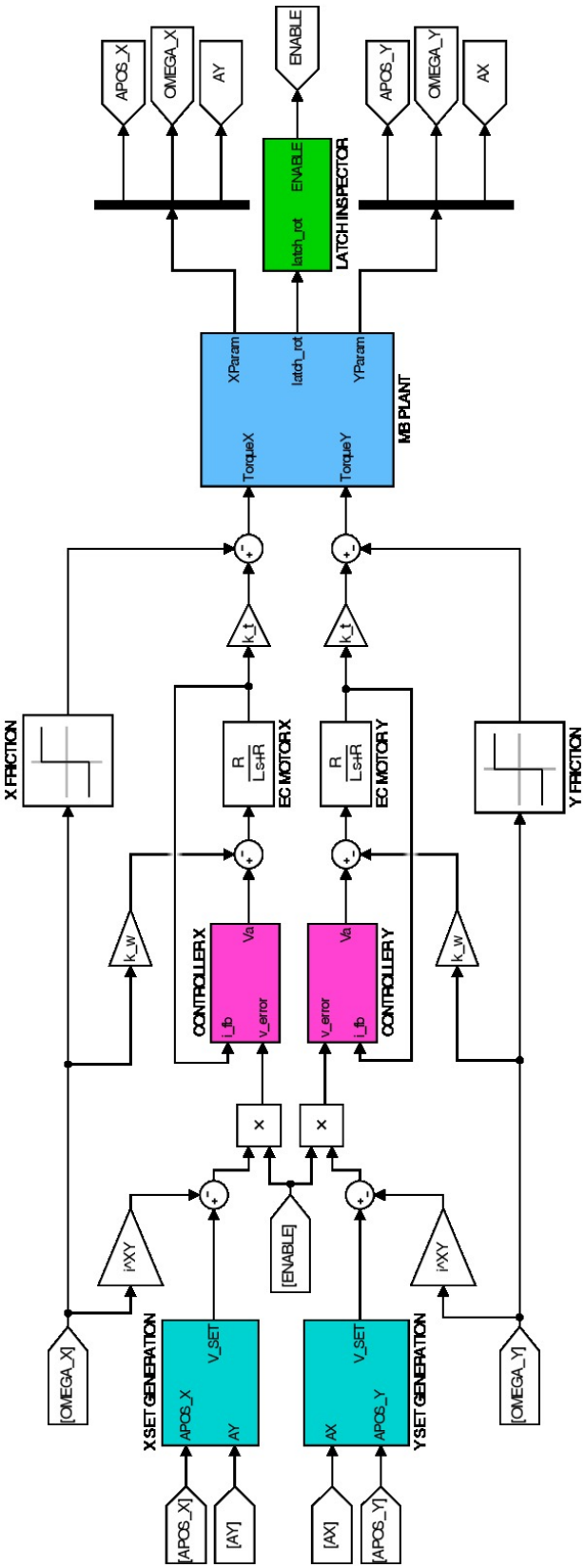

Fig. 6.66 Block diagram of the control system

However, as seen in figure 6.66, the Boolean variable `ENABLE` may modify the velocity sets. At the beginning of the simulation, this variable is equal to `1`. Its value is then governed by the block `LATCH INSPECTOR`. This block compares the latches rotations against a threshold equal to 0.087 *rad* (5 *deg*). If the rotation of at least one of the latches is larger than this threshold, the value of `ENABLE` is set to `0`. The latches rotation means they have started to interact with the female socket. Once this happens, the alignment phase is completed and the slides must stop. If `ENABLE` is `0` the velocity set becomes $0\,mm/s$ which means the motor torques will maintain the slides in their current position.

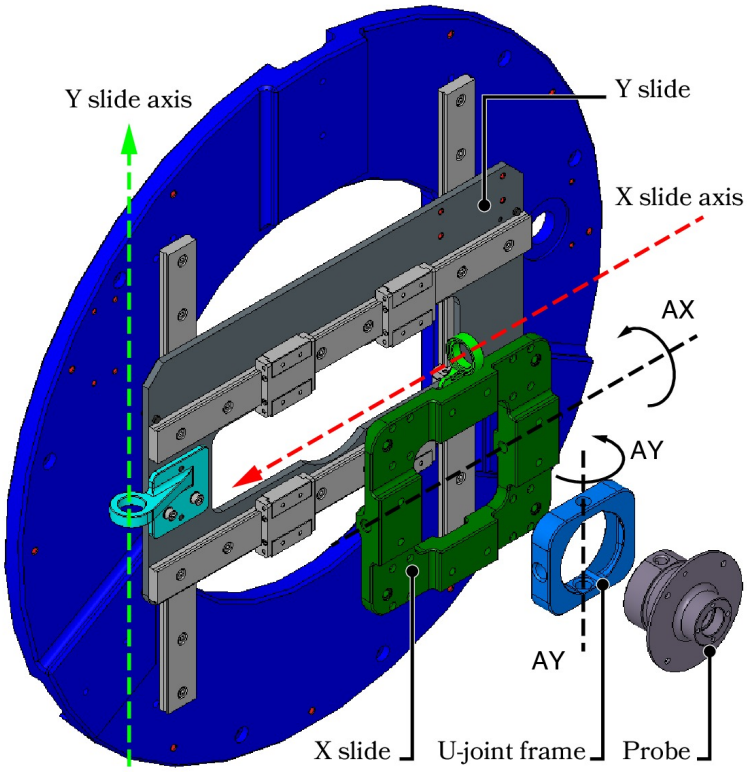

Fig. 6.67 Axes of the universal joint: `AX` and `AY`

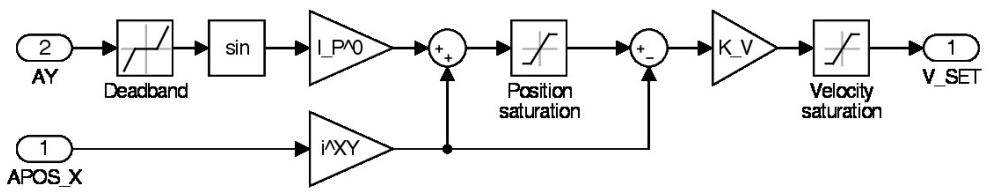

Fig. 6.68 `X SET GENERATION` block

6.8.3 Model results

Several initial conditions and mass combinations were tested during the simulation campaign. Howevere, only two testing cases will be reported herein. The first case, Case 1, considered a maneuver before refueling. The space tug is in Configuration A ($1700\,kg$) and has to dock with the orbital tank ($6000\,kg$). The second case, Case 2, takes into account the maneuver after refueling in which the $3500\,kg$ space tug docks with a $2000\,kg$ satellite platform before the orbit raising.

The relative linear and angular misalignments used in both cases are expressed in table 6.29. These values define the relative pose of the reference systems AH and PH w.r.t. PH (figure 6.69). AH is positioned at the furthermost part of the probe and shares the same orientation as TU. Regarding PH, it is positioned at the apex of the female cone. In each case, the matrix that represents the relative orientations of PH relative to TA, ${}^{TA}A_{PH}$, will be indicated.

Table 6.29 Initial relative linear and angular misalignments between the mechanism halves used in Case 1 and 2

Position misalignment	Lateral Y	$-50\,mm$
	Lateral Z	$50\,mm$
Angular misalignment	Roll	$3\,deg$
	Pitch	$-3\,deg$
	Yaw	$-3\,deg$

Case 1

As stated before, this case considers the orbital tank, and the space tug in Configuration A. Figure 6.70 shows the satellites initial configuration. The figure also shows the world coordinate system used during the simulation. The relative orientation between the target reference system and the reference system of the passive mechanism half is the following:

$$ {}^{TA}\mathbb{A}_{PH} = \begin{pmatrix} 1 & 0 & 0 \\ 0 & 0 & -1 \\ 0 & 1 & 0 \end{pmatrix} \tag{6.90} $$

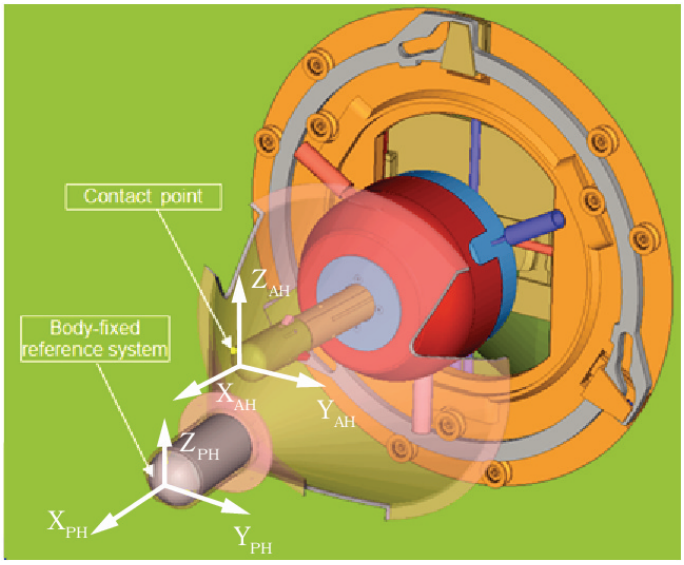

Fig. 6.69 Initial relative pose between the mechanism halves

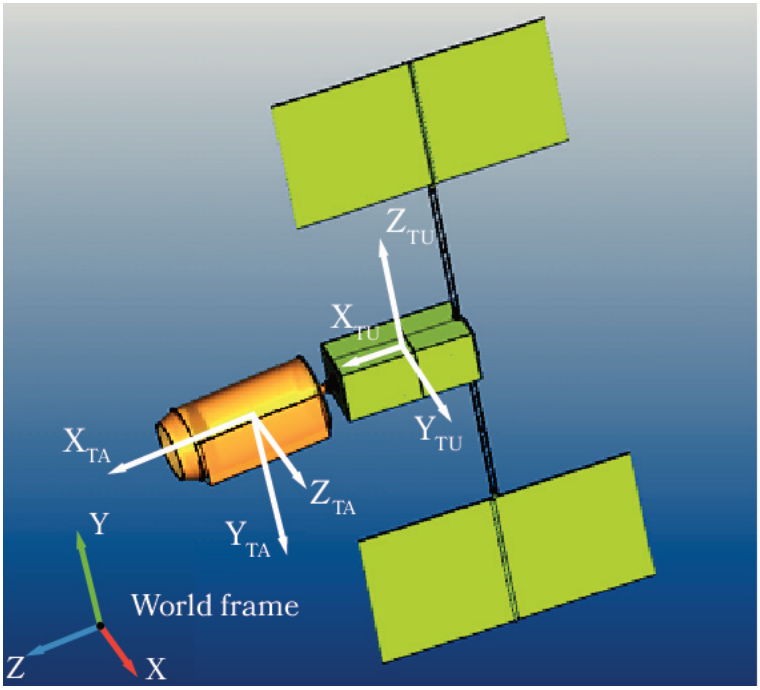

Fig. 6.70 Case 1 initial configuration

Furthermore, the initial relative velocities between TU and TA expressed in TA are shown in table 6.30.

The results of this simulation are the absolute velocities of the spacecraft, the rotation of the probe latches, the velocities of the controlled slides, the contact force

Table 6.30 Case 1 initial relative velocities

Relative velocity	Lateral Y	$-10\,mm/s$
	Lateral Z	$-10\,mm/s$
	Longitudinal X	$30\,mm/s$
Relative angular rate	ω_X	$0.1\,deg/s$
	ω_Y	$0.1\,deg/s$
	ω_Z	$-0.1\,deg/s$

between the cap and the female cone, and the rotations of the probe about the axes of the universal joint.

Figure 6.71 depicts the absolute velocities of the satellites relative to the World frame as generated by HyperWorks. This figure shows that up to the contact between the probe and the damper at approximately $5.6\,s$, the relative longitudinal velocities of the spacecraft decreases only by 7%. This component of the relative velocity vector is useful to guarantee the penetration of the latches inside the socket. Moreover, up to that point, the lateral velocities along X and Y decrease respectively by 40% and 60%. These reductions have a positive effect since the lateral velocities only worsen the conditions of the maneuver.

Another feature worth mentioning about figure 6.71 is the effect of the damping system. At approximately $5.6\,s$, the value of the Z velocity of the chaser plunges while the velocity of the target rises due to the exchanged forces through the damper. However, the presence of the spring in the damping system separates the bodies. This separation makes the target travel faster along Z at a rate equal to $3.9\,mm/s$ up to the collision between the latches and the internal wall of the female socket. All this means that the damping effectively dissipates the kinetic energy associated with the relative longitudinal motion between the satellites. Finally, the final absolute longitudinal velocity of the stack (target plus chaser) is equal to $6.6\,mm/s$ which agrees with the formulation of inelastic collisions.

Figure 6.72 shows the rotations of the probe latches. This figure shows that the rotation threshold of the latches is reached at $5.23\,s$. At this instant both the slides of the XY stage are blocked in their current position. The figure also shows that soft

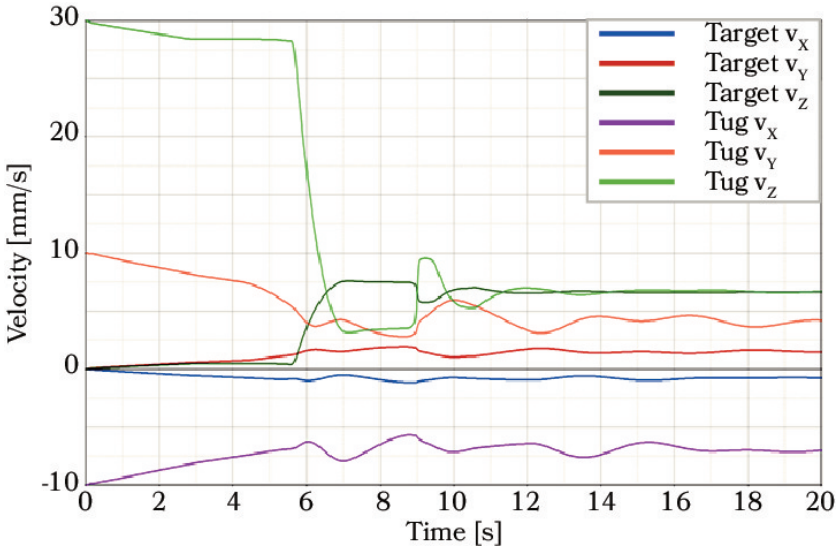

Fig. 6.71 Absolute velocities of the spacecraft w.r.t. the world frame during Case 1

docking occurs at 7.82 *s*: the latches reopen turning to their nominal angular position characterized by a zero rotation.

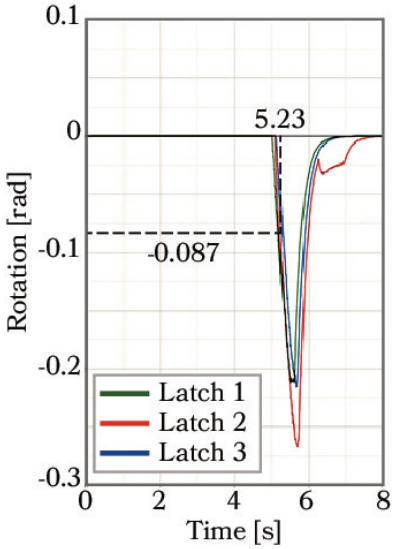

Fig. 6.72 Rotations of the spring-loaded latches during Case 1

The velocities of the controlled axes of the stage (figure 6.73) show the slides reached their software end stop, i.e., the value of the position saturation before 5.23 *s* (latches rotation threshold). However, this did not prevent the soft capture from occurring as shown in figures 6.71 and 6.72. Instead, the system behaves as expected: the motion of the slides maintains the exchanged force (figure 6.74) at

a low level allowing the longitudinal relative velocity to stay at an almost constant value throughout the alignment phase.

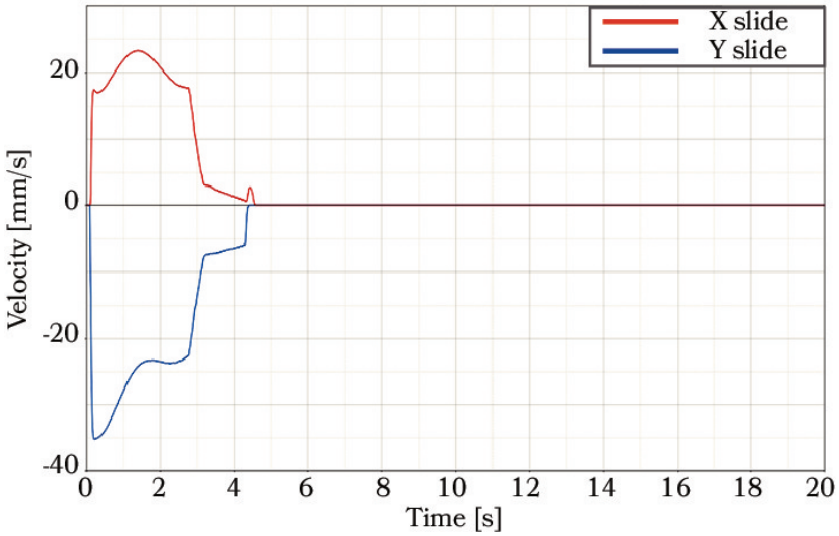

Fig. 6.73 Velocities of the axes of the XY stage during Case 1

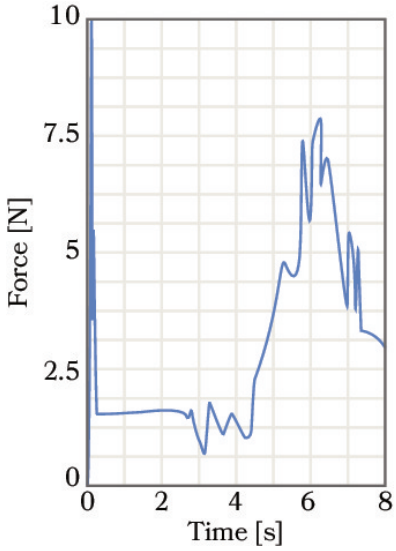

Fig. 6.74 Contact force during Case 1

The rotations of the probe about the the axes of the universal joint, AX and AY, (figure 6.75) are caused by the exchanged force. As stated before, the traction springs at the rear end of the probe tend to realign the probe with the longitudinal axis of the chaser spacecraft causing, in combination with the cap spring, the development of the contact force. Figure 6.75 depicts that the control system works properly up to

the saturation of the slides positions. Initially, the rotations of the probe are contained but nonetheless larger than the imposed deadband. However, during the last part of the slides travel, the angles are controlled to a value slightly greater than $0.2\,deg$.

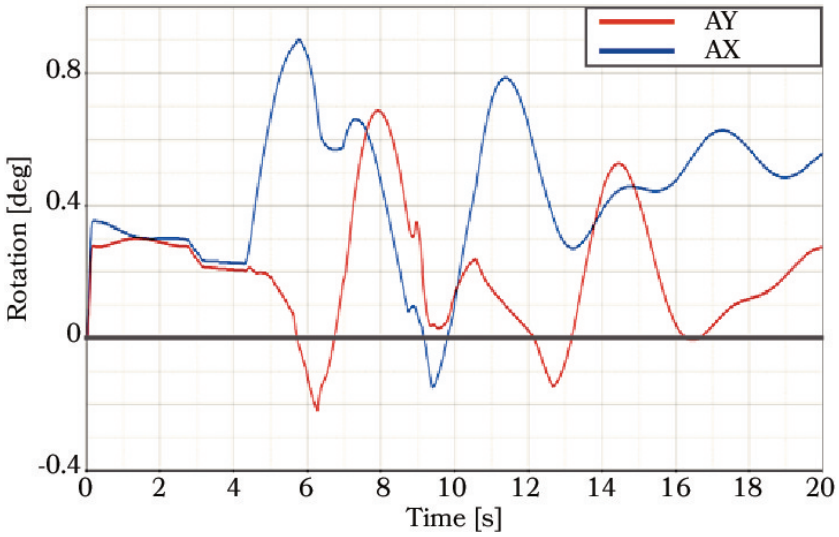

Fig. 6.75 Rotations of the probe about the axes of the universal joint during Case 1

Case 2

This case considers a docking operation between the space tug in configuration B and the satellite platform (figure 6.76). In this case, The relative orientation between the target reference system and the reference system of the passive half is the following:

$$^{TA}\mathbb{A}_{PH} = \begin{pmatrix} 1 & 0 & 0 \\ 0 & 0 & 1 \\ 0 & -1 & 0 \end{pmatrix} \tag{6.91}$$

The initial relative velocities between TU and TA expressed in TA are shown in table 6.31.

Also, in this case, the results reported regarding Case 2 are the absolute velocities of the spacecraft, the rotation of the probe latches, the velocities of the controlled slides, the contact force, and the rotations of the probe.

Figure 6.77 depicts the absolute velocities of the satellites relative to the World frame during Case 2. The figure shows that up to the contact between the probe and

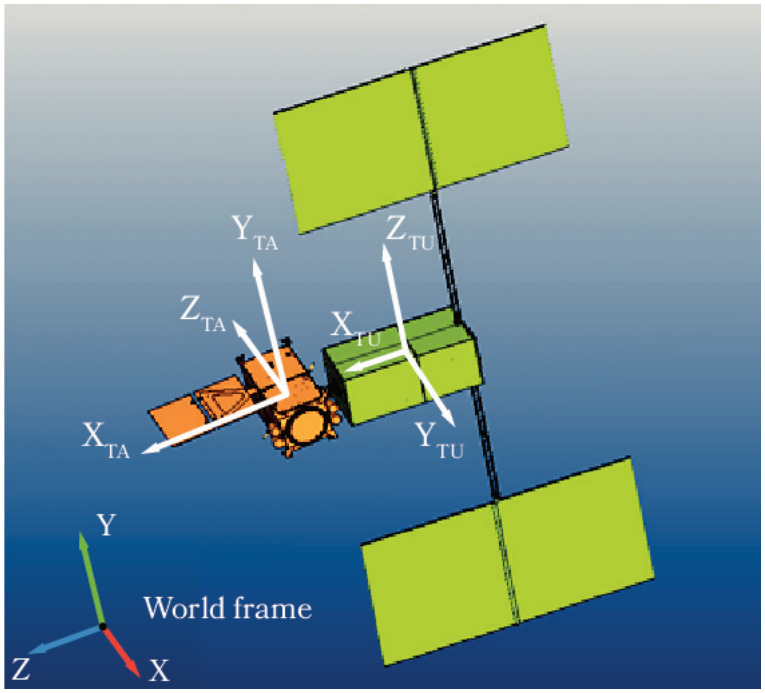

Fig. 6.76 Case 2 initial configuration

Table 6.31 Case 2 initial relative velocities

Relative velocity	Lateral Y	$10\,mm/s$
	Lateral Z	$10\,mm/s$
	Longitudinal X	$30\,mm/s$
Relative angular rate	ω_X	$0.1\,deg/s$
	ω_Y	$-0.1\,deg/s$
	ω_Z	$0.1\,deg/s$

the damper at approximately $5.6\,s$, the relative longitudinal velocity of the spacecraft decreases by only 8%. Moreover, up to that point, the lateral velocities along X and Y decrease respectively by 47% and 69%.

Regarding the damping system, it was designed for the mass combination in Case 1. For this reason, the separation velocity, i.e., the relative velocity between target and chaser after capture, is higher, in this case, being equal to $5.21\,mm/s$. It is nonetheless a large reduction of the kinetic energy. Also, in this case, the final velocity of the stack, $18.96\,mm/s$, agrees with the formulation of inelastic collisions.

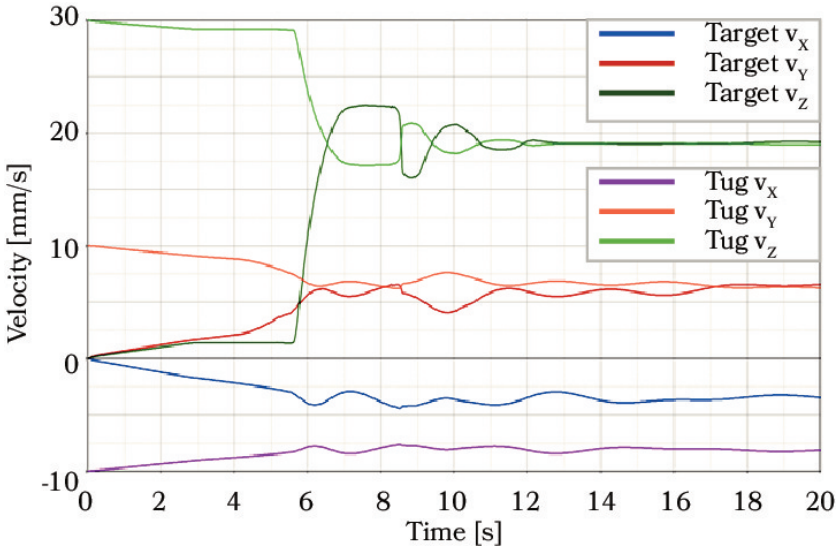

Fig. 6.77 Absolute velocities of the spacecraft w.r.t. the world frame during case 2

The rotation of the probe latches (figure 6.78) shows that the rotation threshold in is reached at 5.30 s. Furthermore, figure 6.78 also shows soft docking occurs at 7.71 s when the latches return to their nominal angular position.

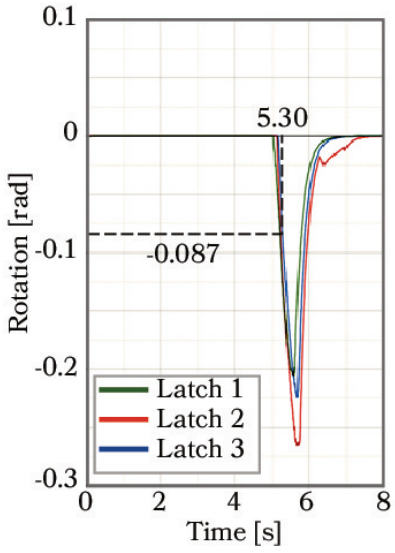

Fig. 6.78 Rotations of the spring-loaded latches during Case 2

In contrast with Case 1, figure 6.79 shows that the X slide is blocked in position when the rotation thresholds of the latches are reached. On the contrary, the Y slide reaches its position saturation before this moment. This further proves that

the system works properly in both cases as it is able to prevent the separation of the satellite with the soft capture.

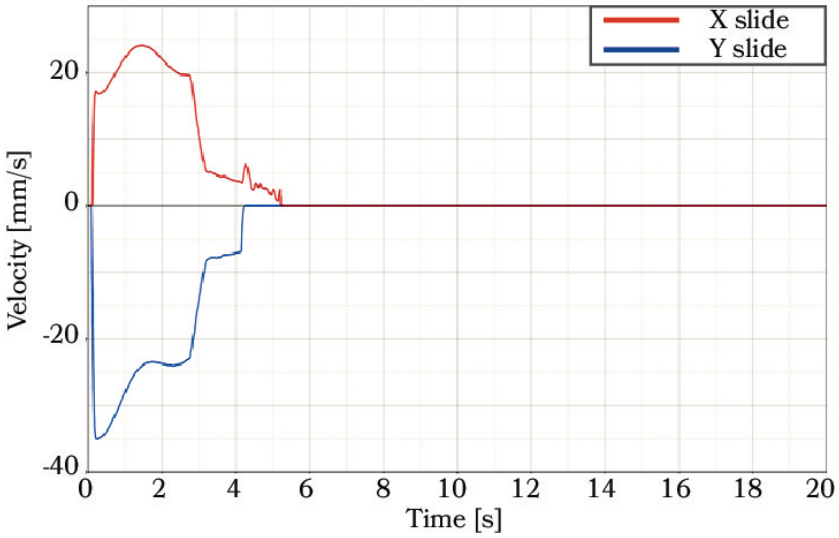

Fig. 6.79 Velocities of the axes of the XY stage during Case 2

Besides the first contact, the exchanged contact force (figure 6.80) is maintained below 5 N throughout the whole alignment phase.

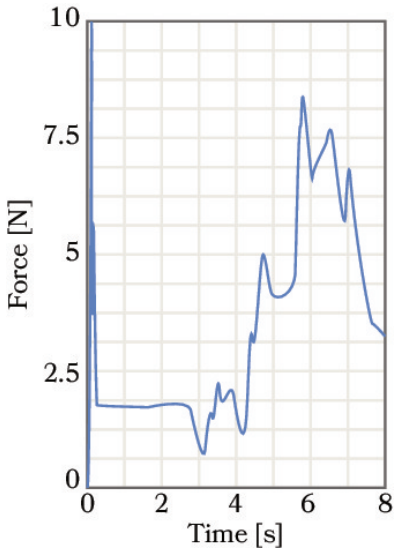

Fig. 6.80 Contact force during Case 2

Figure 6.81 further shows that the slides behave properly: the rotations of the probe about the axes of the universal joint are kept low during the operation of the

slides. In the beginning, the angles grow larger than the value of the deadband. However, during the last part of the travel of the slides, the angles reach values very close to $0.2\,deg$.

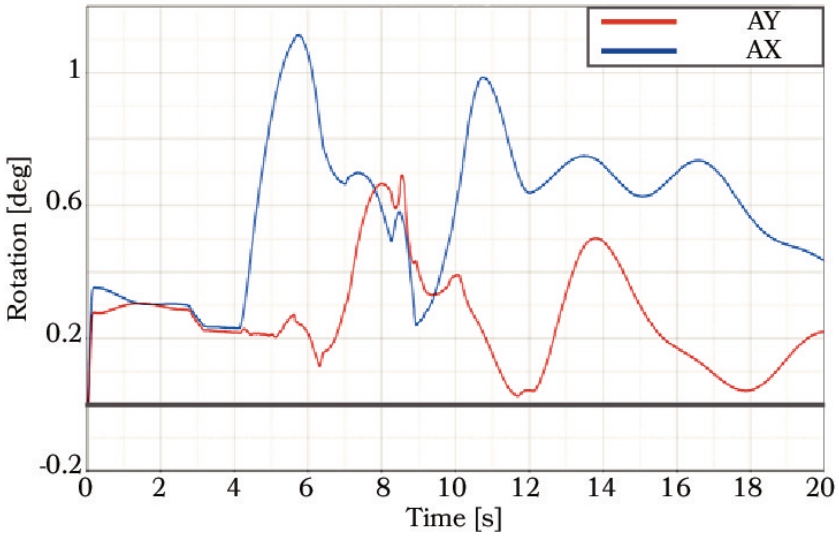

Fig. 6.81 Rotations of the probe about the axes of the universal joint during Case 2

Conclusively, the positive results of this 3D model demonstrate that the mechanism is able to fulfill its purpose. The results also show that the specifications are met in terms of misalignment recovery, dynamic response, and energy dissipation with the different inertial combinations of the mission.

For this reason, the decision to proceed with the detailed design of all the mechanical components, generation of technical drawings, construction, and purchase of commercial hardware was made.

At this point, the only aspect of defining is the control architecture of the mechanism. Each actuator has its driver that allows it to follow a reference value. However, a central unit to coordinate all the actuators is necessary. The following section will deal with this topic.

6.9 Mechanism operation and control architecture

The objective of this section is to evaluate different control architectures for the active part of the docking mechanism. The analysis was conducted considering the target of reaching a TRL 4.

Two possible configurations were studied: one based on a conventional computer with no real-time capabilities and a second option based on a real-time industrial controller.

The docking system is equipped with four electric motors. There is one EC motor for the probe retraction, one stepper motor for the closure of the hard docking hooks, and finally two identical EC motors for positioning the XY stage. These EC motors need external sensors to create the reference set to control the exchanged forces between the tip of the probe and the female cone. In this case, the selected sensors are two laser triangulation displacement sensors. Table 6.32 shows the characteristics of these laser devices.

Table 6.32 Specifications of the laser triangulation displacement sensors ILD1420-25

Supplier	MICRO-EPSILON
Measuring range $[mm]$	25
Start of range $[mm]$	25
Midrange $[mm]$	37.5
End of range $[mm]$	50
Reproducibility $[\mu m]$	1
Analog output	$4-20mA$ $(1-5V)$

Furthermore, each motor has a suitable driver and a power interface. Regarding the drivers, table 6.33 shows some of their characteristics. In particular, the supported communication protocols are useful to identify possible control architectures.

Table 6.33 Specifications of the drivers

Component	Q.ty	Description	Supported protocols	inputs	outputs
EPOS2 24/2	1	Driver for EC motor	CANOpen USB RS232	6 digital 2 analog	4 digital
EPOS2 24/5	2	Driver for EC motor	CANOpen USB RS232	6 digital 2 analog	4 digital
P70530	1	Driver for step motor	RS232	N/A	N/A

6.9.1 Operation of the mechanism

The operation of the mechanism is divided into six Operational Phases (OP). The OPs are *Deployment of the probe*, *Alignment and latch*, *Partial retraction*, *XY homing*, *Final retraction*, and *Hard docking*.

OP 1: Deployment of the probe

During this phase, the central probe is deployed using the probe actuator which is equipped with the magnetic encoder. This deployment starts with a forward motion of the probe followed by a short backward motion that activates the latches.

OP 2: Alignment and latch

In this phase, the motors of the XY stage have to guarantee the alignment of the central probe with the longitudinal axis of the chaser spacecraft. The stage operates in force control mode, and its feedback signals are externally provided by the laser sensors. Since the central probe is connected to the traction springs, the displacements of its rear end produce elastic forces. The laser sensors measure these displacements and create a couple of electrical signals, δ_X and δ_Y. These signal are

respectively the displacement along the axes X, and Y of the stage. Subsequently, a filter and a deadband are applied to the signals. The filter smooths the laser signals in case they are badly conditioned or in case of mechanical vibrations. Regarding the deadband, it may be necessary to eliminate offsets due to mounting errors and undesired displacements due to vibrations.

Once the conditioned signals, δ_X^* and δ_Y^*, reach the EPOS2 24/5 drivers, a velocity gain K_v^{EPOS} and an offset b^{EPOS} are applied to create the velocity set values needed to align the probe:

$$v_X^{set} = K_v^{EPOS}\delta_X^* + b^{EPOS} \tag{6.92}$$

$$v_Y^{set} = K_v^{EPOS}\delta_Y^* + b^{EPOS} \tag{6.93}$$

Figure 6.82 shows a schematic view of the laser signal processing.

OP 3: Partial retraction

Once the soft docking is achieved, the system is preloaded using the motor of the central probe. This motor travels a partial distance of its total stroke so as to preload the male cone springs by pushing against the female cone. The probe is driven in position control mode and the feedback is provided by the encoder assembled with the motor.

OP 4: XY homing

In the fourth OP, the XY stage performs a homing operation controlled by the motor encoders only. This phase operates in position control mode.

OP 5: Final retraction

In OP 5, the remaining stroke of the central rod is traveled and the base of the female meets with the interface plate of the chaser. The probe is driven in position control mode with feedback from the encoder.

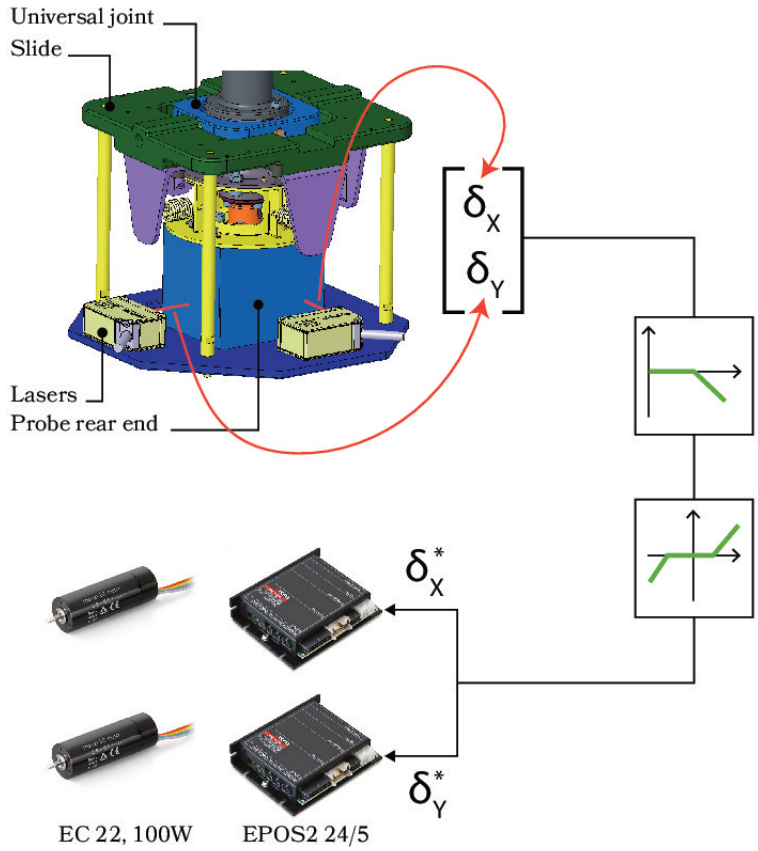

Fig. 6.82 Generation of the velocity set values

OP 6: Hard docking

Finally, the hard docking hooks are actuated in open loop using the stepper motor. This operation ends the maneuver. Figure 6.83 summarizes the operational phases introduced above. This figure shows each phase as a state of a finite state machine. It also shows the transition conditions of each state.

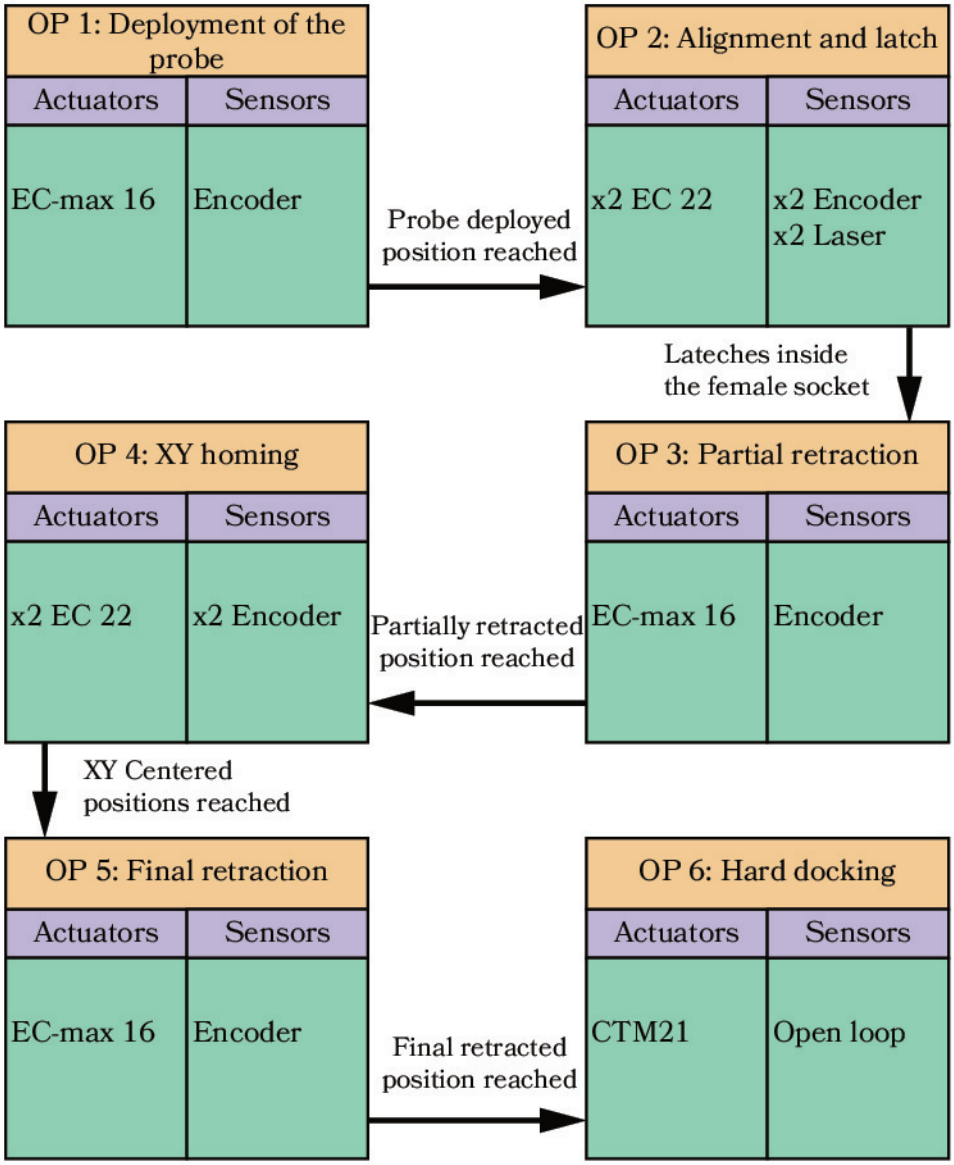

Fig. 6.83 Finite state machine of the control system

6.9.2 Control Architecture

As introduced before two possible control architectures were considered. Configuration 1 (figure 6.84) uses a standard computer to start and stop the operational phases of the maneuver. In this case, the control loop needed in OP 2 is achieved by sending the set values from the lasers to the motor drivers. In this case, the central computer takes care of enabling and disabling the motors and their functioning modes. This

architecture is simple to build and the state machine may be implemented in, e.g., NI LabVIEW.

As seen in figure 6.84, a CANOpen bus is created with the the Maxon drivers for EC motors. One of the drivers of the bus is connected to the master computer using an USB interface. Regarding the P70530 driver for the stepper motor, it is connected to the main PC via an RS232 interface.

The second alternative is shown in figure 6.85. Configuration 2 includes as a master computer a real-time industrial controller. The NI cRIO 9063 was considered as a candidate for this task. A couple of modules were added to it: a CANOpen module and a current measure board. In this case, the analog current signals from the laser sensors are read by the controller. Then, the filter and deadband are applied, and the set values for the EC drivers of the XY stage are given as digital commands. Moreover, the master controller enables and disables the phases of the maneuver as in Configuration 1. This solution is more flexible due to the programmable real-time master and is more similar to a definitive space implementation.

The analysis of these configurations led to the selection of the standard computer mainly for the lower cost, and ease of hardware and software implementation.

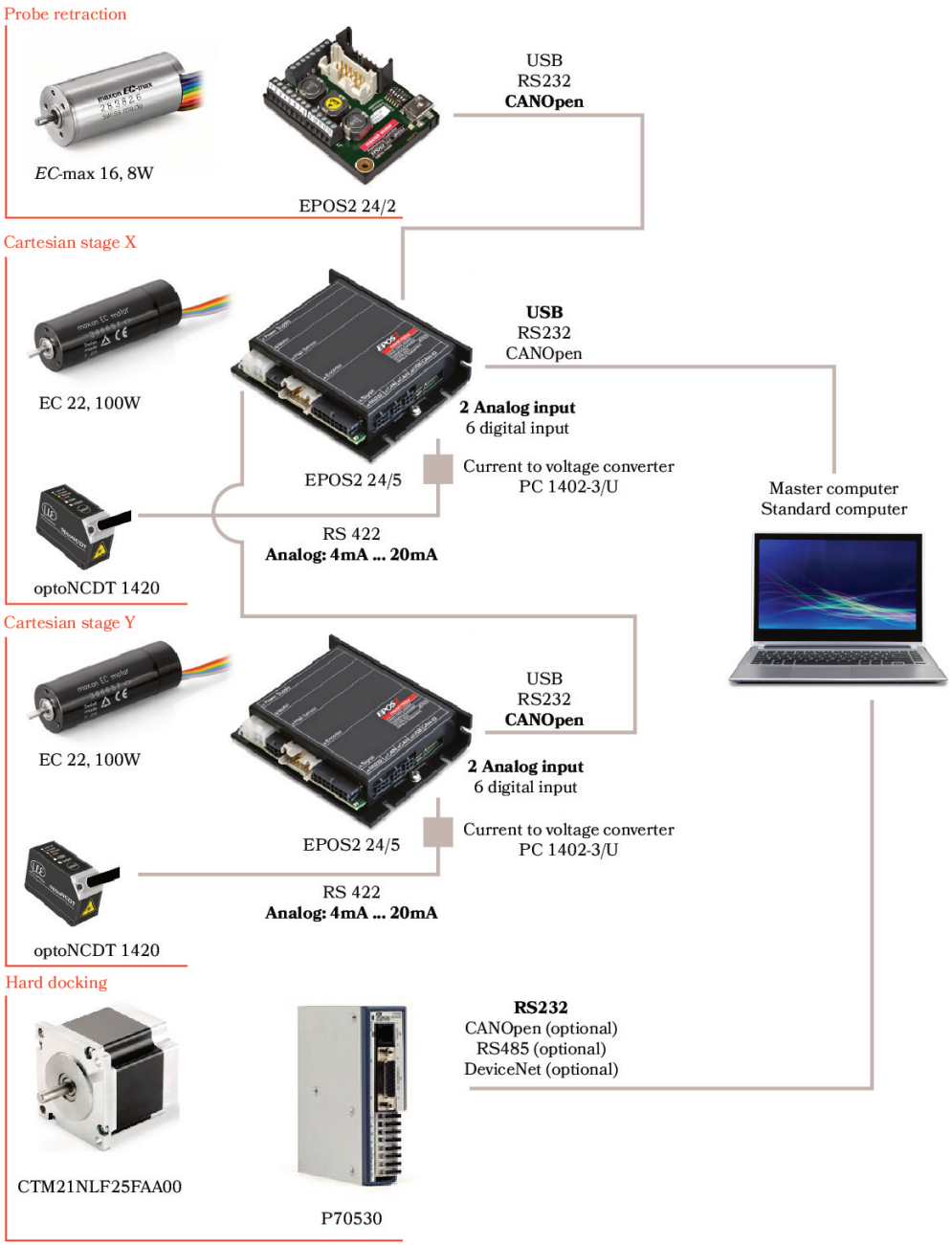

Fig. 6.84 Configuration 1 (the system that applies the filter and the deadband is not shown)

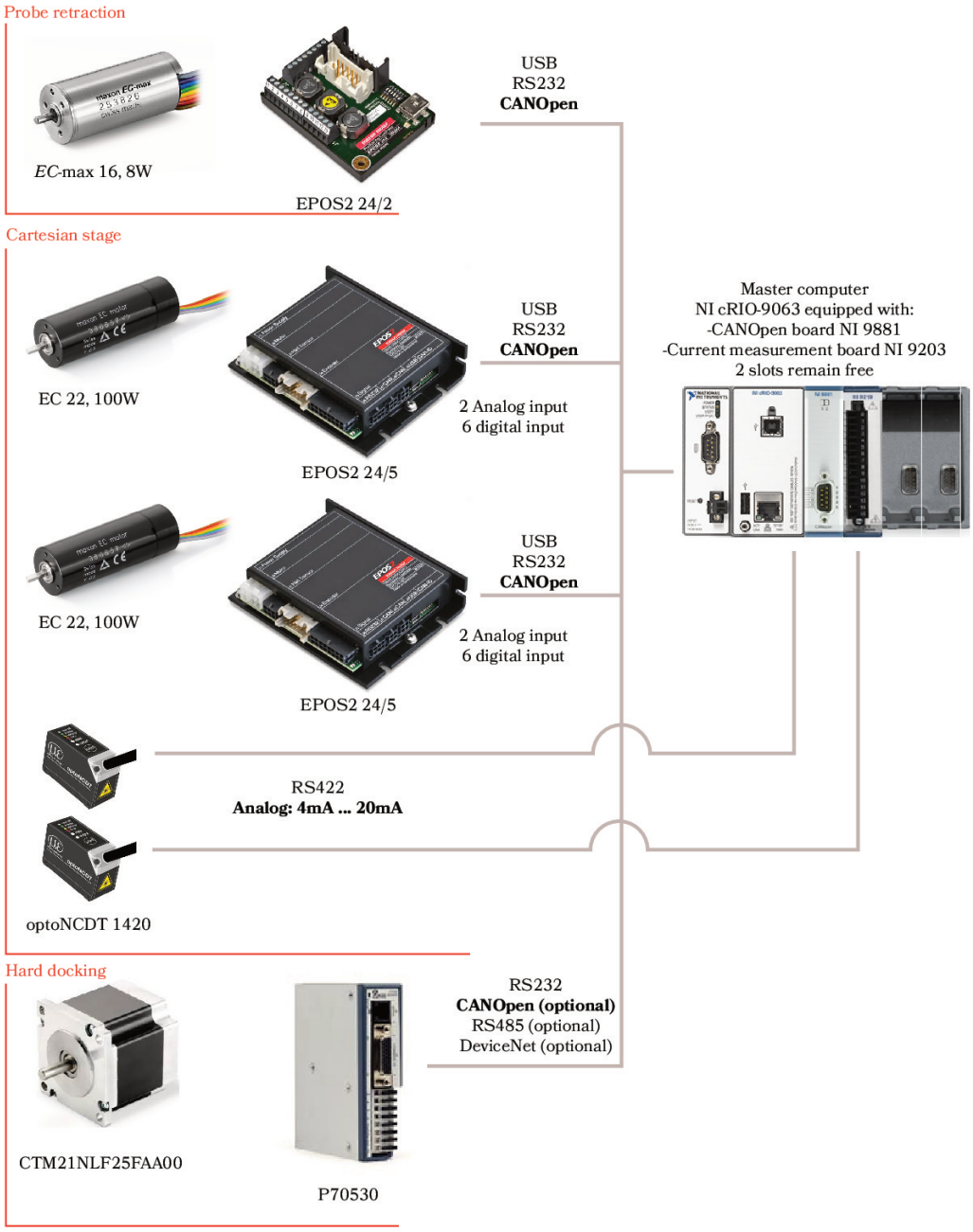

Fig. 6.85 Configuration 2: real-time industrial controller

6.10 CLAS-S: a central docking system with controlled linear axes

The objective of this section is to conclude the design phase by showing the mechanism prototype while outlining its characteristic features.

Following the aerospace industries' tradition of using acronyms, the docking mechanism herein designed is named **C**entral **L**inear **A**ctive **S**ystem for the **S**TRONG mission, CLAS-S.

Figure 6.86 shows a technical drawing of the final prototype of the active part of the mechanism. On the other hand, figure 6.87 shows a cross section of the female cone. The technical drawings of each mechanical component were also created using suitable mechanical tolerances. These drawings were used during the construction process. The parts made of aluminum were clear anodized for corrosion and wear resistance. Moreover, suitable threaded inserts were selected and mounted to increase the life and the strength of the threads machined off aluminum parts.

The active linear axes of the CLAS-S create a highly compliant mechanism during the alignment phase. This feature may improve the range of possible inertial combinations and initial conditions without compromising the probability of successfully achieving soft docking. The compliance also reduces the applied forces during the alignment phase that results in a safer maneuver. In addition, the minimization of the exchanged force makes possible to avoid the usage of propellant to guarantee soft capture in what is called post-contact thrust.

The main objective of this work was to design and build a mechanism compliant with the STRONG mission. Nonetheless, the CLAS-S presents some interesting features that may be advantageous in any on-orbit servicing mission: reduced dimensions, reduced weight, the absence of post-contact thrust, and improved docking success probability and safety. Moreover, the technical specifications of the STRONG mission regarding the initial conditions of the docking maneuver are comparable with the specifications used to design other modern docking systems. As shown in chapter 3, the design process of the OECS and the IBDM used the same lateral and angular misalignments of the STRONG mission. Furthermore, the available data regarding the approaching velocities show highly comparable values.

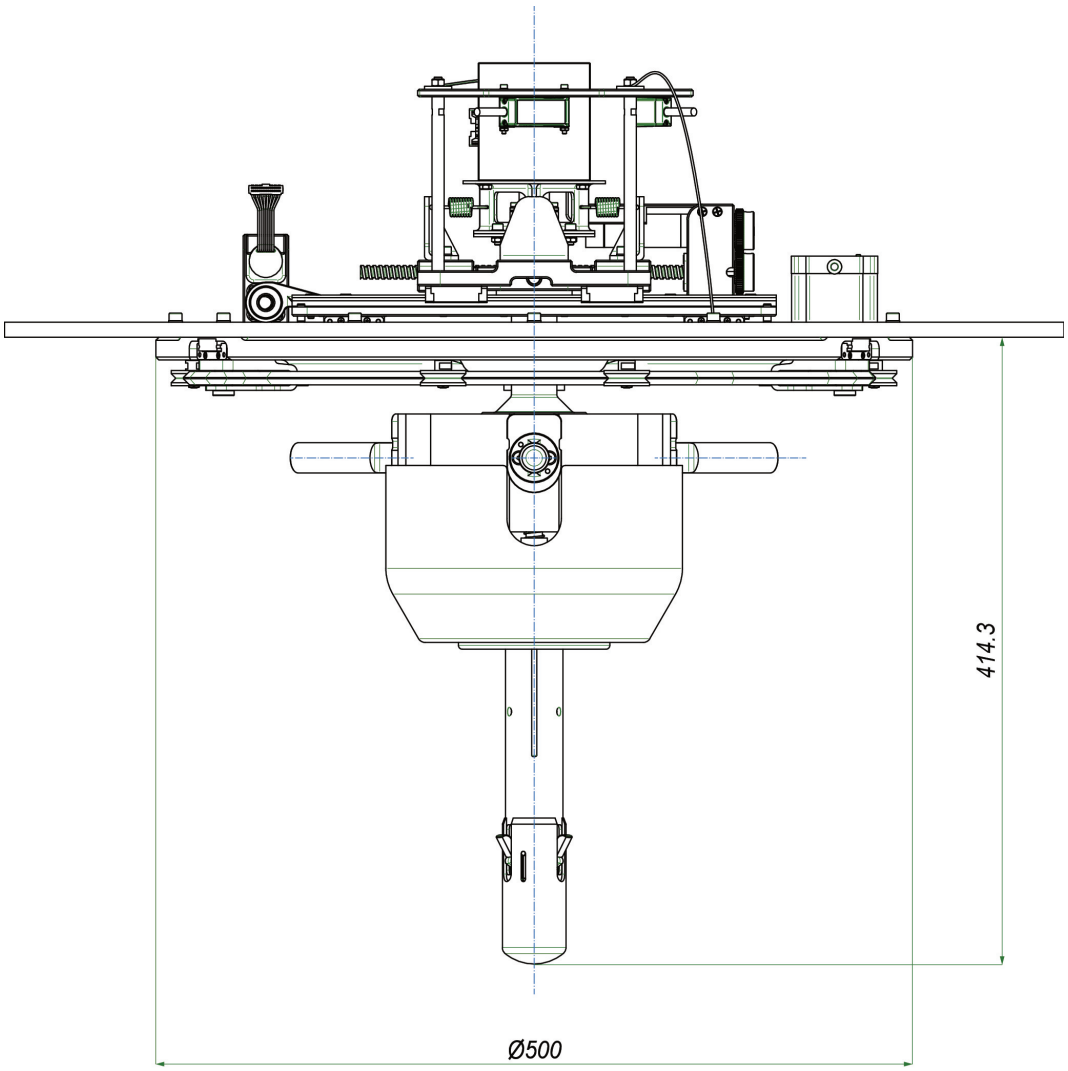

Fig. 6.86 Technical drawing of the male part of the CLAS-S

The current docking mechanisms are designed to allow crew and cargo to move from one vehicle to the other. For this reason, the dimension of the transfer tunnels is selected to be comfortable for the astronauts to move. Regarding the Soyuz docking system, the diameter at the base of the female cone is 820 *mm* [4]. The external diameters of IBDM [26] and NASA's NDS [50] are respectively 1485 *mm* and 1727 *mm*. These dimensions are much larger than the maximum allowable dimensions of the STRONG mission. If that is the case of this particular mission, it may also be the case for all the missions that foresee docking operations without crew

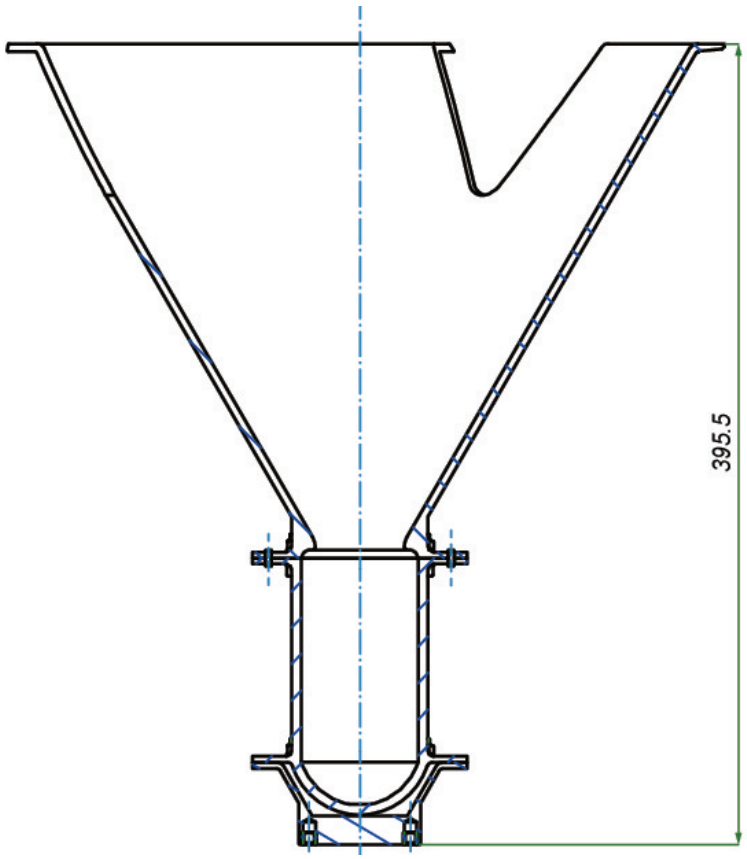

Fig. 6.87 Cross section of the female part of the CLAS-S without the damping system

and cargo transfer. In those cases, the architecture and functioning of the CLAS-S docking mechanism concept might be an option worth considering.

Weight is a very important design factor in a space mission. The mass of the male part of the CLAS-S prototype is 25 kg while the female is 3 kg. The masses of the androgynous platforms created by NASA and ESA are around 340 kg [50]. If we considered the space tug, the weight of one of the state-of-the-art androgynous mechanism would be as much as 20% of its dry mass. This may be the case of any other small and mid-size space vehicle involved in an on-orbit servicing mission.

ESA's scientific divulgation video "Soyuz rendezvous and docking explained" [17] states the following concerning the docking maneuver: "Contact occurs as soon as the probe touches the entrance cone of the docking hatch, then the thrusters give the Soyuz an extra push." That extra push is the post-contact thrust operation. This thrust is used to ensure the capture of the probe latches inside the socket. As stated

before, such a maneuver is not necessary while using a docking mechanism based on a highly compliant system as the CLAS-S.

The next chapter will describe the testing methodology that will be used to experimentally verify the suitability of the mechanism.

Chapter 7

Testing methodology

As stated in section 2.3, docking mechanisms are tested using parallel or serial manipulators combined with force-torque sensors to simulate the relative motion between the customer and the servicer satellites. This will be also the case in this study. The designed test rig is composed of a serial manipulator equipped with a sensor to measure the exchanged wrench between the mechanism halves. This chapter describes the preliminary tests performed with the actuators of the mechanism, in particular, the ones of the XY stage. Moreover, this chapter addresses both the architecture of the test rig and the group of tests designed to assess the functioning of the CLAS-S.

7.1 Actuators tests and control system implementation

These tests represent the first group of functional verifications of the mechanism's subsystems. A test bench was prepared using the servosystems (motor with planetary gearhead and encoder plus driver) of the XY stage combined with the two laser triangulation displacement sensors as well as the servosystem selected for the probe retraction (figure 7.1).

Besides the motors, gearheads, drivers, and sensors of the probe retraction system and XY stage, figure 7.1 shows the microcontroller used to generate the deadband for the output signals of the lasers. Firstly, this test bench was operated using one

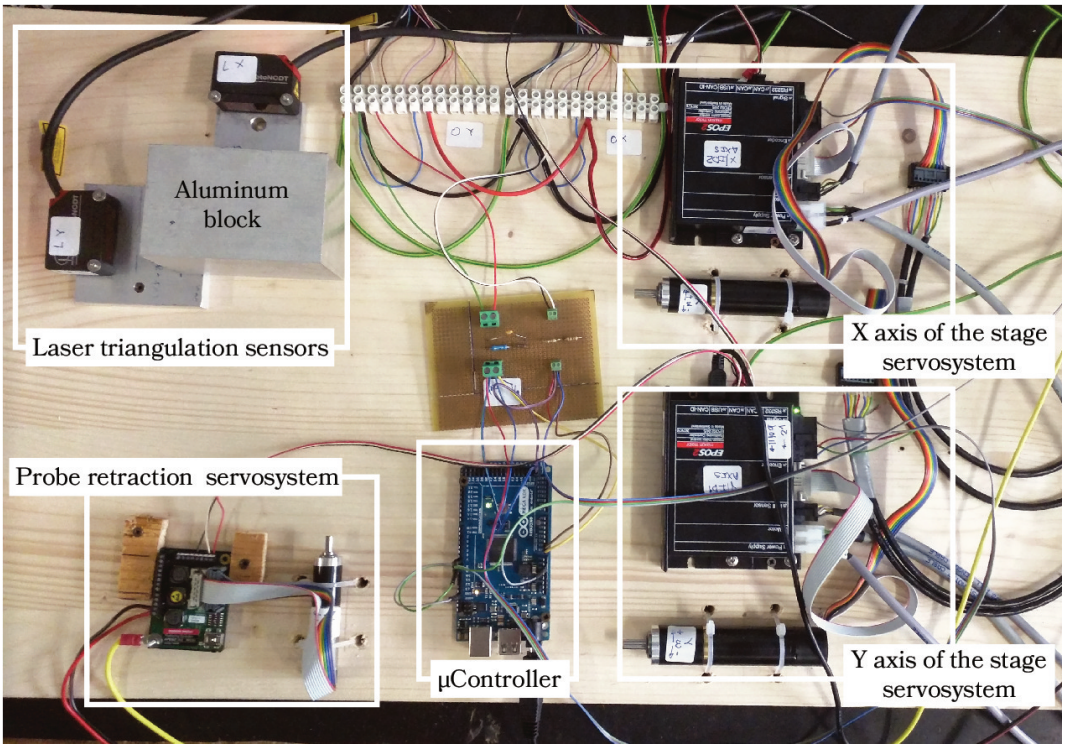

Fig. 7.1 Test bench used to test the actuators and the control system

servosystem at a time. By doing so, all the motors but the hard docking actuator were tested in accordance with the OPs described in section 6.9.1. The servosystem for the probe actuation was controlled in position simulating OP 1, 3, and 5.

OP 4 was also simulated by controlling the motors of the stage with position reference sets. Finally, the alignment of the probe was simulated using the laser sensors to generate the sets for the XY stage motors. An aluminum block was used to interrupt the lasers at their midranges. At the midrange, the lasers generate a voltage equal to $3\,V$. The signals from the lasers were fed into the microcontroller that applied the deadband in the range $[2680\,mV, 3320\,mV]$. This range is equivalent to a displacement equal to $\pm 2\,mm$. The deadband is needed to avoid undesired displacements of the axes of the stage due to mounting errors and vibrations. Subsequently, the aluminum block was displaced laterally to generate the set to the motors. In this regard, figure 7.2 shows both the laser signal and the resultant motor speed of one of the XY motors. It may be seen that within the range of the deadband the speed of the motor is equal to zero. Once the displacement of the aluminum block relative to the

laser was greater than 2 *mm*, the motor started rotating with a velocity proportional to the laser signal as expected.

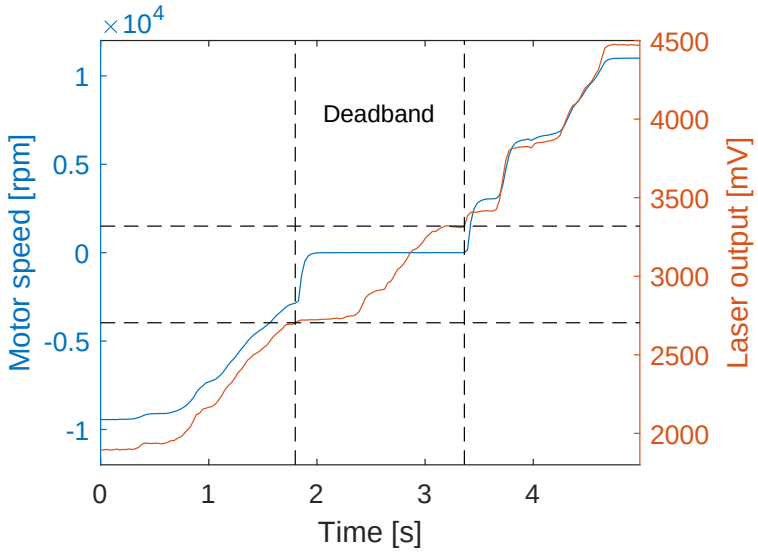

Fig. 7.2 Motor speed and laser output

Once the single OPs were tested at servosystem level, the whole sequence of operations was implemented in LabVIEW. Figure 7.3 shows the state machine that controls the phases. In particular, this figure shows the OP 1: Deployment of the probe.

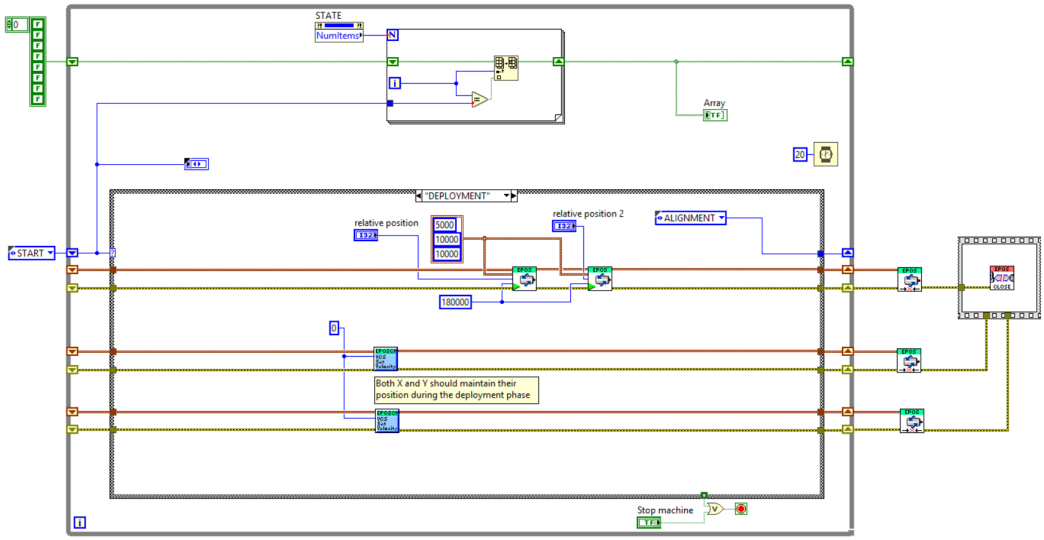

Fig. 7.3 LabVIEW implementation of the state machine. The figure shows the OP 1: Deployment of the probe

7.2 Test rig description

The test rig is based on the POWERBALL LWA 4 6DOF manufactured by SCHUNK GmbH (figure 7.4). Some of the characteristics of this serial manipulator are shown in table 7.1.

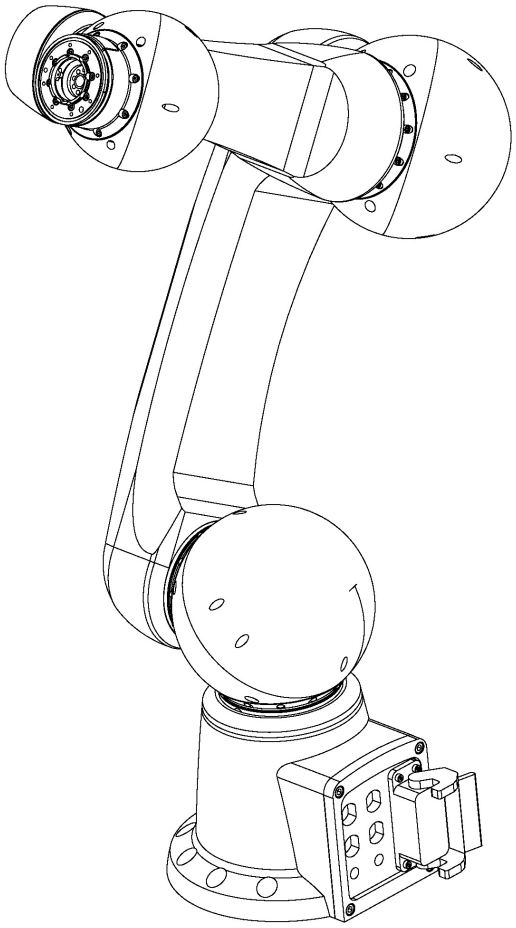

Fig. 7.4 SCHUNK's POWERBALL LWA 4 6DOF

The task of this robot is to translate and rotate the female cone of the mechanism following an imposed trajectory. The female cone is mounted on the robot through a force-torque sensor (figure 7.5). This sensor is also manufactured by SCHUNK. The characteristics of this element are shown in Table 7.2.

The trajectory of the female cone may be generated using two different approaches. The first one considers an open-loop motion of the robot's end-effector. The second approach exploits the measured wrench to solve the dynamic equations

Table 7.1 Characteristics of the POWERBALL LWA 4 6DOF

Maximum payload $[kg]$	6
Number of axes	6
Repeatability $[mm]$	± 0.06
Power supply	$24\,VDC$ - max. $20\,A$
Single axis control via	CANOpen

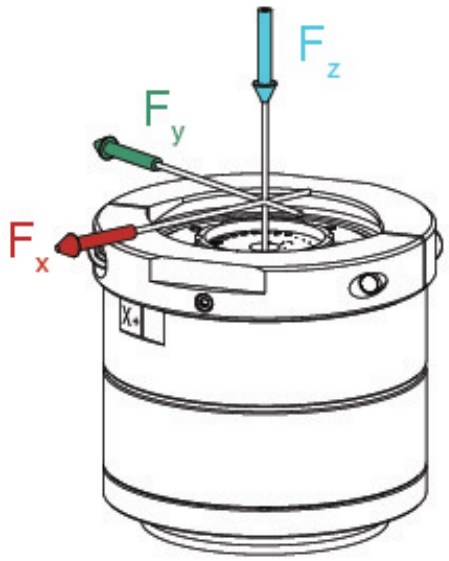

Fig. 7.5 SCHUNK's force-torque Module FTM 115

of the satellites. Solving these equations leads to the calculation of the relative motion of the mechanism halves. The pose of the end-effector is then changed based on the estimated motion.

Both the manipulator and the support plate of the active part of the mechanism are bolted to a Support Equipment (SE). The SE is composed of several structural aluminum profiles. Regarding the manipulator, it is mounted on a plane that may be adjusted in height (Plane A in figure 7.6). On the other hand, the male half is fitted to the Plane B. The distance between these planes ranges from $1200\,mm$ to $1500\,mm$.

Figure 7.6 depicts several reference systems. The first one is the world frame, W, located at the base of the serial manipulator. A second frame is positioned at the

Table 7.2 Characteristics of the FTM 115

Range of measurement F_x, F_y $[N]$	± 580
Range of measurement F_z $[N]$	± 1160
Range of measurement M_x, M_y, M_z $[Nm]$	± 20
Resolution F_x, F_y, F_z $[N]$	$\pm 1/4$
Resolution M_x, M_y $[Nm]$	$\pm 1/188$
Resolution M_z $[Nm]$	$\pm 1/376$
Weight $[kg]$	1.0
Power supply $[V]$	24
Field bus interface	CAN

furthermost part of the last link of the manipulator, EE. Concerning the mechanism parts, the system P is attached to the center of the base of the female half. The pose of the reference system P w.r.t. EE is expressed by the constant homogeneous matrix ${}^{EE}\hat{\mathbb{A}}_P$. The reference system of the active part, A, is positioned at the base in the center of the male support plate. These reference systems will be useful to explain the relative kinematics of the bodies in the next sections.

The SE with the serial manipulator installed is shown in figure 7.7. At the bottom of the SE, the mechanism used to change the distance between Plane A and B may be seen. It is a scissor jack actuated by a hand crank. For safety reasons, this robotic cell was covered with plexiglass.

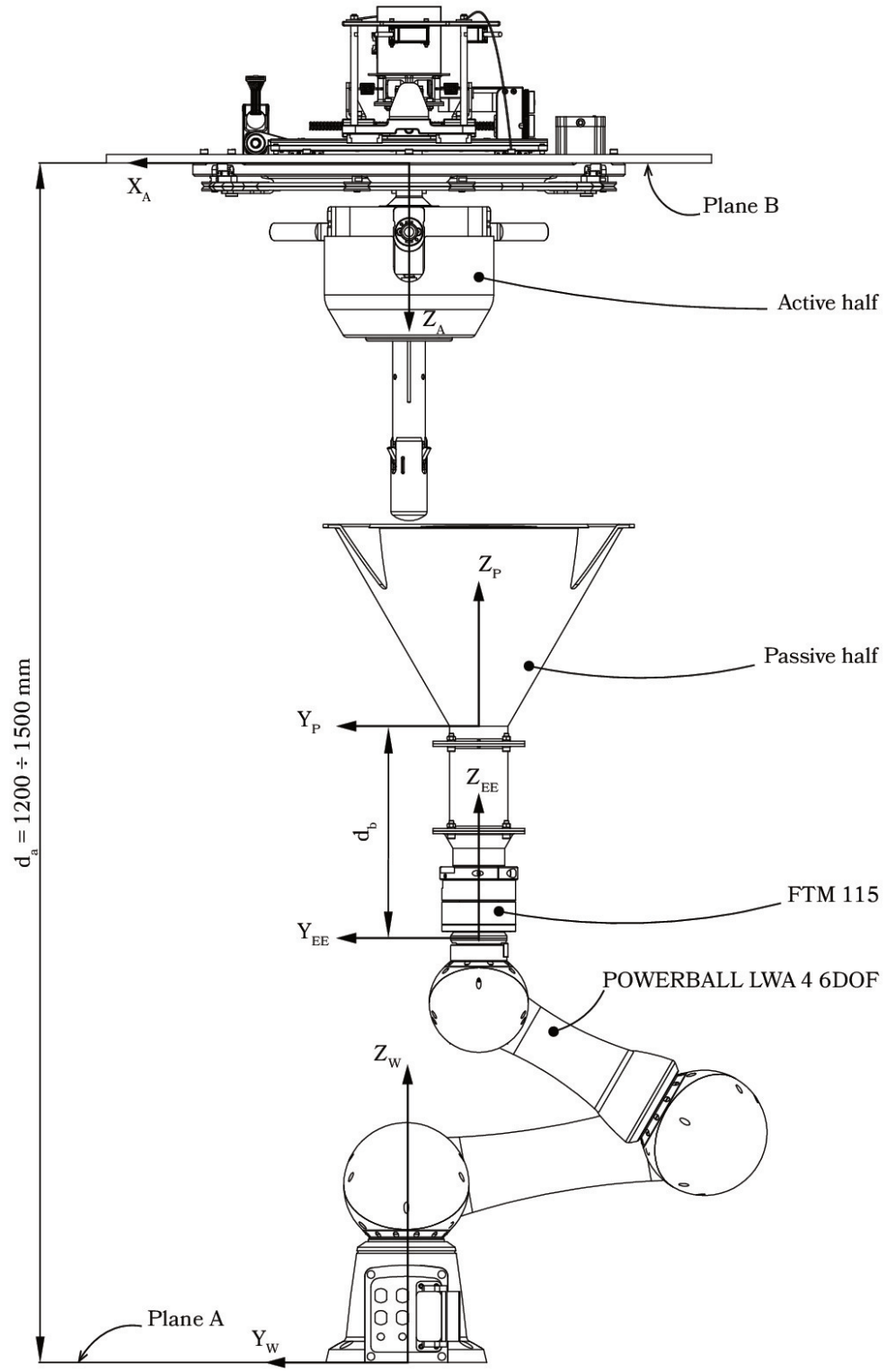

Fig. 7.6 Schematic view of the test rig

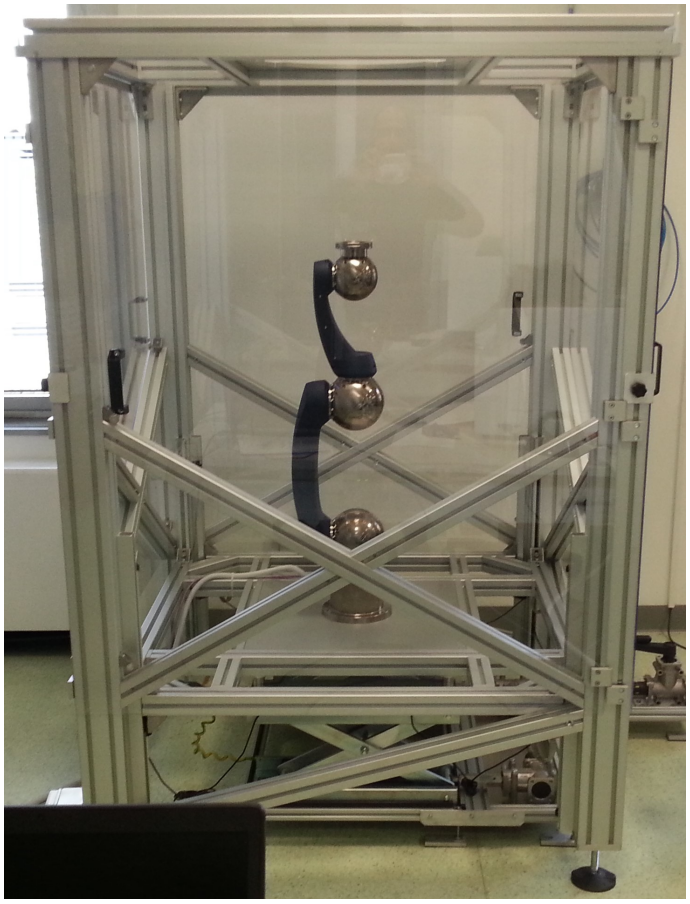

Fig. 7.7 SE with robot

7.3 Functional tests

These tests have the objective of testing the mechanism during all the operational phases. The control systems of the robotic manipulator and the active part of the CLAS-S will be used concurrently. In this regard, the controller of the CLAS-S will execute the state machine shown in figure 6.83. The following subsections will describe the sequence of tests.

7.3.1 OP 1: Deployment of the probe

Starting from a retracted position, the probe will be actuated up to its deployed position. Once this position is reached, the control system of the mechanism will

transition to OP 2. During this test, the robot will position the female cone at a safe distance from the probe.

7.3.2 OP 2: Alignment and latch

Initially, in this test, the manipulator is supposed to change the pose of the end-effector following a reference trajectory. In this case, the forces and torques exchanged between the mechanism halves will not modify the imposed movement of the manipulator.

The trajectory of the end-effector will be generated using the multibody model described in section 6.8. Using different initial conditions and mass combinations, the relative pose of the reference system P w.r.t. A will be calculated for different discrete time instants. The resultant relative pose ${}^{A}\hat{\mathbb{A}}_{P}$ will be then stored.

There are several known geometrical relations in the test rig. Firstly, the relative pose between A and W is known for each position of the Plane A:

$$ {}^{W}\hat{\mathbb{A}}_{A} = \begin{bmatrix} 0 & -1 & 0 & 0 \\ 1 & 0 & 0 & 0 \\ 0 & 0 & -1 & d_a \\ 0 & 0 & 0 & 1 \end{bmatrix} \tag{7.1} $$

Moreover, the flange of the robot makes a rigid body with the force-torque module and the female cone. For this reason, the homogeneous matrix ${}^{EE}\hat{\mathbb{A}}_{P}$ is also known:

$$ {}^{EE}\hat{\mathbb{A}}_{P} = \begin{bmatrix} 1 & 0 & 0 & 0 \\ 0 & 1 & 0 & 0 \\ 0 & 0 & 1 & d_b \\ 0 & 0 & 0 & 1 \end{bmatrix} \tag{7.2} $$

The resultant pose of the end-effector w.r.t. W may be calculated as follows:

$$ {}^{W}\hat{\mathbb{A}}_{EE} = {}^{W}\hat{\mathbb{A}}_{A} \cdot {}^{A}\hat{\mathbb{A}}_{P} \cdot {}^{EE}\hat{\mathbb{A}}_{P}^{-1} \tag{7.3} $$

At each discrete time instant, the calculated pose will be the reference value for the manipulator. Simultaneously, the force and torque module will measure the exchanged wrench. The values of the exchanged actions will be stored and study. To consider this test successful, the magnitude of the contact force should be small, having as a reference the values estimated using the models presented in section 6.8. It is important to note that the measured wrench will also include the effects of the weight of the female cone. For this reason, this contribution will be subtracted based on the pose of the end-effector.

In this case, soft docking will be verified by monitoring the absolute vertical coordinate of the socket of the female cone (reference frame P w.r.t. W) by using the outputs of the control unit of the manipulator. Once the Z_W coordinate of the system P reaches the distance from the origin of W to the furthermost part of the cap, the test terminates. At this point, the serial manipulator will be stopped. Subsequently, the manipulator will slowly translate the female upward to engage the latches. Then, the capture will be verified by pulling the female back while measuring the force along Z_P using the force-torque module. If the force increases it will indicate that the latches are engaged inside the female socket. The force increment will trigger a signal to the control system of the active part of the mechanism. This signal will start the transition from OP 2 to "OP 3: Partial retraction" with a suitable time delay (figure 6.83).

7.3.3 OP 3: Partial retraction

During the retraction of the probe, the manipulator will behave as a compliant mechanism. It will apply a velocity to the end-effector proportional to the applied wrench measured by the force-torque module FTM 115

$$^{EE}\underline{Wr} = \begin{bmatrix} \underline{F} \\ \underline{T} \end{bmatrix} \tag{7.4}$$

In equation 7.4, $\underline{F}$ and $\underline{T}$ are respectively the measured force and torque vectors. This wrench is transformed into a spatial velocity set by multiplying by a diagonal gain matrix

$$^{EE}\underline{V} = \mathbb{K}\, ^{EE}\underline{Wr} \tag{7.5}$$

The values of the entries of the gain matrix will be chosen based on the desired response in terms of promptness and safety. The reference joint angular velocities of the manipulator, $\underline{q}$, are then calculated as follows:

$$\underline{q} = \mathbb{J}^{-1\ EE}\underline{V} \tag{7.6}$$

where $\mathbb{J}$ is the manipulator Jacobian matrix that maps the joint velocities to end-effector spatial velocity. With this technique, the female cone will be carried by the actions of the probe that retracts and centers itself up to the final hard docking. Once hard docking will be achieved, all the systems will be disabled ending the test.

7.3.4 OP 4: XY homing and OP 5: Final retraction

The tests associated with this phases are very similar to the previous one. Firstly, the axes of the XY stage will return to their centered position. By doing so, there will be forces exchanged between the probe and the female cone. Here again, the manipulator will behave has a compliant mechanism. Secondly, the remaining stroke of the probe will be retracted while the robot will be controlled using the previous control logic. Once the base of the female cone meets the support of the mechanism, the command to start OP 6 is issued.

7.3.5 OP 6: Hard docking

Finally, the hooks will be actuated up to their position in contact with the female cone. This will end the testing.

7.4 Mission scenario tests

This is a more ambitious test. In this case, the exchanged wrench measured by the force and torque module is used to estimate the kinematics of the mechanism halves. This estimation is achieved by solving the dynamic equations of both the servicer and the customer satellites.

Figure 7.8 shows the test rig and a block diagram of the control of the robot. In this diagram, the force and torque module measures the exchanged actions between

the passive and active parts of the mechanism. These actions are used to solve the dynamic equations of both target and chaser. Regarding the chaser, the rotational equilibrium equation will depend on the position of the X and Y slides, and the orientation of the probe. The position of the slides will be measured using the encoders of the actuators while the orientation may be reconstructed using the laser signals. With this data, it is possible to calculate the lever arm of the contact force assuming that it is applied on the tip of the probe.

The pose of both the satellites is then estimated by solving the dynamic equations of the bodies (equations 5.2, 5.3, 5.4, 5.5). Once these poses are known, it is possible to calculate the change in the relative position and orientation between the mechanism halves, i.e., the relative motion. This relative motion may be translated into the end-effector trajectory and fed to the inverse kinematics algorithm of the serial manipulator. This procedure will be used in all the phases of the docking maneuver.

Also, in this case, the state machine of the active part will run in parallel to complete the several phases of the docking maneuver. Here again, soft docking will be verified by using the geometry of the test rig. After soft docking, the probe will be retracted and the linear axes of the stage will recover their centered position. The end of the hard docking phase will issue a disable command to the robot and the male part ending the test.

This chapter described the tests that will be executed in the future. Positive results of these tests will validate the readiness level of the mechanism at different degrees. The functional tests will create suitable external disturbances to the active part and will increase the confidence in the functioning of the mechanism and the implemented mathematical models. On the other hand, the mission scenario tests will be a definitive proof for assessing the functioning of the mechanism. However, the implementation of this kind of test will be challenging due to the resolution of the equations of motion in real-time.

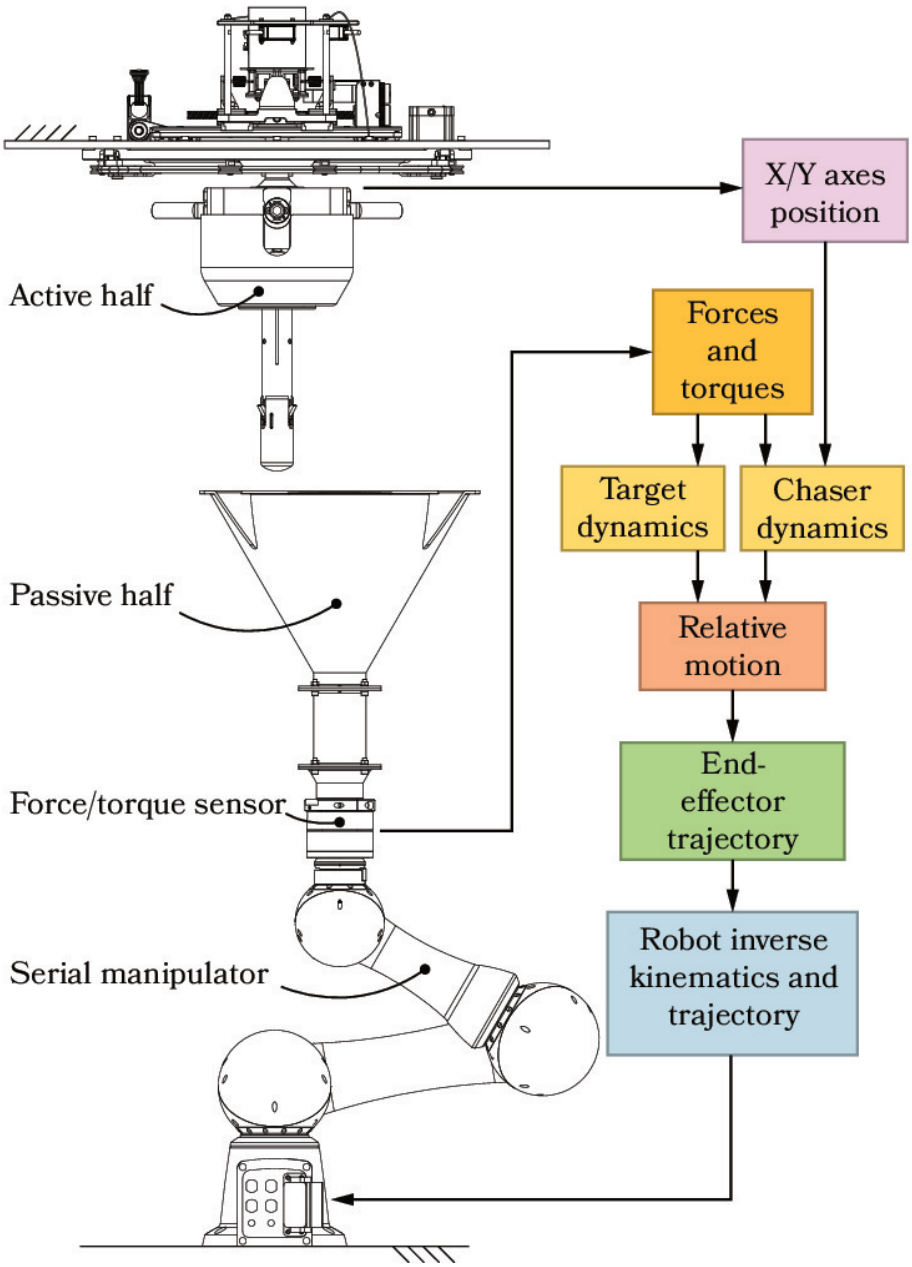

Fig. 7.8 Envisaged operation of the test rig during the closed loop tests

Chapter 8

Conclusions

This chapter summarizes the work presented in this dissertation. It also outlines all the contributions of the research activities, and discusses the envisaged future work.

The focus of this project was the design of a docking mechanism for the STRONG mission. The objective of this mission is the development of a space tug with electric propulsion. The tug is designed for deploying satellite platforms from low injection orbits into their final operational orbits. The maneuver should be executed autonomously and the target should be cooperative.

In order to create a solid technical knowledge base, the terminology and the state of the art regarding docking systems were thoroughly analyzed. In addition, testing methods were also studied.

Five mechanism concepts were proposed by combining the knowledge gathered from the state of the art, the specifications of the mission, and preliminary feasibility analyses. The concepts studied are the following: a mechanism based on the Stewart-Gough platform controlled in position, a Stewart-Gough platform with impedance control, the central passive mechanism developed by TAS-I during the research project STEPS [38], a central active mechanism, and a mechanism equipped with articulated arms. A trade study was conducted to select the most appropriate mechanism for the reference mission. This trade-off considered the following criteria: mass, mechatronic complexity, control complexity, the ability to work with targets with different masses, energy consumption, reliability, and functional confidence. The study showed that the most balanced mechanism was the central mechanism with passive features.

The passive mechanism was initially designed and constructed by TAS-I for tests involving a planar test bed. For this reason, the layout was modified to suit a 3D docking maneuver in space conditions. Subsequently, the functional behavior of this mechanism was studied using numerical models. Three models were implemented with an incremental complexity. The first model simulated the docking maneuver in a 2D environment without taking into account the geometric details of the docking halves. Secondly, another 2D model was implemented using MSC Adams. In contrast with the first model, this implementation used a few of the actual geometries of the docking parts. Finally, a complete multibody model was created using Altair HyperWorks. This last model simulated a 3D maneuver between the spacecraft equipped with the actual mechanism parts. These models showed the mechanism was highly difficult to tune for a single configuration. This difficulty largely reduced the probability of achieving successful docking maneuvers. Consequently, the layout of the mechanism was greatly modified. In particular, two active degrees of freedom were added to the passive existent ones. These degrees of freedom consisted of orthogonal linear axes mounted in series. The objective was to use the controlled axes to maintain the exchanged forces between the docking halves as small as possible.

The second iteration of the mechanism was thoroughly analyzed. All the actuators and transmission chains were fully designed based on the envisaged loads and the guidelines of the ECCS standards. Subsequently, new numerical models were implemented to confirm the functioning of the mechanism and the suitability of the selected electric actuators. Firstly, a 2D maneuver was simulated in Simscape Multibody™. The results of this model increased the confidence on the designed layout. Secondly, a 3D model was implemented in a co-simulation between Altair HyperWorks and solidThinking Activate. The dynamics of the docking maneuver were solved by HyperWorks while Activate simulated the control system. The results of this model further proved the suitability of the whole docking system.

The result of this work is the CLAS-S (**C**entral **L**inear **A**ctive **S**ystem for the **S**TRONG mission), a central docking mechanism that includes several features that may be beneficial in several cooperative servicing missions: reduced dimensions, reduced weight, the absence of post-contact thrust, and potentially improved docking success probability and safety. The reduction of the exchanged contact forces by means of the active system facilitates the capture of the probe by avoiding the separation of the spacecraft after the first contact. Following the successful simulation

results, the technical drawings were generated and the construction process was started.

Finally, the test bench was designed. It is based on a serial manipulator equipped with a force-torque module. The female half of the mechanism is transported by the manipulator while the male part is fixed to a common support. The objective is to simulate relative movements between the halves. In addition, the test protocols were also individuated. Currently, the test rig is under construction and the control software is being implemented. In the future, these tests will verify the technical readiness level of the mechanism. Moreover, they will be used as an optimization tool to improve both the control software and the mechanical parts.

References

[1] National Aeronautics and Space Administration: On-Orbit Satellite Servicing Study, Project Report (2010). URL https://sspd.gsfc.nasa.gov/images/nasa_satellite%20servicing_project_report_0511.pdf

[2] Wormnes, K., Le Letty, R., Summerer, L., Schonenborg, R., Dubois-Matra, O., Luraschi, E., Cropp, A., Krag, H., Delaval, J.: ESA technologies for space debris remediation. In: Proceedings of the 6th IAASS Conference: Safety is Not an Option, pp. 3–4 (2013)

[3] Flores-Abad, A., Ma, O., Pham, K., Ulrich, S.: A review of space robotics technologies for on-orbit servicing. Progress in Aerospace Sciences **68**, 1–26 (2014)

[4] Fehse, W.: Automated rendezvous and docking of spacecraft, vol. 16. Cambridge University Press (2003)

[5] Cook, J., Aksamentov, V., Hoffman, T., Bruner, W.: ISS interface mechanisms and their heritage. In: AIAA SPACE 2011 Conference & Exposition, pp. 27–29 (2011)

[6] Japan Aerospace Exploration Agency: Common Berthing Mechanism Acceptance Test of the Japanese Experiment Module "Kibo". URL http://iss.jaxa.jp/iss/kibo/develop_status_17_e.html

[7] Ezell, E.C., Ezell, L.N.: The Partnership: A NASA History of the Apollo-Soyuz Test Project. Courier Corporation (2013)

[8] NASA Space Science Data Coordinated Archive: Gemini 8. URL https://nssdc.gsfc.nasa.gov/nmc/spacecraftDisplay.do?id=1966-020A

[9] NASA Space Science Data Coordinated Archive: Cosmos 186. URL https://nssdc.gsfc.nasa.gov/nmc/masterCatalog.do?sc=1967-105A

[10] NASA Space Science Data Coordinated Archive: Apollo 9. URL https://nssdc.gsfc.nasa.gov/nmc/spacecraftDisplay.do?id=1969-018A

[11] NASA Space Science Data Coordinated Archive: ASTP-Soyuz. URL https://nssdc.gsfc.nasa.gov/nmc/spacecraftDisplay.do?id=1975-065A

[12] NASA Space Science Data Coordinated Archive: STS 71. URL https://nssdc.gsfc.nasa.gov/nmc/spacecraftDisplay.do?id=1995-030A

[13] Defense Advanced Research Projects Agency: Orbital Express space operations architecture. URL http://archive.darpa.mil/orbitalexpress/index.html

[14] Dotts, H., Nolting, R., Hoyler, W., Havey, J., Carter, T., Johnson, R.: Operational characteristics of the docked configuration. In: Gemini Summary Conference, NASA-SP-138, Huston, TX, pp. 41–54. NASA (1967)

[15] Syromyatnikov, V.: Docking devices for Soyuz-type spacecraft. In: 6th Aerospace Mechanism Symposium (1972)

[16] Syromyatnikov, V.: Docking-mechanism attenuator with electromechanical damper. In: 5th Aerospace Mechanism Symposium (1971)

[17] European Space Agency: Soyuz rendezvous and docking explained. URL https://www.youtube.com/watch?v=M2_NeFbFcSw&t=1100s

[18] Bloom, K., Campbell, G.: The Apollo docking system. In: 5th Aerospace Mechanism Symposium (1971)

[19] Langley, R.D.: The Apollo 14 docking anomaly. In: 7th Aerospace Mechanism Symposium, pp. 191–201 (1972)

[20] Syromyatnikov, V.: Docking system of androgynous and peripheral type. In: 7th Aerospace Mechanism Symposium, pp. 27–35 (1972)

[21] Swan, W.: Apollo-Soyuz test project docking system. In: JPL 10th Aerospace Mechanism Symposium, pp. 27–35 (1976)

[22] Hendrickx, B., Vis, B.: Energiya-Buran: the Soviet space shuttle. Springer Science & Business Media (2007)

[23] Defense Advanced Research Projects Agency: ORBITAL EXPRESS (2007). URL http://archive.darpa.mil/orbitalexpress/pdf/oe_fact_sheet_final.pdf

[24] Christiansen, S., Nilson, T.: Docking system for autonomous, un-manned docking operations. In: Aerospace Conference, 2008 IEEE, pp. 1–14. IEEE (2008)

[25] NASA, Roscosmos, JAXA, ESA, CSA: International Docking System Standard, Interface Definition Document, Revision E (2016). URL http://internationaldockingstandard.com/

[26] European Space Agency: International Berthing Docking Mechanism facts sheet. URL http://wsn.spaceflight.esa.int/docs/Factsheets/27%20IBDM.pdf

[27] Hardt, M., Mas, C., Ayuso, A., Cocho, D., Mollinedo, L., Gracia, O., Urmston, P.: Validation of space vehicle docking with the international berthing & docking mechanism and a kuka robot. In: 14th European Space Mechanisms and Tribology Symposium, Konstanz (2011)

[28] Boesso, A., Francesconi, A.: ARCADE small-scale docking mechanism for micro-satellites. Acta Astronautica **86**, 77–87 (2013)

[29] Olivieri, L., Francesconi, A.: Design and test of a semiandrogynous docking mechanism for small satellites. Acta Astronautica **122**, 219–230 (2016)

[30] World Intellectual Property Organization: International Patent Classification. URL http://web2.wipo.int/classifications/ipc/ipcpub

[31] Tchoryk, P., Pavlich, J., Ritter, G., Hays, A.B.: Autonomous satellite docking system (2004). US Patent 6,742,745

[32] Pruett, E.C., Robertson, K.B., Loughead, T.E.: Satellite retrieval system (1983). US Patent 4,391,423

[33] Hujsak, E.J., Siden, L.E.: Docking system for space structures (1979). US Patent 4,177,964

[34] Gurevich, L.: Adjustable multipoint docking system (2005). US Patent 6,840,481

[35] Howard, N., Nguyen, H.D.: Magnetic capture docking mechanism (2010). US Patent 7,815,149

[36] European Space Agency: Technology Readiness Levels Handbook for Space Applications (2008). URL https://artes.esa.int/sites/default/files/TRL_Handbook.pdf

[37] Arianespace: Vega User's Manual, Issue 4 - Revision 0 (2014)

[38] Messidoro, P., Perino, M.A., Boggiatto, D.: Enabling technologies for space exploration systems: The steps project results and perspectives. Acta Astronautica **86**, 219–236 (2013)

[39] Kapurch, S.J.: NASA Systems Engineering Handbook. DIANE Publishing (2010)

[40] SpaceX: CAPABILITIES & SERVICES. URL http://www.spacex.com/about/capabilities

[41] Romano, M., Friedman, D.A., Shay, T.J.: Laboratory experimentation of autonomous spacecraft approach and docking to a collaborative target. Journal of Spacecraft and Rockets **44**(1), 164–173 (2007)

[42] Yaskevich, A.: Combined equations of motion for description of dynamics of spacecraft docking using the pin-cone system. Cosmic Research **45**(4), 305–316 (2007)

[43] Han, W., Huang, Y., Chen, X., Zhang, X.: Flexible cone impact dynamics based on space probe-cone docking mechanism. Science China Physics, Mechanics and Astronomy **57**(1), 128–137 (2014)

[44] Zhang, X., Huang, Y., Han, W., Chen, X.: Accurate shape description of flexible beam undergoing oblique impact based on space probe-cone docking mechanism. Advances in Space Research **52**(6), 1018–1028 (2013)

[45] European Cooperation for Space Standardization: ECSS-E-ST-33-01C, Space engineering: Mechanisms (2003)

[46] Davis, J.R.: Concise metals engineering data book. ASM international (1997)

[47] Rapisarda, A., Amati, N., Gagliardi, L., Detoni, J., Galluzzi, R., Gasparin, E., Nebiolo, M., Stio, A.: Design and experimental characterization of electromagnetic shock absorbers for landing gears. In: Proceedings of the 63rd International Astronautical Congress, Naples, Italy (2012)

[48] Gosline, A.H., Hayward, V.: Eddy current brakes for haptic interfaces: Design, identification, and control. IEEE/ASME Transactions On Mechatronics **13**(6), 669–677 (2008)

[49] Norton, R.L.: Cam design and manufacturing handbook. Industrial Press Inc. (2009)

[50] Tabakman, A.: NASA Docking System (NDS) Users Guide: International Space Station Program. Type 4 (2010). URL https://ntrs.nasa.gov/archive/nasa/casi.ntrs.nasa.gov/20110011626.pdf